# Contribution to the characterization and 3D modeling of the anisotropy of grain-oriented electrical steels for the calculation of losses at the end-regions of turbo-generators

Leysmir Adriana Millan Mirabal

École doctorale ENGSYS-632 – Collège doctoral de l'Université de Lille
Université de Lille : Sciences et Technologies

**Thèse de**

## Doctorat de l'Université de Lille

Spécialité : **Génie électrique**

par

**Leysmir Adriana MILLAN MIRABAL**

# Contribution à la caractérisation et à la modélisation 3D de l'anisotropie des aciers électriques à grains orientés en vue du calcul des pertes aux extrémités des turbo-alternateurs

Soutenue le **28 Juin 2021** devant le jury composé de :

| | | |
|---|---|---|
| M. Didier TRICHET | Professeur des universités, Université de Nantes | Rapporteur |
| M. Fabien SIXDENIER | Maître de Conférences HDR, Université C. B. Lyon 1 | Rapporteur |
| Mme. Afef LEBOUC | Directrice de Recherche au CNRS, G2Elab | Examinatrice et présidente |
| M. Abdelkader BENABOU | Maître de Conférences HDR, Université de Lille | Directeur |
| M. Yvonnick LE MENACH | Professeur des universités, Université de Lille | Co-directeur |
| M. Oualid MESSAL | Maître de Conférences, Université de Lille | Co-encadrant |
| M. Jean-Yves ROGER | Ing. Chercheur, EDF | Invité |

École doctorale ENGSYS-632 – Collège doctoral de l'Université de Lille
Université de Lille : Sciences et Technologies

**Doctoral thesis from the**

**University of Lille**

Specialty: **Electrical Engineering**

by

**Leysmir Adriana MILLAN MIRABAL**

# Contribution to the characterization and 3D modeling of the anisotropy of grain-oriented electrical steels for the calculation of losses at the end-regions of turbo-generators

Defended the **28th June 2022** before a jury composed of:

| | | |
|---|---|---|
| M. Didier TRICHET | University professor, Université de Nantes | Rapporteur |
| M. Fabien SIXDENIER | Senior lecturer HDR, Université C. B. Lyon 1 | Rapporteur |
| Mme. Afef LEBOUC | Research Director at CNRS, G2Elab | Examiner and president |
| M. Abdelkader BENABOU | Senior lecturer HDR, Université de Lille | Director |
| M. Yvonnick LE MENACH | University professor, Université de Lille | Co-director |
| M. Oualid MESSAL | Senior lecturer, Université de Lille | Supervisor |
| M. Jean-Yves ROGER | Research engineer, EDF | Guest |

# Résumé

Récemment, les gestionnaires de réseau et de système de transmission, comme le Réseau européen des gestionnaires de réseau de transport d'électricité (ENTSO-E), mettent en place des réglementations pour étendre la plage de fonctionnement des équipements connectés au réseau électrique. Les principaux objectifs de ces modifications sont : d'augmenter la flexibilité du réseau en le rendant capable de supporter des variations de fréquence et de tension (dues aux modifications de l'équilibre des puissances active et réactive) et de faciliter l'intégration et la production d'énergie renouvelable. Cependant, de nombreux équipements installés et raccordés au réseau n'ont pas été conçus pour être exploités dans ces plages de fonctionnement et leur utilisation dans ces conditions peut avoir un impact négatif sur le cycle de vie des équipements, en particulier dans les turbo-alternateurs.

Les grands turbo-alternateurs, utilisés pour la production d'électricité dans les centrales nucléaires et hydroélectriques, sont impactés par ces nouvelles réglementations. Cet impact est particulièrement observé aux extrémités de ces machines électriques où les pertes fer sont susceptibles d'augmenter significativement. Ces pertes peuvent entraîner des échauffements, notamment des points chauds, qui peuvent conduire à la fusion de l'isolation entre les tôles du noyau du stator, provoquant ainsi des courts-circuits et des dommages irréversibles à l'équipement. Afin de pouvoir analyser et limiter l'impact des mécanismes physiques mis en jeu, la société EDF s'appuie sur des simulations numériques tridimensionnelles de la machine électrique pour calculer les pertes pour différents régimes de fonctionnement.

Une partie de ce travail a déjà été réalisée au laboratoire L2EP, où le logiciel d'analyse par éléments finis code_Carmel a été adapté pour le calcul des pertes dans le noyau du stator et des pertes joule dans les modèles tridimensionnels. Cependant, la complexité physique des propriétés des circuits magnétiques aux extrémités des turbo-alternateurs doit être prise en compte pour obtenir des résultats fiables. En effet, compte tenu du schéma tridimensionnel du chemin du flux magnétique et des propriétés fortement anisotropes du circuit magnétique en acier électrique à grains orientés (GO), la description des pertes fer nécessite des modèles de matériaux magnétiques anisotropes précis combinés à une modélisation numérique efficace.

Dans le cadre de ce travail de thèse, des modèles anisotropes dédiés aux aciers GO, notamment pour décrire la loi de comportement et les pertes fer, ont été étudiés puis implémentés dans un environnement de simulation par éléments finis (FEM) au sein du logiciel code_Carmel. La mise en œuvre a été validée par rapport à des données expérimentales obtenues sur un acier GO de qualité industrielle conventionnelle

généralement utilisée dans les turbo-alternateurs. De plus, un démonstrateur expérimental a été développé pour étudier plus finement le comportement magnétique d'un empilement de tôles GO soumis à des excitations de flux magnétique 3D non conventionnelles. Un modèle numérique du démonstrateur expérimental a été développé et étudié, incluant les modèles de matériaux anisotropes, en comparant le comportement global du matériau GO ainsi que les pertes de fer dans l'échantillon d'intérêt.

Les résultats montrent que, dans des configurations d'attaque de flux magnétique non conventionnelles, en particulier avec une attaque de flux magnétique normale au plan de laminage, les caractéristiques anisotropes de l'acier GO peuvent influencer la distribution du flux magnétique dans l'empilement de tôles étudié ainsi que les pertes de fer associées. Notamment, et comme attendu, les pertes par courants de Foucault classiques constituent la contribution majeure aux pertes fer dans l'empilement de tôles étudiées.

# Abstract

Recently, network and transmission system operators like the European Network of Transmission System Operators of Electricity (ENTSO-E) have started to create regulations to extend the range of operation of the equipment connected to the electrical grid. The main purposes of these changes are: to increase the flexibility of the grid by making it able to withstand variations of frequency and voltage (due to alterations in the active and reactive power balance), and to ease the integration of renewable energy generation. However, many of the installed equipment connected to the grid have not been conceived to be exploited in these operating ranges and their use under these conditions will have a negative impact, especially on the turbo-generators life cycle.

Large turbo-generators, used for the generation of electricity in nuclear and hydroelectric power plants, are affected by these new regulations. This impact is especially evident at end-regions of these electrical machines, where the iron losses are likely to increase significantly. These losses can lead to overheating, in particular hot points which can lead to the melting of the insulation layers between the lamination of the stator core, causing short-circuits and irreversible damage to the equipment. To be able to analyze and limit the impact of the involved physical mechanisms, the EDF Company works with tridimensional numerical simulations of the electrical machine to calculate the losses under different regimes of operation.

Part of this work has already been realized in the L2EP laboratory, where the finite element analysis software code_Carmel have been adapted for the calculation of core losses and joule losses in tridimensional models. However, the physical complexity of the magnetic circuit properties at the end-regions of turbo-generators must be accounted for, in order to have reliable results. Indeed, considering the tridimensional pattern of the magnetic flux path and the strongly anisotropic properties of the magnetic circuit made from grain oriented electrical steel (GOES), the description of the iron losses requires accurate anisotropic magnetic material models combined with an efficient numerical modelling.

In the framework of this PhD work, anisotropic GOES models, related to the behavior law and iron losses, have been studied and successfully implemented in a finite element method (FEM) simulation environment within the software code_Carmel. The implementation has been validated against experimental data achieved on an industrial conventional GO grade typically used in turbogenerators. Also, an experimental demonstrator has been developed to investigate more closely the magnetic behavior of a lamination stack made of GOES under non-conventional 3D magnetic flux excitations. A numerical model of the experimental demonstrator has been developed and studied with

the implemented material models by comparing the global behavior of GOES as well as the iron losses in the sample of interest.

The results show that under non-conventional magnetic flux attack configurations, especially with a magnetic flux attack normal to the lamination plane, the anisotropic characteristics of the GOES can influence the magnetic flux distribution within the lamination stack and the associated iron losses. In particular, the classical eddy current losses constitute, as expected, the most significant contribution of the total iron losses in the GOES laminations.

# Remerciements

Je tiens tout d'abord à remercier les membres du jury pour leur présence, pour leur lecture attentive de ma thèse ainsi que pour les remarques qu'ils m'ont adressé lors de cette soutenance afin d'améliorer mon travail.

Je voudrais exprimer ma gratitude à mes directeurs de recherche, *Abdelkader Benabou*, *Yvonnick Le Menach* et ainsi à mes encadrants *Oualid Messal* du laboratoire L2EP, ainsi que *Jean-Yves Roger* et *Jean-Pierre Ducreux* du côté EDF pour m'avoir accompagnée et soutenue tout au long de ce doctorat. J'ai eu la chance de pouvoir travailler avec une très bonne équipe et je vous remercie sincèrement.

*Abdelkader*, merci de ta patience, et d'avoir été toujours là pour résoudre mes doutes, mes problèmes, et pour tes exigences qui me poussent à faire toujours de mon mieux.

*Oualid*, merci pour tout ton travail, de m'avoir épaulée, je suis vraiment reconnaissante de l'aide et des conseils donnés et aussi pour avoir toujours pris le temps de m'écouter et m'avoir aidé à résoudre des problèmes.

*Yvonnick*, merci pour ton assistance, tu m'as beaucoup soutenu sur la partie numérique, également à voir le côté positif des choses. Tes conseils et critiques constructives ont été importants pour l'avancement de ma thèse.

*Jean-Yves*, merci d'avoir résolu tous mes doutes sur les turbo-alternateurs, pour m'avoir écoutée quand il y avait des problèmes et pour m'avoir facilité l'intégration lors de mon passage chez EDF.

Et finalement *Jean-Pierre*, merci pour toutes les corrections, pour m'avoir toujours envoyé des articles intéressants et pour le support que tu m'as donné tout ce temps.

J'aimerais remercier également tout le personnel du laboratoire L2EP et les membres du département ERMES à EDF R&D, une mention spéciale à *Loic Chevallier* et *Julien Korecki* pour votre support avec la prise en main du code_Carmel. Par ailleurs, merci à *Thierry Dusquene* et *Olivier Ferla* pour leur aide précieuse pour la mise en place de la maquette et les moyens de mesure. Un grand merci aussi à mes collègues du L2EP, pour tous les bons moments qu'on a passés ensemble à Lille et pour avoir partagé cette expérience avec moi : *Angelica Torres*, *Hossein Taha*, *Florentin Salomez*, *Florian Tournez*, *David Ramsey*, *Ryan O. Berriel*, *Hugo Helbling*, *Marwane Dherbécourt*, *Meryeme Jamyl*, *Wissem Bekir*, *Marwane Dherbécourt*, *Antony El Hajj*, *Luis Ramirez, Vincent Martin* et tous ceux qui ont partagé avec moi pendant ces trois ans.

Finalement, à titre plus personnel, je remercie chaleureusement ma famille qui m'a toujours encouragé de loin, mes parents, ma sœur et aussi mes tantes, oncles et cousins,

pour leur soutien moral ininterrompu et leurs nombreux conseils tout au long de ma thèse.

Para cerrar quisiera agregar algunas palabras en español. Muchas gracias a toda mi familia y amigos por su apoyo, esta tesis no hubiera sido posible sin ustedes. Me alegra mucho poder compartir este logro con ustedes.

Los amo,

Leysmir ♥

# Table of Contents

# List of figures

# List of Tables

# Introduction

The development of efficient and sufficient energy sources to sustain industrial and economic grow is one of the most important challenges in modern society. This need for energy has continuously impulsed major technological advances concerning the development of electrical machines and even the electrical network, making them increasingly efficient, reliable and recently also more environmentally friendly.

In the last decades the global warming and the need for sustainable energy production has led to the rapid development of clean energy solutions, powered by solar, wind, and other renewable resources. These energy sources have been progressively integrated into the electrical network, representing up to 20% of the electricity produced in France in 2021.

However, the increasing volume of renewable energies, such as wind and solar power production, integrated in the electrical grid causes an important impact on the power system stability. This results from the high dependence of renewable energies on weather-related factors including sunlight, wind speed and water availability. As a consequence, the voltage and frequency stability of the grids can be significantly disturbed. For example, the voltage profile of the network may be modified leading to a modified active and reactive power balance in the network. This results in more losses that affect not only the stability of the grid but also the equipment, such as conventional synchronous generators.

Important developments are being made at this time, to solve these problems, but it is clear that the operating conditions of the electrical grid will not be the same in the future. A better control and prediction of the impact of renewable energy sources is then required.

Recently network and transmission system operators like the European Network of Transmission System Operators of Electricity (ENTSO-E) have started to create regulations to extend the range of operation of the equipment connected to the electrical grid. The main purposes of these changes are: to increase the flexibility of the grid by making it able to withstand variations of frequency and voltage (due to alterations in the active and reactive power balance), and to ease the integration of renewable energy sources. However, many of the installed equipment connected to the grid have not been conceived to be exploited in these operating ranges and it is possible that their use under these conditions will have a detrimental impact on the machine's life cycle.

Large turbo-generators, used for the generation of electricity in nuclear and hydroelectric power plants, are especially affected by these new regulations. This impact is particularly important at the end-regions of these electrical machines where the iron losses are likely to increase significantly. These losses, called 'end-region losses', cause overheating, in particular hot spots that may lead to significant damage requiring the equipment to be taken out of service for maintenance. Indeed, in these scenarios, the overheating can lead to the melting of the insulation layers between the laminations, causing short-circuits and irreversible damage to the equipment. Therefore, in order to analyze and estimate the impact of end-region losses and the involved physical mechanisms, the EDF Company develops tridimensional (3D) numerical simulations of the electrical machine to calculate the losses under different regimes of operation.

Part of this work has already been realized in the L2EP laboratory, where the finite element analysis software code_Carmel have been adapted for the calculation of conventional core losses and Joule losses in 3D finite elements (FE) numerical models. However, the physical complexity of the magnetic circuit properties at the end-regions of turbo-generators must be taken into account in order to have reliable results. Indeed, considering the tridimensional pattern of the magnetic flux path and the strongly anisotropic properties of the magnetic circuit, made from grain oriented electrical steel (GOES), the description of the iron losses requires accurate anisotropic magnetic material models combined with an efficient numerical modelling.

This PhD work deals with this problematic within the framework of a CIFRE agreement between the company Electricité de France, Research and Development division (EDF R&D) based in Saclay and the Laboratory of Electrical Engineering and Power Electronics (L2EP) from Lille. This thesis is also part of the CAMELIA 2 project in EDF R&D, which aims to develop new strategies and methods for the preservation of electrical rotating machines. The main objective of the present work is to study the behavior of GOES subjected to unconventional magnetic flux attacks. To that end, anisotropic material models (magnetic behavior law and losses) are investigated and applied to a conventional GOES used in turbo-generators. A dedicated experimental device is also developed to analyze different configurations of magnetic flux in the GOES of interest. Finally, FE numerical models are considered to assess the ability of the numerical tool to represent the experiment.

The manuscript is divided in four chapters:

- The first chapter introduces the industrial context of the study with specificities of end-region losses in high power turbo-generators, and the magnetic properties of GOES. First, a state of the art concerning the estimation and modelling of end-region losses as well as the relation between the end-losses and the operating range of the turbo-generators are presented. The second part of this chapter is dedicated to the state of the

art regarding the anisotropic models, of magnetic behavior law and iron losses, for GOES. The ability of different models to take into account the magnetic anisotropy of GOES and their limits will be treated in this chapter together with the commonly employed techniques for the characterization of magnetic properties of electrical steels.

- In the second chapter, the selected anisotropic models of behavior law and iron losses are introduced, as well as the procedures followed for their implementation in the FEM software code_Carmel. First, the particularity for the characterization of GOES materials is presented, especially the effect of the demagnetizing field when considering the characterization of GOES with the Epstein frame method. Secondly, the selected behavior law and iron loss models are presented and validated with experimental measurements made on the GOES of interest. Then, the numerical study of academic examples (Epstein frame and a ring core) are presented, discussed and compared with the experiment.

- The third chapter deals with the development of the experimental demonstrator that will be used for the investigation, under different excitation conditions, of the magnetic flux penetration into a GOES lamination stack, as well as the associated iron losses. First, the chapter introduces a brief state of the art of experimental devices developed in other studies dealing with similar problematics. Then, the design of the demonstrator specific to our work is presented together with the adopted experimental protocol. At last, the effects of a magnetic flux directed at the plane surface of the GOES lamination stack and the associated losses are experimentally investigated, analyzed and discussed.

- Finally, the fourth chapter closes this manuscript by a FE analysis of the demonstrator. Its numerical model is developed and studied with the implemented GOES material models. A detailed analysis of the magnetic flux distribution inside the GOES lamination stack, including the eddy currents and anisotropy of the stack, is realized. Two simulations cases have been considered: a linear anisotropic case and a non-linear isotropic case. The simulation results are compared with the measured magnetic fluxes and iron loss values.

# Chapter I. State of the Art

---

*The aim of this first chapter is to introduce the issue of end region losses encountered in the turbo-generators and to provide an overview of literature models and experimental demonstrators used to evaluate them.*

*The stator core fabrication of the turbo-generators relies on the use of grain oriented electrical steel (GOES). Main physical properties of interest are briefly recalled for electrical steels in general and for GOES in particular. An overview of existing anisotropic behavior laws and iron loss models for GOES is made from the literature.*

---

# Table of content

# 1. Turbogenerators and end region losses

## 1.1. Turbo-generators

Generators are electromechanical converters used to generate electricity in a variety of power plants (nuclear, hydro, gas, oil, etc.). They are designed to be used with turbine drives. The turbine, actioned by vapor of water or gas, provides the mechanical energy necessary to drive the generator which converts it to electrical power. They are very reliable, stable, efficient and have a great capacity to withstand peak-demand scenarios.

During the last 20 years, over 80% of the energy in France has been generated by large turbo-generators in nuclear plants [1]. These large turbo-generators present a rated power ranging from 900 MW up to 1900 MW. An illustration of a turbo-generator from General Electric is shown in Figure I.1.

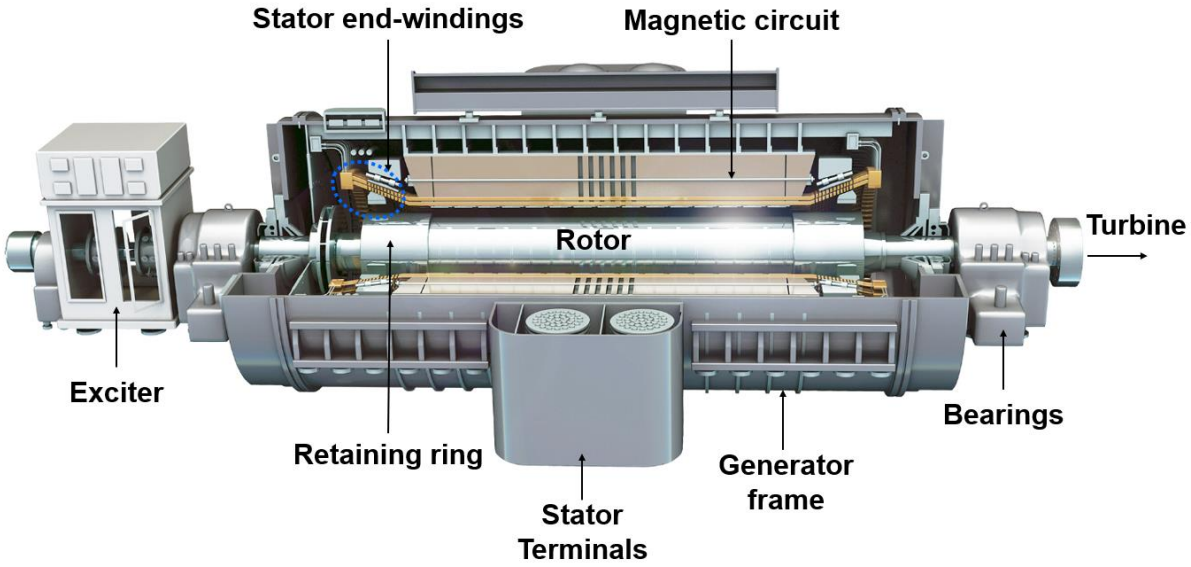


Figure I.1. Water cooled turbo-generator from General Electric. [2]

The stator core of the large turbo-generators is built up from GOES laminations with special attention to exploit the privileged magnetization direction RD. The associated magnetic properties are advantageous (high permeability, low losses) and permit to reduce the total size of the magnetic core of the stator while providing sufficient performances of the turbogenerator.

Due to their large dimensions, the stator core of turbogenerators is segmented in sectors or segments (generally from 10 to 24 sectors per ring layer [3] depending on the turbogenerator pole number and size). The segments are then laid side by side to form a full 360-degree ring layer. An overlapping of the segments, between two layers, is achieved in order to ensure mechanical stiffness of the core [4]. Finally, the ring layers are

stacked and held tightly together to form the stator core which contains several thousands of segments in total.

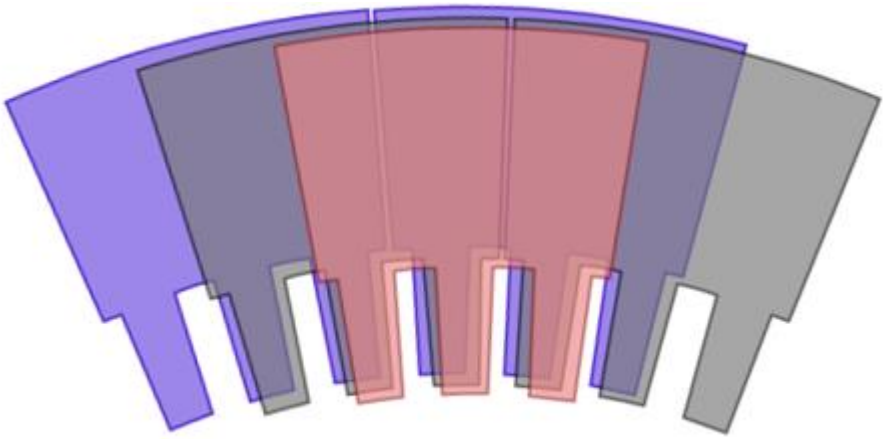

Figure I.2. Lamination stacking to form the stator magnetic circuit. [4]

Figure I.3. Stator core of the Hydro generator La Coche – G5 (237,8 MW) during the assembly step (Image from EDF).

Furthermore, different fasten elements in the end region of the stator hold the magnetic core laminations together and withstand the different forces during machine operation.

### 1.1.1. Losses in turbo-generators

The turbo-generators are synchronous machines, and like all the other electrical machines, they are subjected to power losses during operation. These losses come from different physical phenomena:

- Mechanical losses, mainly due to the friction and windage. They represent a significant percentage of the total losses.
- Copper losses also denominated as Joule losses due to the circulation of current through the stator and rotor conductors. They are the most predominant losses in turbo-generators.
- Iron losses, described in section 3.1.3. They depend on the magnetic flux density, the frequency and the quality of the electrical steel of the machine.

- Stray/additional losses, in the surrounding metallic parts of the turbogenerator. They are mainly due to the leakage and fringing fluxes leading to eddy current losses in the metallic parts.

Figure I.4 gives the proportion of the typical losses for a turbo-generator.

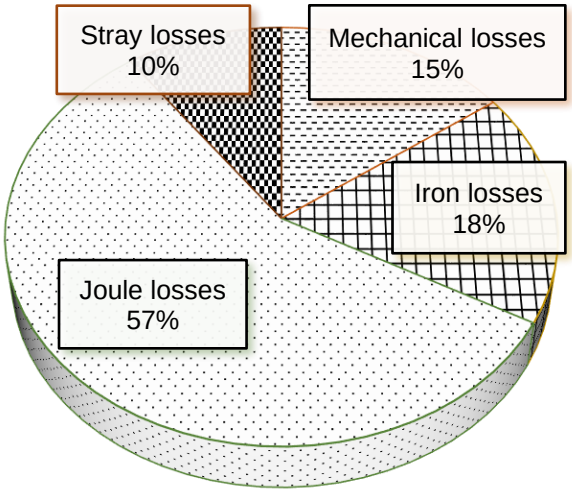


Figure I.4. Medium loss distribution for a turbo-generator. Plotted from [5].

All these losses reduce the energy efficiency of the turbogenerator. The knowledge of these losses is thus fundamental in order to be able to anticipate their effects on the performances, and to accurately determine the hot spots in the machine.

In this work, we focus on the iron losses, particularly in the end region of the stator magnetic core of turbogenerators.

## 1.2. End region losses

The end region losses that appear in the end region of the turbo-generators are due to the axial magnetic flux. The latter causes the saturation of the end regions of the stator magnetic core laminations and important eddy currents resulting in overheating and hot-spots that can be detrimental for the turbo-generator.

In this section, we briefly describe the end region losses, their origins according to the operating range of the turbo-generator, and different strategies that have been developed for their reduction.

### 1.2.1. Origin of end region losses in turbo-generators

In order to understand the origin of end region losses in turbo-generators, it is important to understand its end region geometry. This region has a particularly complex geometry where the main fixation elements are placed:

- *The press plate and press fingers*: these are used for fastening the stator core stacks over the entire stator end surface;
- *The rotor retention ring*: this element is made of non-magnetic steel, which restrains the end-rotor windings while providing mechanical support for the rotor against the centrifugal forces during its rotation;
- *The magnetic flux screen* that shields the stator core against the stray leakage flux. It can be made of either: an electrical conductor (e.g. copper in Figure I.5), a magnetic shunt shield (see Figure I.7), or a truncated ring, avoiding the concentration of large stray fields in the end region, as presented in Figure I.6.
- *The stator end-windings*: these are conductive bars with a particular complex geometry interconnecting the stator windings (see Figure I.10).
- *The rotor end-windings*: made also from conductive bars with a simpler geometry interconnecting the rotor bars.

All these elements are shown in Figure I.5 representing a real 3D geometry of a turbogenerator from EDF.

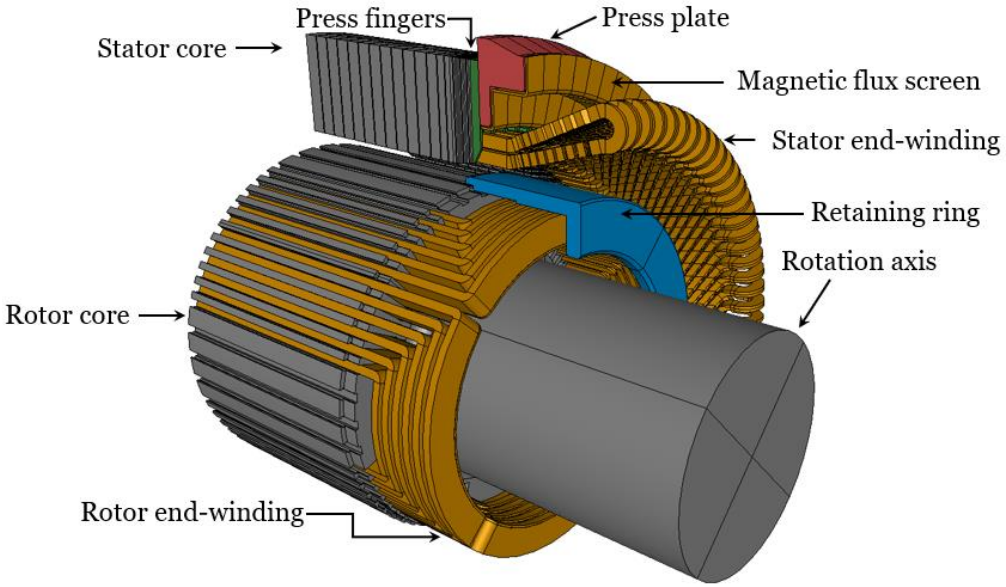


Figure I.5. End region of a large turbo-generator.

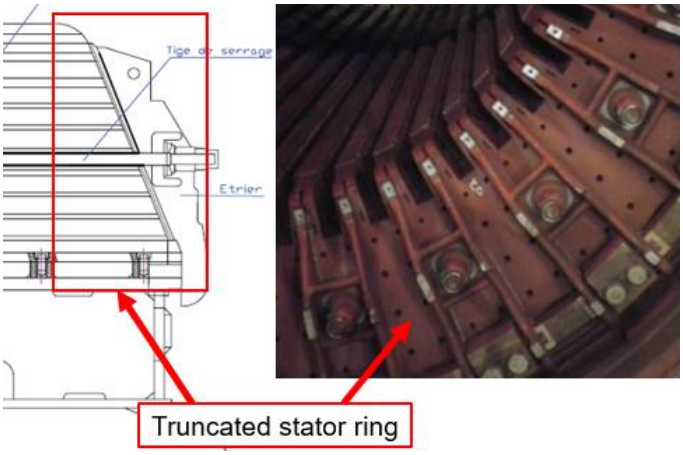


Figure I.6. Truncated ring in the end of the stator core (Image from EDF).

When the machine operates, three different leakage flux components appear in the end region as shown in Figure I.7.

- *The stator end-winding leakage flux*, due to the currents in the stator windings. It is the most problematic, due to its three-dimensional nature;
- *The rotor end-winding leakage flux*;
- *The fringing flux,* due to the fringing of the magnetic field in the airgap area (between the stator and rotor cores).

One must note that the resultant leakage flux orthogonally penetrates all the conductive parts of the end region. This generates important eddy current losses and a significant rise in temperature. The magnetic field in the end region is represented in Figure I.8.

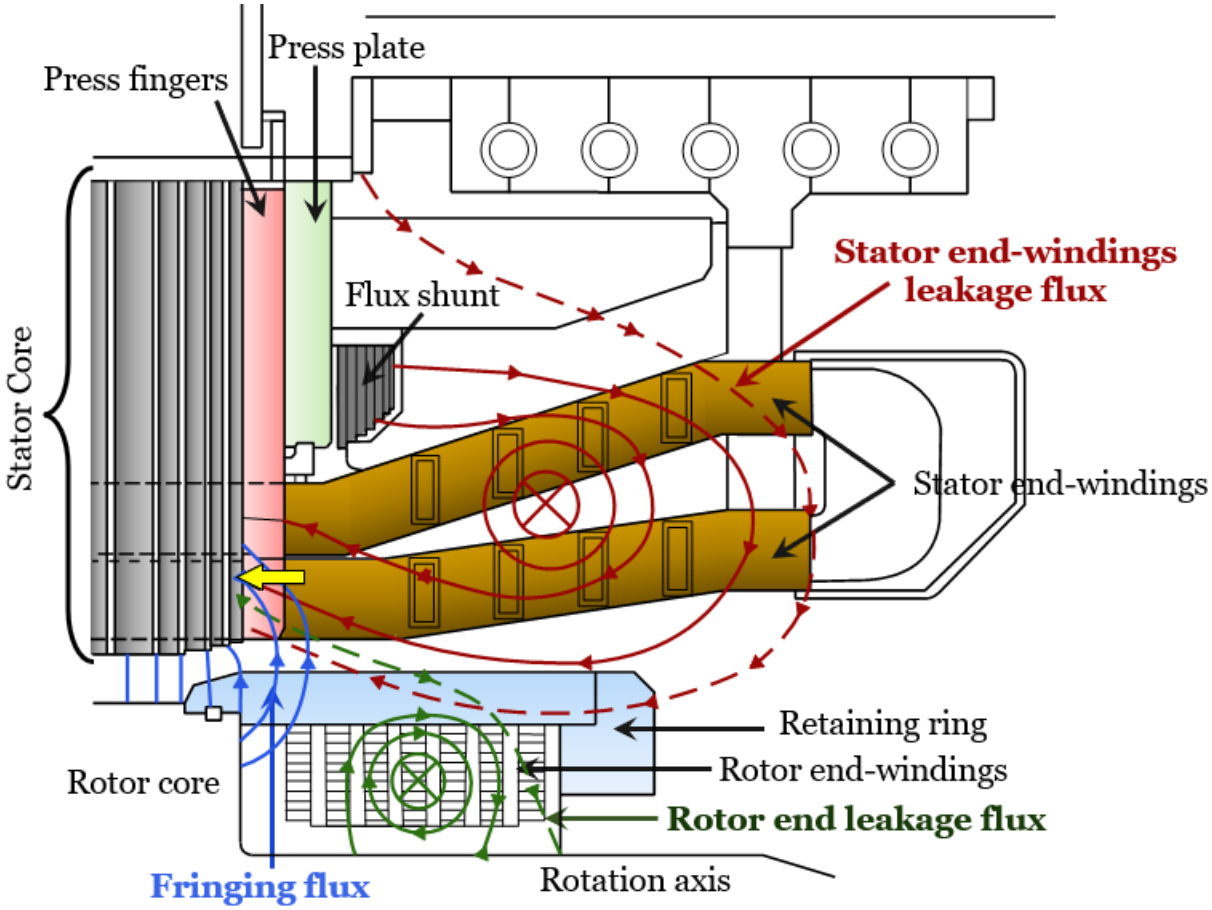


Figure I.7. Distribution of the axial flux sources in the end region. The yellow arrow indicates the position of the stator teeth.

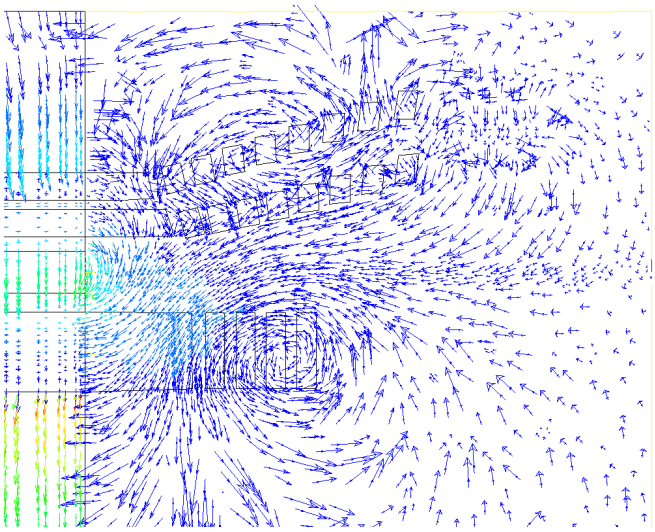

Figure I.8. Distribution of the magnetic induction in the front part of the machine. [6]

These losses can be really detrimental for the stator core-end area. Indeed, the resulting overheating can lead to hot spots, short-circuits between the laminations, burning of the insulation coating, etc. Figure I.9 shows the disastrous consequences of such overheating where the insulation between the magnetic laminations is completely degraded. In some cases, this can even increase the risk of melting of the magnetic circuit.

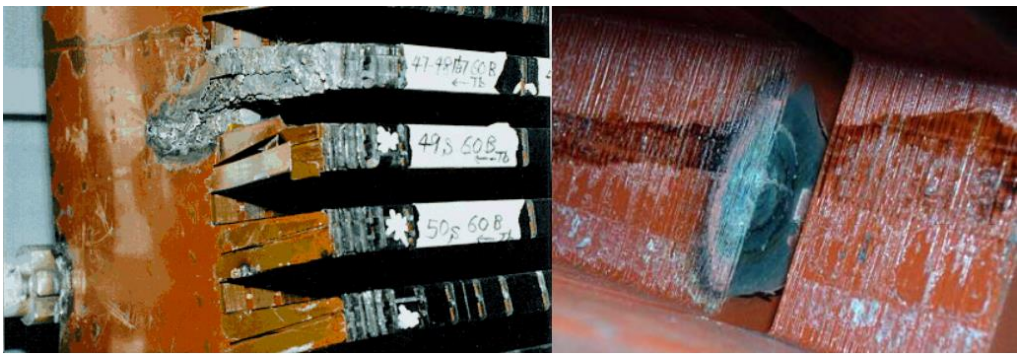

Figure I.9. Degradation of stator core due to a short-circuit between the stator laminations. [4]

### 1.2.2. Strategies for reducing the end region losses

The overheating and losses in the turbo-generator end regions were studied around the 60's, with the advent of high-power turbo-generators of around 500 MW [7]. Different strategies to reduce the losses causing this overheating were investigated. The most popular strategies can be summarized as follows:

- *Reduction of the rotor size*, the idea behind this proposal is that if we reduce the rotor length, the fringing flux passing through the rotor and the stator end is reduced as well, consequently, the losses in the end region are reduced.
- *Use of a flux shield*, as mentioned before, to shield the stator core end surface, preventing the eddy-current formation in the latter. This flux screen does not cover the stator teeth.

- *Stepping of the stator core end areas*, as shown in Figure I.10. This leads to a higher reluctance path in the stator *core end areas* and reduces the impact of the axial flux and the resulting losses.
- *Addition of radial slits*, known as Pistoye slots [8] in the stator core end teeth. This reduces the eddy current path widths within the teeth (see Figure I.10).
- *The use of a non-magnetic retaining ring*, which provides higher reluctance path for the leakage flux, and thus reduces the end region losses.

Almost all of these strategies have been integrated into modern turbo-generators. However, the end region losses are still present and limit the operating range of these turbo-generators.

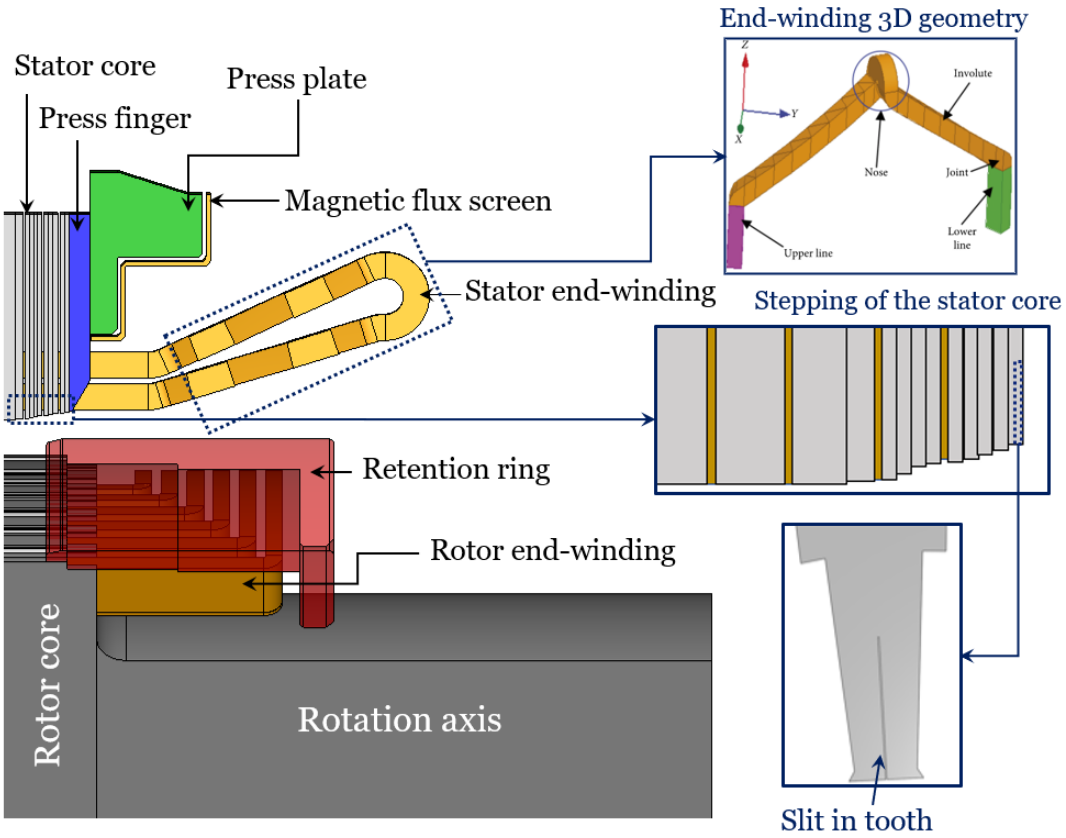


Figure I.10. Steeping and radial slits in the stator core of a turbo-generator. 3D End-winding geometry from [9].

### 1.2.3. Operating regime and end region losses

Turbo-generators have well defined operating ranges, depending on their characteristics: power range, operating points, nature of the load, insulation class, etc. The operating range is generally set by the manufacturers, and can be adapted by the operators, generally by introducing additional safety limits according to their experience. During operation, one of the main constraints is overheating which can degrade the insulation quality of the different parts of the turbo-generator. In this framework, turbo-generators are fabricated with a given insulation class type, according to the international

standard IEC 60085 which classes electrical machine insulations into four main categories: E, B, F and H represented in Figure I.11.

Each insulation class has a maximum temperature limit, which, if exceeded, can lead to the degradation of the machine and reduce its expected lifetime. The close connection between overheating and ageing in electrical machines is well known in the literature. Indeed, if an electrical equipment operates at the maximum temperature allowed by its insulation class, the expected lifetime is about 20 000 h. This lifetime can considerably increase or decrease according to the operating temperature, as shown in Figure I.12.

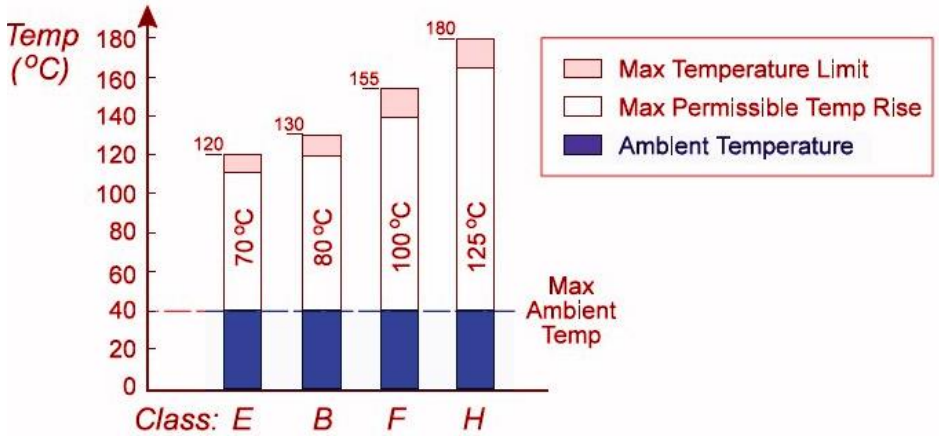


Figure I.11. Insulations classes according to IEC 60085:2007 for electrical machines. [10]

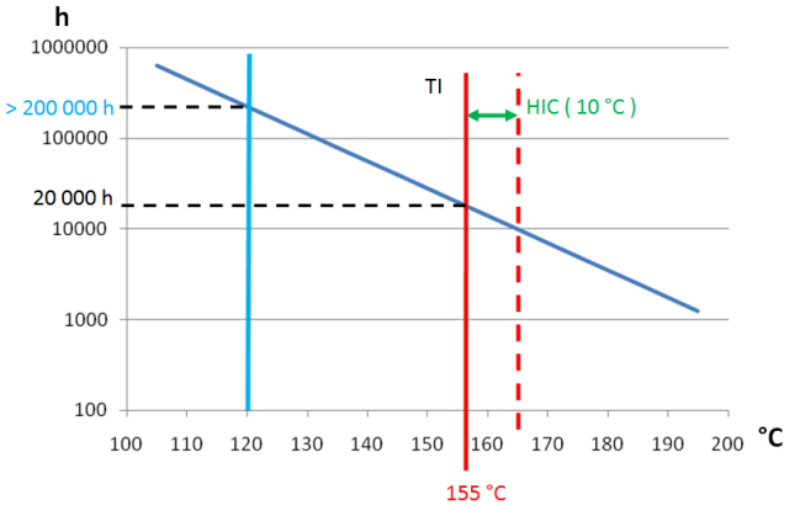


Figure I.12. Thermal endurance graph for a Class F insulation. By limiting the operating temperature to 120°C lifespan reaches 200,000 h. [11]

These principles apply for the case of EDF turbo-generators. Indeed, the latter have an insulation class F, with a temperature upper limit of 155 °C, but they are operated as class B (with a temperature upper limit of 130° C), in order to ensure an acceptable insulation lifetime.

The safety temperature limits within which a turbo-generator can operate are given by the capability curve or the P-Q diagram (P and Q being respectively the active and reactive powers). This diagram results from the turbo-generator phase diagram (see details in Appendix A). It is divided into two operating regimes:

- *The under-excited regime* (Q < 0), in which the reactive power is absorbed by the generator.
- *The over-excited regime* (Q > 0), in which the generator provides reactive power Q to the grid.

The boundaries of the turbo-generator operating diagram in normal conditions are defined by the curve segments numbered from 1 to 5 in Figure I.13. They mainly depend on: the voltage, the frequency and the temperature of the cooling fluid.

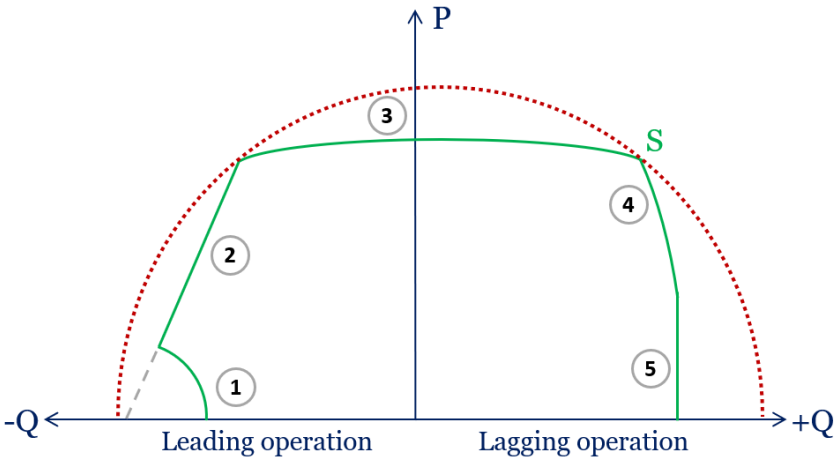


Figure I.13. P-Q Diagram for a turbogenerator.

- *Limit 1*, corresponds to the minimum field current necessary to operate the machine within a stable safety margin.
- *Limit 2*, imposed by the heating of the stator end zones due to the axial magnetic flux component creating eddy current and iron losses.
- *Limit 3*, corresponds to the stator current producing acceptable maximum heating in the stator core.
- *Limit 4*, corresponds to the maximum rotor current (or field current) producing acceptable maximum heating in the rotor.
- *Limit 5*, it appears only in large turbo-generators, it corresponds to a limit in terms of flux density in the airgap.

In particular, the 2nd limit is imposed by the heating of the turbo-generator end region parts in the under-excited operating regime, *i.e.*, it is the limit of absorption of reactive power. In practice, we consider that the heating remains acceptable if the internal angle δ (angle between the internal induced voltage E and the phase voltage V) is still inferior

to a certain limit value $\delta_o$. The value of $\delta_o$ is established by EDF engineers based on their own experience *(I.2)*

Starting from the phasor diagram of the turbo-generator, the limit 2 can be described in the plane *P*-*Q* by the following equations:

$$Q = -\frac{3V^2}{X_s} + P\ cotg\delta_o \qquad (I.1)$$

The angle $\delta_o$ is such that the limit passes through the nominal operating point in the under-excited operating regime imposed by the couple ($P_n$, $-0.8\times Q_n$). Hence:

$$cotg\delta_o = \frac{\frac{S_n}{X_s} - 0.8\ Q_n}{P_n} \qquad (I.2)$$

Where $S_n$, $Q_n$ and $P_n$ are respectively the nominal apparent, reactive and active powers and $X_s$ is the synchronous reactance.

For generators with a rated power of 500 MW or higher, because they all have the same nominal power factor $cos\phi \approx 0.9$, the formula becomes:

$$cotg\delta_o = \frac{\frac{V_n I_n}{X_s} - 0.8\ V_n I_n\ sin\phi}{V_n I_n cos\phi} = \frac{\frac{1}{X_s} - 0.8\ sin\phi}{cos\phi} = \frac{\frac{1}{X_s} - 0.8 \sin(\text{acos}(0.9))}{0.9}$$
$$cotg\delta_o = \frac{1/X_s - 0{,}35}{0.9} \qquad (I.3)$$

It clearly appears in *(I.1)* that the voltage has a very sensitive influence on the limit 2. The frequency, via the synchronous reactance, impacts also this limit.

In some operating scenarios voltage and frequency variations can appear on the network, due to the balance between the power requested by the sources and that requested by the loads (active and reactive). In such cases, the variations of voltage and frequency will move this limit outside the predefined operating area which may result in more end region losses and lead to overheating. To better understand and analyze these losses and their consequences, the development of experimental prototypes and analytical and/or numerical approaches are necessary. An overview of literature models is introduced in the following section.

# 2. End region losses in the literature

In this section, we present a synthesis of the literature investigations about the end region losses in electrical machines performed by means of analytical calculations, numerical modellings as well as by experimental approaches.

## 2.1. Analytical and numerical approaches

### 2.1.1. First developments (1940s to 1990)

The first studies were realized in the decade of 1950s we can cite those developed by Richardson [12] and Winchester [13] respectively in 1945 and 1955. These first models relied on the usage of heavy and time consuming, graphical and analytical approaches. They required tracing the magnetic induction by hand. Nevertheless, they were relatively precise, considering the exact geometry of the end region.

In the 60s, further analytical methods were developed [14] with important simplifications concerning the geometry and the magnetic behavior of the material. Important mentions are the developments of Lawrenson [15] in 1961, who was the first to take into account the real geometry of the stator coils in the analytical calculations and the works of Tegopoulos that in 1962-63 [16], [17] represented the end-winding currents with equivalent current sheets, and later used complex analytical calculations to study the axial magnetic field and eddy currents distribution in the simplified 2D end-region geometry of a turbo-generator.

In the same framework, in 1975, Colot (from EDF company) [18] established an analytical model to study the behavior of the axial flux and the distribution of the eddy currents in the stator core laminations at the end regions of a turbo-generator. This model was checked against measurements realized on an experimental demonstrator. The deviations were more than 30%.

During the 70s and 80s, with the advent of numerical methods, the analytical models were replaced by axiperiodic and quasi-3D finite element analysis. At this time due to the numerical limitations the models started to be developed for more specific purposes, whether to:

- Investigate the distribution of eddy currents and the effects of axial stray flux in stator laminations [19], [20].
- Study of the nature of the stray flux itself and the mechanical efforts produced inside the end-windings of the stator [21], [22] and [23].
- Reduce the axial flux and the end-region losses, testing different strategies: a shorter rotor length, the addition of slits and stepping in the ends of the stator

teeth [24] [25], use of a flux shunt in the ends of the stator core [26], or a combination of strategies [27].

Most of these first numerical methods considered the complex geometry of the stator end regions, but they were based on strong simplifying hypotheses.

At last, is important to mention the works of Jacobs *et al.* [28] in 1977, which offered a very good model of the end-region of a turbogenerator. He considered the saturation of the material and observed the eddy current and magnetic field distribution using a quasi-3D model and T-Ω formulation. His works inspired the developments of Jack and Mecrow [8], which also produced a quasi-3D model, and validated their results experimentally through measurements with a 600 MW turbo-generator.

### 2.1.2. 1990 – present (exclusively finite element simulation approaches)

Through the 90s, with the higher computational capacities, the first 3D finite element models were developed. The geometry of the end region parts was taken into account with more accuracy than in the previous quasi-3D models. Silva *et al.* in 1995 [29] and 1996 [30] established a very complete 3D model to evaluate the end region eddy current losses of a turbo-generator. A good agreement with previous works in the matter was obtained; however, in the study the saturation effects were neglected, and her results were not validated by experimental measurements. Richard *et al.* [31], in 1997, modeled (by using the software Flux 3D) the real geometry of a generator end-region including among other elements, the flux shields and end-windings. She analyzed the magnetic flux distribution in the steady state and the forces and vibrations in the end-windings during transient scenarios. In this case, however, the results were uncertain due to the position of the sensors.

During the decade of the 2000s, the 3D finite element studies continued [32] [33], most of the works focused on the distribution of the eddy-currents and stray flux density within the stator core and metallic parts surrounding the end regions, while looking for some strategies to reduce the computation time.

In 2006 Yao *et al*. [34] developed a non-linear 3D finite element model for the analysis of eddy currents in the end region of a turbo-generator by using reduced vector potential formulation. Equivalent magnetic permeability was used to take into account the anisotropy of homogeneous laminated cores. However, the mesh was not fine enough to perform a joule loss calculation.

Yamasaki *et al.* in 2008 [35] studied the effect of the eddy currents at the end region of a synchronous machine and their impact on the total losses. He was one of the first to consider a layer of insulation between the modeled laminations. Also, the method was validated by comparing the result with a simple test-bench.

Lin *et al.* [36] in 2010 studied, by means of 3D simulation, the effect of eddy-currents on the end shield and the frame of a large induction machine, and the influence of the material non-linearity through a 2D model. The authors concluded that the majority of the losses in the machine end region are produced in the stator core, and that the closeness of the metallic parts to the stator end-windings considerably increased the eddy current losses. Hamalainen [37] in 2012 developed a 3D model for the analysis of the stator, clamping ring and finger plate losses of a permanent magnet wind generator. In this case the use of a very fine mesh, allow an accurate calculation of the joule losses. Vogt [4] in 2013 developed a 3D finite element model using A-φ formulation to study the distribution the radial and axial fluxes in the end regions of a 900 MW turbo-generator. Given the complexity of the problem, the anisotropy of the GOES constituting the stator core was not taken into account in the proposed modelling.

More recent works have analyzed the overheating in end regions of some electrical machines [38] [39] and the effect of the operating and load conditions [40] [41] [42]. These issues have been treated by different authors, which presented some strategies to limit the temperature in the end region areas.

Finally, the most recent development concerning the modeling of the losses and eddy current in the stator core laminations is that of W. Wang *et al*. [43] in 2021. They evaluated the effects of the normal leakage flux and the distribution of eddy currents in the laminated core of a transformer with GO laminations, by means of a simple test-bench accompanied by a 3D simulation. The main focus of this work was to study the phase difference between the magnetic fluxes inside the lamination (alternative and stray flux) influenced the total losses. However only laminations oriented in the RD and TD were considered.

The majority of the models found in the literature focused either on the calculation of the distribution of the eddy current losses, or on the heat estimation in the end region of large turbo-generators. In all of these works, to our best knowledge, the anisotropy of the GOES that build up the stator core of turbo-generators is not taken into account. This is one of the main objectives of our work. Thus, in the following sections the grain-oriented materials will be introduced as well as the behavior law and iron loss models to represent their anisotropic behavior.

# 3. Generalities on magnetic materials

Magnetic materials are essential for the fabrication of the magnetic core/circuit of electrical energy conversion devices such as rotating electrical machines, transformers, sensors, etc. The following section briefly introduces the soft magnetic materials (SMM), particularly, the silicon-iron (Si-Fe) alloys used for the manufacture of the magnetic circuit of most electrical machines.

## 3.1. Soft magnetic materials

The magnetic materials are classified regarding their response to an applied magnetic field. Soft magnetic materials (SMM) are magnetically "soft" due to their ease of magnetization induced by an applied external field.

The main SMM categories are: soft iron (Fe), silicon-iron (Si-Fe), nickel-iron (Ni-Fe), cobalt-iron (Co-Fe), amorphous, nanocrystalline alloys and soft ferrites (Ni,Zn) and (Mn,Zn) ferrites. For a given application, the SMM to be used must be designed to meet the requirements of the application (magnetic performances, mechanical and thermal characteristics, operating frequency, cost, etc.). The SiFe alloy category is by far the largest category in terms of tonnage. In the framework of energy conversion applications, the SiFe alloys are more often called "electrical steels". Among these electrical steels we find: the non-oriented (NO) electrical steels more generally used in electrical motors and generators and the grain oriented electrical steels (GOES) used in power transformers as well as for the manufacturing of the stator core of large hydro and turbogenerators.

### 3.1.1. SMM and magnetic domain structure

As previously mentioned, SMM can be easily magnetized by applying an external magnetic field $\boldsymbol{H}$ [A/m]. This is an inherited characteristic of these materials due to their atomic structure. Indeed, at the atomic scale, a ferromagnetic material is composed of atoms wherein free electrons orbit the nucleus. The electronic structure leads to a regular assembly of localized magnetic moments associated to each of the atoms that build up the crystal. As a response to an external field $\boldsymbol{H}$, the resulting macroscopic magnetization $\boldsymbol{M}$ [A/m] is given by the ratio of the resultant magnetic moment $\boldsymbol{\mathcal{M}}$ [A.m$^2$] over the volume $v$ of the material according to *(I.4)*.

$$\boldsymbol{M} = \frac{\partial \boldsymbol{\mathcal{M}}}{\partial \mathrm{v}} \qquad (I.4)$$

The magnetization $\boldsymbol{M}$ is linked to the applied field $\boldsymbol{H}$ by:

$$\boldsymbol{M} = \chi \boldsymbol{H} \qquad (I.5)$$

Where: $\chi$ is the so-called magnetic susceptibility.

This material response in terms of magnetic flux density $\boldsymbol{B}$ [T] is given by *(I.6)*:

$$\boldsymbol{B} = \mu\boldsymbol{H} = \mu_0\mu_r\boldsymbol{H} = \mu_0(\boldsymbol{H} + \boldsymbol{M}) \qquad (I.6)$$

Where: $\mu$ is the absolute magnetic permeability, $\mu_0 = 4\pi 10^{-7}$ [H/m] the permeability of the vacuum and $\mu_r$ the relative permeability of the material. Also, $\mu_0\boldsymbol{M}$ ca be defined as the magnetic polarization **J** [T].

The relation *(I.6)* is the constitutive law that describe the magnetic behavior of the material, relating all the different fundamental magnetic quantities.

The absence of magnetization of a magnetic material without an external magnetic field is a consequence of the magnetic domain structure formed to reduce the total energy of the material. Indeed, at an intermediate scale between the atomic scale and the macroscopic scale, a ferromagnetic sample is spontaneously structured in uniform magnetization domains in order to minimize the total energy of the magnetic moment system. Two adjacent domains are separated by a transition layer called "a magnetic wall" or "Bloch wall".

The existence of these domains was theorized by Pierre Weiss in 1907 [44] [45]. This theory was approved in the 1930s when the magnetic domains (also called Weiss domains) were observed for the first time by F. Bitter in 1931 [46].

The magnetization processes in a SMM under external magnetic field $\boldsymbol{H}$ can be summarized in two processes: the displacements of the domain walls and the rotation of spontaneous magnetization within each domain.

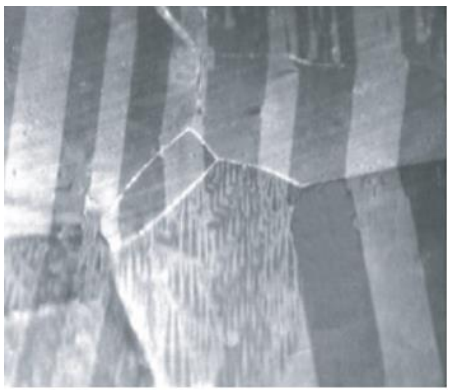

Figure I.14. Example of magnetic domains of a Fe-3%Si grain-oriented material [47]

–*Domain wall displacements:* under the effect of an external field, the volume of the favored domains (domains with a spontaneous magnetization which is oriented in the same direction, or close direction, as the magnetic field) increases to the detriment of other less-favored domains. This is a very important magnetization process in SMM. Some magnetic walls can be easily moved by a very weak field. Removing this field does not necessarily lead the walls to return to their initial position, hence the origin of the hysteresis in SMM.

–*Rotation of the magnetization:* the atomic moments, initially in a direction of easy magnetization, gradually deviate from their initial direction under the effect of an external field. It is a process of coherent rotation on the scale of all the moments of a same domain. The lower the anisotropy of the material, it appears more easily. Its main characteristic is that the moments return to their initial position as soon as the field disappears, that is what we call reversible magnetization process.

These two mechanisms can take place at the same time or separately depending on the material, the direction and the strength of the applied magnetic field. [48]

### 3.1.2. Normal B(H) characteristic and hysteresis loop

A SMM under a direct magnetic field describes a normal $B(H)$ curve (see the dotted blue curve in Figure I.15). However, when the SMM is submitted to an alternative magnetic field, the macroscopic behavior of the material results in a $B(H)$ loop; the hysteresis loop (see Figure I.15). It has to be mentioned that the normal magnetization curve can be obtained starting from the demagnetized state of equilibrium ($\boldsymbol{H} = 0$, $\boldsymbol{B} = 0$) by the extrema of centered stabilized loops measured in quasi-static regime (at the lowest possible frequency).

The hysteresis loop reflects all the main usage properties with regard to electrical engineering applications: the permeability $\mu$ (initial, differential, etc.) and the iron losses dissipated per magnetization cycle $P$ under given excitation conditions (the area enclosed by the loop). Other important magnetic properties that can be extracted from the hysteresis loop and give additional information about the material are: the remanence induction $B_r$, the saturation induction $B_s$, coercive magnetic field $H_c$, etc.

In practice, SMM are most often excited cyclically, especially in stator iron cores, and the evolution of iron losses (and permeability) with the frequency must be taken into account (see section 3.1.3). Indeed, the static properties are not sufficient to characterize the performance of SMM because they are rarely used in quasi-static regimes. Also, the iron losses are conditioned by the electrical resistivity of the material, the thickness of the sheets or ribbons and the nature of the magnetization mechanisms (coherent rotation of the magnetization vector or wall displacements) (see section 3.1.3).

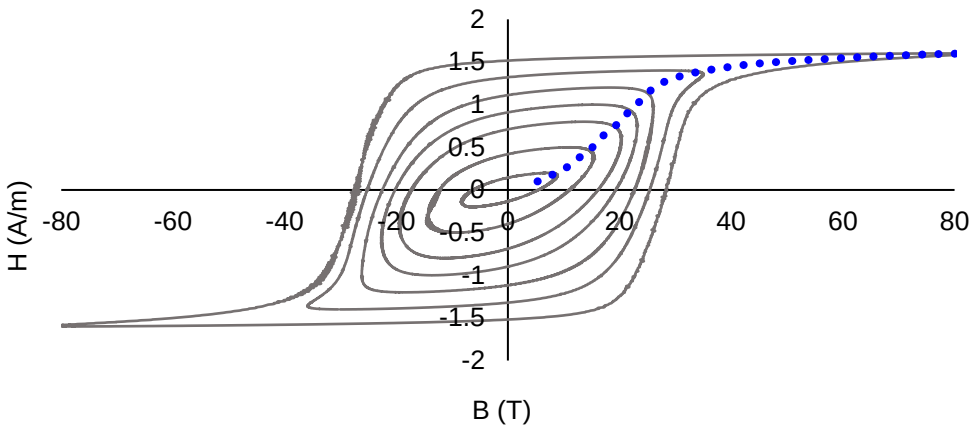


Figure I.15. Illustration of a normal B(H) characteristic (dotted line) and a hysteresis loops obtained from a conventional GOES Fe-Si grade CS150-35S magnetized in the RD at 50 Hz.

### 3.1.3. Iron losses

The total iron losses are generally decomposed into three terms:

- *The hysteresis losses ($P_h$):* the quasi-static losses, *i.e.*, the losses measured at the lowest possible frequency. Briefly, they are due to the evolution of the domain wall structure hindered by imperfections in the material (pinning sites) between the increasing and decreasing phases of the magnetic field.
- *The classical or eddy current losses* ($P_{cl}$): they are one of the dynamic loss components. They appear because SMM are electrically conductive. They are due to the induced currents under a time varying magnetic field [49]. These losses increase with the excitation frequency and the electrical conductivity of the material.
- *The excess losses* ($P_{exc}$): they are the second dynamic loss component. These losses, as theorized by G. Bertotti [50], are basically due the interactions between groups of domain walls (the domain walls of a group are strongly correlated by their mobility characteristics under a time varying magnetic field). Like the classical losses, the excess losses increase as the magnetization frequency increases.

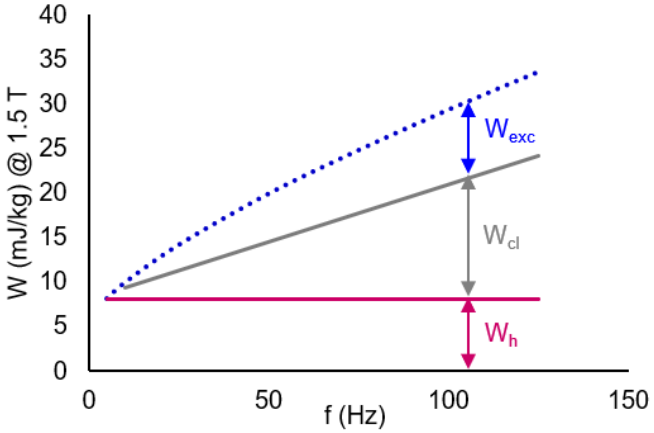


Figure I.16. Procedure of decomposition of the total iron losses per cycle at 1.5 T, in the case of a conventional GOES. Notice that W = *P*/*f*.

## 3.2. Grain oriented electrical steels (GOES)

After describing the general magnetic properties of SMM in section 3.1, this section deals with the GOES.

### 3.2.1. Goss texture

A very important step in the history of electric steels is the fortuitous discovery in 1934 of the texture {110} <001> which owes its great popularity to its inventor Norman P. Goss [51]. Indeed, by applying a succession of specific metallurgical procedures to a Fe-(3 wt%)Si such as cold rolling, heat treatments or annealing for the recrystallization, etc., N. P. Goss observed that the metallurgical grains grow with an easy direction of magnetization <100> along the RD of the strip, *i.e.*, with the best magnetic properties. The [110] at 90° to RD represents the transverse direction (TD) and the direction [100] at 54.7° to RD is the so-called the hard magnetization direction.

Thanks to the grain orientation, the magnetic properties of the material along its RD are greatly improved. This is very suitable for example in transformers where unidirectional flux is desired. Nevertheless, this orientation is not perfect: around 6-8° of grain misorientation in conventional GOES, and 2-3° in high permeability GOES.

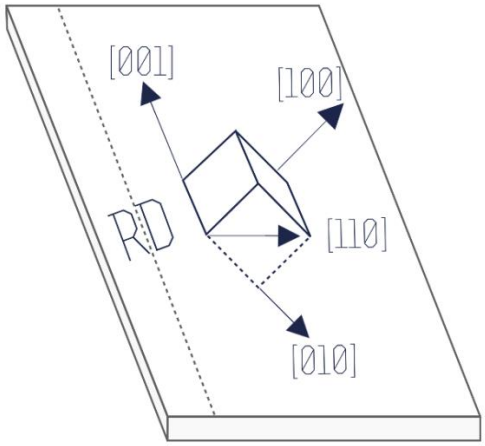


Figure I.17. Goss texture of industrial GO steel.

### 3.2.2. The development of GOES

Since the discovery of the Goss texture and for about fifteen years, the American steelmaking company ARMCO has improved the industrial production processes by optimizing all stages for the manufacturing of GOES: initial hot rolling, decarburization process, final annealing, etc. [52]. ARMCO efforts were fruitful in 1945 with the marketing of the first conventional grain-oriented (CGO) sheets. Industrial sheets were marketed in Europe in the early 1950s. They were produced under ARMCO license and exclusively in Western countries, the product being classified as “strategic material”.

The performance of GOES had been continuously improved. Only few large steel groups participated to the development and the improvement of the manufacture of GO sheets: initially the Americans ARMCO and Allegheny and then the Japanese Nippon Steel and Kawasaki Steel from the 1970s [53]. This exclusivity of steelmakers corresponds to a certain logic given the heavy equipment, such as hot rolling mills used in the processes for obtaining the texture. No laboratory equipment, however sophisticated, can perfectly simulate the production tool. In 1968, Nippon Steel improved the selective inhibition of the crystallographic orientations during the final grain growth and developed the HiB sheets [54] by introducing the aluminum nitride (AIN) to the mixture. HiB sheets reach a flux density $B_{800}$ ($\boldsymbol{B}$ at 800 A/m) of 1.95 T, a saturation polarization of 2.03 T and exhibit less than 1 W/kg losses at 50 Hz, 1.7 T.

Furthermore, the application of a mechanical tensile stress in the laminations had been proven beneficial as a mean to reduce the domains walls spacing in the material and further decreases the magnetic losses [55]. These positive effects had been exploited by applying specific coatings for the sheets.

In the same framework, the refinement of the magnetic domains by the use of scratching techniques (laser scratching developed by Nippon Steel [56] or plasma scratching developed by Kawasaki Steel [57]) allowed the enhancement of magnetic characteristics of GOES. For example, the results of scratching by laser treatment on the surface of a GOES can be observed in Figure I.18. Moreover, spark ablation developed by British Steel [58] have also proven efficient by increasing the permeability of the material and reducing the losses.

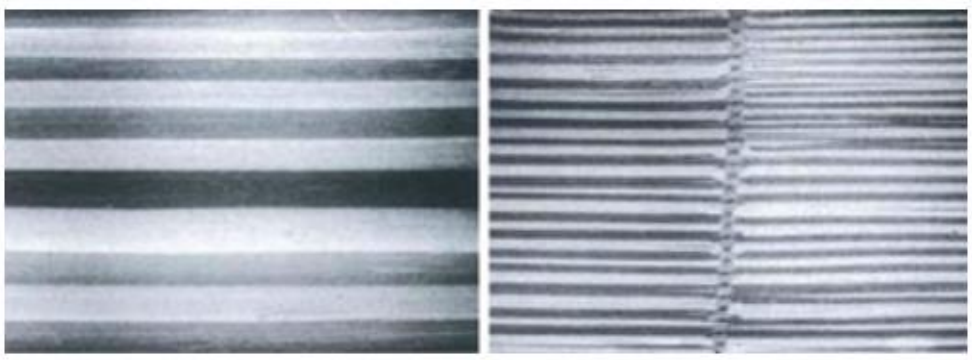

Figure I.18. Magnetic domains before and after laser domain refinement. [56]

### 3.2.3. Magnetization mechanisms in GOES

In 1944 L. Néel established his theory of “phases” [59] based on the study of the magnetization of a perfect single crystal of iron. Néel divided the elementary domains (in the sense of Weiss) into phases, each corresponding to a well-determined direction of spontaneous magnetization. He showed that the magnetization curve of a perfect single crystal of iron is composed of four successive parts each corresponding to a different

magnetization mode. These modes correspond to a certain number of phases in equilibrium.

Recently the Néel's theory has been used by F. Fiorillo [60] and C. Appino [61], to describe the magnetization processes in GOES sheets excited along a generic direction. To explain these processes, it is necessary to recall some fundamentals about the domain wall structure (dws) in SMM and in particular in GOES.

A GOES sheet is characterized, in the demagnetized state, by a slab-like domain pattern. Figure I.19 shows such structure imaged by Kerr effect at the L2EP lab. The domains are directed along the RD with spontaneous antiparallel magnetizations and they are separated by the so-called 180° domain walls.

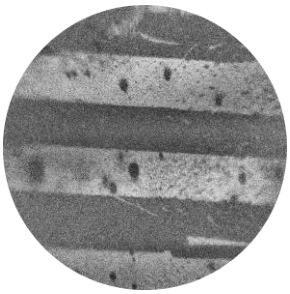

Figure I.19. Slab domains on a GOES sheet imaged by Kerr effect at L2EP.

Under alternating field applied along the RD, one dimensional process operates and the domain walls are subjected to back-and-forth motion, perpendicularly to RD. Hereinafter, the terminology "180° phase" will be used in this manuscript to designate this domain configuration.

However, when the field is applied along TD, the evolution of the domain wall structure is more complex. Like for a single crystal, the evolution of the domain wall structure can be represented as shown in Figure I.20. The magnetization process is of vectorial nature. Indeed, when the field increases, the 180° domain wall structure being unable to move (because it is perpendicular to $\boldsymbol{H}$), a phase transformation driven by 90° domain wall structure operates and the basic 180° domains transform into a pattern made of bulk domains and of surface closure domains (*i.e.*, flux-closure) as shown in Figure I.20. The closure domain structure was predicted by Néel in 1944 and observed in 1947 by Williams [62]. The terminology "90° phase" will be used in this manuscript to designate this structure.

Now, if the magnetic field is applied along an intermediate direction (between RD and TD) of the GOES, both processes described before (180° phase and 90° phase) are involved during the magnetization processes with proportions depending on the angle between the applied field and the RD.

An example of such behavior has been shown experimentally by C. Appino *et al.* on a GO strip for an angle of 45° between the applied field and the RD. As shown in Figure I.21, from $J = 0$ to $J = 0{,}25$ T. $\boldsymbol{J}$ being the magnetic polarization, which is equivalent to the magnetic flux density $\boldsymbol{B}$ in soft magnetic materials following the equation *(I.6)*. We can observe the evident 180° domain wall structure displacement, and that a partial 180°→90° phase transformation can be inferred from the surface domain structures.

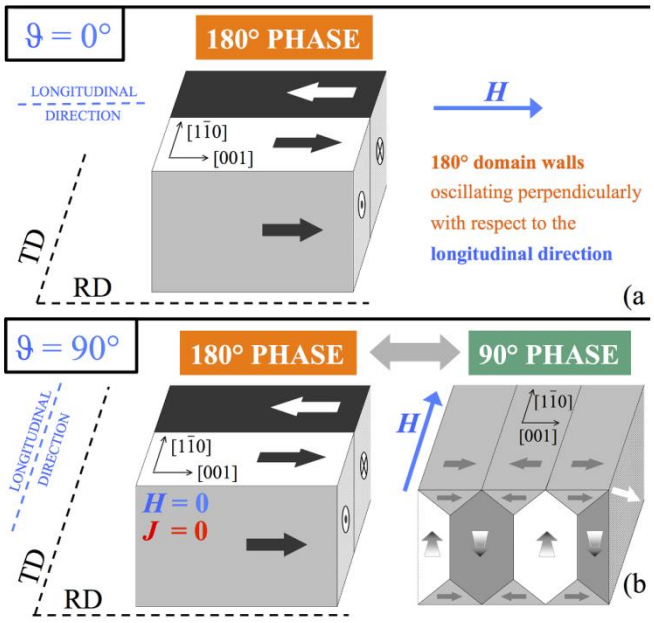


Figure I.20. Domain wall structure in high-permeability GO sheets, emulating the ideal single-crystal case. Different domain configurations vs. the applied field $\boldsymbol{H}$ for strips cut along RD (top) and TD (bottom), with the demagnetized state on the left. Extracted from [61]

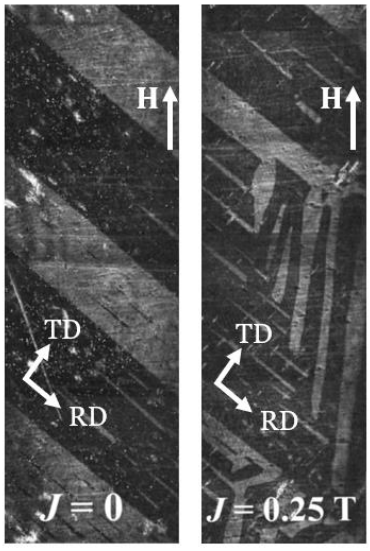


Figure I.21. Surface domain structures of GOES, observed by Kerr microscopy, of a strip cut with its longitudinal direction making an angle θ = 45° to RD. Two situations, corresponding to the demagnetized state and $J = 0.25$ T, are reported. Extracted and modified from [61]

### 3.2.4. Experimental characterization

To investigate the magnetic behavior of a given SMM, it is necessary to perform experimental characterizations. Several characterization methods exist. These methods can be classified in two main categories: the normalized or standard methods and the non-standardized methods. This section briefly describes the measurement methods of magnetic properties of electrical steel strips and sheets. They are applicable to NO electrical steel as well as to GOES.

— *Standard or normalized methods*

These methods, as their name indicates, have been normalized by international standards. They are widely used by industrial manufacturers and users of electrical steels to determine the magnetic properties of magnetic steel strips and sheets. They can be summarized as follows:

- *Epstein frame method* [63] : it is normalized by the standard IEC 60404-4. It requires a large quantity of specimen material cut into lamination strips of [280 - 300 mm] x 30 mm, these strips have to be introduced (four by four) into a squared frame and stacked so that they overlap alternately in the corners. The Epstein frame contains two windings: a primary or magnetizing winding and a secondary winding for the voltage (flux) measurement (see Figure I.22).
- *The toroidal measurement method* [64] : it is normalized by the standard IEC 60404-6. The magnetic measurements are carried out on a toroidal core made from the material to be measured. As the Epstein frame, it contains a primary winding for magnetizing and a secondary winding for the voltage (flux) measurement (see Figure I.22).
- *The Single sheet tester* (SST) [65] : it is normalized by the standard IEC 60404-3. The electrical steel sheet sample to be measured is placed in the center of two concentric windings: a primary or magnetizing winding and a secondary or voltage winding. The flux closure is made by two identical magnetic yokes (see Figure I.22). According to the IEC 60404-3, the length of the test specimen shall be not less than 500 mm.

These methods rely on the same measurement principle, *i.e.*, transformer-type fluxmetric measurement. From the Ampère's law, the magnetic field strength (in ampere per meter) can be calculated from the primary current $i_1$ by:

$$H = \frac{n_1 i_1}{l_m} \qquad (I.7)$$

where:

$n_1$ is the number of turns of the primary winding.

$l_m$ is the conventional effective magnetic path length ($l_m$= 0,94 m for the Epstein frame, $l_m$ = 0,45 m for a SST).

If $i_1$ (and therefore $\boldsymbol{H}$) varies over time, then the magnetic polarization $J(H)$ is also variable and induces a voltage $v_2$ in the secondary winding. By measuring $v_2(t)$, we obtain by integration the magnetic flux density **B** (t).

The magnetic flux density (in Tesla) is given by the formula *(I.8)* derived from Faraday's law:

$$B = -\frac{1}{n_2 S}\int v_2(t)dt \qquad (I.8)$$

where:

$n_2$ is the number of turns of the secondary winding;

$S$ is the cross section of the test specimen in square meter.

Thus, from the corresponding values of $\boldsymbol{B}$ and $\boldsymbol{H}$, the magnetization curve $\boldsymbol{B}(\boldsymbol{H})$ can be drawn and the usage magnetic properties determined.

In this PhD thesis, it is mainly the Epstein frame method which has been used for characterizing the GOES samples of interest. Some of the experimental results are reported in section 4 titled "GOES modelling" and others in Chapter II.

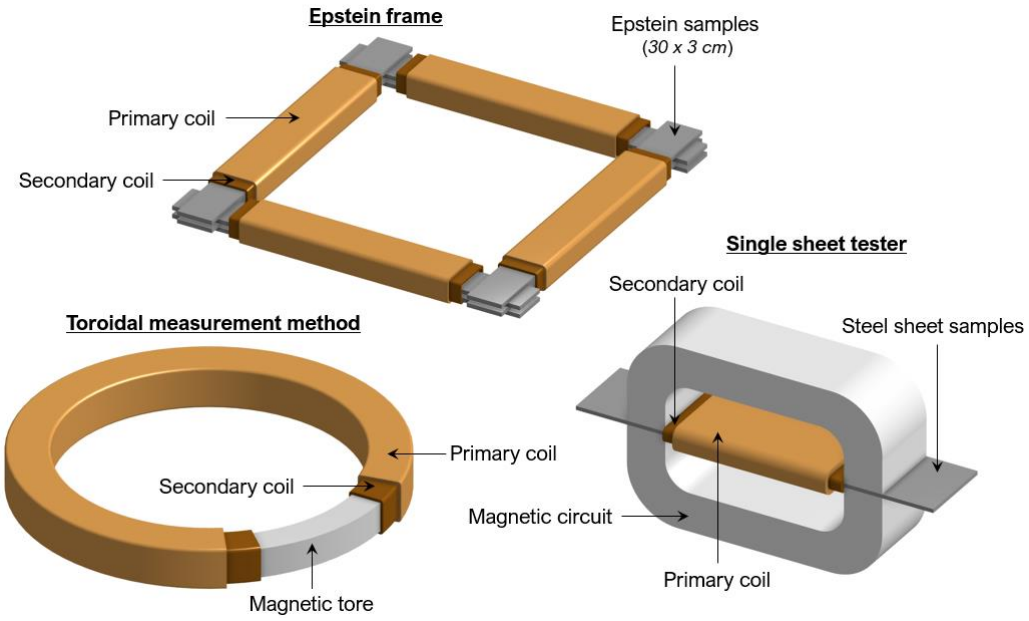


Figure I.22. Standard characterization methods for SMM. Epstein frame (top), Toroidal core (bottom left), Single sheet tester (bottom right).

— *Non- standardized Methods*

Other methods have been developed to meet specific requirements in terms of the knowledge of the magnetic characteristics of SMM under certain operating conditions. One of the most widely spread non-standardized methods is the *Rotational single sheet tester (RSST)*, used to measure the magnetic properties of an electrical steel sheet under the influence of a rotational magnetic flux [66] [67] [68]. The main objective is to reproduce the excitation conditions of electrical steel sheets encountered for example in rotating electrical machines. In principle, the rotating field is created in the test specimen by two primary excitation coils placed perpendicularly on the x- and y-axis, supplied by sinusoidal voltages in phase quadrature (see Figure I.23).

Others experimental methods have been developed to meet specific needs in terms of understanding of the magnetic behavior of electrical steels. There are for example reduced version of the normalized methods: Epstein frame [69] or SST [70] [71], to evaluate materials with different geometries, or compact dimensions, demonstrators to study the behavior of electrical steels at higher temperatures [72], [73], [74], [75] or to investigate the changes in the magnetic properties of the material, when submitted to mechanical stresses from industrial manufacturing procedures, like cutting [76], welding [77], and others [78], [79]. In the framework of this PhD thesis, we focus on the issue of end region losses met in the turbo-generators. An overview of literature demonstrators developed for the study of the end region losses will be presented in Chapter III.

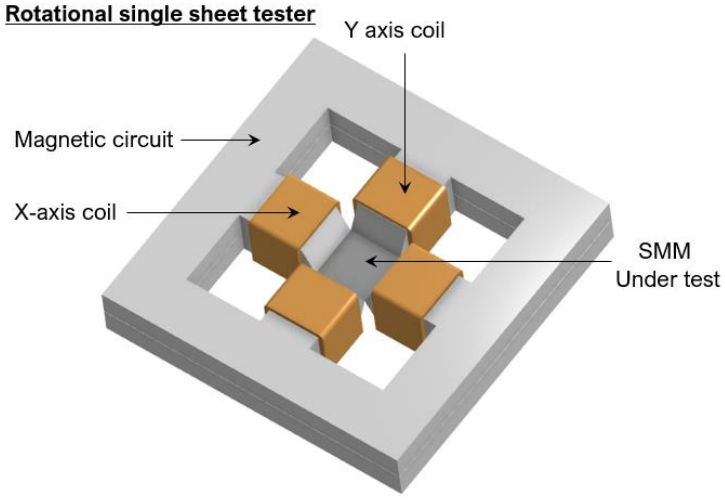


Figure I.23. 3D representation of the rotational single sheet tester

# 4. GOES Modelling

As it is well known GOES present a very strong anisotropic behavior. Their magnetic properties vary not only with the strength of the applied magnetic field but also with its direction. This behavior is shown in Figure I.24 for a conventional GOES under unidirectional applied field in different directions. Notice that if the GOES was perfectly non-oriented, *i.e.*, isotropic, these curves would be circles whatever the magnetic flux density level.

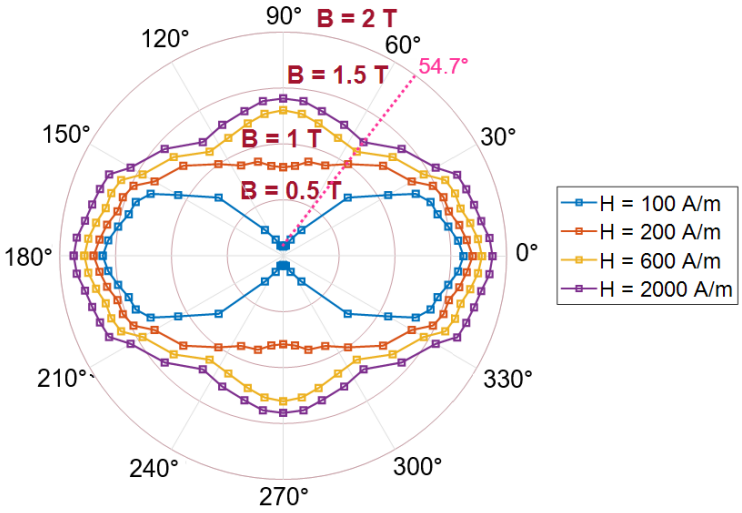


Figure I.24. Anisotropy of the magnetic flux density in a conventional GOES for different levels of applied field.

This anisotropic behavior can also be reflected in the shape of the hysteresis loops at different magnetic field directions, as shown in Figure I.25. The loops are considerable elongated in the angles close to the TD, in contrast with the cycle in the RD which is much smaller.

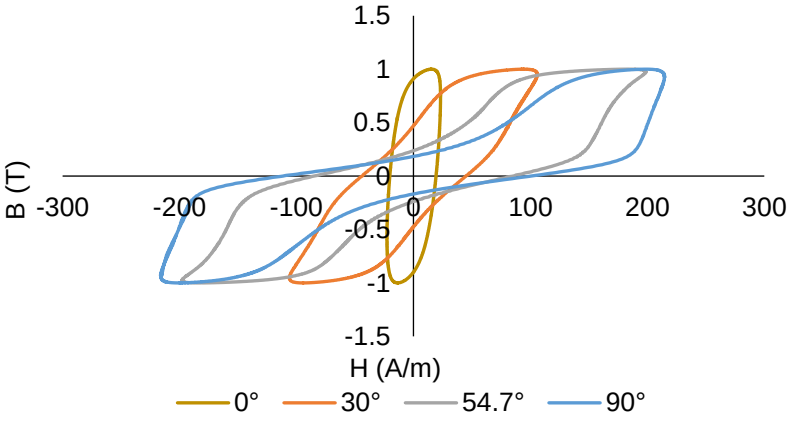


Figure I.25. Hysteresis loops as a function of the angle θ for an induction of 1T.

The iron losses of the material are also affected by the anisotropy, as presented in Figure I.26. We observed that these are much more significant towards the hard direction around 54.7° and 75°, and the lowest towards the RD. Indeed, the hard macroscopic direction will not always coincide with the crystallographic hard direction (54.7°), but in general it

follows the angles in between 54.7° and 90°. This has been observed experimentally in previous works [60] [80].

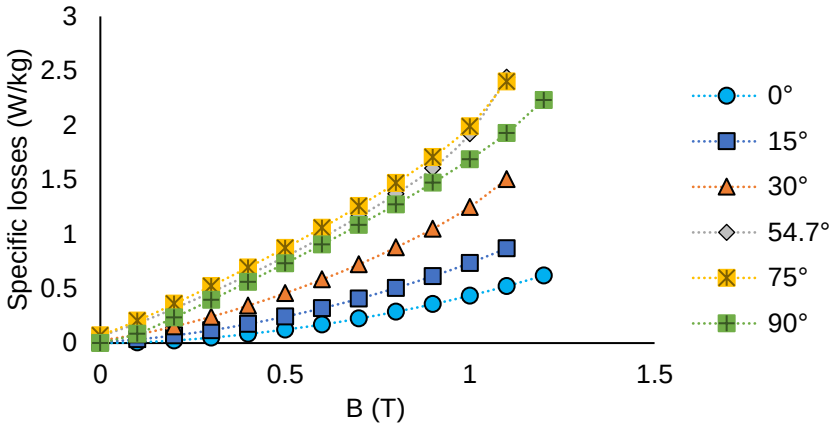


Figure I.26. Specific iron loss evolution as a function of B and θ from GOES measurements.

At last, the non-linear behavior together with the strong anisotropy and hysteresis, make difficult the modelling of the behavior of GOES. In this section, an overview of existing anisotropic behavior laws and iron loss models for GOES is presented and discussed.

## 4.1. Anisotropic behavior law models

### 4.1.1. Few words about hysteresis models

Different approaches have been used to define behavior law models, one of the most popular are based in the consideration of the hysteresis cycle to represent the magnetic behavior of GO materials. These are denoted as hysteresis models.

These models were originally developed for isotropic materials, following three main approaches, the ones from Jiles-Atherton [81], Rayleigh [82] or Preisach [83]. In the literature, various authors have adapted these models for anisotropic materials.

One of the most interesting adaptations, was developed by Jiles D. C. [84] in 1997 and further improved by Baghel [85] in 2016. Starting from the Jiles-Atherton approach, the model considered the evolution of the domain structure for GOES in the anhysteretic component of the model. The hysteresis loops were then reconstructed through the identification of the model parameters for different magnetization directions.

Still, the main problem with these types of models is that they are difficult to implement in the FEM. Besides the nonlinear numerical issues already known for isotropic hysteresis models, the complexity of these model considerably increases the computation time. Therefore, in the present work we focus on anhysteretic behavior law models.

### 4.1.2. Elliptic model

The idea of the elliptic model was proposed by Di Napoli [86]. Its principle is based on the consideration of an ellipse to describe the equal magnetic field curves ($H$-curves) in the $B_x$ – $B_y$ plane. The major and minor axes of the ellipse coincide respectively with the RD and TD [see Figure I.27].

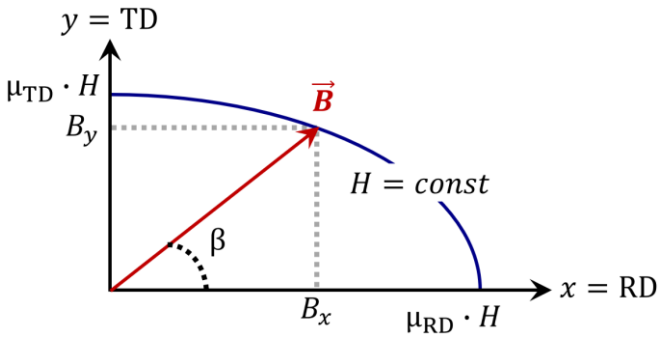


Figure I.27. Elliptical model diagram.

For a given constant magnitude of $H$:

$$\frac{B_x^2}{a^2} + \frac{B_y^2}{b^2} = 1 \tag{I.9}$$

Considering $\boldsymbol{B}$ along the direction $x$ of easy magnetization (RD), we will have its modulus verifying $B^2 = a^2$ and $B = \mu_{RD}(H)H$; hence: $\mu^2_{RD}(H)H^2 = a^2$; $\mu_{RD}(H)$ being the magnetic permeability along the RD.
Also, if $\boldsymbol{B}$ is along the $y$ direction (TD), we will have $B^2 = b^2$ and $B = \mu_{TD}(H)H$; hence: $\mu^2_{TD}(H)H^2 = b^2$; $\mu_{TD}(H)$ being the permeability along the TD.

Thus, (I.9) becomes:

$$\frac{B_x^2}{\mu_{RD}^2(H)} + \frac{B_y^2}{\mu_{TD}^2(H)} = H^2 \tag{I.10}$$

Knowing that $B_x = B\ cos\ \beta$ and $B_y = B\ sin\ \beta$ (where β is the angle between $\boldsymbol{B}$ and the RD), we obtain the elliptic model equation given by:

$$B = \frac{H}{\sqrt{\frac{cos^2\beta}{\mu_{RD}^2(H)} + \frac{sin^2\beta}{\mu_{TD}^2(H)}}} \tag{I.11}$$

with:

$$\beta = \text{atan}\left(\frac{\mu_{TD}(H)}{\mu_{RD}(H)} tan\theta\right) \tag{I.12}$$

where θ is the angle between the applied magnetic field and the RD.

This model is then based on the knowledge of $\mu_{RD}$ and $\mu_{TD}$, *i.e.*, on the two sets of *B-H* data obtained in the RD and TD. The ellipses traced by the model for different magnetic field values are presented in Figure I.28.

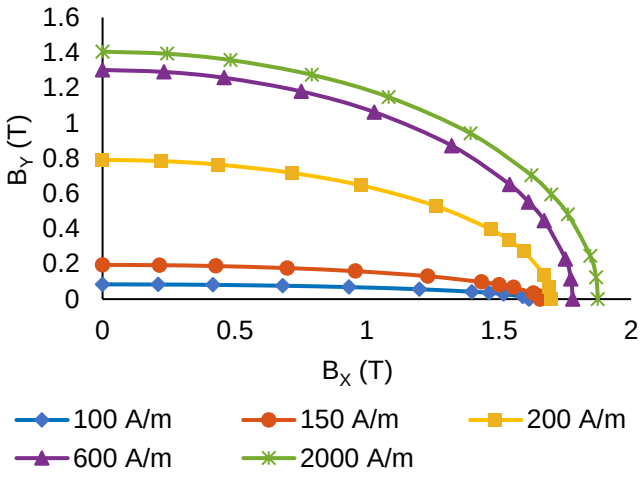


Figure I.28. *H*-curves in the *B*x – *B*y plane obtained for the elliptic model.

However, the main drawback of this model is that it does not reflect the real behavior of the material (see Figure I.29). It remains quite far from the experimental measurements, especially at low flux density levels. In addition, the lowest flux density modulus is always obtained along the TD, which is not in accordance with the physical reality of the hard magnetization axis of GOES at 54.7°.

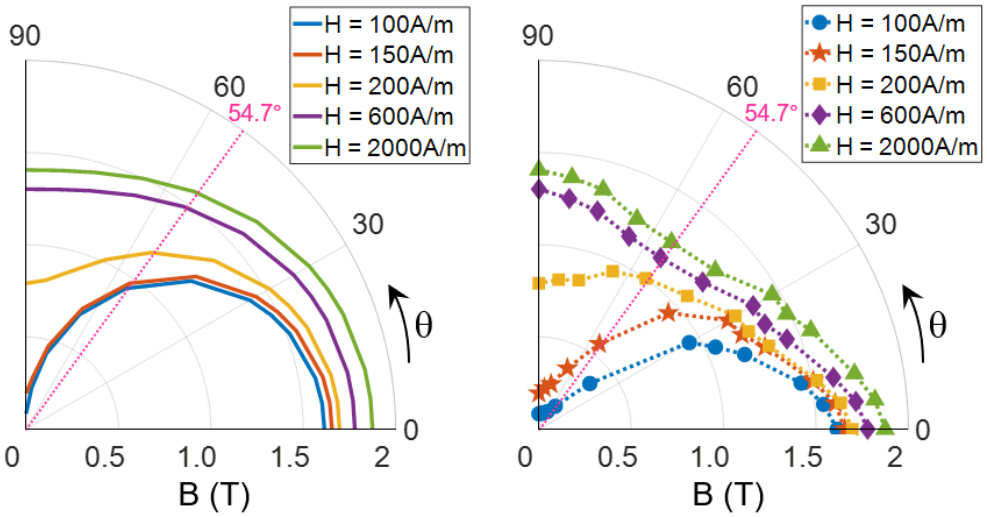


Figure I.29. Trace of the modules of ***B*** as a function of the angle θ at different magnetic field levels. Results from the elliptic model (left) vs measured behavior of a CGO steel (right).

These results presented in Figure I.30 in terms of *B-H* curves, show, as expected, the inability of the model to represent the hard magnetization direction of GOES.

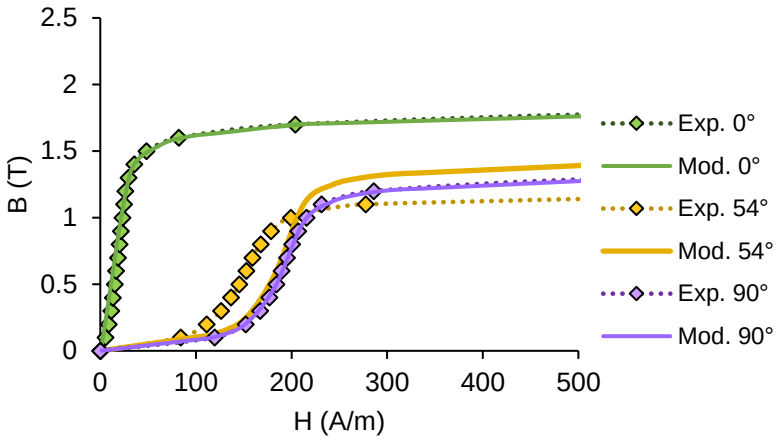


Figure I.30. Results of the elliptic model in terms of B-H curves for the three main directions.

The rocked elliptic model presented hereafter was developed to better take into account the hard magnetization direction.

— *Rocked elliptic model*

This enhanced version of the previous elliptic model, also proposed by Di Napoli [86] and presented by Péra *et al.* [80], wherein the ellipse is rocked by an angle $\delta$ = 35,3° corresponding to 90° − 54.7°. Doing so, the minor axis of the ellipse coincides with the most difficult magnetization direction at 54.7° from the RD as shown in Figure I.31.

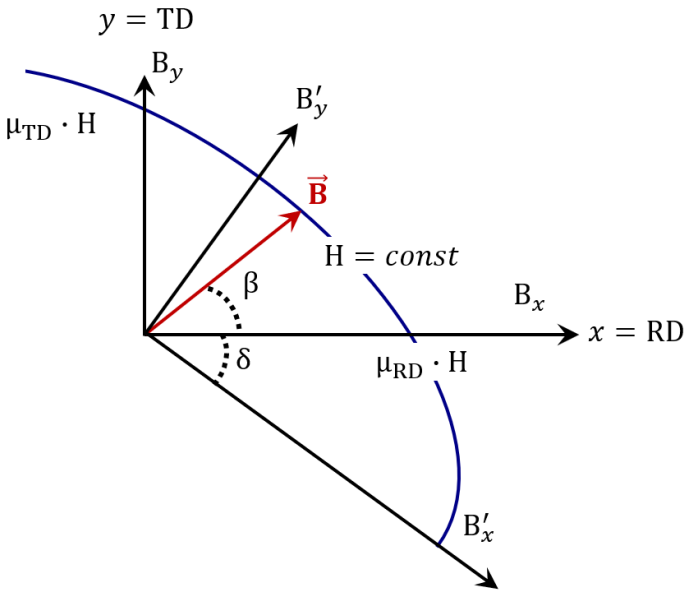


Figure I.31. Rocked elliptical model.

Starting from the rocked ellipse equation in the coordinate system ($x'$,$y'$) and the boundary conditions in the (RD, TD) reference system, we obtain the model equation given by:

$$B = \frac{H}{\sqrt{a\cos^2(\beta+\delta) + b\sin^2(\beta+\delta)}} \qquad (I.13)$$

with:

$$a = \frac{\mu_{RD}^2 \sin^2\delta - \mu_{TD}^2 \cos^2\delta}{\mu_{RD}^2\mu_{TD}^2(\sin^2\delta - \cos^2\delta)} \quad (I.14)$$

$$b = \frac{-\mu_{RD}^2 cos^2\delta + \mu_{TD}^2 sin^2\delta}{\mu_{RD}^2\mu_{TD}^2(\sin^2\delta - \cos^2\delta)} \quad (I.15)$$

By applying these equations, the rocked ellipses traced by the model at different magnetic field levels have been obtained for the same GOES tested before with the elliptic model see Figure I.32.

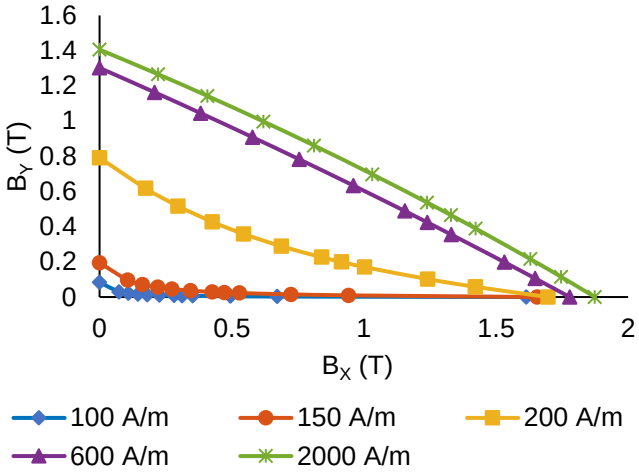


Figure I.32. *H*-curves in the *B*x – *B*y plane obtained for the rocket-elliptic model.

Figure I.33 and Figure I.34 report the results of the rocked elliptic model. The results show that the model reflects quite well the global behavior of the GOES. Nevertheless, it remains inaccurate especially for low excitation field levels where a noticeable deviation in comparison with the measurements is observed.

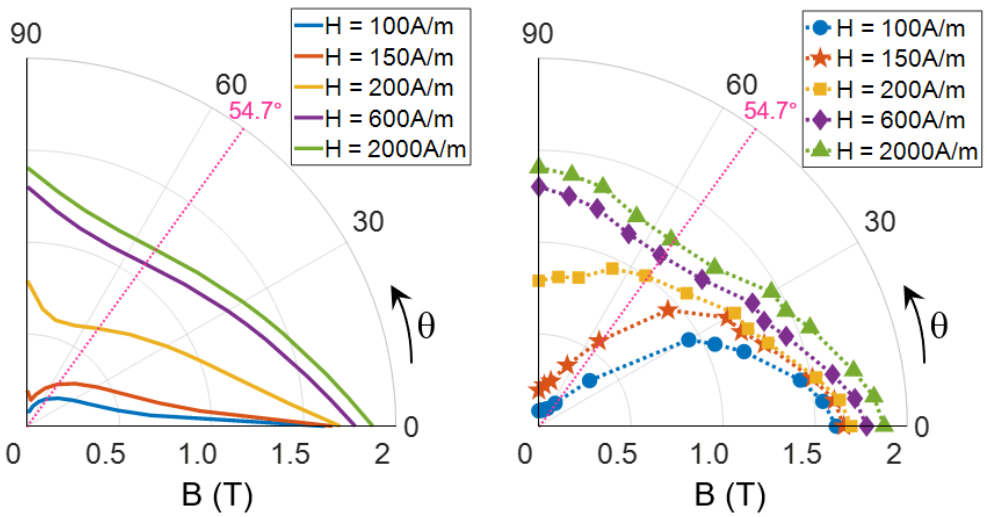


Figure I.33. Trace of the modules of B as function of the angle θ at different magnetic field levels. Results of the rocked elliptic model (left) vs measured behavior of a CGO steel (right).

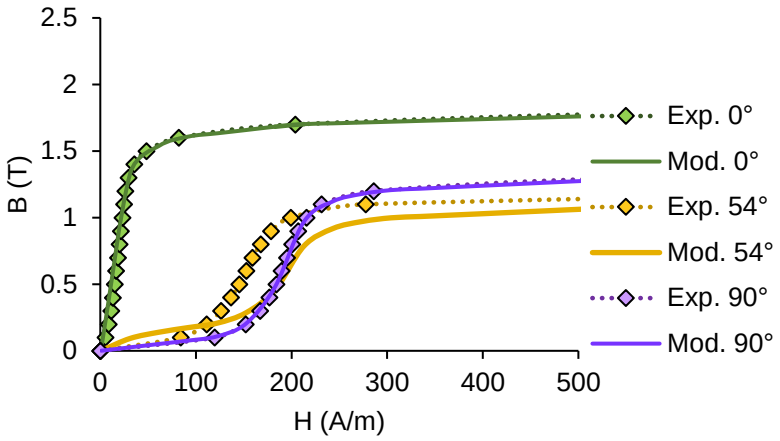


Figure I.34. Results of the rocked elliptic model in terms of B-H curves for the three main directions.

— *Modified elliptic model*

In this approach [87], Biro *et al.* introduced a slight modification in the elliptic model to better represent the GOES behavior. The authors proposed to replace the exponent 2 of the ellipse equation by a parameter $n$ as follows:

$$\frac{B_x^n}{\mu_{RD}^n} + \frac{B_y^n}{\mu_{TD}^n} = H^n \qquad (I.16)$$

$$B = \frac{H}{\sqrt{\frac{cos^n \beta}{\mu_{RD}^n(H)} + \frac{sin^n \beta}{\mu_{TD}^n(H)}}} \qquad (I.17)$$

The authors showed, by a heuristic choice, that the value $n$ = 1.4 allows to obtain behaviors that are qualitatively correct with a most difficult magnetization direction around 55°. Taking into account this change, the modified ellipses in the $B_x$ – $B_y$ plane for different magnetic field values (on the same GOES tested before) are presented in Figure I.35.

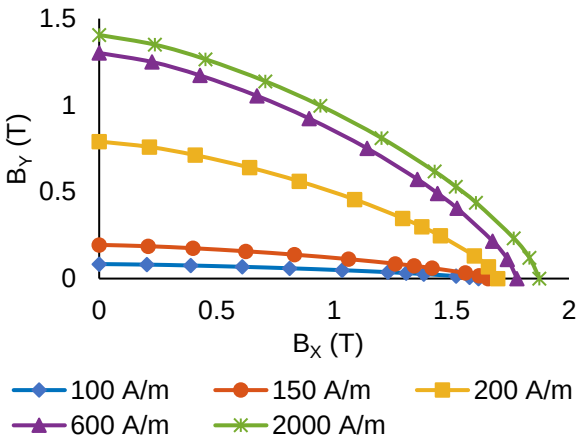


Figure I.35. $H$-curves in the $B$x – $B$y plane obtained for the modified elliptical model.

The ellipses are very similar to those of the elliptic model, but slightly flatter. Moreover, the test of the modified elliptic model confirms the author's conclusion as it can be seen

in Figure I.36 and Figure I.37. However, deviations remain between the model results and the measurements mainly for intermediate directions (directions different from the principal ones) and for low excitation field levels.

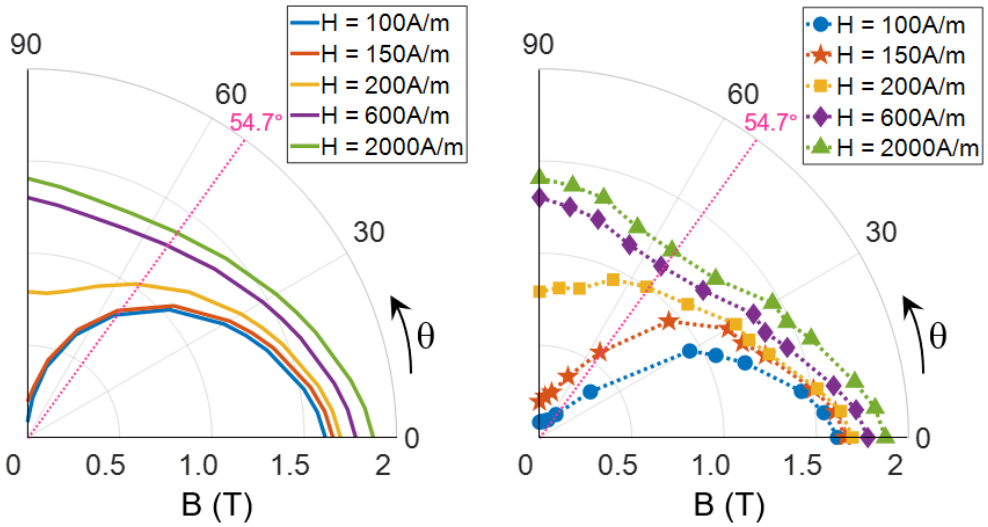


Figure I.36. Trace of the modules of $\boldsymbol{B}$ as a function of the angle θ at different magnetic field levels Results of the modified elliptic model (left) vs measured behavior of a CGO steel (right).

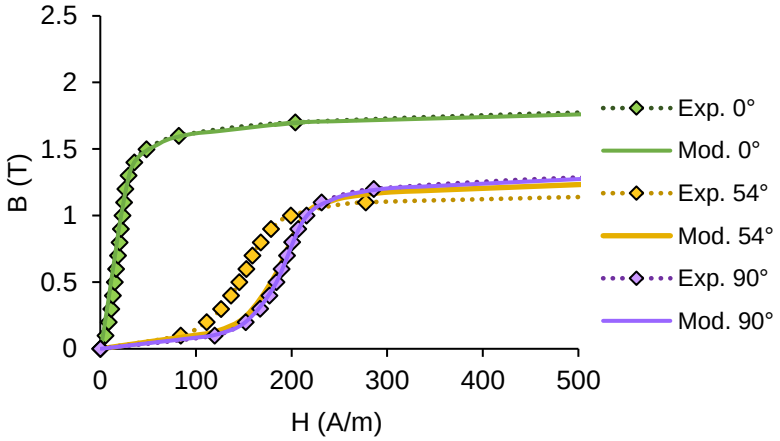


Figure I.37. Results of the modified elliptical model in terms of *B-H* curves for the three main directions.

### 4.1.3. Co-energy model

The co-energy model [80] is a vectorial ***B-H*** anisotropic model based on the interpolation function:

$$\left(\frac{H_x}{H_x{}^{RD}}\right)^n + \left(\frac{H_y}{H_y{}^{TD}}\right)^n = 1 \qquad (I.18)$$

It is based on the equivalence between the relationships ***H-B*** and $E$–$\boldsymbol{H}$ ($E$ being the magnetic co-energy) given in *(I.19)*:

$$E = \int_0^{H_x{}^{RD}} B_{RD}(H)dH = \int_0^{H_y{}^{TD}} B_{TD}(H)dH \qquad (I.19)$$

In the model, $\boldsymbol{H}_x{}^{RD}$ and $\boldsymbol{H}_y^{RD}$ define the $\boldsymbol{H}_x$ and $\boldsymbol{H}_y$ components of the co-energy line, while the curvature of the line is defined by the exponent $n$ in eq. *(I.18)* (see Figure I.38)

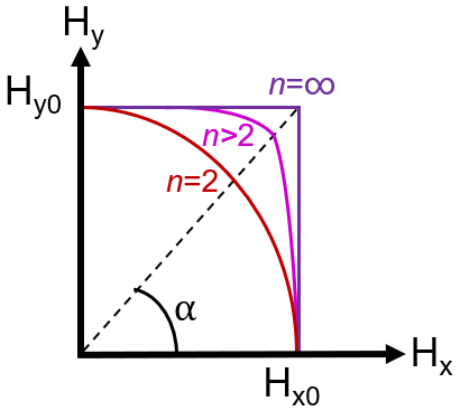


Figure I.38. Representation of co-energy lines for different values of n.

For a given co-energy $E$ level, the modulus of $\boldsymbol{H}$ is maximum when $\boldsymbol{H}$ lies with the difficult magnetization direction. In most cases for GOES the difficult direction is assumed to be same as the difficult crystallographic direction 54.7°. However, as previously mentioned this is not always the case. Therefore, the value of $n$ can be estimated by calculating the angle $\alpha$, given by the equation *(I.20)*.

$$\tan \alpha = \frac{H_y^{TD}}{H_x{}^{RD}} \qquad (I.20)$$

and the value of $n$ can be obtained by applying the equation *(I.21)*:

$$n = \frac{2\ln\left(\tan(54.7)\right)}{\ln\left(\tan(54.7)\right) - \ln\left(\tan\alpha\right)} \qquad (I.21)$$

At last, solving eq. *(I.19)* allows to obtain the co-energy $E$ and then $\boldsymbol{B}(B_x, B_y)$ such that:

$$B_x = \frac{dE}{dH_x} \quad \text{and } B_y = \frac{dE}{dH_y} \qquad (I.22)$$

Waeckerlé *et. al* in [88] showed that the co-energy model allows a more correct description of the 2D anisotropic behavior of GO sheets in comparison with the elliptical models. Péra *et al.* [80] [89] implemented this modelling approach in magnetostatic field computations using the 2D finite element method. However, significant issues of numerical convergence were observed.

### 4.1.4. Orientation distribution fonction model

The mathematical theory of orientation distribution function (ODF) was proposed in 1982 [90] to describe mathematically the physical properties of a polycrystalline material and applied in [91] [92] to express the magnetic flux density $B$ in GOES through third order *cosine* series as a function of the applied filed strength $H$ and the angle $\theta$ between $H$ and RD.

$$B(H,\theta) = A_1(H) + A_2(H)cos(2\theta) + A_3(H)cos(4\theta) \quad (I.23)$$

The coefficients $A_1, A_2$ and $A_3$ are given by the equations *(I.24)(I.25)* and *(I.26)*. They can be determined from Epstein measurements along three directions: RD (0°), TD (90°) and 45°.

$$A_1 = \frac{1}{4}[B(H,RD) + B(H,TD) + 2B(H,45°)] \quad (I.24)$$

$$A_2 = \frac{1}{2}[B(H,RD) - B(H,TD)] \quad (I.25)$$

$$A_3 = \frac{1}{4}[B(H,RD) + B(H,TD) - 2B(H,45°)] \quad (I.26)$$

The main drawback of this model version is that by limiting the decomposition to only three values it does not correctly represent the GOES behavior, presenting inaccuracy in some specific parts of the magnetization curves. More recently, Jiang *et al.* [93] have proposed to increase the $B(H,\theta)$ representation accuracy by modifying the determination method of the coefficients $A_i$ based on a fast Fourier transform (FFT) as well as the expression of $B(H,\theta)$:

$$B(H,\theta) = \sum_{i=1}^{n} A_i(H)cos(2(i-1)\theta) \quad (I.27)$$

where n is the decomposition order.

The authors have showed that the representation accuracy of the $B(H,\theta)$ curves is obtained with the 12th order decomposition, which considerably increases the required experimental data for the coefficient identification (12 $B(H,\theta)$ experimental curves required for a 12th order decomposition).

More recently, the ODF model has been implemented in a 2D FEM simulation by Tolentino [94] in 2020. The model was identified by a with a 10th order decomposition of the $B(H,\theta)$ curves and applied to a RSST test case in the FE environment. Interpolations were needed to adapt the non-continuous experimental data, increasing the simulation time. Finally,

some convergence problems between the model and the FEM analysis were found, limiting the tests to low flux density values.

### 4.1.5. Enokizono Model

In the 1990s, Masato Enokizono established a formalism to identify a full reluctivity tensor linking the internal magnetic field $\boldsymbol{H}_i$ to the flux density $\boldsymbol{B}$ in a GOES. This formalism is based upon measurements under rotating field [68].

To explain the principle of the model, let us recall that in GOES, the directions of $\boldsymbol{H}$ and $\boldsymbol{B}$ fields are identical if the GOES remains excited along one of its main directions RD and TD. On the other hand, as soon as we deviate from RD or TD, $\boldsymbol{H}$ and $\boldsymbol{B}$ are no longer in phase and we are dealing with a vectorial behaviour as shown Figure I.39 (a) which gives a schematic representation of the vector link between $\boldsymbol{B}$ and $\boldsymbol{H}$ in the plane of a GOES. The *x* direction is assumed to be the RD.

The internal magnetic field $\boldsymbol{H}_i$ and the flux density $\boldsymbol{B}$ are phase shifted by an angle $\theta_{BH}$. A magnetic field $\boldsymbol{H}_i'$ which is parallel to $\boldsymbol{B}$ can be defined by a rotation of $\boldsymbol{H}_i$ by an angle $\theta_{BH}$ according to eq. *(I.28)*.

$$\begin{bmatrix} H_{i_x}' \\ H_{i_y}' \end{bmatrix} = \begin{bmatrix} cos\theta_{BH} & -sin\theta_{BH} \\ sin\theta_{BH} & cos\theta_{BH} \end{bmatrix} \begin{bmatrix} H_{i_x} \\ H_{i_y} \end{bmatrix} \qquad (I.28)$$

Under these conditions, we can define an <u>effective</u> reluctivity tensor [ν'] linking $\boldsymbol{H}_i'$ to $\boldsymbol{B}$ according to:

$$\begin{bmatrix} H_{i_x}' \\ H_{i_y}' \end{bmatrix} = \begin{bmatrix} \nu' & 0 \\ 0 & \nu' \end{bmatrix} \begin{bmatrix} B_x \\ B_y \end{bmatrix} \qquad (I.29)$$

From equations *(I.28)* and *(I.29)* it follows:

$$\begin{bmatrix} H_{i_x} \\ H_{i_y} \end{bmatrix} = \begin{bmatrix} cos\theta_{BH} & sin\theta_{BH} \\ -sin\theta_{BH} & cos\theta_{BH} \end{bmatrix} \begin{bmatrix} \nu' & 0 \\ 0 & \nu' \end{bmatrix} \begin{bmatrix} B_x \\ B_y \end{bmatrix} \qquad (I.30)$$

Finally, we obtain a full reluctivity tensor linking $\mathbf{H_i}$ to $\mathbf{B}$:

$$\begin{bmatrix} H_{i_x} \\ H_{i_y} \end{bmatrix} = [\nu] \begin{bmatrix} B_x \\ B_y \end{bmatrix} \qquad (I.31)$$

where:

$$[\nu] = \begin{bmatrix} \nu_{11} & \nu_{12} \\ \nu_{21} & \nu_{22} \end{bmatrix} = \begin{bmatrix} cos\theta_{BH} & sin\theta_{BH} \\ -sin\theta_{BH} & cos\theta_{BH} \end{bmatrix} \begin{bmatrix} \nu' & 0 \\ 0 & \nu' \end{bmatrix} \qquad (I.32)$$

<u>Of course, the effective</u> reluctivity tensor [ν'] and the angle $\theta_{BH}$ are nonlinear and vary with the flux density level $\boldsymbol{B}$ and the angle β of $\boldsymbol{B}$ to the RD.

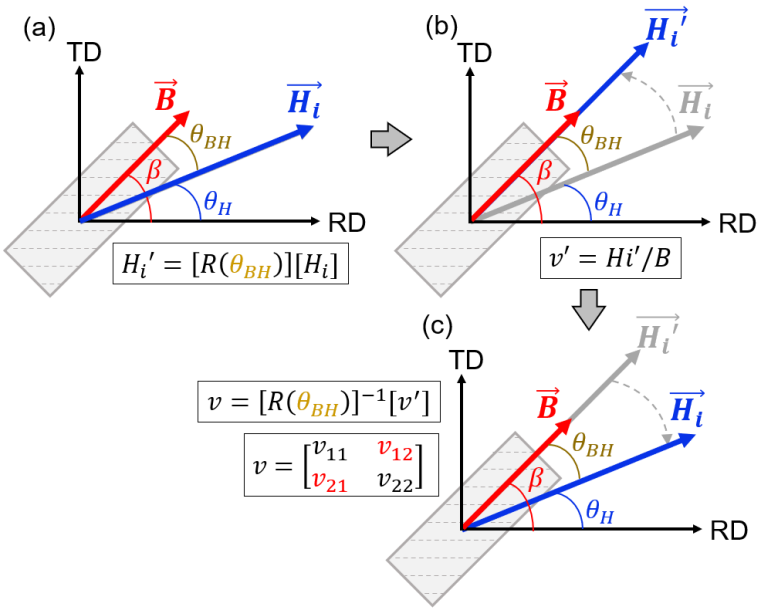


Figure I.39. Principle of the Enokizono model. (a) initial magnetization state, (b) rotation of the applied magnetic field $\boldsymbol{H}_i$ to the position of $\boldsymbol{B}$, (c) calculation of the reluctivity tensor [$v$]' and inverse rotation into the original position.

Although the Enokizono formalism requires several experimental data, it is very suitable for integration in a FEM simulation environment. In this regard, it was implemented by Enokizono in FEM simulation environment to simulate a transformer. Further developments to improve the convergence of the model in the FEM environment have been realized by Fujiwara *et al.* [95] in 2002, which transformed the tensor in an equivalent diagonal tensor and by Yoon *et al.* [96] in 2009. This latter tested the model for the case of a single-phase transformer core, and incorporated it into a non-linear FE formulation using the Newton Raphson method.

### 4.1.6. Fiorillo's model

Developed in 2002 by F. Fiorillo this model is capable of predicting the magnetization curves and hysteresis loops in any direction of GO Fe-Si laminations using only the magnetic curves in the two main directions RD and TD. It is based on the physical principles of the Neel phase theory, considering that the domain wall structure evolution during the magnetization of highly anisotropic grain-oriented materials is similar to that of an iron monocrystal, as describe in section 3.2.3.

The geometry of the samples and the stacking configuration of the GO material are taken into account for the model prediction. These characteristics play an important role in the effect of the demagnetizing field inside the sample. Two stacking configurations are possible: parallel stacking and X-stacking configuration.

- *Parallel stacking:* When the RD axes of the anisotropic samples are aligned in the same direction.

- *X-Stacking:* When the RD axes of the anisotropic samples are aligned in opposite directions.

A more detailed analysis of the stacking configuration and the nature of the demagnetizing field are presented in Chapter II.

The model has been initially validated by means of an Epstein frame. Therefore, only the parallel stacking configuration of the model have been considered. In this configuration the behavior law emulates more closely the behavior of an individual Epstein strip (see Figure I.40).

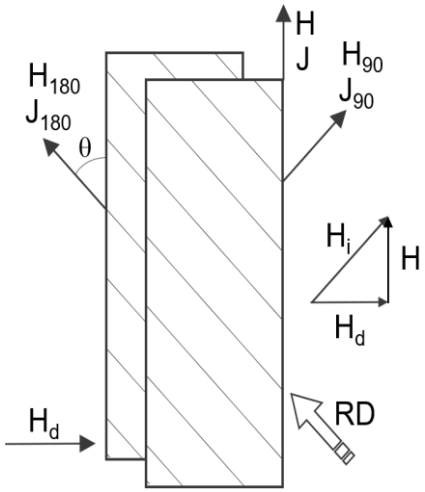


Figure I.40. Magnetic field and polarization components for two parallel longitudinal strips of GOES.

In this case, the applied magnetic field $\boldsymbol{H}$ follows the longitudinal direction of the sample and is collinear with the total polarization $\hat{J}$. Moreover, the demagnetizing field $\boldsymbol{H}_d$ is orthogonal to the strip length and this, in addition to the narrow geometry of the strip, difficult the orthogonal polarization of the material. Making the transversal polarization $\hat{J}_\perp$ component is approximately zero, and $\hat{J} \approx \hat{J}_{//}$.

For a sample cut at an intermediate angle θ (between the RD and TD), the magnetization process will involve both the 180° and 90° domains in the material domain structure. The peak magnetic polarization $\hat{J}$ is the result of two contributions $\hat{J}_{180}$ and $\hat{J}_{90}$ the polarization values in the 180° and 90° domains respectively. These values are calculated by using the following coefficients:

$$\hat{J}_{90} = \hat{J} sin\theta \qquad (I.33)$$

$$\hat{J}_{180}^{r} = \frac{\hat{J}}{1 - \sqrt{2}\frac{\hat{J}}{\hat{J}_s} sin\theta} cos\theta \qquad (I.34)$$

$\hat{J}_s$ being the saturation polarization. Moreover, for soft magnetic materials the peak polarization $\hat{J}$ is equivalent to the peak induction $\hat{J} \approx \hat{B}$. By evaluating the applied magnetic

field $\boldsymbol{H}$ as a function of $\hat{J}_{90}$ and $\hat{J}_{180}^{r}$; we can obtain the contributions of the magnetic field to each domain structure $\boldsymbol{H}_{180}$ and $\boldsymbol{H}_{90}$.

$$H_{180}(\theta,\hat{J}) = H_{EXP}^{DL}[\hat{J}_{180}^{r}] \quad (I.35)$$

$$H_{90}(\theta,\hat{J}) = H_{EXP}^{DT}[\hat{J}_{90}] \quad (I.36)$$

And finally, considering both magnetic field contributions we can estimate the demagnetizing field and the applied magnetic field contributions in the Epstein strip as a function of the angle θ, as follows.

$$H_d = H_{90}cos\theta + H_{180}sin\theta \quad (I.37)$$

$$H = H_{90}sin\theta + H_{180}cos\theta \quad (I.38)$$

From these equations, it is possible to obtain the hysteresis loop, as well as the normal magnetization curves, for any intermediate angle of GOES strips. The results of this model are really promising (see Figure I.41). However, some discrepancies exist between the experimental and modeled curves for lower angles to the RD. This model will be further developed in Chapter II.

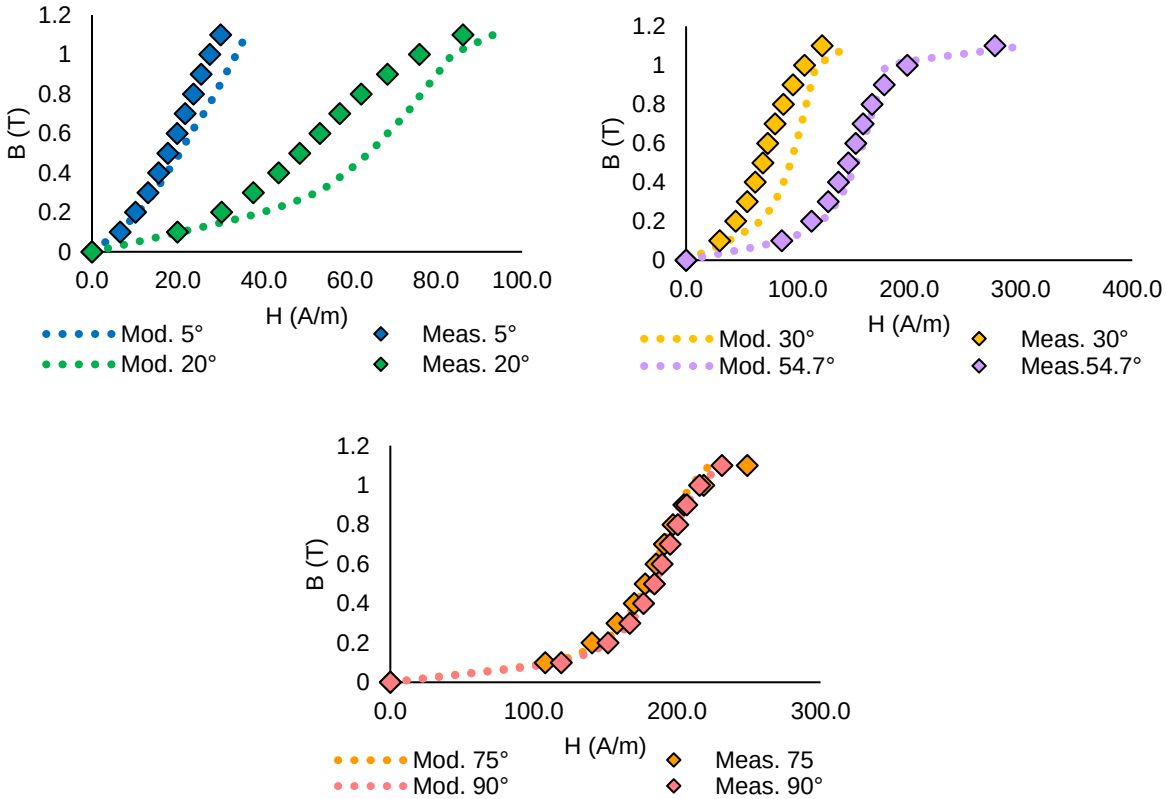


Figure I.41. Comparison between Fiorillo model and the experimental measurements of H. 5° and 20° B-H curves (top left), 30° and 54.7° B-H curves (top right), 75° and 90° B-H (bottom).

### 4.1.7. Synthesis of behavior law model

Having reviewed the different behavior law models for anisotropic materials in this section, Table I.1 compares them according to different criteria. From this comparison, we chose to implement the Enokizono model. However, there is a need to develop the model further in order to consider uni-directional field measurements; this problematic is presented in Chapter II.

Table I.1. Comparison of anisotropic behavior law models

| MODEL | Accuracy | Need for experimental data |
|---|---|---|
| Elliptical models | Low | Low |
| Hysteresis models | High | High |
| ODF models | Medium | High |
| Enokizono model | High | High |
| Fiorillo model | Medium | Low |

## 4.2. Iron loss models

In general, the iron loss models can be classified in three main categories according to their characteristics.

- *Models based on the Steinmetz equation* [97]: the total iron losses are fitted with the experimental data using an empirical expression depending on the frequency and peak magnetic flux density. Such approach is quite basic and generally limited to low frequency operating conditions.
- *Models based on the loss separation principle*: originally Jordan [49] proposed in 1924 a model with two contributions (quasi-static and classical eddy current losses) but some discrepancies between measure and calculated losses were still remaining (named anomalous losses). In 1985 Bertotti [50] proposed a physical interpretation to explain the origin of the anomalous losses that he called excess losses. This approach finally considers three contributions: quasi-static hysteresis losses, classical eddy current losses and excess losses. The losses can be predicted in a wider range of excitation frequencies as long as no skin effect is involved.
- *Hysteresis loss models*: in such approaches, the representation of the hysteresis loop allows to calculate the associated losses. However, several levels of hysteresis modelling can be considered: models with only the quasi-static behavior or including the dynamic terms associated to the classical and/or excess losses. In practice, such approaches require extensive material data for a precise calculation of the iron losses. Also, as previously mentioned, the implementation of hysteresis

models in numerical tools is still an issue regarding the robustness of the nonlinear solving aspect.

The majority of these models are isotropic, meaning that they calculate the iron losses in machines with isotropic magnetic cores, or anisotropic magnetic cores assuming that the effective magnetic path length inside the machine will mainly follow the rolling direction of the electrical steel.

However, considering the double non-linearity of the losses in GOES (their magnetic properties depend on the flux density $\boldsymbol{B}$ and on the angle $\theta$ of $\boldsymbol{H}$ to the RD), previously illustrated in Figure I.26. The "classical" isotropic models have not been considered for iron loss modelling.

In the literature there are very few developments concerning the estimation of the losses in anisotropic GOES materials. Indeed, the majority of the anisotropic iron loss models derivate from anisotropic behavior law models, especially from hysteresis models [98] [99]. These models, however, require important developments for their integration in the FEM, and have a considerably long calculation time.

Other approach is to rely in a model based on the Bertotti approach, identifying the iron loss coefficients for each $B(H,\theta)$ magnetizing curve. However, a fitting procedure is required for each given direction and a considerable set of experimental data would be required for such a task. This can be a long process and will required additional developments to identify the losses as function of H and $\theta$.

Therefore, we decided to focus on a recently developed model that follows the loss separation approach. This model, developed by C. Appino in 2020, is a continuation of Fiorillo's model presented in section 4.1.6. It follows the principles of Néel phase theory and is capable of predicting the losses in GOES, for a given flux density level $\boldsymbol{B}$ and magnetic field $\boldsymbol{H}$ orientated with an angle $\theta$ to the RD. The model can be easily implemented in the FEM environment in post-processing to reduce the computation time, and only requires the hysteresis and excess losses of the material in the two main directions RD and TD without any adjustable parameters. The classical eddy current losses are calculated using their theoretical expression associated to an infinite lamination.

The selected iron loss model and its implementation in the finite element environment will be discussed in Chapter II, section 4.

# 5. Synthesis

In this chapter, with the purpose of characterization and modelling of end-region losses in turbo-generators, a state of the art has been realized. Taking into account the magnetic properties of the GOES used in these turbo-generators, especially their strong anisotropic behavior, is necessary for a better understanding of the end-losses. In this framework, the ability of different existing law and loss models to take into account the magnetic anisotropy of GOES and their limits have been exposed in this chapter together with the methods of measurement of the magnetic properties of electrical steels.

Existing studies rarely accounts for the anisotropy of GOES. Therefore, our objective is to contribute to this aspect by means of 3D modeling taking into account the GOES physical characteristics. This will be achieved together with the design and realization of an experimental prototype to study different orientations of the magnetic flux path with regard to the lamination plane, combined with different in-plane orientations of the GOES easy magnetization axis.

# Chapter II. Modelling of GOES

---

*The finite element method (FEM) is a practical tool for the in-depth study of electrical machines. Through numerical simulations, various operating scenarios of these machines can be reproduced, and the evolution of electromagnetic phenomena within the machines can be studied and analyzed. However, the reliability of FEM numerical results relies on the modelling hypotheses; especially the material models used to represent the behavior of the magnetic cores.*

*To account for the anisotropic behavior of GOES in numerical tools, the material models must be accurate and adapted for a numerical implementation in FEM.*

*In this chapter, the selected behavior law and iron loss models, as well as the procedures followed for their implementation in the FEM software code_Carmel are presented. The validity of these models has been experimentally verified.*

---

# Table of content

# 1. Effect of the demagnetizing field

Before addressing the modelling of GOES, an experimental characterization step is required in order to understand the behaviors and identify the inherent magnetic properties for any direction of the applied field to RD. This step is fundamental as it establishes a reference to validate the behavior law and iron loss models.

The experimental characterization methods do not always allow measuring the intrinsic magnetic properties for the special case of GOES. However, this can be done taking the right considerations. In the Epstein method, commonly applied for measuring the magnetic properties of industrial electrical steels (see Chapter I), a set of laminations cut along a direction making an angle θ to RD are assembled together in a standardized square frame. The experiments show that the magnetic characteristics obtained from an Epstein frame will depend on how the laminations are stacked [100], [60], [61]. In fact, due to the strong magnetic anisotropy of GOES, Epstein strips are subjected to a demagnetizing field of which the magnitude and the direction depend on the angle θ of the applied field to RD.

There are two possible stacking configurations of Epstein strips:

- parallel stacking i.e., an angle of 0° between the RD of the stacked laminations [see Figure II.1 (a)];
- x-stacking i.e., an angle of 2×θ° between the RD of two stacked laminations [see Figure II.1 (b)].

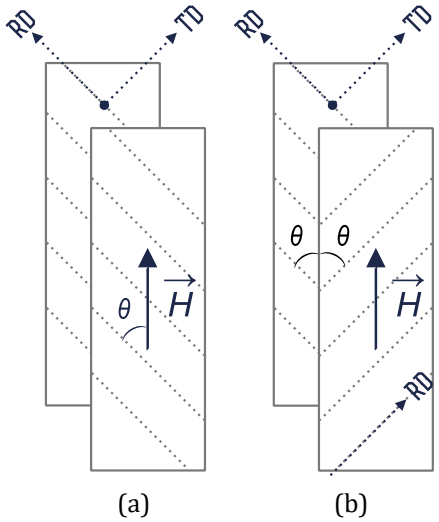


Figure II.1. (a) Parallel and (b) X-stacking configurations for Epstein measurements.

Both stacking configurations are investigated and analyzed on a conventional GOES, typically used for the manufacture of the stator magnetic core of turbo generators. Thirteen angles between the RD and TD have been considered.

## 1.1. Background

When characterizing GOES Epstein strips along the main directions RD and TD, the resulting or internal magnetic field $\mathbf{H_i}$ coincides with the applied field **H**, the latter being collinear with the magnetic flux density **B**. This means that the measured magnetic behavior reflects the intrinsic magnetization properties as no demagnetizing field is present in both situations [see Figure II.2]. However, if the applied magnetic field **H** is along Epstein strips cut with an intermediate angle θ to RD, a demagnetizing field $\mathbf{H_d}$ appears orthogonally to the strip length [60]. In this case, the resulting or internal magnetic field $\mathbf{H_i}$ within the strips is no longer the applied one [see Figure II.3]. The existence of the demagnetizing field $\mathbf{H_d}$ can be seen as the appearance of magneto-static charges on the opposite lateral faces of the Epstein strip as the material is polarized. The corresponding measured properties cannot be assumed as intrinsic and the demagnetizing field must be reduced as much as possible in order to determine the intrinsic behavior of the material. For a soft material, the demagnetizing field can be 1000 or 10,000 times greater than the internal field in [101].

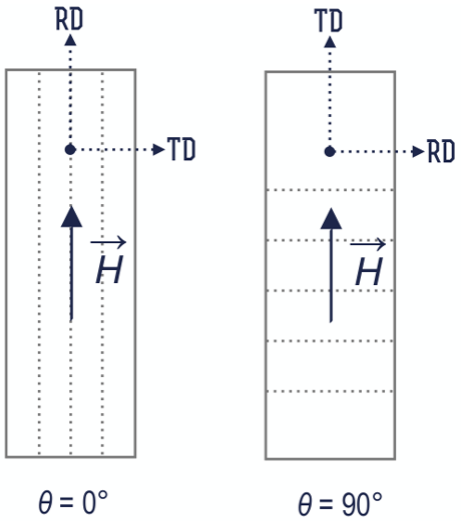


Figure II.2. Magnetization of Epstein GOES strips in RD and TD, $\mathbf{H_d} = 0$ and $\mathbf{H_i} = \mathbf{H}$.

Thus, in the Epstein frame method, it is possible to strongly reduce the demagnetizing field component by considering the x-stacking configuration.

To analyze the magnetic behavior for both parallel and x-stacking configurations, Epstein characterizations have been realized for strips made of a conventional GOES cut along different angles θ to the RD. This is the subject of the next section.

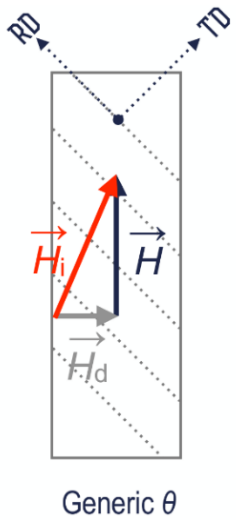


Figure II.3. Demagnetizing field in Epstein GOES strips for an intermediate angle θ between the applied field **H** and RD, $\mathbf{H}_d \neq 0$ ($\mathbf{H}_i = \mathbf{H} + \mathbf{H}_d$).

## 1.2. Experimental characterization

### 1.2.1. Preparation of the samples and experimental conditions

Several stator segments (of 0.35 mm thickness) of a turbogenerator have been provided by EDF. They are made of a conventional GOES. From these segments, Epstein-type strips of standard dimensions (300 mm x 30 mm) have been cut along different directions to RD [see Figure II.4]. In order to minimize the effect of the cutting on magnetic properties, the wire electrical discharge machining (WEDM) has been used.

The magnetic characteristics of the samples have been then measured on the MPG200D equipment from Brockhaus Measurements$^{GmbH}$, in accordance with the IEC standard [63] for both parallel and x-stacking configurations, under controlled sinusoidal magnetic flux density waveforms, from the demagnetized state to saturation. Frequencies of 5, 10, 25, 50 and 100 Hz have been considered.

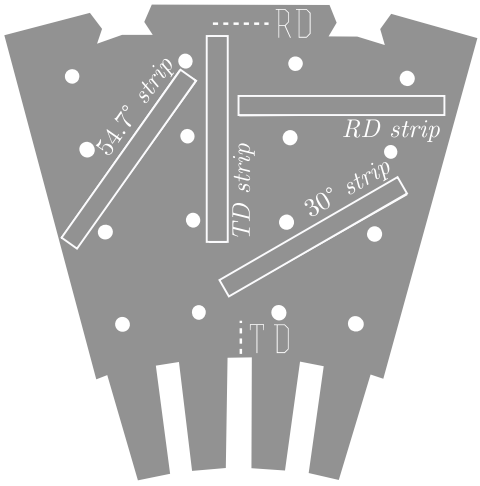


Figure II.4. One segment of a turbo-generator and some cut sample locations. RD designates the rolling direction and TD is parallel to the axis of the teeth.

### 1.2.2. Results

Results of the experimental characterization for both RD (θ = 0°) and TD (θ = 90°) are shown in Figure II.5 in terms of normal magnetization curves, hysteresis loops, as well as specific losses for parallel and x-stacking configurations.

As expected, the experiments demonstrate that, for both RD and TD, the results are identical whatever the stacking configuration. This is in accordance with the expected theoretical behavior, *i.e.,* that no demagnetizing field exists in these configurations. Indeed, the measured properties are the intrinsic properties of the GOES.

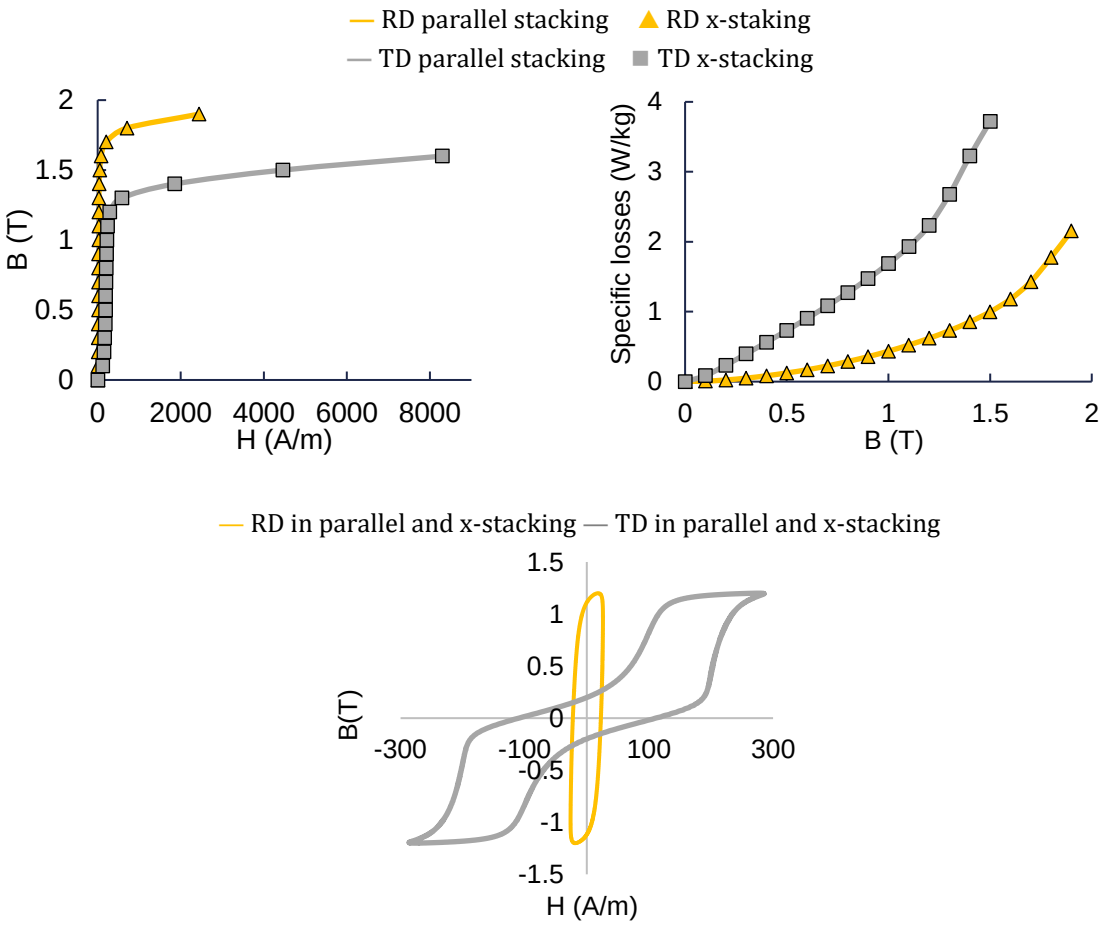


Figure II.5. 50 Hz normal magnetization curves, hysteresis loops at 1.2 T and specific losses measured along the two main directions (RD and TD) for both parallel and x-stacking configurations.

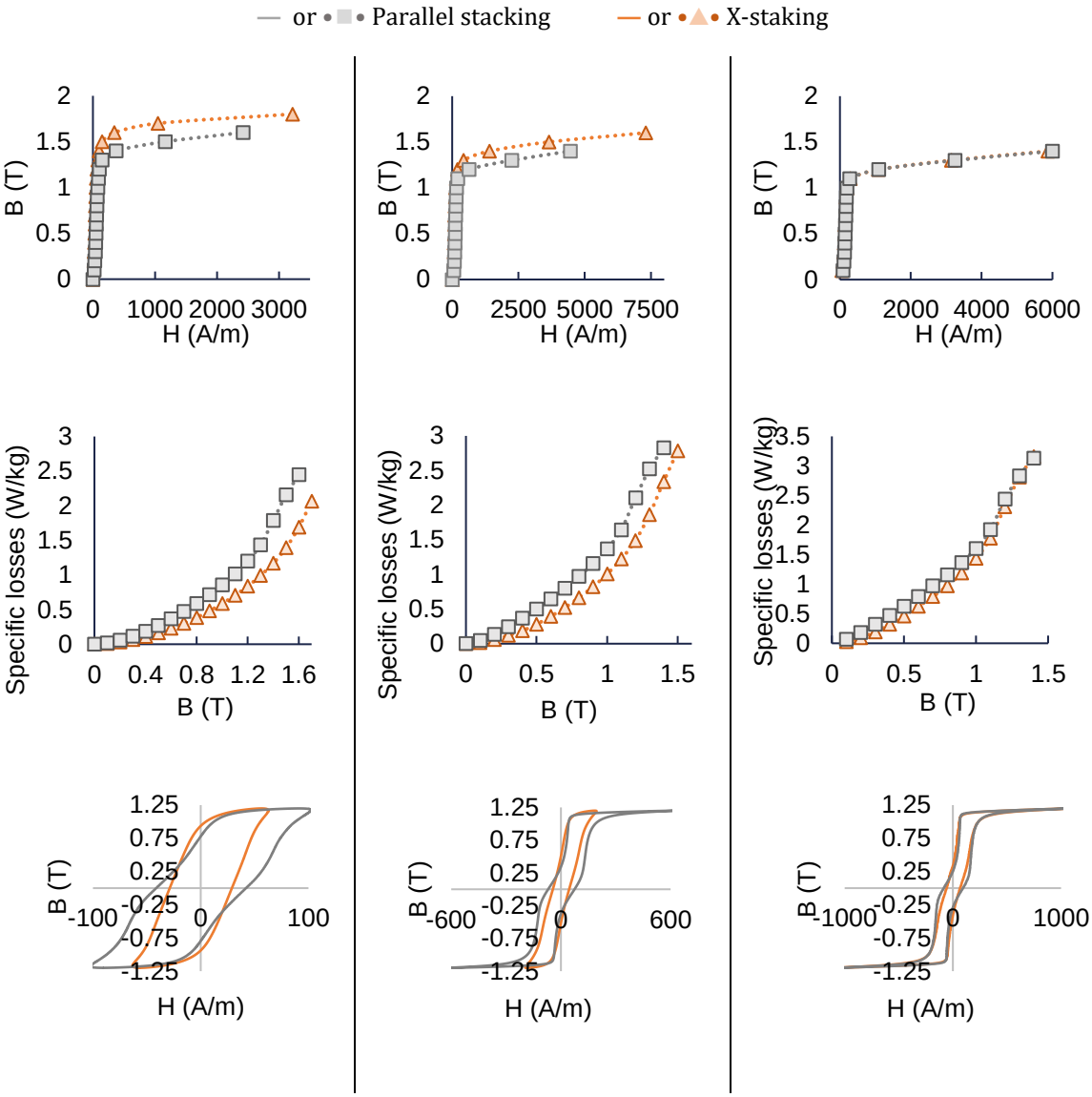


Figure II.6. 50 Hz normal magnetization curves, hysteresis loops at 1.2 T and specific losses measured for intermediate angles for both parallel and x-stacking configurations.

For intermediate directions, different from 0° and 90°, B(H) magnetization curves, hysteresis loops, as well as specific losses are shown in Figure II.6. The stacking configuration of the strips influence the resulting magnetic characteristics. In the parallel configuration, the GOES presents lower magnetic properties and higher losses than in the x-stacking configuration. The difference between the two configurations is due to the demagnetizing field effect. In the x-stacking configuration, the demagnetizing field component is assumed to be canceled as the GOES strips are stacked in opposite directions [60]. Notice that, for the investigated GOES, the demagnetizing field effect is more pronounced for angles between 20° and 42°. For the so-called difficult magnetization direction (θ = 54.7°), the behavior between the parallel and x-stacking situations is very similar. The same goes for higher angles as shown by other results we

have obtained at 75° and 82.5°. This would be due to the predominant 90° dws leading to a macroscopic magnetic behavior which is close to that of the TD. Notice that a similar behavior had already been observed in [102] for the hard magnetization direction of a GOES.

Although the problem of stacking of GOES strips and the related demagnetizing field had been discussed in early works [60], they had never been numerically simulated. An earlier numerical work dealing with the stacking of GOES within a single sheet tester can be found in [103] but this study was limited to a two-dimensional (2D) analysis. Similarly, a 2D non-linear study performed on an Epstein frame can be found in [102], where only the parallel stacking case was studied.

In the next section, we present three-dimensional (3D) finite element simulations performed for both parallel and x-stacking of GOES Epstein strips. The phenomena are interpreted in terms of the demagnetizing field which combined with the applied field affects the GOES magnetization. To our best knowledge, there are no existing 3D numerical studies comparing both stacking configurations, and this work contributes to better comprehension, through numerical analysis, of the demagnetizing field effect in GOES.

## 1.3. FE numerical modeling of the parallel and x-stacking of GOES Epstein strips

### 1.3.1. Simulation conditions

The studied geometry corresponds to a quarter of a standardized Epstein frame with periodic boundary conditions, obtained by taking advantage of the symmetries of the Epstein device. Four GOES strips with dimensions of 14 cm x 3 cm and a thickness of 0.35 mm, have been stacked (in two layers) to replicate the Epstein frame magnetic circuit. Two corner joint types have been considered: plain miter joint and step-lap joint (see Figure II.7). The case of plain miter joint is presented in [104]. In this chapter, the step-lap joint configuration corresponds to the conventional magnetic length path (0.94 m) of the standardized Epstein frame contrary to the plain miter joint configuration for which the magnetic length path exceeds 0.94 m (1 m exactly). A total of 700 turns has been considered for the excitation coils in the numerical model i.e., 175 turns for one quarter of the Epstein frame.

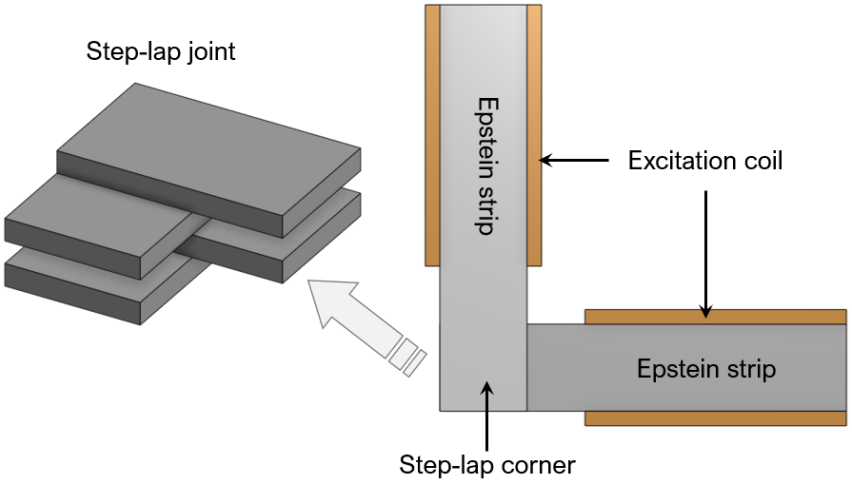


Figure II.7. The modeled geometry of the Epstein frame (one fourth).

To represent the anisotropic magnetic properties of the GOES in the FEM simulation environment, in a first approach, a diagonal tensor has been considered [see eq. *(II.1)*].

$$[\mu_r]=\begin{bmatrix}\mu_{RD} & 0 & 0\\ 0 & \mu_{TD} & 0\\ 0 & 0 & \mu_{ND}\end{bmatrix} \qquad (II.1)$$

This representation of the anisotropy means that the behavior between the main directions RD, TD and the normal direction to the plane (ND) is magnetically decoupled. The in-plane permeabilities $\mu_{RD}$ and $\mu_{TD}$ of the investigated GOES are respectively measured in the RD and TD, and the normal relative permeability $\mu_{ND}$, has been assumed very low (of ≈ 34) as experimentally measured in [105] for a GOES.

Furthermore, within the context of FEM, the local RD axis is identified by means of a local coordinate system in each of the Epstein strips. A tensor rotation operation is achieved from the global referential (x, y, z) to the local one (RD, TD, ND) as shown in equation (3).

$$[\mu_r(\theta)] = [R(\theta)]\begin{bmatrix}\mu_{RD} & 0 & 0\\ 0 & \mu_{TD} & 0\\ 0 & 0 & \mu_{ND}\end{bmatrix}[R(\theta)]^t \qquad (II.2)$$

[R(θ)] is the rotation matrix, that for a rotation referenced to the z axis can be expressed as:

$$[R(\theta)]=\begin{bmatrix}cos\theta & -sin\theta & 0\\ sin\theta & cos\theta & 0\\ 0 & 0 & 1\end{bmatrix} \qquad (II.3)$$

This operation is necessary to consider the lamination orientation for both stacking configurations (parallel and x-stacking), and to perform simulations at different angles θ between the applied field **H** and the RD.

Magnetostatic linear simulations, using vector potential formulation have been performed for different ampere-turns (NI) corresponding to the same applied magnetic field **H** as in the experimental characterization. The considered mesh includes 476,000 elements and the simulation time is of about 10 minutes.

### 1.3.2. Simulation results and comparison with experimental data

A first simulation has been done for the difficult magnetization direction (θ = 54.7° between the applied field and the RD). A current of 0.2 A has been imposed in the excitation coil. This current corresponds to a theoretical applied magnetic fields of 145 A/m. This field strength is experimentally equivalent to an average magnetic flux density of 0.5 T for the parallel stacking and of 0.65 T for the cross-stacking configuration, The components of the linear permeability tensor used in the simulation have been identified from the measurements performed at 0.5 T. The tensor components are $\mu_{RD}$ = 26282 and $\mu_{TD}$ = 2159 while $\mu_{ND}$ has been assumed to be equal to 34 as mentioned before.

The obtained magnetic field distribution for both parallel and x-stacking situations are highlighted in Figure II.8 and Figure II.9.

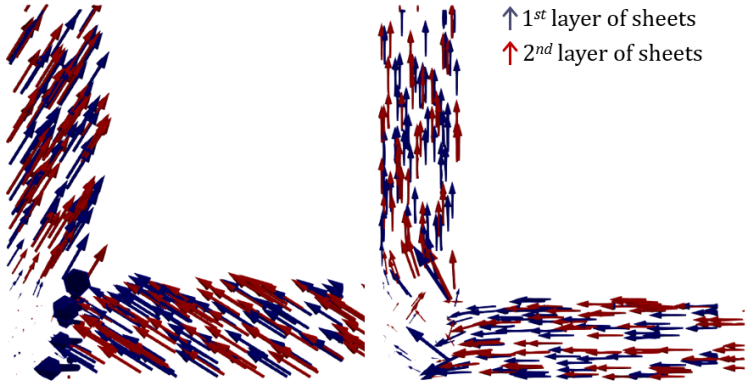


(a) Internal magnetic field $\boldsymbol{H}_i$ (b) Flux density $\boldsymbol{B}$

Figure II.8. Internal magnetic field and flux density maps for parallel stacking.

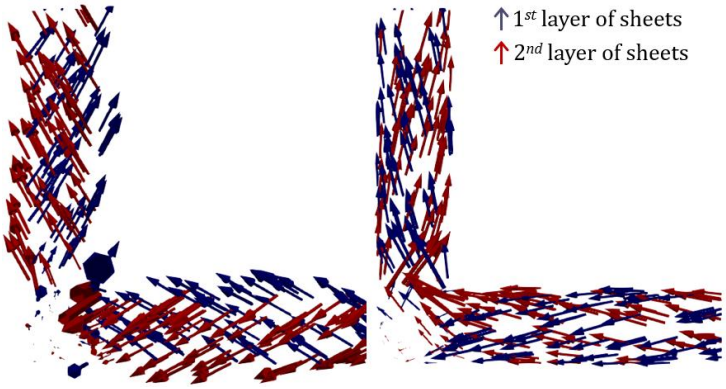


(a) Internal magnetic field $\boldsymbol{H}_i$ (b) Flux density $\boldsymbol{B}$

Figure II.9. Internal magnetic field and flux density maps for x-stacking.
Note 1: the colors differentiate one layer from another.
Note 2: the results given here are those of the step-lap joint configuration.

The results demonstrate the difference in the behavior of the magnetic field and the flux density vectors between the parallel and x-stacking situations. For the parallel stacking configuration, the distribution of the internal magnetic field $\mathbf{H_i}$ vectors can be observed in Figure II.8 (a). It is remarkable that the internal magnetic field $\mathbf{H_i}$ does not follow the average magnetic path of the Epstein frame. In addition, $\mathbf{H_i}$ is not collinear with **B** which is parallel to the longitudinal axes of the strips as shown in and Figure II.8 (b). The internal field $\mathbf{H_i}$ is drastically altered by the influence of the demagnetizing field $\mathbf{H_d}$ according to the vectorial sum $\mathbf{H_i} = \mathbf{H} + \mathbf{H_d}$ [see Figure II.3], where **H** is the applied field along the longitudinal axes of the strips. The magnitude of the internal magnetic field ($\mathbf{H_i}$ = 169 A/m) has increased in comparison with that of the applied field (**H =**145 A/m), Besides, it is interesting to notice that the magnitude of **B** obtained in this configuration (**B** = 0.61 T) is higher than the expected flux density of 0.5 T for which the tensor components have been identified.

Figure II.8(b) displays the magnetic field and flux density vectors for the x-stacking configuration. We can see that the magnetic field vectors of the two stacked strip are in two opposite directions. In this configuration, the influence of $\mathbf{H_d}$ is drastically reduced, resulting in an internal field $\mathbf{H_i} \approx \mathbf{H}$ ($\mathbf{H_i}$ = 150 A/m and **H** = 145 A/m). The obtained average flux density is higher than in the parallel stacking configuration: **B** = 0.7 T. The flux density vectors are displayed in Figure II.9(b).

Another series of FEM simulations has been made considering different angles between the applied magnetic field and RD. Like for the difficult magnetization direction (θ = 54.7°), same Ampère-turns (NI) experimentally imposed have been used in simulation. The permeability tensors have been identified from the measurements according to the tested angle θ at 0.5 T, as before. The simulation results are highlighted in Table II.1 for both parallel and x-stacking and compared to experimental results in terms of the obtained average flux density.

Table II.1. Average magnetic flux density in the Epstein frame: FEM computations vs measurements for some cutting angles.

| *Cutting angle θ (°)* | *NI (At)* | *Epstein measurements* | | *FEM Step-lap* | |
|---|---|---|---|---|---|
| | | Parallel stacking ⟨B⟩ (T) | X-stacking ⟨B⟩ (T) | Parallel stacking ⟨B⟩ (T) | X-Stacking ⟨B⟩ (T) |
| **20** | 11.37 | 0.5 | 1 | 0.75 | 0.87 |
| **30** | 16.2 | 0.5 | 0.7 | 0.65 | 0.80 |
| **42** | 25.9 | 0.5 | 0.9 | 0.66 | 0.80 |

As expected, the average magnetic flux density obtained for the X-stacking configuration are higher than the parallel stacking due to the reduction of the demagnetizing field. However, in both configurations, significant differences between the measured and

computed values have been observed. This difference can be reasonably attributed to the diagonal permeability tensor used in FEM, which neglects the non-diagonal terms, and consequently, the coupling between the magnetization directions within the GOES. To overcome this issue, a full permeability tensor with a nonlinear resolution scheme needs to be implemented in the FEM simulation environment.

# 2. Behavior law

In chapter I, different behavior law models from the literature have been presented and compared. Most of them are anhysteretic analytical models that describe the non-linear B-H relationship. A comparison is given in Table I.1 of chapter I in terms of accuracy, ease of implementation in FEM and need for experimental data. The approach proposed by Enokizono in [68] has been retained to account for the non-linear anisotropic behavior of GOES for FEM simulation.

The Enokizono model (presented in Chapter I, section 4.1.5) allows to obtain, for any angle of magnetic field to RD, full permeability tensors (with anti-diagonal terms) linking the internal magnetic field $\mathbf{H_i}$ to the magnetic flux density **B,** that account for the coupling between the different directions of the GOES $\mathbf{H_i}$ and **B** being diphase by $\theta_{BH}$. For that purpose, Enokizono relies on experimental data obtained from measurements performed on Epstein samples cut along different directions to RD. Let us recall the expression of [ν] (which is also $[\nu] = [\mu]^{-1}$); already given in *(II.4)*.

$$[\nu] = \begin{bmatrix} \nu_{11} & \nu_{12} \\ \nu_{21} & \nu_{22} \end{bmatrix} = [R(\theta_{BH})]^{-1} \begin{bmatrix} \nu' & 0 \\ 0 & \nu' \end{bmatrix} \qquad (II.4)$$

Enokizono approach was originally established based upon measurements under rotating field. Thus, for Enokizono, the angles $\theta_B$, $\theta_H$ and $\theta_{BH}$ as well as the field $\mathbf{H_i}$ are known and the determination of the tensor [**ν**] is relatively simple. However, in our case, we only dispose of experimental data in unidirectional regime, we know neither the angle $\theta_{BH}$ nor the field $\mathbf{H_i}$, that are necessary for the identification of [**ν**]. As the time allocated to this PhD thesis did not allow us to develop a characterization bench under rotating field, we have sought to adapt Enokizono's method to the case of measurements acquired in a unidirectional regime.

In the following, we propose an approach for identifying adequate full permeability tensors for FEM simulation of GOES. This approach relies on the one hand, on the Enokizono approach and on the other hand on the Fiorillo model [60] of magnetization processes in GOES described in Chapter I.

## 2.1. Advanced approach for identifying full permeability tensors based on Enokizono model

To describe the idea behind our approach for identifying full permeability tensors based on Enokizono model, let us recall that in the case of a GOES strip, the internal (or resulting) magnetic field $\mathbf{H_i}$ is the result of the applied magnetic field **H** and the demagnetizing magnetic field $\mathbf{H_d}$, according to *(II.5)*.

$$\mathbf{H_i} = \mathbf{H} + \mathbf{H_d} \qquad (II.5)$$

In practice, from unidirectional measurement based on Epstein frame, we have access only to **H** (the measured applied field). We know neither the demagnetizing field component $\mathbf{H_d}$ nor the internal field $\mathbf{H_i}$.

From these considerations, our approach consists of using the formalism established by Fiorillo *et al.* [60] applied to Epstein strips, which leads to an analytical expression of the demagnetization field $\mathbf{H_d}$ as a function of the polarization level ĵ and the angle θ of the applied field to RD. This expression is given by equation *(I.37)* which is based on the components of the applied field along RD and TD respectively denoted $\mathbf{H_{180}}$ and $\mathbf{H_{90}}$ and the same theoretical parameters $\hat{J}_{90}$ and $\hat{J}_{180}^{r}$ defined in chapter I [equations *(I.33)* and *(I.34)*].

Knowing $\mathbf{H_d}$ and **H**, we can obtain the internal field $\mathbf{H_i}$ *(II.6)* and its angle $\theta_{BH}$ *(II.7)* with respect to the magnetic flux density **B** direction; **B** being assumed to be parallel to the longitudinal axis of the strip.

$$|H_i| = \sqrt{H^2 + H_d^2} \qquad (II.6)$$

$$\theta_{BH} = \text{acos}\left(\frac{|H|}{|H_i|}\right) \qquad (II.7)$$

Thus, the full permeability tensor can be determined using Enokizono's procedure as mentioned before.

A scheme of the procedure followed for identifying the permeability tensors for given angle of magnetic field to RD and polarization level has been highlighted in the Figure II.10.

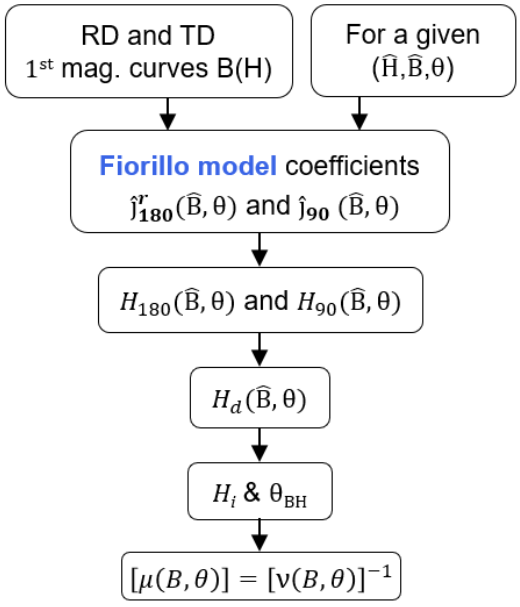


Figure II.10. Scheme of the procedure for identifying the reluctivity tensors.

## 2.2. Results

Both models (Enokizono and Fiorillo) have been tested and checked against experimental data achieved on GOES Epstein samples cut along a direction making an angle θ to RD. Thirteen angles have been considered. Examples of full relative permeability tensors identified for 0.5, 1 and 1.2 T are given in Table II.2. For some of these angles, the obtained tensors are asymmetrical with anti-diagonal values of opposite signs.

Table II.2. Examples of full relative permeability tensors identified at 0.5, 1 and 1.2 T for the investigated GOES.

| *Angle* | *0.5 T* | *1 T* | *1.2 T* |
|---|---|---|---|
| 15 | $\begin{bmatrix} 675.9 & -3064.4 \\ 3064.4 & 675.9 \end{bmatrix}$ | $\begin{bmatrix} 1487.4 & -4865.4 \\ 4865.4 & 1487.4 \end{bmatrix}$ | $\begin{bmatrix} 2089.9 & -5365.7 \\ 5365.7 & 2089.9 \end{bmatrix}$ |
| 30 | $\begin{bmatrix} 1284.2 & -2375.0 \\ 2375.0 & 1284.2 \end{bmatrix}$ | $\begin{bmatrix} 2605.6 & -3568.3 \\ 3568.3 & 2605.6 \end{bmatrix}$ | $\begin{bmatrix} 3259 & -3041.3 \\ 3041.3 & 3259 \end{bmatrix}$ |
| 54.7 | $\begin{bmatrix} 1956.0 & -1230.3 \\ 1230.3 & 1956.0 \end{bmatrix}$ | $\begin{bmatrix} 3287.0 & -1543.9 \\ 1543.9 & 3287.0 \end{bmatrix}$ | $\begin{bmatrix} 8723.1 & -705.6 \\ 705.6 & 8723.1 \end{bmatrix}$ |
| 75 | $\begin{bmatrix} 2135.0 & -469.9 \\ 469.9 & 2135.0 \end{bmatrix}$ | $\begin{bmatrix} 3546.0 & -573.2 \\ 573.2 & 3546.0 \end{bmatrix}$ | $\begin{bmatrix} 2354.2 & -188.3 \\ 188.3 & 2354.2 \end{bmatrix}$ |

## 2.3. Interpolation for FEM

For the numerical simulation based on FEM, the normal direction of the GOES strip plane has to be taken into account. To do so, we have considered a relative permeability of 34 according to [105]. Indeed, Hihat *et al.* have measured the normal permeability for a 0.35 mm thickness GOES and the author results showed that the studied GOES presents a linear behavior up to ≈ 40000 A/m with a constant relative permeability value. The full description of the measurement setup is detailed in Chapter III.

As mentioned before, the experimental data used as inputs for identifying the permeability tensors as function of θ and B are simply B(H) anhysteretic curves measured in different directions. In a FEM environment (A-φ formulation), for each finite element, the values of the magnetic flux density B do not necessarily coincide with that of the experimental data. On the other hand, the angle θ of the applied field to RD for each of the elements does not necessarily coincide with the directions measured experimentally. Therefore, a double interpolation is necessary to obtain the magnetic field values for any angle and flux density level i.e., H(B,θ). A Piecewise Cubic Hermite Interpolating Polynomial (PCHIP) has been used for this purpose in MATLAB [106]. For example, to obtain the value of H for an angle θ of 35° and a flux density level of 0.5 T, the 30° and 42° experimental B(H) curves have been used for interpolation.

Table II.3 shows the robustness of PCHIP interpolation for two directions: 20° and 54.7° and for two magnetic flux density levels: 0.5 and 1 T. The tensors calculated from the interpolated H(B, θ) data have been obtained without the corresponding experimental B(H) curves i.e. without 20° and 54.7° B(H) experimental curves. Overall, the interpolated tensors are quite similar to the reference tensors determined from the measured data.

Table II.3. Interpolated permeability tensors

| *Angles (In degrees)* | *B (T)* | *Permeability tensors* | |
|---|---|---|---|
| | | *Reference* | *Interpolated H(B,θ)* |
| 20 | 0.5 | $\mu_r = \begin{bmatrix} 1067.1 & -2765.8 \\ 2765.8 & 1067.1 \end{bmatrix}$ | $\mu_r = \begin{bmatrix} 926.4 & -2718.3 \\ 2718.3 & 926.4 \end{bmatrix}$ |
| | 1 | $\mu_r = \begin{bmatrix} 2176.0 & -4242.7 \\ 4242.7 & 2176.0 \end{bmatrix}$ | $\mu_r = \begin{bmatrix} 1977.4 & -4332.5 \\ 4332.5 & 1977.4 \end{bmatrix}$ |
| 54.7 | 0.5 | $\mu_r = \begin{bmatrix} 1956.0 & -1230.3 \\ 1230.3 & 1956.0 \end{bmatrix}$ | $\mu_r = \begin{bmatrix} 1981.6 & -1285.0 \\ 1285.0 & 1981.6 \end{bmatrix}$ |
| | 1 | $\mu_r = \begin{bmatrix} 3287.0 & -1543.9 \\ 1543.9 & 3287.0 \end{bmatrix}$ | $\mu_r = \begin{bmatrix} 3343.9 & -1609.9 \\ 1609.9 & 3343.9 \end{bmatrix}$ |

The use of these tensors in FEM environment is presented in section 5.1.

# 3. Iron losses

As discussed in Chapter I section 4.2, among the existing iron loss models for GOES, we have retained that of Appino *et al.* [61] because its underlying physical principles and its limited number of parameters.

## 3.1. Description of the selected model

The selected model relies on the formalized approach developed by Fiorillo *et al.* (see [60]) to describe the magnetization processes in high permeability HiB GO sheets, extended in 2020 by Appino *et al.* to take into account the magnetic losses [61] based on the loss separation principle [50]. It requires the knowledge of the domain wall structure and its evolution with the applied magnetic field. In HiB GO sheets, and based on the single crystal approximation, the magnetization processes can be described through the different domain families known as "Néel phases" [59]. Unlike a non-oriented grain material of which the domain subdivision is very complex or even impossible to interpret, in a textured material, the domain structure within each grain tends to be established according to the same pattern as for a single crystal. The transposition of the magnetization mechanisms of a perfect single crystal to the case of an oriented polycrystalline sheet is reasonable. Detailed explanations of the model are provided in [61]. Herein, the model is briefly described. As mentioned before, the model relies on the decomposition of the total losses into three terms (hysteresis, classical and excess losses). The originality of the retained loss model concerns the first loss term *i.e.,* the quasi-static losses dissipated per magnetization cycle, depending on the peak polarization $\hat{J}$ and on the angle $\theta$ of the applied field to RD [60]. This term is built from the two sets of P-$\hat{J}$ quasi-static experimental data obtained in the principal directions RD and TD, respectively denoted $P_{h,EXP}^{RD}$, $P_{h,EXP}^{TD}$ in [61]. Based upon the evolution of the main domain families within the material (driven by 180° and 90° dws), the quasi-static losses are expressed by the analytical relationship in [61] involving the volume fraction occupied by these domains for any direction of the magnetic field.

$$P_h(\theta,\hat{J}) = \langle v_{180}\rangle_T \, P_{h,EXP}^{RD}\left[\hat{J}_{180}^{r}\right] + P_{h,EXP}^{TD}\left[\hat{J}_{90}\right] \qquad (II.8)$$

Where:

$\langle v_{180}\rangle_T$ is the fractional sample volume occupied by the 180° domains, averaged over a period T.

$\hat{J}_{180}^{r}$ and $\hat{J}_{90}$ are the associated polarizations for the volume fractions $\langle v_{180}\rangle$ and $\langle v_{90}\rangle$.

Under a sinusoidal polarization waveform, the expressions of the theoretical model parameters $\hat{J}_{90}$ and $\hat{J}^{r}_{180}$ as function of θ, $\hat{J}$ and $J_s$ are given in Chapter I in *(I.33)* and *(I.34)* and recalled here:

$$\hat{J}_{90}=\hat{J}\sin\theta$$

$$\hat{J}^{r}_{180}=\frac{\hat{J}}{1-\sqrt{2}\frac{\hat{J}}{J_s}\sin\theta}\cos\theta$$

$$\langle v_{180}\rangle_T=1-\frac{2\sqrt{2}\hat{J}}{\pi J_s}\sin\theta \qquad \textit{(II.9)}$$

where $J_s$ represents the saturation polarization.

The evolution of the three coefficients versus θ and $\hat{J}$ as well as their theoretical limit values are given in [61].

The same principle is applied for the determination of the excess losses. At this stage, the corresponding input data are the excess losses measured in both RD and TD that are respectively denoted $P^{RD}_{exc,EXP}$ and $P^{TD}_{exc,EXP}$ in *(II.10)*

$$P_{exc}(\theta,\hat{J},f)=\langle v_{180}\rangle_T P^{RD}_{exc,EXP}\left[\hat{J}^{r}_{180}\right]+P^{TD}_{exc,EXP}\left[\hat{J}_{90}\right] \qquad \textit{(II.10)}$$

Concerning the classical loss term, it takes the expression resulting from the classical eddy current theory which is independent of the angle θ of the applied field to RD. Indeed, the case of an infinite homogeneous sheet of thickness e, with an electrical conductivity σ and under a sinusoidal magnetic flux density of frequency f, allows an entirely analytical resolution of the magnetic diffusion equation. The resulting power losses per unit mass are expressed by *(II.11)*:

$$P_{cl}(\hat{B},f)=\frac{\pi^2}{6}\frac{\sigma e^2\hat{B}^2f^2}{\rho} \qquad \textit{(II.11)}$$

where ρ is the material density (in $kg/m^3$).

Let us recall that for soft magnetic materials B ≈ J. Thus, for more convenience, $\hat{B}$ will be used instead of $\hat{J}$. Finally, in *(II.12)*, we get a description of the total losses $P(\theta,\hat{B},f)$ as a function of the angle θ of the applied field to RD, without any adjustable parameter.

$$P(\theta,\hat{B},f) = P_h(\theta,\hat{B}) + P_{cl}(\hat{B},f) + P_{exc}(\theta,\hat{B},f) \qquad \textit{(II.12)}$$

## 3.2. Model results vs experimental data

First, from the RD and TD measured data at different frequencies 5, 10, 25, 50 and 100 Hz, the loss decomposition has been performed. The static losses have been estimated through an extrapolation of the total energy losses to 0 Hz. The classical losses were calculated according to equation *(II.11)*, and the excess losses are deduced from the difference between the total losses and the two previous components. The iron loss model was then tested for intermediate angles θ between RD and TD. The model results are displayed in Figure II.11, and show a very satisfactory agreement between the modeled and experimental losses as function of the angle θ.

The relative difference between the modeled and experimental loss values have been calculated by using the expression *(II.13)*.

$$Relative\ difference\ (\%) = \frac{|Mod.value - Exp.value|}{Exp.value} x100 \qquad (II.13)$$

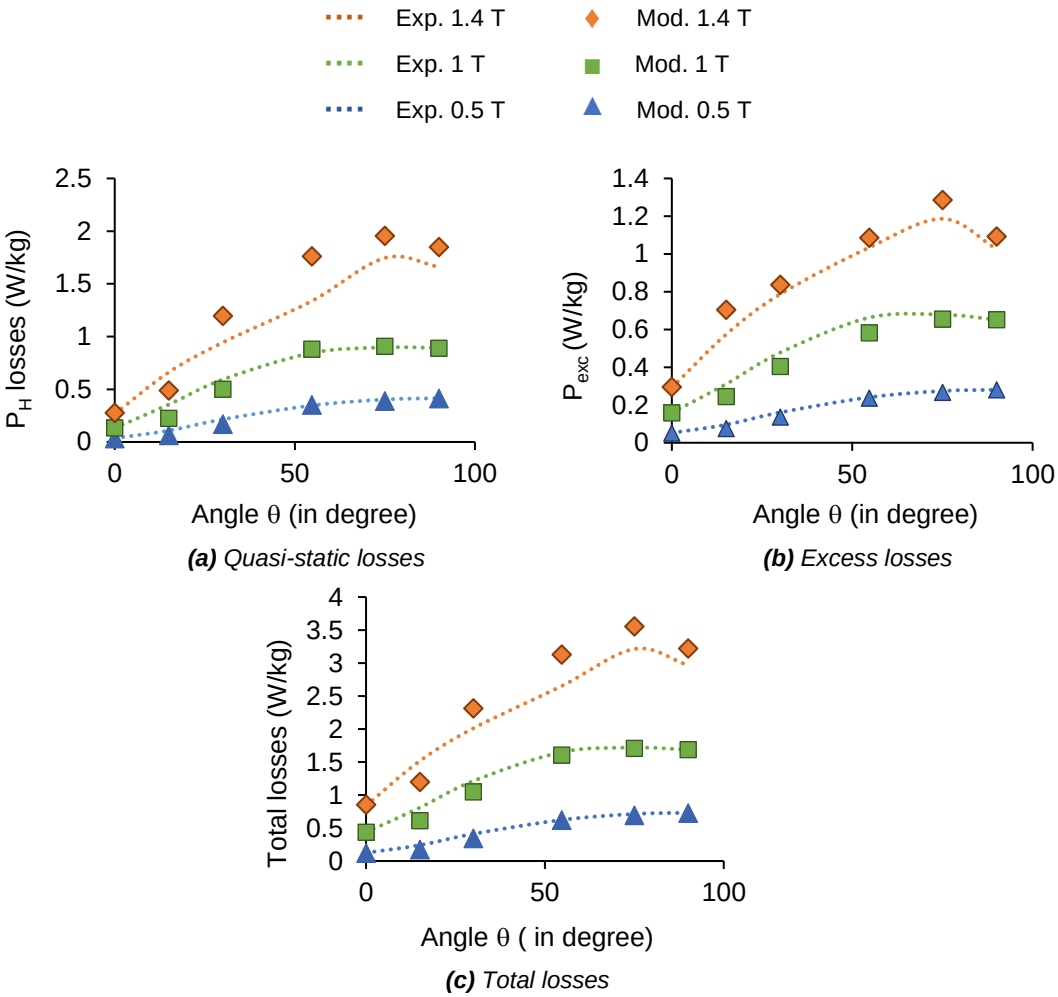


***(a)*** *Quasi-static losses*

***(b)*** *Excess losses*

***(c)*** *Total losses*

Figure II.11. Comparison of the different loss contributions for different angles at 0.5, 1 and 1.4 T.

Overall, the model restitutes the total measured losses for almost all angles within 12%. The highest relative differences have been observed for 15° and 30° (respectively 37% and 20% at 0.5 T).

For comparison purposes, the maximum relative differences observed by Appino *et al.* in 2020 on a high permeability GO Fe-3%Si alloy (Nippon steel M2H) reached 22% (for the excess loss component) and 12% for the total losses [61]. According to the author, these discrepancies can be ascribed to the idealized nature of the model which does not take into consideration the whole domain structure, in particular the surface domains. In our case, the nature of the tested GO material (conventional GOES) could justify the relative differences for 15° and 30°. These differences remain quite reasonable for an iron loss model.

# 4. Finite element Method

In this work, the finite element software code_Carmel [107] is used for the implementation of the GO models. This computation code, developed by the L2EP laboratory in association with EDF R&D, allows to perform finite element simulations to represent the electromagnetic phenomena, especially in electrical machines.

In this section we present the Maxwell equations and the mathematical formulations used in this work for the magnetostatic and magneto quasi-static simulations.

## 4.1. Maxwell Equations

Maxwell equations are considered the base of all electromagnetic phenomena, they represent the laws of electricity and magnetism (Faraday, Ampere, Thompson and Gauss respectively), and mathematically describe the relations and interactions between the magnetic and electric fields in a continuous domain [108] [109]. They can be expressed as follows:

$$\nabla \times \mathbf{E} = -\frac{\partial \mathbf{B}}{\partial t} \qquad (II.14)$$

$$\nabla \times \mathbf{H} = \mathbf{J} + \frac{\partial \mathbf{D}}{\partial t} \qquad (II.15)$$

$$\nabla \cdot \mathbf{B} = 0 \qquad (II.16)$$

$$\nabla \cdot \mathbf{D} = \rho \qquad (II.17)$$

Where $\mathbf{E}$ represents the electric field [V/m], $\mathbf{B}$ is the magnetic induction [T], $\mathbf{H}$ is the magnetic field [A/m], $\mathbf{D}$ is the electric field density [C/m$^2$], $\rho$ is the electric charge density [C/m$^3$] and $\mathbf{J}$ is the density of current [A/m$^2$] that can be divided in two terms: $\mathbf{J_s}$ which represents the source current density, from the excitation coils and $\mathbf{J_{ind}}$ which represents the current induced within the conductive domains.

$$\mathbf{J} = \mathbf{J_s} + \mathbf{J_{ind}} \qquad (II.18)$$

## 4.2. Magnetic behavior law

In addition to the Maxwell equations, behavior law formulations are required to denote the characteristics of the materials subjected to these fields in the finite element analysis, in particular the highly anisotropic GOES. For this purpose, we recall:

- Ohm's law, which relates the electric field $\mathbf{E}$ with the current density $\mathbf{J_{ind}}$ through the electrical conductivity $\sigma$ [S/m].

$$\mathbf{J_{ind}} = \sigma\mathbf{E} \qquad (II.19)$$

- Magnetic behavior law (*I.6*), previously presented in chapter I, which relates the magnetic field **H** with the flux density **B**, through the magnetic permeability μ [H/m].

These expressions are valid for isotropic, linear materials at a constant temperature. Since σ and μ can evolve as function of numerous parameters, like the temperature, time, frequency, etc.

For our work, the conductivity of the material is considered linear and isotropic. The permeability, however, has been adapted for anisotropic materials and is represented as a full permeability tensor. With this approach it is possible to consider the directional properties of the material.

In this scenario the magnetic behavior law is given by:

$$\mathbf{B} = [\mu]\,\mathbf{H} \qquad (II.20)$$

In which $[\mu]$ is a permeability tensor that accounts for the interactions of all the magnetization directions and the GOES nonlinearity.

## 4.3. Boundary conditions

Aiming to unify the possible resolution of the Maxwell equations with the given behavior laws, some boundary conditions have been established.

These conditions are defined in the boundary Γ of any given domain D and can be decomposed in two parts: the boundary $\Gamma_b$ relative to the magnetic induction and the boundary $\Gamma_h$ relative to the magnetic field. These boundaries comply with the relations $\Gamma = \Gamma_b \cup \Gamma_h$ and $\Gamma_b \cap \Gamma_h = 0$.

Moreover, if the studied domain D includes a conductive material ($\sigma \neq 0$), the boundary of this material $\Gamma_c$ has to be considered. This boundary can be decomposed in two contributions as well: the frontier $\Gamma_e$ relative to the electric field and the frontier $\Gamma_j$ relative to the current density. These frontiers are subjected to the following relations $\Gamma_c = \Gamma_e \cup \Gamma_j$ and $\Gamma_e \cap \Gamma_j = 0$.

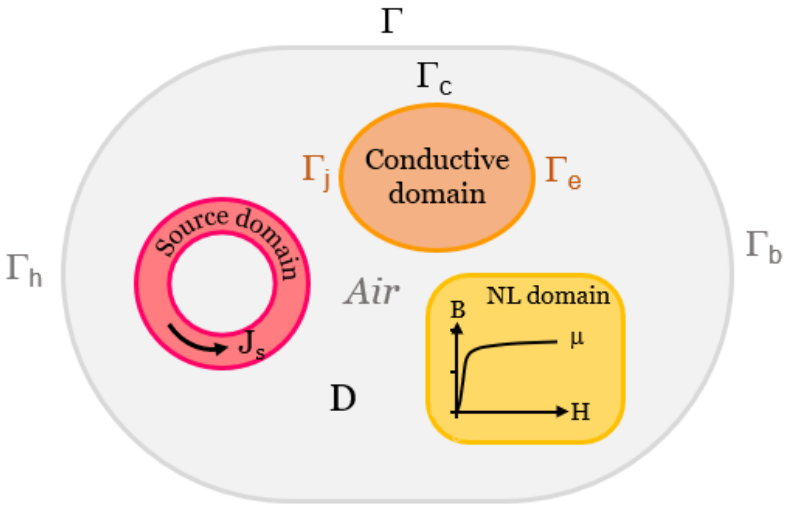


Figure II.12. Domain of study D.

The boundary conditions are considered homogeneous in terms of the magnetic field and induction, thus be enounced as follows:

$$\mathbf{H} \times \mathbf{n}|_{\Gamma_h} = 0 \qquad (II.21)$$

$$\mathbf{B} \cdot \mathbf{n}|_{\Gamma_b} = 0 \qquad (II.22)$$

**n** is a vector that corresponds to the normal frontier of Γ. Lastly, by combining the equation *(II.14)* with *(II.22)*, and *(II.15)* with *(II.21)* it is possible to obtain the boundary conditions for the conductive domains:

$$\mathbf{E} \times \mathbf{n}|_{\Gamma_e} = 0 \qquad (II.23)$$

$$\mathbf{J} \cdot \mathbf{n}|_{\Gamma_j} = 0 \qquad (II.24)$$

## 4.4. Formulations: Magnetostatic and Magneto quasi-static

In this thesis, we will limit ourselves to the magnetic vector potential formulations. We will therefore only present the A-formulation for magnetostatics and the A-φ-formulation for Magneto quasi-static problem.

### 4.4.1. Magnetostatic problem

The magnetostatic formulation is used to study the magnetic phenomena in static conditions, where there are not conductive materials, and the current density **J** corresponds only to the source term $\mathbf{J_s}$. The system of equations to solve is given by:

$$\nabla \times \mathbf{H} = \mathbf{J_s} \qquad (II.25)$$

$$\nabla \cdot \mathbf{B} = 0 \qquad (II.26)$$

The intrinsic magnetic behavior law of the material is added to these equations as previously defined in *(II.20)*, as well as the boundary conditions given by the equation *(II.21)* and *(II.22)*.

In general, these equations are not solved directly, but by using potential formulations. For the magnetostatic case, two types of formulations can be used, the magnetic scalar potential formulation Ω and the magnetic vector potential formulation **A** but as we have just explained only the formulation in A will be treated

From the magnetic Gauss law formulation*(II.26)*, it is possible to introduce a magnetic vector potential **A** that verifies the relation

$$\mathbf{B} = \nabla \times \mathbf{A} \qquad (II.27)$$

By replacing this expression in (*I.3*) and *(II.26)* the vector potential formulation can be obtained as in *(II.28)*.

$$\nabla \times ([\mu]^{-1} \nabla \times \mathbf{A}) = \mathbf{J_s} \qquad (II.28)$$

Due to the infinite solutions for the value of the vector potential **A** the Coulomb gauge is applied [110] to assure the uniqueness of the solution.

### 4.4.2. Magneto quasi-static problems

The magneto quasi-static formulation is used when there are conductive materials within the domain of study. In consequence, for this case, the eddy currents cannot be neglected, and the equations to solve are:

$$\nabla \times \mathbf{E} = -\frac{\partial \mathbf{B}}{\partial t} \qquad (II.29)$$

$$\nabla \times \mathbf{H} = \mathbf{J_s} + \mathbf{J_{ind}} \qquad (II.30)$$

$$\nabla \cdot \mathbf{B} = 0 \qquad (II.31)$$

$$\nabla \cdot \mathbf{J} = 0 \qquad (II.32)$$

Where $\mathbf{J_{ind}}$ represents the induced current density in the material by the eddy currents. The intrinsic behavior laws of the materials from *(II.20)* and *(II.19)* are considered, as well as the boundary conditions described in section 4.3. Many formulations can be used to solve the equations but we will only use the **A**-φ formulation. and.

This formulation is obtained from the equations *(II.30)* and *(II.32)*, and follows the same principle of the **A** formulation, in which the relation *(II.27)* is true.

By replacing *(II.27)* in *(II.29)* we have that

$$\nabla \times \left( \mathbf{E} + \frac{\partial \mathrm{A}}{\partial \mathrm{t}} \right) = 0 \qquad \textit{(II.33)}$$

Given that for the rotational of $\left( \mathbf{E} + \frac{\partial \mathrm{A}}{\partial \mathrm{t}} \right)$ is equal to zero, an electric scalar potential $\varphi$ can be introduced as equal to the gradient of this expression, and thus, using this scalar the electric field expression can be written as:

$$\mathbf{E} = -\frac{\partial \mathrm{A}}{\partial \mathrm{t}} - \nabla \varphi \qquad \textit{(II.34)}$$

Finally, by using the electric behavior law, the magnetic field **H** and the current density $\mathbf{J_{ind}}$ can be replaced as function of the vector potential **A** and $\varphi$ at *(II.30)*. And the formulation equation is obtained:

$$\nabla \times ([\mu]^{-1} \nabla \times \mathbf{A}) = \mathbf{J_s} - \sigma \left( \frac{\partial \mathrm{A}}{\partial \mathrm{t}} + \nabla \varphi \right) \qquad \textit{(II.35)}$$

For this formulation, as in the case of the **A** formulation, a gauge condition must be established to assure the uniqueness of the solution [110].

## 4.5. Domain discretization

In the case of systems with complex geometries (turbo-generators, motors, transformers, etc.) the Maxwell equations are difficult to solve analytically. However, the problem can be discretized to simplify the resolution by applying the finite element method [111], [112].

A complex geometry could be discretized by considering an ensemble of finite geometrical elements. The physical properties of each element coincide with those of the material under study. Therefore, the problem can be solved by applying the analytical formulations in each element, and the final solution is considered to be the sum of all the solutions of the finite element.

The finite elements, also called interpolations or Whitney's elements [112], can have simple geometrical forms of 1D, 2D or more complex forms of higher orders [see Figure II.13]. Their geometries can be adapted to accurately represent the domain under study. Furthermore, they are interconnected with one another through their nodes, edges, faces and volumes, creating a mesh. These additional elements serve for the discretization as well, the nodes represent the scalar potentials and the edges the vector potentials.

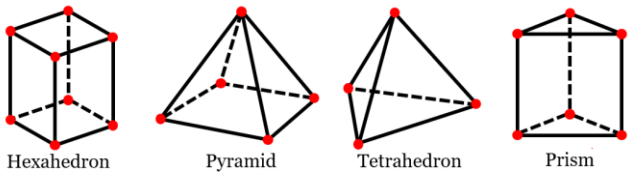


Figure II.13. Geometries of the elements available in code_Carmel.

The magnetostatic and magneto quasi-static formulations previously presented in this section, have to be adapted to be used in the discrete domains. This can be done, by applying the weighted residual method of Galerkin (detailed in [113] [114]), that transforms the magnetostatic and magneto quasi-static equations to their 'weak' form, by integrating the equation over the studied domain D and weighting it by a test function.

The integral formulation of the magnetostatic formulation in vector potential A, can be written as follows. Where **W** is a test function. Similarly, the weak magnetostatic formulation in vector potential **A** can be expressed as follows.

$$\int_D (\nabla \times \mathbf{Wa} \,.[\mu]^{-1}.\, \nabla \times \mathbf{A})\, dD = \int_D (\,)\, dD \qquad (II.36)$$

Where $\mathbf{W_a}$ is a test function applied to edge

Finally, for the magneto quasi-static formulations in **A**-φ the weak formulation can be written using a two-equation system, as shown:

$$\int_D \left[ (\nabla \times \mathbf{Wa} \,.\, [\mu]^{-1}.\, \nabla \times \mathbf{A}) + \sigma \mathbf{Wa} \left( \frac{\partial \mathbf{A}}{\partial t} + \nabla \cdot \Omega \right) \right] dD = 0 \qquad (II.37)$$

$$\int_D \sigma\, \nabla \cdot \mathbf{Wn} \left( \frac{\partial \mathbf{A}}{\partial t} + \nabla \varphi \right) dD = 0 \qquad (II.38)$$

Where $\mathbf{W_n}$ is a test function applied to the node.

Once discretized these weak formulations can be written in the matrix form and the system of equations can be solved as in:

$$[\mathbf{S}] \cdot [\mathbf{X}] = [\mathbf{F}] \qquad (II.39)$$

Where, [**S**] is the global stiffness matrix that describes the system, [**X**] represents the unknowns and [**F**] the vector forces external to the system.

Finally, in the case of non-linear materials, the matrix [**S**] will depend on the vector [**X**]. In this case, an iterative method will be needed to solve the non-linear matrix system. For this purpose, the Newton-Raphson iteration method and the Fixed-point iteration method have been adopted in code_Carmel.

Thus, the finite element method must be solved in the following matrix form for the discretization of a non-linear system.

$$[\mathbf{S}(\mathbf{X})] \cdot [\mathbf{X}] = [\mathbf{F}] \qquad \textit{(II.40)}$$

# 5. Implementation in FEM

The anisotropic B-H law model as well as the iron loss model for GOES, described previously, have been implemented in the FEM simulation environment code_Carmel carried by L2EP laboratory. In this section, the key steps followed for the implementation of the models are introduced. Applications on simple magnetic structures such as the Epstein frame and a ring core are presented, discussed and compared with experimental measurements.

## 5.1. Advanced approach for identifying full permeability tensors based on Enokizono model (modified Enokizono model)

This section aims to verify the validity of the advanced approach proposed for identifying full permeability tensors based on Enokizono model (i.e., modified Enokizono approach) within numerical simulation. The case of the standardized Epstein frame has been chosen for this purpose. The complete geometry of the Epstein frame has been considered in the modeling with two layers of GOES strips (of 28 cm x 3 cm) while including the step-lap corner joint type in order to compare with experimental measurements, it has to be mentioned that depending on the considered angle to RD, the same experimental currents have been imposed in the simulations in order to get the same magnetic field which is experimentally applied.

As described in section 2.1, for each considered direction with respect to RD, the permeability tensors have been identified from unidirectional measurements performed on Epstein samples cut along the considered direction. A permeability tensor is assigned for each single strip volume and thus, the considered measurements for identifying the tensors are those of the parallel stacking configuration.

Figure II.14 shows 3D simulations of the Epstein frame made of GOES strips with a longitudinal direction making an angle of 54.7° to RD with:

- a full permeability tensor (Figure II.14-a) based on the proposed advanced approach (i.e., modified Enokizono approach);
- a diagonal tensor (Figure II.14-b) with only three components $\mu_x$, $\mu_y$ and $\mu_z$, which assumes that the material behavior along its different directions is magnetically decoupled.

Both permeability tensors have been identified at an average experimental magnetic flux density of 0.5 T. This is the reference point to verify the ability of both approaches to reproduce the experiment.

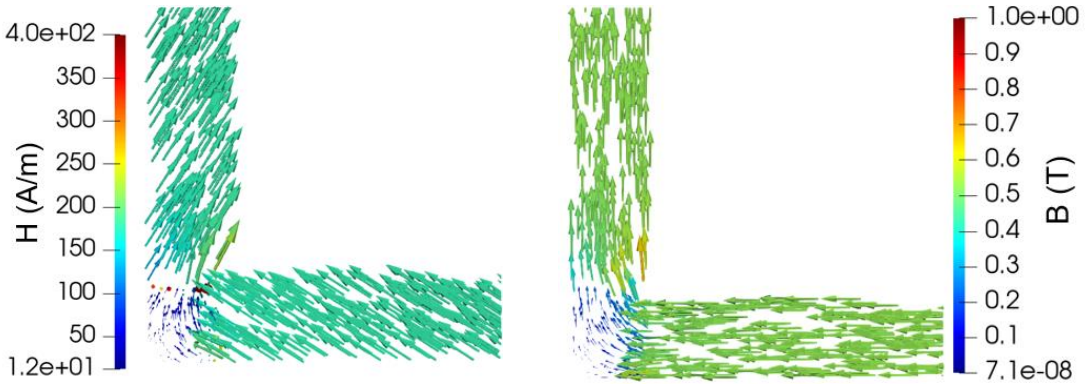


(a) with a full permeability tensor

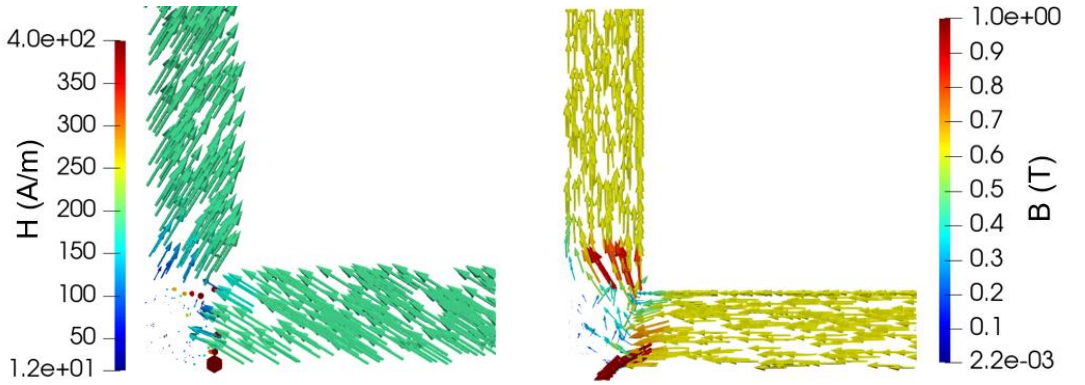


(b) with a diagonal tensor

Figure II.14. Field maps at 50 Hz with diagonal and full permeability tensors identified at 0.5 T for an applied field direction of 54.7° to RD (a quarter of the geometry is displayed).

From field map point of view, for both approaches, $\mathbf{H_i}$ and $\mathbf{B}$ vectors follow the same typical behavior already shown in Figure II.8 for the parallel stacking configuration. However, a difference can be observed in the corners of the frame. Indeed, $\mathbf{H_i}$ and $\mathbf{B}$ vectors seems more consistent in the case of the maps obtained with a full permeability tensor.

Furthermore, the full tensor gives more realistic results in terms of the average magnetic flux density than the simple diagonal tensor. The average magnetic flux density obtained with the latter exceeds 0.5 T which is the reference point experienced in theses simulations (around 0.60 T). The magnetic field strength for both cases is very similar in view of the same imposed ampere-turns.

In order to further test the relevance of the proposed approach for identifying full permeability tensors, another series of FEM simulations have been performed for other angles $\theta$ between the applied magnetic field and RD. Figure II.15 summarizes the results in terms of the obtained average magnetic flux density and compares them against the reference point (0.5 T) for which the permeability tensors have been identified for each of the considered angles.

This figure emphasizes the ability of the proposed approach based on full permeability tensors to improve the representation of the anisotropic behavior GOES strips within the Epstein frame with quite good accuracy in comparison with the diagonal tensor-based approach.

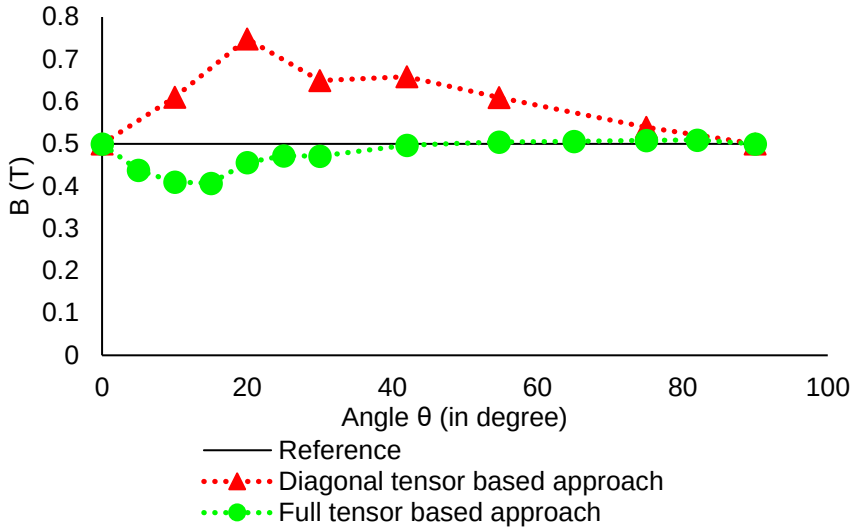


Figure II.15. FEM simulation results in terms of average magnetic flux density versus the angle θ between the applied magnetic field and RD.

Finally, the angle $\boldsymbol{\theta}_{\mathbf{Hi,H}}$ between the internal magnetic field $\mathbf{H_i}$ and the applied magnetic field $\mathbf{H}$ is given in Table II.4 for different simulated angles θ.

Table II.4. The angle $\boldsymbol{\theta}_{\mathbf{Hi,H}}$ between $\mathbf{H_i}$ and $\mathbf{H}$

| *Angle θ* | *Full permeability tensor-based approach* | *Diagonal tensor-based approach* |
|---|---|---|
| 10 | 76.7 | 54.98 |
| 20 | 69.10 | 57.04 |
| 30 | 61.61 | 51.78 |
| 42 | 46.108 | 42.71 |
| 54.7 | 32.44 | 31.92 |
| 75 | 12.215 | 13.72 |

The angle $\boldsymbol{\theta}_{\mathbf{Hi,H}}$ reduces as the angle θ increases. This means that the orthogonal demagnetizing field $\mathbf{H_d}$ is reduced when the considered direction is close to TD. This tendency has been observed during the experimental measurements made on the investigated GOES (see section 1.2.2).

## 5.2. Iron loss model

The selected anisotropic iron loss model from C. Appino *et al.* has been implemented in code_Carmel in post-processing. This section aims to verify the validity of the iron loss model within numerical simulation.

A basic scheme of the overall loss computation procedure is shown in Figure II.16. The retained anisotropic loss model is scalar i.e., it depends on the magnitude of the magnetic flux density. To apply it in a FEM simulation environment for computing the local and total iron losses wherein the variations of the flux density vector **B**(t) are usually two-dimensional in the plane of the magnetic circuit, a new local orthonormal referential linked to the flux density vector **B**(t) is considered for each element of the simulated magnetic circuit. The axes of this referential are parallel and perpendicular to the direction of the maximum module of **B**(t). New components $B_{//}(t)$ and $B_{\perp}(t)$ are then obtained from $B_x(t)$ and $B_y(t)$ given by FEM. In view of the loss model equations expressed as function of the peak value of the magnetic flux density, the peak values $\widehat{B}_{//}$ and $\widehat{B}_{\perp}$ of both components $B_{//}(t)$ and $B_{\perp}(t)$ are used as inputs of the uniaxial loss model to post process the iron loss calculation for both // and ⊥ directions and for each element (see Figure II.16). For each element, the local loss value is obtained by the addition of the two loss contributions along the parallel and perpendicular axes. This approach is applied for all the elements and the total iron losses are obtained from the sum of the local losses associated to each element. Indeed, knowing the volume of the elements, the corresponding local iron losses per unit mass (volume, respectively) can be converted in Watt and then summed in order to get the total iron losses in the whole magnetic circuit.

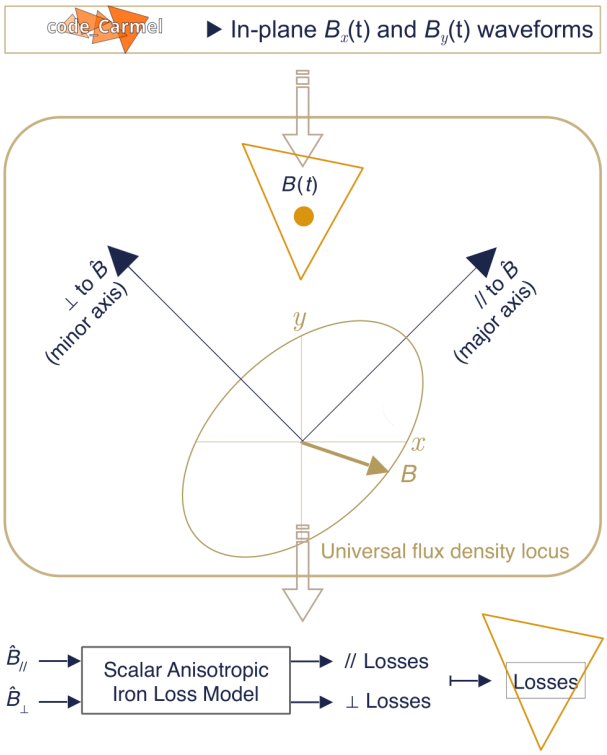


Figure II.16.Local referential for the decomposition of the vector **B**(t) for in plane loss computation.

It should be noted that the choice of the in-plane (//,⊥) local referential is not arbitrary because it enables a direct application of the loss scalar model in the case of a uniaxial flux

density. This bi-axial decomposition of the local iron losses is based on the well-known principle of superimposition which assumes that the losses are composed of two alternating contributions respectively in the parallel (major) and perpendicular (minor) axis.

This is the assumption of the application of the implemented scalar loss model to treat 2D excitations rigorously requiring a vectorial hysteresis model. This method was adopted in the past under circular and elliptic B(t) [115]. It was experimentally validated on the relatively isotropic semi-process material (M1000-65D) under non-uniform rotating B(t) loci similar to those met in electrical machines [116]. The decomposition was applied up to 1.5 T and the loss error introduced by this approximation remains less than 10% [115].

## 5.3. Experimental validation

Simple test cases under periodic waveforms have been studied: the Epstein frame and a toroidal core made of the same conventional GOES previously characterized (see section 1.2). 3D linear magneto-static simulations have been achieved. The two full and diagonal permeability tensor-based approaches have been tested to account for the anisotropic behavior law of the GOES. Then, from the FEM distributions of **H** and **B** fields, the iron loss calculations have been executed and checked against experimental data.

### 5.3.1. Epstein frame test case

Magnetostatic simulations of the standardized Epstein frame have been performed following the same approach described in section 5.1 while considering the same mesh. To account for the anisotropic behavior law of the GOES, full permeability tensors (from the modified Enokizono approach) have been identified for 6 different cutting angles $\theta$ (0°, 15°, 30°, 54.7°, 75° and 90°) and 4 flux density levels (0.1, 0.5, 1 and 1.2 T). Two periods have been simulated under sinusoidal excitation currents for which the peak values correspond to those of the experimental currents.

The iron loss model has been applied in post-processing for each of the angles $\theta$ (between the applied magnetic field and the RD) and for each of the experienced flux density levels. The computed iron losses (hysteresis, classical and excess loss components) are given in Figure II.17, and compared in the same figure with the measured losses.

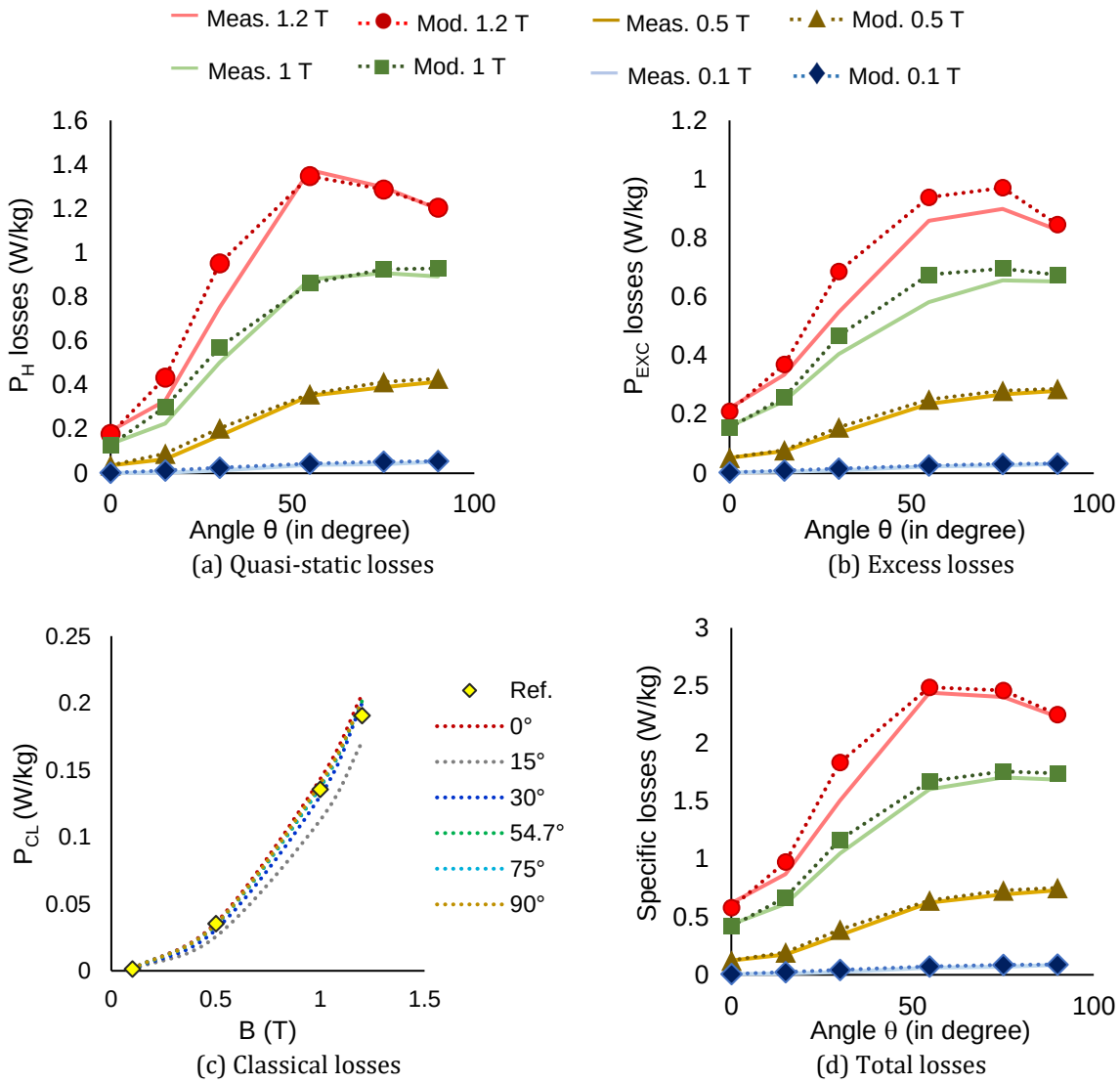


Figure II.17.Computed iron losses vs experimental losses on the standardized Epstein frame.

The computed quasi-static losses (Figure II.17-a) are in good agreement with the measured ones with a noticeable difference which can be observed for 15 and 30°.

For the excess loss component (Figure II.17-b), this relative error between the computed and the measured losses is particularly evident at 1.2 T where it reaches its maximum value of 25% for 30°. Let us recall that the discrepancies at 15° at 30° have already been observed in section 3.2 dedicated to the validation of the iron loss model against experiment. They can be possibly attributed on one hand to the idealized nature of the model itself which does not take into consideration the whole domain structure, in particular the surface domains, and on the other hand to the numerical errors.

Concerning the classical loss component, as mentioned in section 3.2, it depends on the peak flux density value and it is independent of the angle θ of the applied field to RD. Figure II.17-c shows the computed values as function of the peak magnetic flux density

and for different angles in order to confirm the validity of the numerical implementation. For 15°, there is a slight difference between the expected and computed classical losses. This difference can be attributed to the magnetic flux density map obtained at 15° and for which the peak lux density values are slightly lower in comparison with the other angles.

In terms of the total losses, the computed losses are in accordance with the experimental ones. We notice a relative difference of around 6-7% for most directions and for the tested flux density levels, except for 30° at 1.2 T where the losses are overestimated by 22%.

Regardless, the model estimates the iron losses with a good accuracy by relying only on the measured iron loss data along RD and TD and without any adjustable parameter.

Finally, for comparison and in order to account for the GOES behavior law. The total computed losses within numerical simulation from the flux density maps obtained with both diagonal and full permeability tensor based-approaches, are shown in Figure II.18 for a cutting angle of 54.7°. We see a clear difference between the two approaches. The proposed approach based on the full permeability tensor clearly improves the results of the iron loss model in comparison with the diagonal tensor based-approach. Notice that for the diagonal tensor based-approach, the simulations have been limited to 1 T because it gives unrealistic field maps at higher flux densities.

This comparison with the Epstein frame has allow us to verify the validity of the models in GOES under relatively homogenous magnetic flux density and where the magnetic flux is relatively unidirectional (except the corners). In the next sub-section, another case test has been studied: a ring core for which the magnetic flux follows all the directions between the RD and TD.

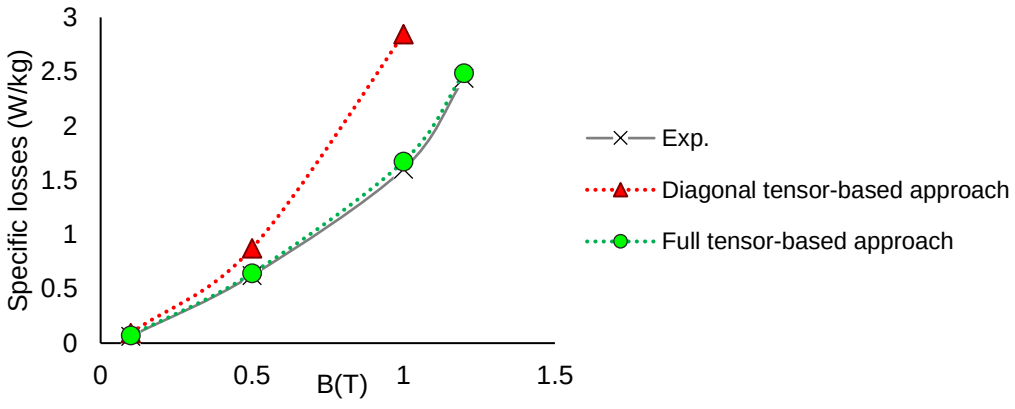


Figure II.18. Total specific losses comparison, simulated vs experimental values.

### 5.3.2. Anisotropic ring core

Ring specimens of 60 mm-internal diameter, 120 mm-external diameter and 0.35 mm-thickness have been obtained by WEDM from the provided turbogenerator segments (see Figure II.4). The choice of this ring geometry permits the evaluation of the total losses

for a magnetic flux that follows all the directions between the RD and TD. Seven single rings are stacked and two coils are wound on the core: a primary coil with 184 turns and a secondary coil with 28 turns. The ring core has been characterized with the Brockhaus MPG200D equipment. Then, it has been simulated in the FEM environment code_Carmel.

To calculate the iron losses in code_Carmel, it is necessary to have the angle θ between the applied field **H** and the RD for each element of the mesh [see *(II.12)*]. The angle θ is not straightforward to calculate, especially for complex geometries. Indeed, the numerical simulation provides the distribution of the resulting field $\mathbf{H_i}$ such as $\mathbf{H_i} = \mathbf{H} + \mathbf{H_d}$ ($\mathbf{H_d}$ is the demagnetizing field) and the angle associated to $\mathbf{H_i}$ with respect to RD is different from the angle θ. In the previous test case (Epstein frame test case), θ is the cutting angle of the Epstein strips and it is known for all the elements of the mesh contrary to the ring core case where the angle (to RD) associated to $\mathbf{H_i}$ is different from that of **H**. To overcome this difficulty for the case of the ring geometry, an isotropic law based- simulation has been made to obtain and store this angle for all the elements of the mesh. Indeed, in the isotropic case, given the fact that there is no demagnetizing field, the internal field $\mathbf{H_i}$ coincides with the applied field **H** and the angle θ can be easily obtained within FEM. Then, the anisotropic simulations have been performed to obtain the distributions of the **B** and $\mathbf{H_i}$ fields and the iron loss model applied afterwards to post-process the local and total iron losses. Finally, the computed losses are compared with the experimental measurements made on the GOES ring core.

In a first step, a diagonal permeability tensor has been used to account for the GOES behavior law. Figure II.19 displays an example of the **B** and **H** field distributions in ring core where the RD is along the horizontal axis for a diagonal permeability tensor identified at 0.5 T (linear B(H) zone).

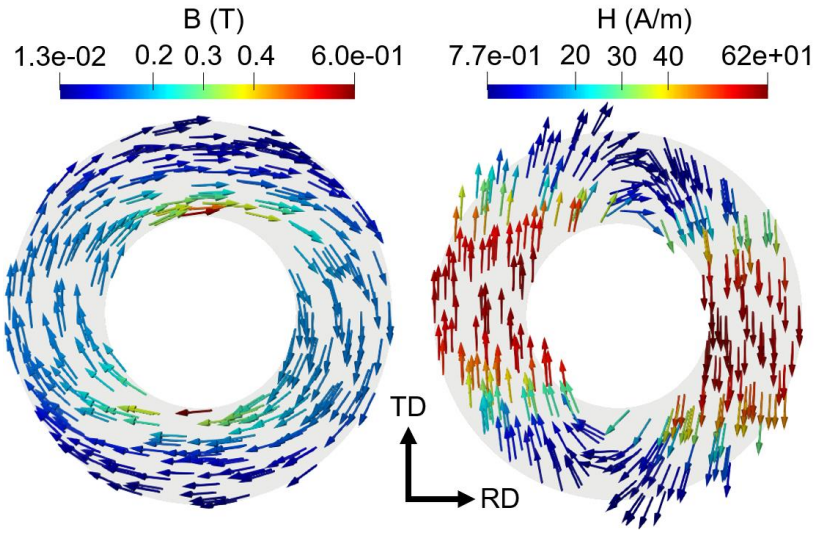


Figure II.19. **H** (A/m) and **B** (T) field distributions in the ring core (anisotropic case).

Table II.5 shows a comparison of the computed total iron losses in the ring core with the experimental losses at 50 Hz and for different ampere-turns. Also, the distribution of the losses in the magnetic circuit is displayed in Figure II.20 for an NI of 7 A.t.

Table II.5. Comparison of calculated and experimental losses for the ring core at 50 Hz

| NI (A.t) | Experimental total losses (W/kg) | Computed total losses (W/kg) |
|---|---|---|
| *6* | 0.062 | 0.071 |
| *7* | 0.089 | 0.089 |
| *8* | 0.121 | 0.108 |
| *10* | 0.193 | 0.150 |

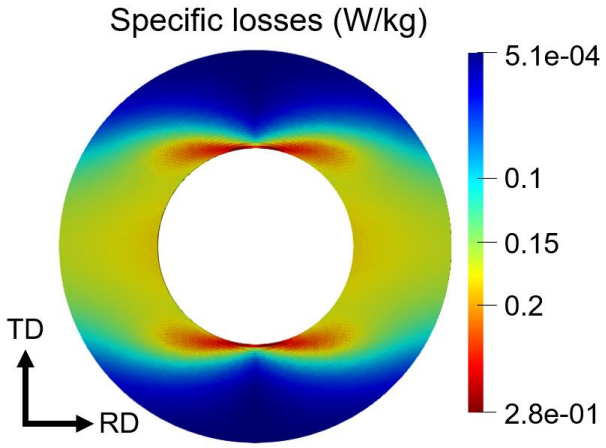


Figure II.20. Distribution of the specific losses (W/kg) in the toroidal geometry at 50 Hz for and NI of 7 A.t.

Overall, the model gives satisfactory results especially for lower ampere-turns. Nevertheless, significant deviations appear for higher ampere-turns. This can be explained by the inhomogeneity of the magnetic flux density within the ring core as well as by the nonlinearity which is not taken into account by the considered diagonal permeability tensor. Rigorously, the problem being non-linear, the tensor should be adapted locally (for each element of the mesh) with a non-linear resolution scheme. The non-linear simulations have not been achieved given the convergence problems encountered, particularly with the fixed-point method. Further developments should be carried out to investigate the ability of the non-linear resolution methods to take into account the non-asymmetrical nature of the full permeability tensors based on the modified Enokizono approach.

# 6. Synthesis

Advanced approach to account for the GOES behavior law within numerical simulation has been proposed together with a phenomenological iron loss model implemented in post-processing. Applications on simple magnetic devices (Epstein frame and a ring core) are presented, discussed and compared with experimental measurements.

The developed models are applied in chapter IV on an experimental demonstrator made of GOES, developed in order to reproduce the excitation conditions encountered in turbo-generators.

# Chapter III. Experimental Demonstrator

---

*The experimental study of complex 3D magnetic fluxes at the end-region of turbo-generators, especially their effects on the iron losses, is not straightforward and hardly achievable on real electrical machines. An experimental demonstrator has been developed to investigate the flux penetration into a GOES lamination stack as well as the associated iron losses under different excitation conditions indented to be representative of the working conditions of turbogenerators.*

*In this chapter, a brief state of the art of literature experimental devices is made. Then, the design of the demonstrator is presented together with the adopted experimental protocol. Finally, the effects of a flux directed at the plane surface of the GOES lamination stack and the associated losses is experimentally investigated, analyzed and discussed.*

---

# Table of content

# 1. Literature demonstrators

The development of experimental devices to study magnetic circuits submitted to non-conventional excitation flux has been dealt with by previous works in the literature. This section gives an overview of some of these devices, most of them served to validate numerical or analytical models of the end-region losses and to observe the distribution of eddy currents and heating in the regions of interest.

## 1.1. Brief overview

### 1.1.1. COLOT Demonstrator

In 1975, Colot [18], from EDF, developed a test bench to emulate the end-region area of an electrical machine. A 3D representation of the demonstrator can be observed in Figure III.1**.** It consists of three magnetic circuits:

- A first excitation circuit with its coils providing radial magnetic flux (labelled C1, C2, C3 in Figure III.1).
- An auxiliary circuit, with its excitation coil providing axial flux with a certain inclination (labelled C5, S, C4 in Figure III.1) in order to give a flux distribution as close as possible to reality.
- The test sample, which is a stator segment having the equivalent of two teeth (a trapezoidal tooth in the center and a half-tooth on each side, labelled D in Figure III.1), Five packets of stacked GOES laminations were used, each separated by ventilation canal.

The magnetic field measurements were realized with Hall effect probes and thermocouples were used to follow the temperature evolution. The main drawback of this demonstrator was overheating. Long pauses were required between two experimental measurements to cool down the magnetic circuits under test.

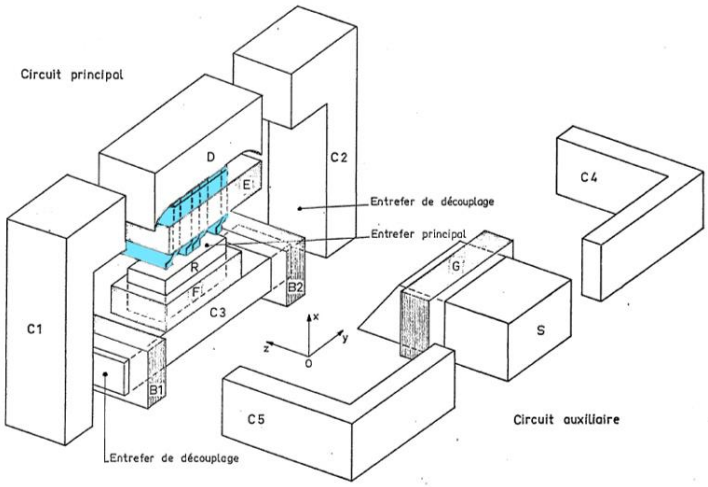


Figure III.1. Colot demonstrator (1975), sample under test in blue. [18]

### 1.1.2. Yamazaki demonstrator

The Yamazaki's demonstrator represented in Figure III.2 was developed in 2008 [35]. Its geometry, simpler than the previous one, was used to validate a 3D simulation of the end region flux distribution. It consisted of:

- an Epstein frame type core made of the laminations to be characterized with an exciting coil generating the parallel flux (parallel to the plane of the sheets);
- a C-shaped core, which is mounted over the Epstein core, with its exciting coil generating the normal flux (perpendicularly to the plane of the sheets).

Search coils have been used to measure the influence of eddy currents and the interaction of the radial and axial magnetic fluxes. In this demonstrator, there were no particular constrains; however, only global measurements in terms of losses and flux distributions were realized, and the geometry was kept simple to simplify the 3D modelling of the test bench.

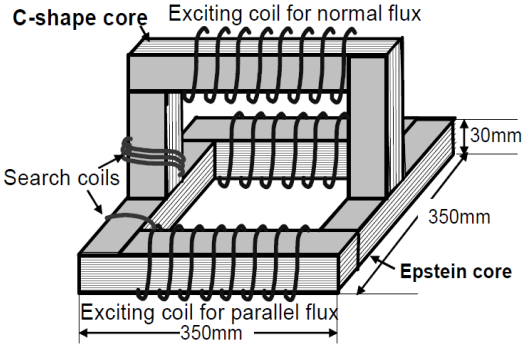


Figure III.2. Yamazaki demonstrator. [35]

### 1.1.3. Hihat demonstrator

In 2010 [105], Hihat developed a specific test bench to characterize the permeability $\mu_z$ of different electrical steel sheets in the direction normal to their plane. Together with the in plane permeabilities $\mu_x$ and $\mu_y$, $\mu_z$ is also an important data for the finite element modeling step. This demonstrator relies on an original way to access the normal magnetic permeability.

The test bench is formed by using four U shaped magnetic cores arranged to form a closed magnetic circuit, with four airgaps between the junctions of the magnetic cores (see Figure III.3). In the two airgaps between the (c,b) and (c,d) magnetic cores, the samples to be characterized (50 x 50 mm) were placed. Two other airgaps, of 0.6 mm thickness, are located between the (a,b) and (a,d) magnetic cores. One of them is used to perform the measurement while the second one is filled with a non-magnetic spacer to keep the symmetry of the system. A primary DC excitation coil of 1200 turns is uniformly distributed along the four U cores. The characterization method of the normal permeability $\mu_z$ of the test samples is achieved in static regime by means of a search coil

(a flat rectangular coil of 0.2 mm thick) placed in the airgap between the (a,b) cores. This search coil is set in motion by means of a dedicated shaker. Consequently, having its section facing the sample varying in time, a voltage is induced.

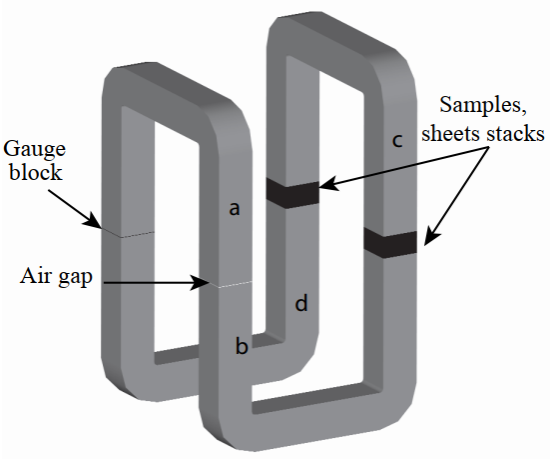


Figure III.3. Hihat demonstrator. [105]

The experimental protocol consists of two measurements without and with the samples to be characterized. The corresponding Ampère's laws are respectively:

$$H_{iron}l_{iron} + H_{ag}l_{ag} = nI \qquad (III.1)$$

$$H_{iron}l_{iron} + H_{ag}l_{ag} + H_z(B)l_z = n'I' \qquad (III.2)$$

where:

- $H_{iron}$ and $l_{iron}$ are the magnetic field in the U cores and the iron mean length path.
- $H_{ag}$ and $l_{ag}$ are the magnetic field in the airgap and the total airgap length.
- $H_z$ and $l_z$, the magnetic field in the test samples and the total thickness of the test samples.
- $nI$ are the total ampere-turns without the test samples.
- $n'I'$ are the ampere-turns with the test samples.

The equations *(III.1)* and *(III.2)* become:

$$\frac{B_{iron}}{\mu_{iron}}l_{iron} + \frac{B_{ag}}{\mu_0}l_{ag} = nI \qquad (III.3)$$

$$\frac{B_{iron}}{\mu_{iron}}l_{iron} + \frac{B_{ag}}{\mu_0}l_{ag} + \frac{B_z}{\mu_z}l_z = n'I' \qquad (III.4)$$

Taking into account the conservation of the magnetic flux density normal component ($B_{iron} = B_{ag} = B_z = B$), the equations, *(III.3)* and *(III.4)* can be merged into:

$$nI + \frac{B}{\mu_z}l_z = n'I' \qquad (III.5)$$

Finally, the permeability $\mu_z$ can be calculated for a given induction value.

$$\mu_z = \frac{B l_z}{[n'I' - nI]} \qquad (III.6)$$

For a GOES with 0.35 mm thickness, Hihat measured a relative permeability $\mu_z$ of about 34.3 (see Figure III.4). Hihat *et. al.* showed that $\mu_z$ presents a linear behavior up to relatively high excitation field levels (up to 40 kA/m). This coincides with the observations of [117] and [118] which estimated the value of the relative permeability in the normal direction to be around 100. This value of $\mu_z$ will be further considered in this PhD thesis for the numerical simulation.

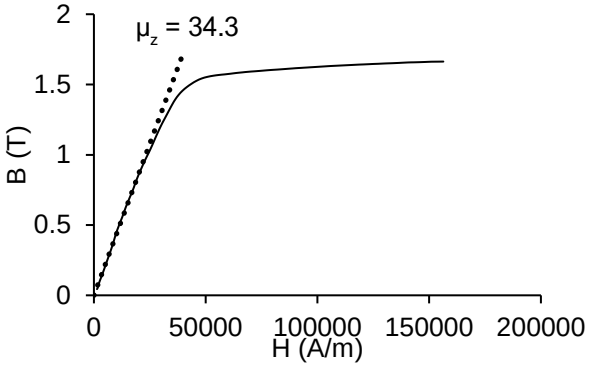


Figure III.4. Normal magnetization curve for a 0.35 mm GO lamination magnetized in the RD. Extracted and modified from [105].

### 1.1.4. Vogt demonstrator

Vogt in 2013, in the framework of his PhD thesis [4], analyzed the effects of the radial and axial magnetic field in the end region of a large turbo-generator by means of an experimental demonstrator (see Figure III.5), which imitates the real excitation conditions of the end region areas, including the leading and lagging operating conditions.

The demonstrator is composed of three main components [see Figure III.5]:

- The stator yoke and tooth samples (labelled C in Figure III.5), obtained from a segment of a 900 MW turbo-generator and assembled in two packets of stacked GOES laminations.
- The exciter frame (labelled A in Figure III.5), with two coils generating the radial fluxes (in-phase or de-phased) in the plane of the laminations.
- And, the second U-shaped frame (labelled E in Figure III.5) generating an axial flux which orthogonally penetrates the normal plane of the stator tooth sample under test.

Search coils were used to measure the global flux distribution and thin-planar coils (150 μm thick) were inserted in between the laminations to measure the penetration of the

axial flux through the stacked laminations. A high-precision watt-meter has been used to measure the losses.

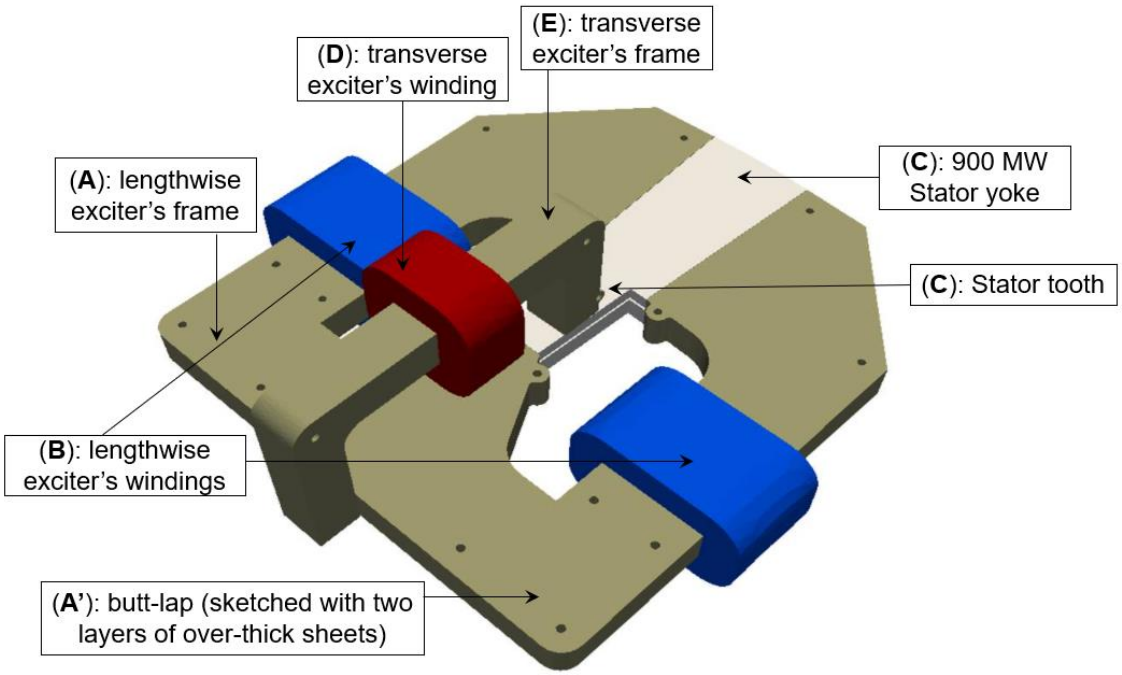


Figure III.5. Gilles Vogt demonstrator. [4]

The use of several planar coils between the staked laminations of the test sample introduced important airgaps into the stack, increasing the reluctance between the laminations and affecting the flux measurement. In addition, a cooling system was installed to limit the overheating of the main parts of the prototype. It has to be noted that Vogt neglected the anisotropic behavior of the GOES laminations in the numerical study part of his work. This is one of the important aspects we have examined in this PhD thesis.

## 1.2. Synthesis

To summarize, various experimental demonstrators intended for the study of the end-region losses of electrical machines have been reviewed in the previous section. However, to our best knowledge, none of these devices has considered the anisotropic properties of the stator magnetic core made up GOES.

G. Vogt, in the framework of his PhD thesis with EDF [4], studied the electromagnetic phenomena (particularly the axial magnetic flux density) in the end region of a large turbo-generator with regard to the working conditions. His study was based on an experimental demonstrator (see section 1.1.4) together with a FEM numerical modelling. Nevertheless, the anisotropic behaviour of the magnetic stator core was not taken into account. In the continuity of the Vogt's works, an experimental demonstrator is proposed in this PhD thesis to study the effects of not only 3D magnetic flux excitations, but also the anisotropic nature of the magnetic stator core made up of GOES.

# 2. Presentation of the demonstrator

The experimental demonstrator has two main purposes:

- The investigation of the magnetic behaviour of a lamination stack made up of GOES under 3D non-conventional flux path at different configurations with regard to the lamination plane combined with different in-plane orientations of the GOES easy magnetization axis.
- The experimental validation of the behavior law and iron loss models developed and implemented in the FEM software code_Carmel.

The characteristics of the demonstrator and the steps followed for its design are presented in the following subsections.

## 2.1. General description

As mentioned before, the idea behind the proposed demonstrator is that the magnetic behaviour of a GOES lamination stack can be studied under 3D magnetic flux path in order to reproduce as far as possible the excitation conditions of turbogenerators. To do so, one of the required features for the experimental device is then the possibility to generate magnetic fluxes penetrating into the GOES lamination stack of interest in a direction at right or intermediate angles to the plane of the laminations. In addition, it must be possible to orient the RD of the GOES stack in any arbitrary in-plane direction. Considering these requirements, the most relevant geometry choice of the GOES lamination stack of interest is a disk type geometry. The flux closure is made by a magnetic circuit consisting of one yoke made up of insulated sheets of GOES with low reluctance and low specific total losses. This circuit is equipped with an excitation (magnetizing) coil made up of cooper designed for a maximum current of 8 A r.m.s. The experimental demonstrator is illustrated in Figure III.6.

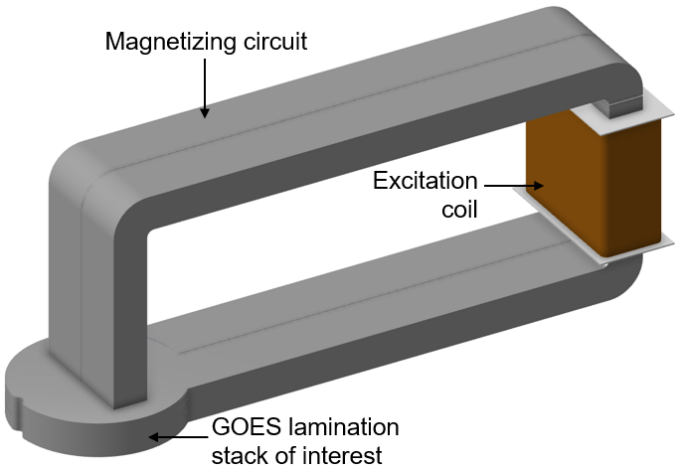


Figure III.6. 3D Geometry of the experimental demonstrator (90° configuration).

The experimental demonstrator includes a non-conducting and non-magnetic support ensuring a direct contact between the magnetizing circuit and the lamination stack of interest with an airgap which shall be maintained as small as possible. Finally, flexible planar coils have been designed and manufactured for the measurement of the signals of interest.

The different parts of the demonstrator have been manufactured by different subcontractors, from 3D plans designed and realized by using the 3D CAD design software (OnShape [119]). The main steps up to the final design and fabrication are described hereafter.

## 2.2. Detailed description

### 2.2.1. Preparation of the GOES lamination stack of interest (test specimen)

Considering the main requirements for the demonstrator described previously, the first step concerned the preparation of the test specimen i.e., the GOES lamination stack of interest. The latter has been made up from the same batch of stator segments supplied by EDF and from which Epstein strips have been extracted for the experimental characterization and modeling achieved in Chapter II. The geometry of one stator core segment and the extracted disks to form the lamination stack of interest are illustrated in Figure III.7.

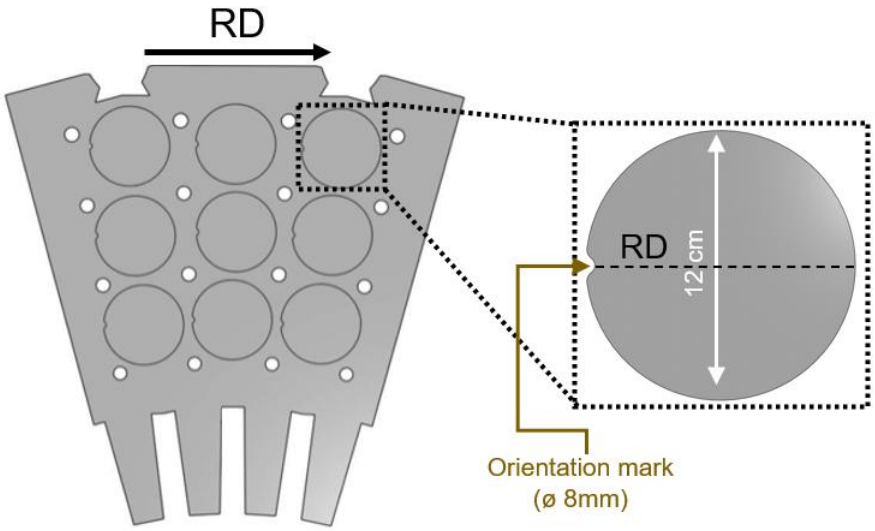


Figure III.7. Cut disks from a stator core of a 900 MW turbo-generator to form the lamination stack of interest

In view of the specific geometry of the supplied stator segments including regularly positioned holes for the cooling circuit, the diameter of the cut disks has been fixed to 12 cm. As for the Epstein cut samples studied in Chapter II, the disks have been cut using the wire electrical discharge machining (WEDM) technique while considering at least a

distance of 1 cm from the cutting edges of the segments. This precaution allows to avoid any potential degraded region from a magnetic point of view (holes and sector edges) because of the cutting technique used for the stator segments. Each cut disk includes a small mark to identify the RD, easily and accurately align the disks with each other, as well as to well maintain the lamination stack during the measurements.

The GOES lamination stack of interest is made up of 68 laminated disks of 0.35 mm thickness each. To facilitate the handling and positioning of the stack of laminations of interest during the experiments, some of the cut disks have been glued together with a thermostatic industrial glue dedicated for electrical steels. Four different sets of laminations have been made up with respectively 25, 20, 8 and 5 laminations. A separate set of 10 disk laminations not glued together complete the GOES stack of interest. The same stack has been used for the measurements and for all the configurations of the demonstrator.

Figure III.8. Photos of the cut disks and the sets of laminations constituting the stack of interest.

### 2.2.2. Magnetizing circuit and excitation coil

The flux closure is made by a wound magnetic circuit consisting of yokes made up of insulated sheets of GOES with low reluctance and low specific total losses. Two circuit configurations baptized 90° and 120° have been considered. They allow to generate magnetic fluxes penetrating into the GOES lamination stack of interest in a direction at right or intermediate angles to the plane of the laminations [see Figure III.9].

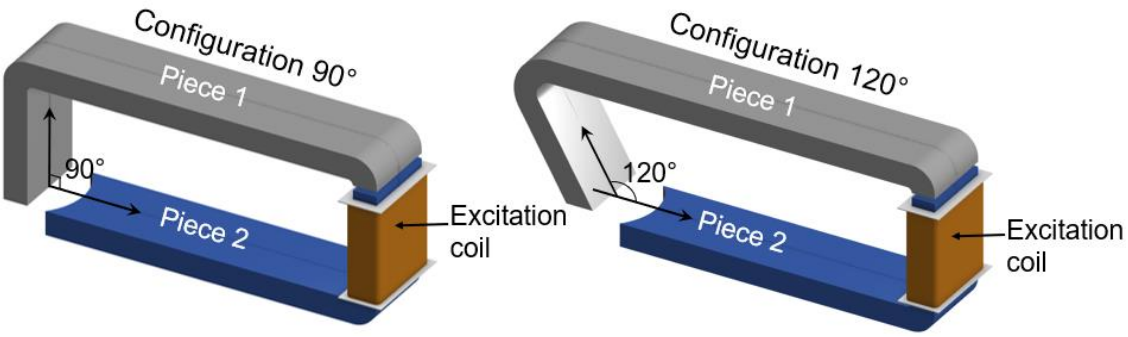


Figure III.9. The configurations of the magnetizing circuits.

The magnetizing circuit of each configuration includes two pieces: one piece corresponding to the suitable configuration of the flux attack i.e., 90 or 120° (Piece 1) and another piece on which is inserted the excitation coil (Piece 2). This choice has been made for practical reasons in terms of insertion of the excitation coil as well as the change of Piece 2 of the circuit according to the desired configuration.

— *Preliminary design*

An analytical calculation has been performed on the basis of a simple magnetic equivalent circuit (reluctance network) in order to estimate the dimensions of the magnetizing circuits (including the airgaps between the different pieces) and the needs in terms of excitation coil (current level, number of turns) allowing to obtain a magnetic flux density of the order of the Tesla.

The estimated characteristics from this preliminary design are:

- 100 turns for the excitation coil and a nominal current of 7 A r.m.s;
- a mean magnetic path length of around 1 m for the excitation circuits;
- an average flux density peak value of around 1 T.

In order to validate the design, a 3D magnetostatic linear simulation has been performed in the FEM software code_Carmel. A diagonal permeability tensor identified at 1 T has been considered and a current of 7 A r.m.s. has been imposed. The simulation results in terms of the distribution of the magnetic flux density are shown in Figure III.10 for the 90° configuration of the demonstrator. The obtained average magnetic flux density is of the order of the Tesla within the magnetizing circuit as well as within the first laminations of the GOES stack of interest. In this simulation, the first seven laminations of the stack of interest have been modelled individually.

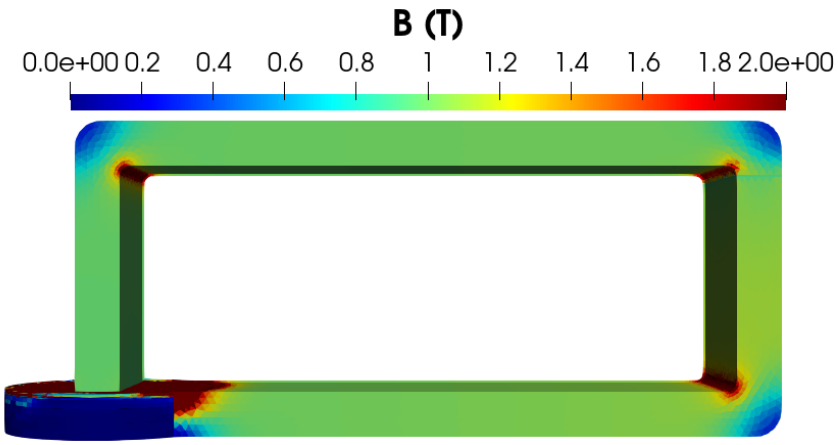


Figure III.10 Distribution of the magnetic flux density for a current of 7 A r.m.s (90° ).

The nominal dimensions of the 90° configuration of the demonstrator parts are shown in Figure III.11.

This same procedure has been followed to design the 120° configuration of the demonstrator shown in Figure III.9.

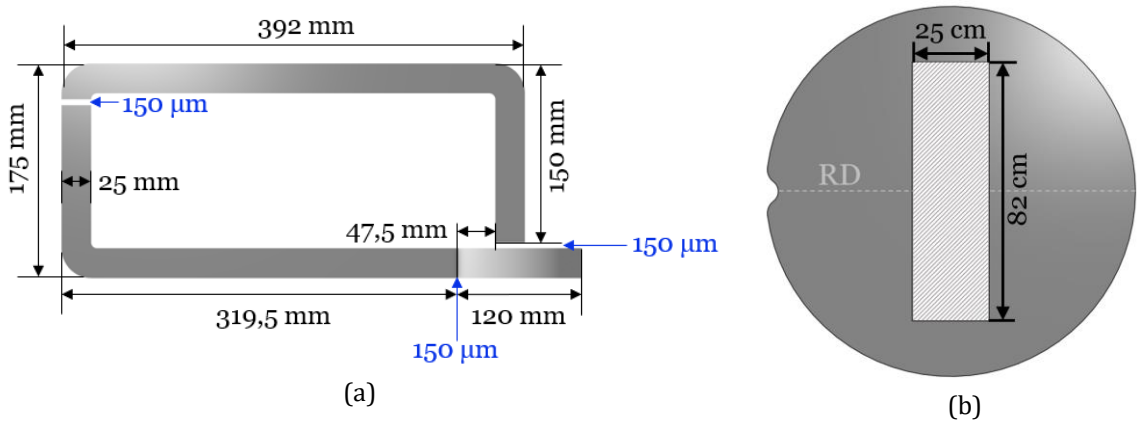


(a) (b)

Figure III.11. Dimensions of the 90° configuration of the demonstrator: (a) general dimensions (b) stack of interest.

— *Magnetizing circuit*

Closed magnetizing circuits (of 41 mm width) have been supplied by TCT Company (see Figure III.12). They have been manufactured from a wound GOES: the 100H23 grade. For each configuration (90 and 120°), two copies have been delivered to be mounted side by side in order to obtain the desired cross section according to the pre-established design. Then, the circuits have been cut in order to obtain the pieces no. 1 and 2 as detailed before (see Figure III.9). The WEDM cutting technique has been employed for that purpose to limit the impact of cutting on the magnetic properties of the magnetizing circuits.

(a) 90° configuration (b) 120° configuration

Figure III.12. Magnetizing circuits corresponding to the configurations 90 and 120° of the demonstrator.

For illustration, Figure III.13 shows the cutting for the 90° configuration of the demonstrator.

Figure III.13. View of the end-parts of the cut pieces no.1 and 2 obtained from the delivered closed magnetizing circuits for the 90° configuration of the demonstrator.

Additional closed magnetizing circuits of each demonstrator configuration have been delivered in order to characterize them and obtain their magnetic properties. The latter are necessary for the modelling of the demonstrator as well as for the experimental power balance presented later in this chapter.

— *Excitation coil*

Excitation coils made of cooper and composed of 100 turns wound around a plastic support adapted to the dimensions of the magnetizing circuit have been fabricated. They have been designed for a maximum current of 7 A r.m.s and a maximum operating temperature of about 80°C.

Figure III.14. Photography of an excitation coil.

### 2.2.3. Mechanical Support

The demonstrator includes a rigid non-conducting and non-magnetic support ensuring a direct contact between the magnetizing circuit and the GOES lamination stack of interest with an airgap which shall be maintained as small as possible. On the other hand, it allows easy access to the GOES stack under test.

This mechanical support has been designed using a 3D CAD software and adjusted to fit the dimensions of the magnetizing circuit and the lamination stack of interest. It has been

manufactured from high-density polyethylene based-material (HDPE) exhibiting good mechanical characteristics up to 90°C.

The base of the support consists of two main parts, one holding up the GOES stack of interest (piece A1) and another one for the magnetizing circuit (piece A2) [see Figure III.15].

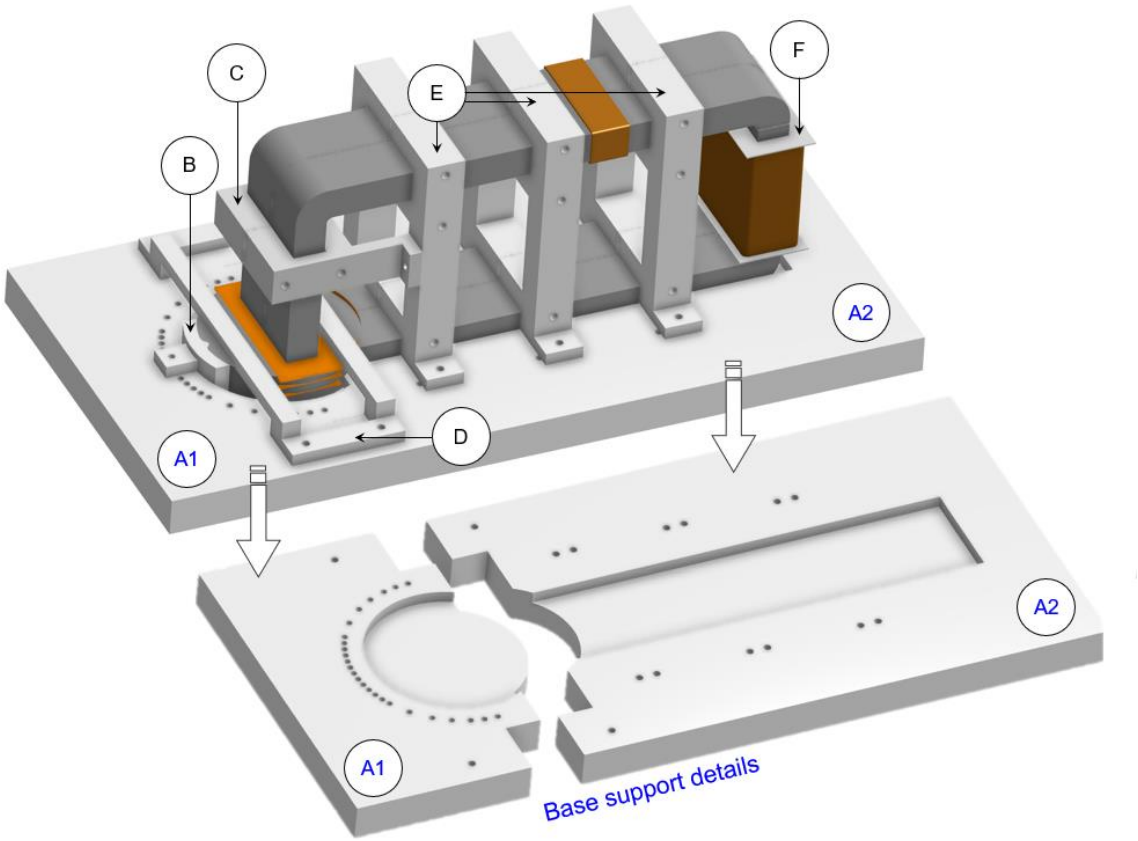


Figure III.15. Detail of the pieces of the mechanical support.

These two parts are designed in such a way that they can be easily separated. This allows to easily change the orientation of the GOES stack of laminations without moving the magnetizing circuit. Both pieces are held tight together during the measurements by an additional hold piece [piece D in Figure III.15] which also serves to maintain the lamination stack of interest in place.

Additional pieces have designed and manufactured:

- Piece B: to accurately adjust the orientation of the RD of the lamination stack of interest with respect the RD of the magnetizing circuit;
- Piece E: six E-shaped pieces to hold the magnetizing circuits together;
- Piece C: to maintain the magnetizing circuit leg in place during the measurements.

All these elements are fixed to the support plate, and maintain all the components of the demonstrator in place. Moreover, the support parts have been realized considering the different magnetizing circuit configurations i.e., 90° and 120°.

At last, Figure III.16 illustrates how the orientation of the GOES stack of interest is fixed for the measurements, by using the reference piece [labelled B in Figure III.15]. This piece connects with the mark of the lamination stack of interest and fixes the position of the RD within the laminations. Notice that when the stack is oriented at 0°, it is aligned with the RD of the base of the magnetizing circuit. Therefore, in the following, when referring to the in-plane direction or orientation of the GOES stack under test, we refer to the angle $\alpha$ between the RD of the GOES stack and the RD of the magnetizing circuit base.

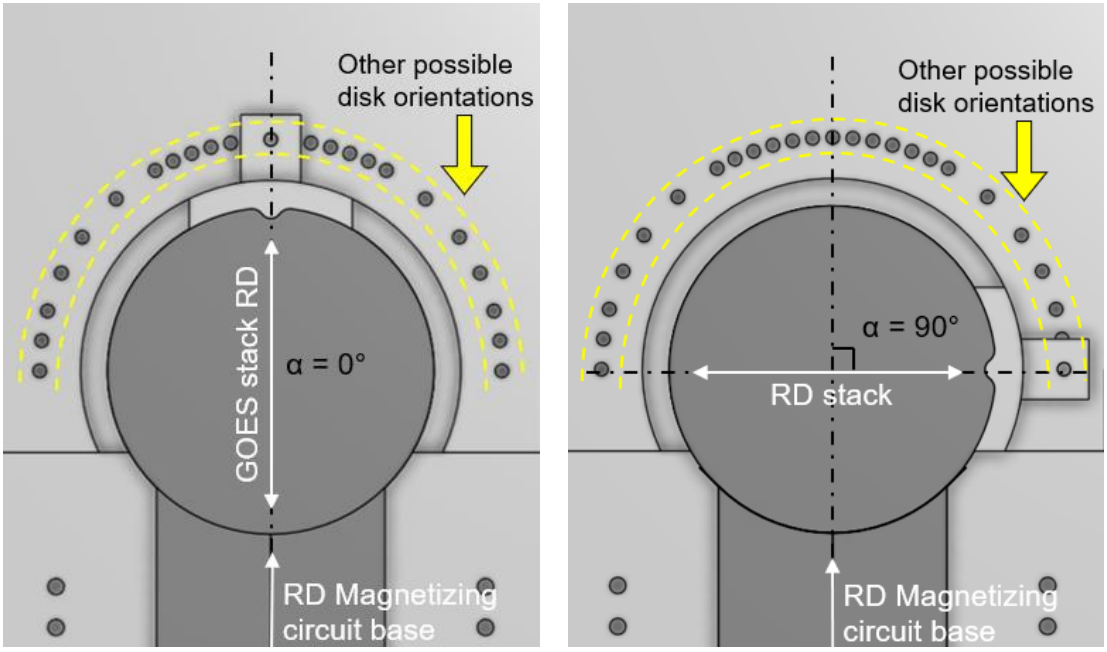


(a) Stack oriented at 0° (b) Stack oriented at 90°

Figure III.16. Illustration of how the orientation of the GOES stack of interest is made for two different measurements.

## 2.2.4. Sensors

In order to investigate the effects of magnetic fluxes directed at the plane surface of the GOES lamination stack of interest, different planar and search coils have been designed and manufactured. They have been basically used to measure the AC induced voltages over different locations between the laminations of the GOES stack under test and then get the corresponding magnetic fluxes.

— *Planar coils*

Different prototypes of planar coils have been designed to match the cross section of the magnetizing circuits on the basis of double-sided flexible printed circuits. The

production has been subcontracted to Speeflex company, manufacturer of flexible printed circuits for integrated electronic systems. These sensors include two conductive layers printed on a Kapton flexible insulating film. They are especially suitable due to their thin thickness (135 µm) that is at least two times thinner than one single lamination of the GOES stack of interest. Figure III.17 shows two main categories of the prototypes produced and used in the measurements:

- a prototype made up of one single coil (with 6 turns) matching the cross section of the magnetizing circuits.
- a prototype made up of an array of 12 coils (of 8 turns each) evenly distributed over the whole cross section of the magnetizing circuits, for measuring the magnetic flux distribution. The terminals of the 12 coils are quite close to each other. They have been connected to the data acquisition unit by welding. This step has been particularly delicate.

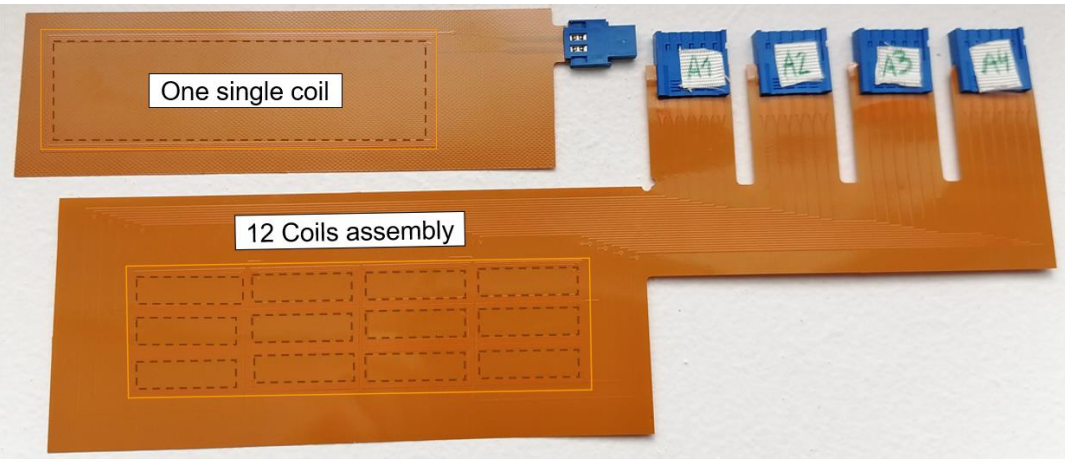


Figure III.17. The double-sided flexible planar coil prototypes and with their connectors.

The planar coils have designed on the basis of the available acquisition equipment. They allow to measure peak magnetic flux densities of 10 mT corresponding to a measurable voltage of 20 mV peak between the terminals of a single planar coil and 2 mV peak between the terminals of one of the array planar coils. Furthermore, the planar coils, (either single or array type), can be positioned at three main locations as illustrated in Figure III.18:

- Position 1: between the opposite faces of the magnetizing circuit leg and the GOES stack under test.
- Position 2: between the GOES stack under test and the base of the magnetizing circuit.
- Position 3: between the laminations of the GOES stack under test.

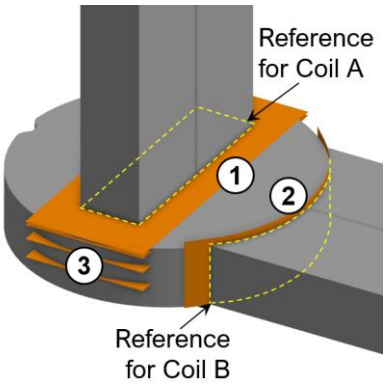


Figure III.18. Planar coil positions within the experimental demonstrator.

Particular attention has been paid to the positioning of the planar coils at the center of the stack of laminations. To do so, the position of the magnetizing circuit leg has been used as a reference mark. Idem for the positioning of the planar coil between the GOES and the base of the magnetizing circuit [see Figure III.18].

An overview of the planar coil positions in the experimental demonstrator is given in Figure III.19.

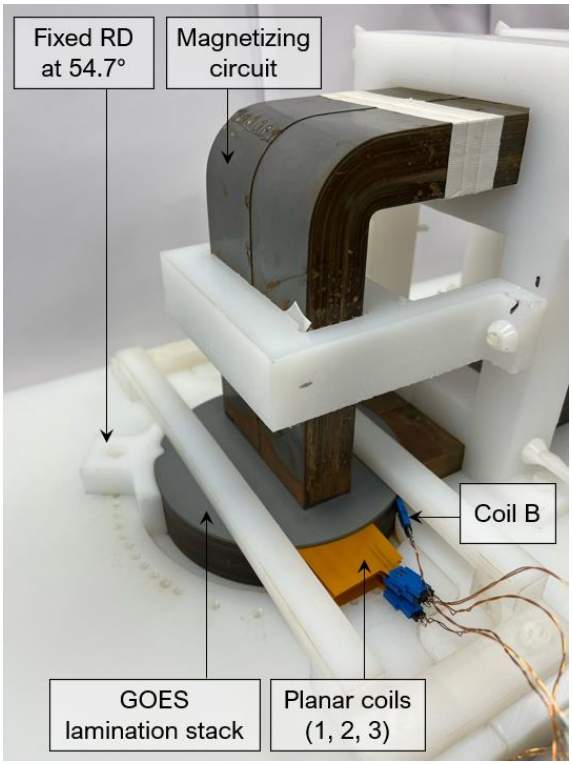


Figure III.19. Close look to the stacked sample positioning.

— *Additional search coil*

In addition to the planar coils, a handmade wired coil has been used to measure the global flux in the magnetizing circuit [see Figure III.20].

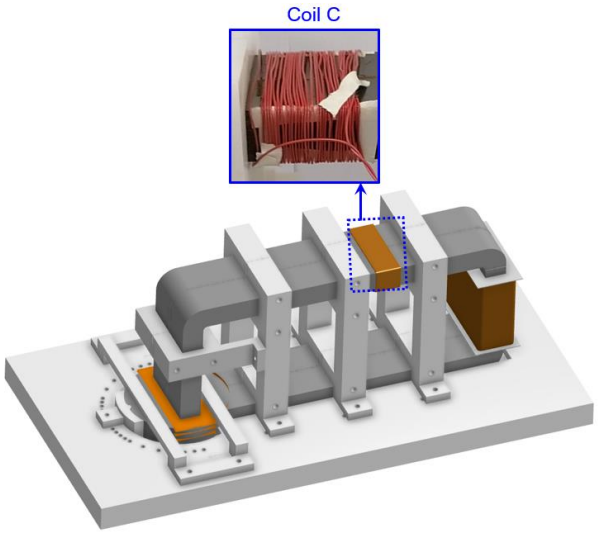


Figure III.20. Handmade wired coil for global flux measurements.

### 2.2.5. Data acquisition and measurements

— *Flux measurements*

In order to measure the electrical induced voltages between the terminals of the planar and search coils, a combined system of a data acquisition equipment (from National Instruments) and a software (DAQ Express) has been used. The latter is an interactive application software allowing visualizing and exploring the acquired data without prior programming. Nevertheless, given the large number of the signals to measure, an automation of the acquisition chain was necessary. This has been achieved with the help of Alicia Aiadi in the framework of her internship of Physics and applied sciences. Alicia was a student at the Institute of Technology Créteil-Vitry of the University Paris-Est Créteil.

The quantity measured being the electrical voltage across the sensor terminals, the corresponding magnetic flux is obtained by integrating the induced measured voltage with respect to the time within a constant (number of turns × flux cross section).

— *Temperature measurements*

It is expected that the penetration of flux into the stack under test, in a direction at right or intermediate angles to the plane of the laminations, will generate, at least for the first lamination of the stack, more significant eddy currents than in the conventional case with in-plane magnetic field. These currents result in local hot spots and overheating. Therefore, in view of the temperature limit of the mechanical support (90 °C) and in order to monitor the temperature evolution during the measurements, thermocouples have been positioned on the surface of the stack under test.

— *Iron loss measurement*

The total active power absorbed by the experimental demonstrator (including copper losses together with iron losses) has been measured under AC excitation by means of the AC power meter included in the used high-performance programmable AC and DC power source CSW5550 from California instruments. This active power includes the copper losses in the excitation coil and the iron losses in both the magnetizing circuit and the GOES stack under test.

To separate the different loss components and get the iron losses corresponding to the GOES laminations stack of interest, a power balance procedure has been performed. The followed experimental procedure is detailed in section 3.4.

### 2.2.6. Assembly of the demonstrator

At last, the different parts of the experimental demonstrator have been assembled. In Figure III.21 and Figure III.22, photos of both 90° and 1200 configurations of demonstrator are given.

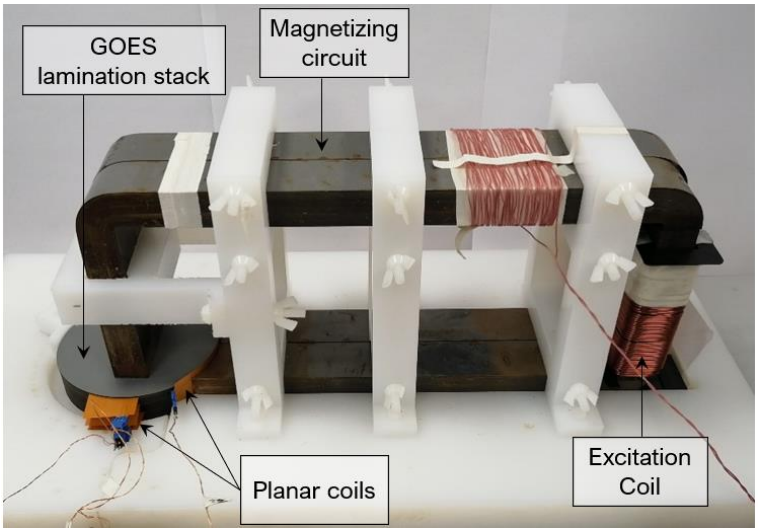


Figure III.21. Photo of the 90° configuration of the demonstrator.

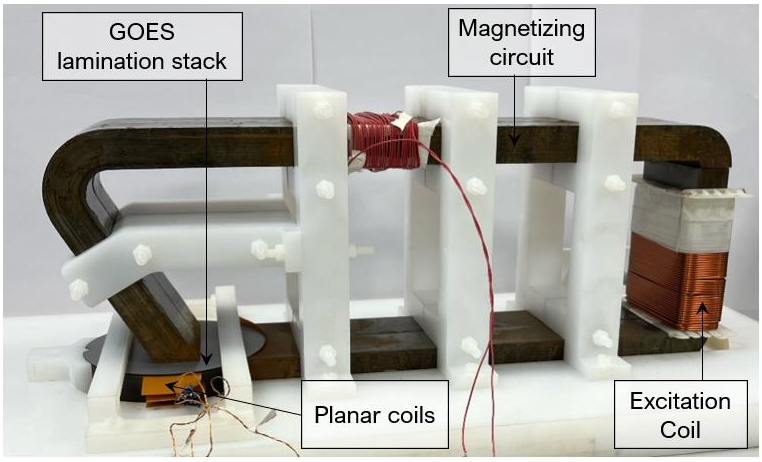


Figure III.22. Photo of the 120° configuration of the demonstrator.

# 3. Experiments

Different series of measurements have been achieved. A series constitutes a set of measurements in which only one parameter is modified. Two parameters have been considered:

i. The in-plane orientation of the GOES stack under test.
ii. and the direction of penetration of flux into the stack under test: at right angle to the plane of the laminations (90° configuration) or at intermediate angle to the plane of the laminations (120° configuration of the demonstrator).

This can influence the total magnetic flux, the iron losses and the distribution of the flux between the laminations of the GOES stack of interest.

In the following subsections, the general experimental protocol is briefly presented.

## 3.1. Protocol

To facilitate the positioning of the measuring planar coils as well as the execution of the measurements for each configuration of the demonstrator and for each orientation of the GOES stack, the following protocol has been established:

i. Positioning and locking of a given in-plane orientation of the GOES stack.
ii. Positioning of the planar coils and fastening of the mechanical support pieces of the demonstrator.
iii. Execution of the measurements at 50 Hz for r.m.s. voltages between 5 and 70 V and acquisition of the data.
iv. Wait until the test circuit stabilizes before doing any other measurement. The interval necessary for an operating point to become stable is around 30 minutes.

The measurements have been done under imposed voltage via the power source previously mentioned. A photography of the demonstrator entirely assembled is given in Figure III.23.

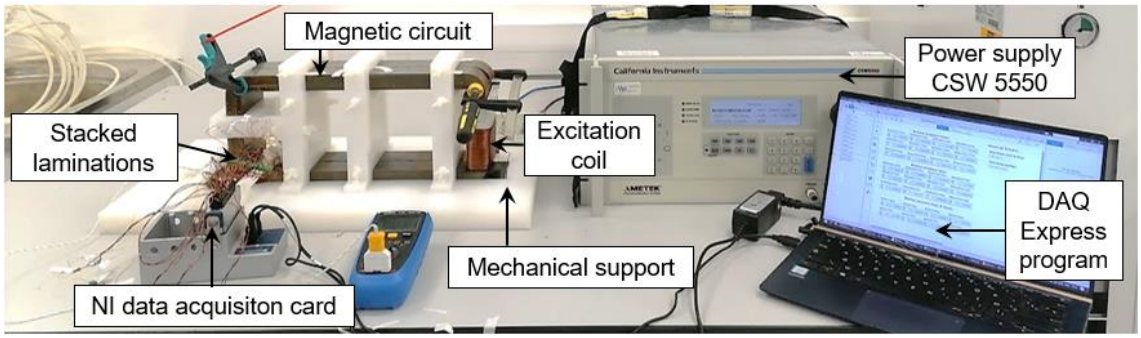


Figure III.23. Photography of the demonstrator entirely assembled.

- Vibrations

Because of electromagnetic forces, even at 50 Hz, high voltage excitations have a tendency to physically move the parts of the demonstrator and cause vibrations. These mechanical vibrations result in an important noise level. In consequence, noise protection was required to do the measurements. Notice that additional pieces as well as screw-clamps have been used to reinforce the mechanical support and better maintain the magnetic circuits so as to reduce the different airgaps as much as possible and thus reduce the vibrations and noise.

## 3.2. Repeatability study

Repeatability tests have been realized to evaluate the standard deviation and the relative errors related to the positioning of the sensors. The 90° configuration of the demonstrator has been considered for that, and the RD of the GOES stack of interest has been aligned with the RD of the magnetizing circuit base.

Five flexible planar coils have been distributed around the GOES stack under test. These coils are designated by coil 1, coil 2, coil 3, coil A, coil B and coil C as shown in Figure III.24.

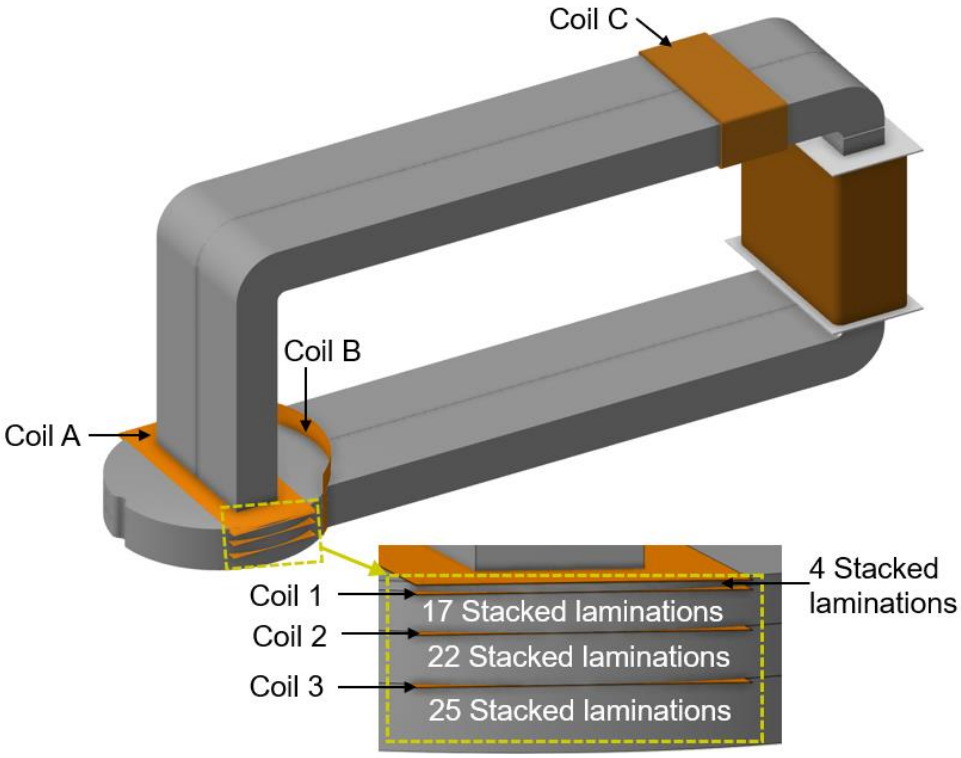


Figure III.24. Position of the flexible planar coils in the 90° configuration of the demonstrator.

The measurements have been repeated 10 times, for two imposed voltage levels: 5 and 10 V r.m.s (sine waveform excitation).

The standard deviation of the magnetic flux measurements has been calculated according to the formula:

$$Std_{dev} = \sqrt{\frac{\sum_{i=1}^{n}(x_i - \bar{x})^2}{n}} \quad \text{(III.7)}$$

in which, *n* is the total number of measurements, $x_i$ is a given measured value and $\bar{x}$ is the average value of the *n* measurements. Moreover, the relative repeatability error has been evaluated by using the formula (*III.5*)

$$Error_{relative} = \frac{\bar{x} \times 100}{Std_{dev}} \quad \text{(III.8)}$$

The results of the repeatability study related to the flux measurements (coil A, coil B, coil 1, coil 2 and coil 3), and to the current, active power and as well as the temperature are synthetized in Table III.1.

Table III.1. Relative errors related to the flux measurements (coil A, coil B, coil 1, coil 2 and coil 3), and to the current, active power and temperature measurements

| *SENSOR* | $Error_{relative}$ *(%) (5 V)* | $Error_{relative}$ *(%) (10 V)* |
|---|---|---|
| Coil A | 1.74 | 1.80 |
| Coil B | 1.28 | 1.20 |
| Coil C | 0.53 | 0.41 |
| Coil 1 and Coil 2 | 3.24 | 4.14 |
| Coil 3 | 4.07 | 5.26 |
| Current | 4.54 | 4.28 |
| Active power | - | 1.51 |
| Temperature | 2.98 | 2.19 |

One must note that for flux measurements, the errors slightly increase with the voltage level. This can be attributed to the electromechanical effects resulting in vibrations that probably move the position of the sensors inside the GOES stack of interest. The most important errors are observed for the planar coils inserted inside the GOES stack under test. The errors related to the planar coils 1 and 2 are equivalent, and increase in the same manner with the voltage level. The planar coil 3 presents the highest errors for the two imposed voltage levels. Given the low voltages detected at the location of coil 3, these errors are partly due to the limitations of the NI 9205 acquisition equipment at low voltages. It should be mentioned the difficulty of maintaining the sensors in place

throughout the measurements, as the GOES stack of interest is removed and repositioned for each measurement.

For the planar coils A and B, the repeatability errors are considerably lower (around 1.2 and 1.8% respectively). Idem for coil C exhibiting a relative error of around 0.5%. These sensors are less impacted by the vibrations and the control of their positioning was much better.

For the relative errors corresponding to the total active power, current and temperature measurements, the temperature measurements present the lowest relative error which remains constant during the measurements due to the limited heating for the considered voltages in this study of repeatability. It is expected that this error could increase at higher voltages. For the current measurements, they present a maximum relative error of around 4.5% which could be explained by small variations of the airgaps because of the repositioning of the GOES stack under test from one measurement to another. These airgaps were difficult to control and resulted in fluctuations of the total impedance (or reluctance from the magnetic point of view) seen by the power source. Hence the variations recorded for the excitation current.

In the following, the repeatability of the measurements is considered to conclude on the significance of the observed variations for the measurements made under different conditions (in-plane orientation of the GOES stack and 90° or 120° configuration of the demonstrator).

## 3.3. Magnetic characterization of the magnetizing circuits

As mentioned in subsection 2.2.2, closed magnetizing circuits of each configuration have been delivered by TCT in order to characterize them and obtain their magnetic characteristics. The latter are necessary for the numerical modelling of the demonstrator (in Chapter IV) as well as for the experimental power balance presented in the next section.

A primary coil of 100 turns (for magnetizing) and a secondary coil of 50 turns (to measure the induced voltage) have been wound on the magnetizing circuits. Then, based on the flux-metric method, the circuits have been characterized at 50 Hz from 0.1 up to 1.7 T with the MPG200D equipment from Brockhaus Measurements$^{GmbH}$.

The results of the experimental characterizations in terms of magnetization B-H curves and iron loss curves are given in Figure III.25. These characteristics have been compared in the same figure with those of the specified characteristics of the 100H23 grade provided by TCT.

The differences observed in Figure III.25 between the measured characteristics and TCT characteristics could be due to the effect of the manufacturing process that is detrimental for the magnetic properties. Indeed, the process consists in rolling up a single electrical steel sheet to build up the closed circuits, which causes high plastic deformations on the angular zones.

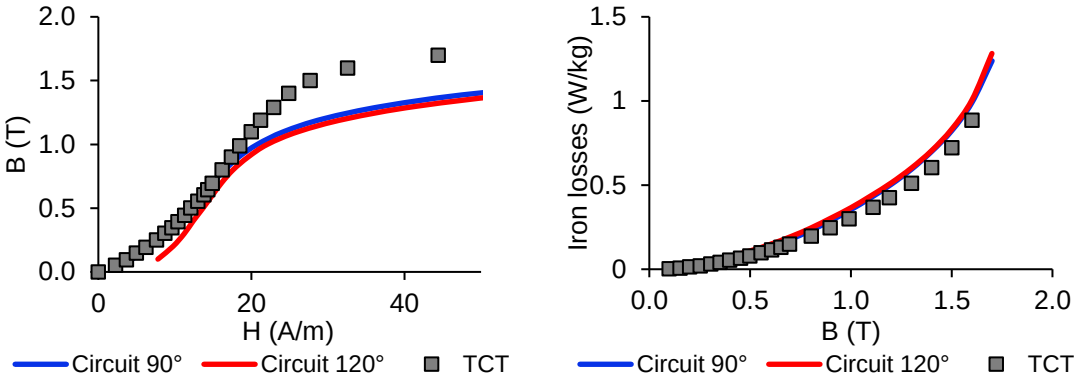


Figure III.25. Comparison of the measured characteristics with TCT characteristics at 50 Hz.

For comparison, at 50 Hz, 1.5 T, TCT grade presents a relative permeability in the RD of around 43092 against 24767 (in-plane permeability) for the EDF GOES investigated in this PhD thesis. For the iron losses, TCT grade still better (0.72 W/kg) against 0.9 W/kg for the EDF GOES. Notice that on the wound magnetizing circuits delivered by TCT, the measured losses at 50 Hz, 1.5 T are of 0.83 W/kg and remain inferior than the EDF GOES losses.

## 3.4. Power balance

A power balance has been made in order to get the iron losses within the GOES stack of interest from the total active power absorbed by the demonstrator given by:

$$P = P_{copper} + P_{magnetizing\ circuit} + P_{GOES\ stack} \quad \text{(III.9)}$$

where:

- $P$ is the total active power absorbed by the demonstrator in watts;
- $P_{copper}$ designates the copper losses in the excitation coil in watts;
- $P_{magnetizing\ circuit}$ designates the iron losses in the magnetizing circuit in watts;
- $P_{GOES\ stack}$ designates the iron losses in the GOES stack under test in watts.

In the following, the detailed procedure for the determination of each loss component is presented.

### 3.4.1. Copper losses

The copper losses have been estimated by using the classical formula:

$$P_{copper} = RI^2 \quad \text{(III.10)}$$

where $I$ is the r.m.s value of the magnetizing current and $R$ the electrical resistance of the excitation coil.

During the experimental measurements, the temperature of the excitation coil increases, due to the Joule heating. The temperature increases with the imposed coil voltage which is roughly proportional to the excitation current. In practice, the electrical resistance of the excitation coil increases with the temperature. This behavior has to be considered to correctly achieve the power balance. Therefore, two tests have been realized: one with the 90° demonstrator and another with the 120° demonstrator in order to estimate the resistance value as function of temperature.

First, the AC output of the voltage source has been applied to the demontrator. Voltages ranging from 5 to 40 V r.m.s. have been imposed and the correponding r.m.s current values have been acquired after the temperature has stablized (usually after 30 minutes). Then, the DC output of the power source has been used and applied to the demonstrator. The same r.m.s current values as in AC tests have been applied and from Ohm's law, the electrical resistance of the excitation coil has been then determined. Its evolution with the temperature for both 90° and 120° demonstrator configurations is given in Figure III.26

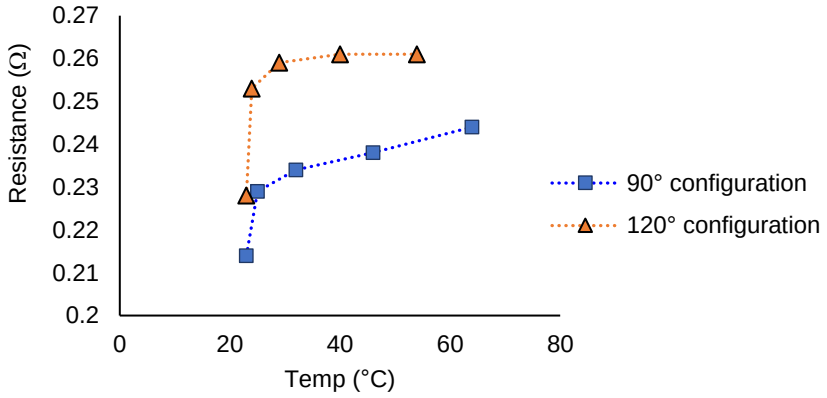


Figure III.26. Evolution of the excitation coil resistance with the temperature.

The resistance values varied with the temperature and are very similar in both configurations.

Knowing the excitation coil resistance and r.m.s. current values, the excitation coil copper losses have been determined for both 90° and 120° demonstrator configurations and for three in-plane orientations of the GOES stack of interest i.e., three angles $\alpha$ between the

RD of the GOES stack and the RD of the magnetizing circuit base: 0°, 54.7° and 90°. The results are shown in Figure III.27.

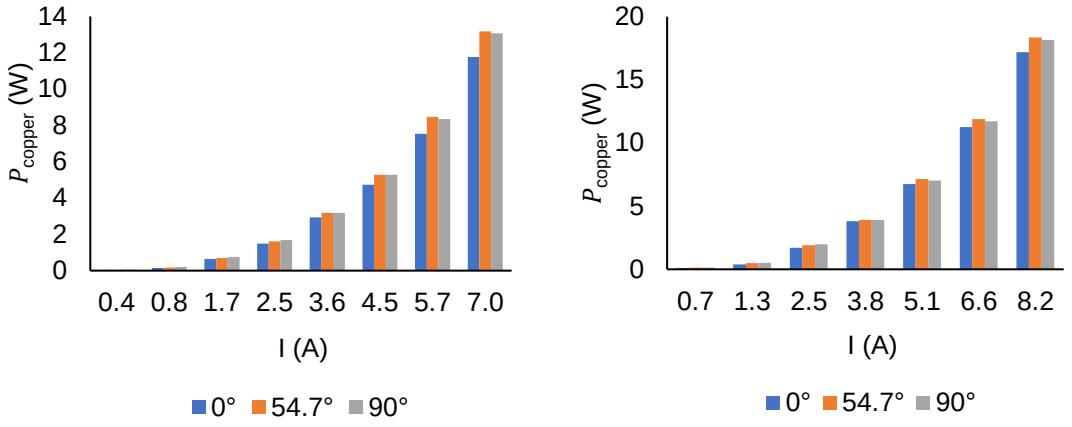


(a) 90° configuration (b) 120° configuration

Figure III.27. Copper losses vs r.m.s current values for both 90° and 120° demonstrator configurations and for three in-plane orientations of the GOES stack of interest i.e., three angles $\alpha$ between the RD of the GOES stack and the RD of the magnetizing circuit base: 0°, 54.7° and 90°.

For each configuration, the copper losses are overall comparable for the three in-plane orientations of the GOES stack. Nevertheless, we notice that they are slightly higher when the RD of the GOES stack under test is oriented at 54.7° and 90° with respect to the RD of the base of the magnetizing circuit, than when it is aligned with magnetizing circuit base (0°).

Moreover, the copper losses measured on the 120° configuration demonstrator surpass those of the 90° configuration. This can be explained by the considered geometries of the magnetizing circuits. Indeed, the magnetic path length of the 120° magnetizing circuits is higher than that of the 90° circuits. This results in a high magnetic reluctance of the 120° magnetizing circuits and thus higher excitation currents in comparison with the 90° circuits under the same imposed voltage.

At last, it is important to remember that this approach is limited by potential variations of the airgaps. Rigorously the DC resistance shall be measured immediately after each measurement before the cooling of the excitation coil.

### 3.4.2. Magnetizing circuit losses

From the specific iron losses measured in W/kg as described in section 3.3 (see Figure III.25), and knowing the masses of the magnetizing circuits used in the demonstrator (15.9 kg for the 90° circuits and 16.1 Kg for the 120° ones), their iron losses in watts have been determined. Figure III.28 shows the results as function of the peak magnetic flux density

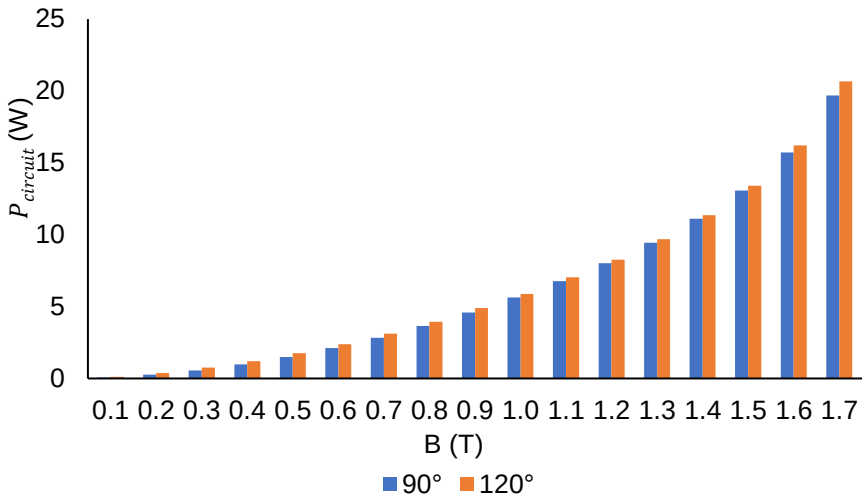


Figure III.28. Magnetizing circuit losses as function of the peak magnetic flux density.

These loss curves have been later interpolated as function of the in the magnetizing circuit peak flux density measured through the coil C (See Figure III.20) for each configuration of the demonstrator.

Figure III.29 gives the magnetizing circuit loss values as function of the excitation r.m.s currents for both 90° and 120° demonstrator configurations and for three in-plane orientations of the GOES stack of interest i.e., three angles $\alpha$ between the RD of the GOES stack and the RD of the magnetizing circuit base: 0°, 54.7° and 90°.

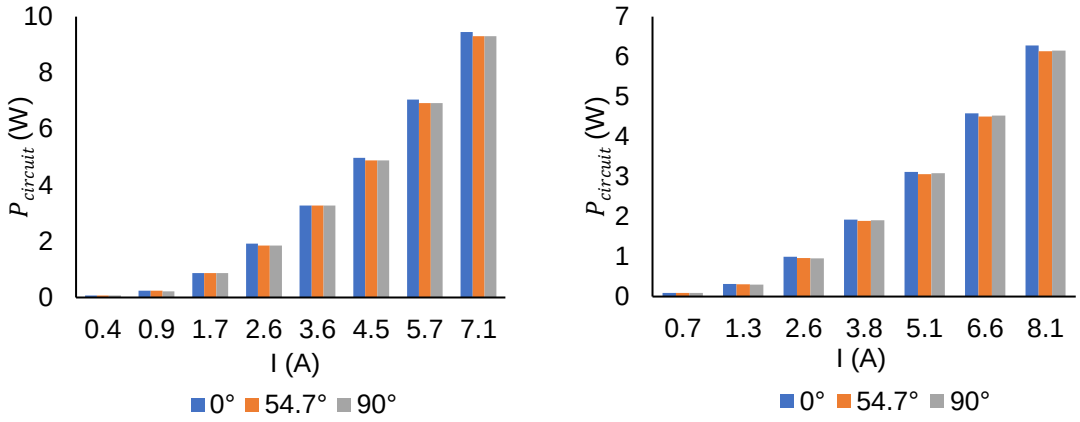


Figure III.29. Magnetizing circuit losses vs r.m.s current and for both 90° and 120° demonstrator configurations and for three in-plane orientations of the GOES stack of interest i.e., three angles $\alpha$ between the RD of the GOES stack and the RD of the magnetizing circuit base: 0°, 54.7° and 90°.

In this case, the iron losses corresponding to the 0° in-plane orientation of the stack are a little bit higher than 54.7° and 90° in-plane orientations. This seems to be bizarre but in fact, as the magnetic flux density has been the parameter used interpolating and taking into account that the total magnetic flux density is always more important for the 0° in-plane orientation, the interpolated losses are slightly higher.

Finally, to complete the power balance, the iron losses within the GOES stack under test have been obtained by subtracting the copper losses of the excitation coil and magnetizing circuit iron losses from the total active power absorbed by each configuration of the demonstrator under the investigated measuring conditions. The obtained results are presented in the following section.

## 3.5. Investigation of the effects of a flux directed at the plane surface of the GOES lamination stack and associated losses

For more convenience, the experimental results are detailed for the 90° configurations of the demonstrator and for three in-plane orientations of the GOES stack: 0°, 90° and 54.7°. Let us recall that for an orientation $\alpha$, the RD of the GOES stack of interest makes an angle $\alpha$ to the RD of the magnetizing circuit base.

Other results for other orientations of the GOES stack are given in Appendix B.

### 3.5.1. Incident magnetic flux normal to the lamination surface (90° configuration)

Two main measurement series have been realized on the 90° demonstrator configuration:

- A first series to measure the global distribution of the magnetic flux between the laminations of the GOES stack under test by means of the sensor prototypes made up of single planar coils (see subsection 2.2.4).
- A second series to measure the flux distribution in the laminations themselves by means of the sensor prototypes made up of arrays of 12-planar coils (see subsection 2.2.4.

The measurements have been performed for seven in-plane orientations of the GOES stack (0°, 10°, 20°, 30°, 54.7°, 75° and 90°), following the experimental protocol described in section 3.1.

#### — Excitation current

The measurements have been made under imposed voltage. Therefore, the changes in the magnetizing current and temperature of the excitation coil have been monitored during the experiments. Figure III.30 illustrates the evolution of the magnetizing current as function of the applied voltage for three in-plane orientations of the GOES stack under test: 0°, 90° and 54.7°.

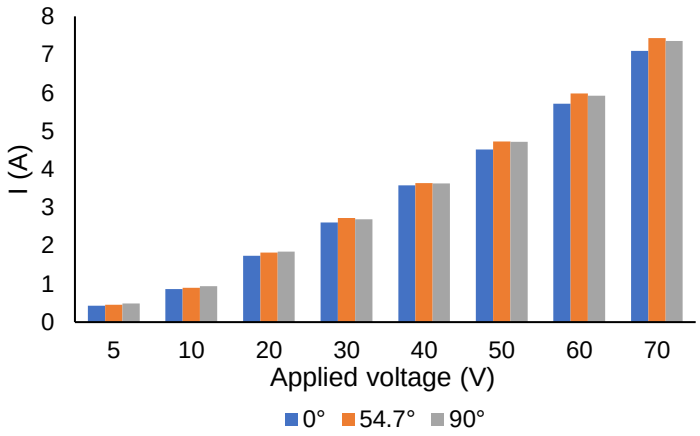


Figure III.30. Magnetizing current vs applied voltage for three in-plane orientations of the GOES stack under test: 0°, 90° and 54.7° (90° configuration of the demonstrator).

The current slightly varies with the in-plane orientation of the GOES stack under test. However, the observed relative variations are not significant as they are of the order of 4.5%, that is equivalent to the repeatability errors related to the excitation current measurements (see Table III.1). From a qualitative point of view, for all the measurements, the magnetizing current has tendency to increase when the GOES lamination stack under test is oriented towards the TD and difficult magnetization direction (54.7°). This is in accordance with the expected theoretical behavior, i.e., a difficult magnetization direction is characterized by a lower permeability, this results in a higher magnetizing current under the same imposed voltage.

On the other hand, the imposed voltage across the magnetizing coil has two components: a resistive component due to the electrical resistance of the coil together with an inductive component. Given that the voltage drop across the coil resistive component represents only around 2-3% of the total applied voltage (for example, it is of the order of 2 V r.m.s for an applied voltage of 70 V r.m.s), it can be neglected. Thus, in other words, an imposed voltage is equivalent to an imposed magnetic flux.

In the following, the experimental results are presented regarding the applied voltage.

— Magnetic flux measurements with single planar coil prototypes

As previously mentioned, different planar and search coils have been used for measuring the AC induced voltages over different locations between the laminations of the GOES stack under test and then get the corresponding magnetic flux distribution. The objective here is to investigate the flux penetration into the GOES lamination stack of interest. The position of the different flexible planar coils is given in Figure III.24 and recalled in Figure III.31.

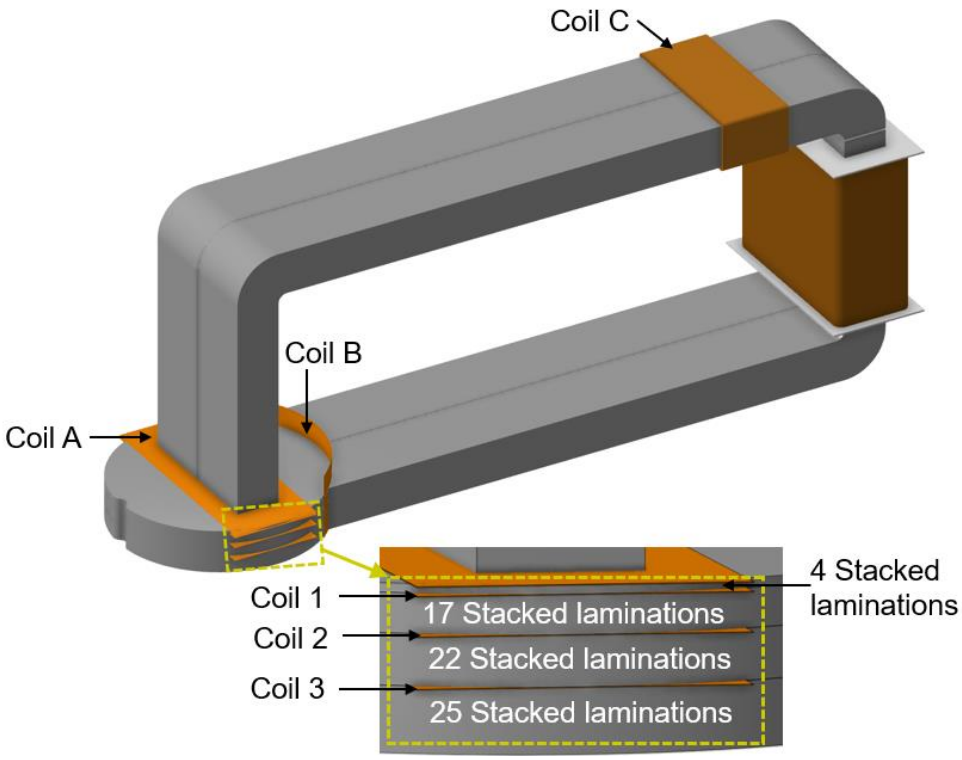


Figure III.31. Position of the flexible planar coils within the 90° demonstrator.

For an in-plane orientation at 0° of the GOES stack under test (to the RD of the magnetizing circuit base), Figure III.32 shows the measured fluxes by coils C, B, 1, 2 and 3 at different locations between the stack laminations as function of the imposed voltage. The figure has been divided into two subfigures to better show the evolution of the measured fluxes by the different coils.

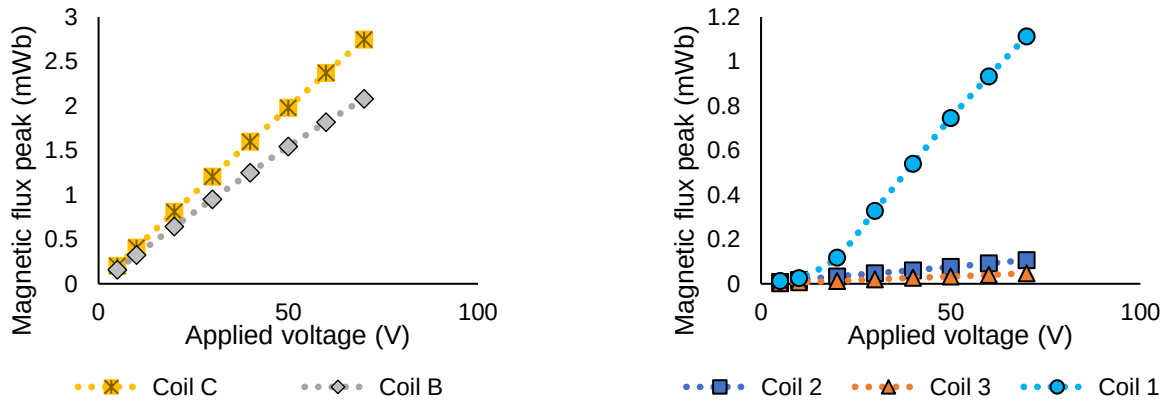


(a) Coils B and C (b) Coils 1, 2 and 3

Figure III.32. Flux penetration into the laminations of the GOES stack under test for an in-plane orientation at 0° to the RD of the magnetizing circuit base (90 ° configuration of the demonstrator).

The incident flux is measured by coil A and coil B the measurements of which are really similar. Thus, only the measurements acquired by coil B are represented in Figure III.32-a. The highest flux peak value is recorded by the coil C positioned near the excitation coil. The difference between this flux and that of acquired by coils A and B would be mainly due to the airgaps and the stray flux around the stack.

Within the GOES stack under test itself, the measured magnetic flux peak value decreases as the distance of the planar coil position from the stack top surface increases (see coil 1, coil 2 and coil 3 flux vs voltage curves). The total amount of flux is mostly concentrated within the first laminations of the stack as shown by the planar coil 1. A much-reduced amount of flux reaches the planar coil 2 and 3 located further down within the GOES stack. This tendency has been observed in all the measurements. It coincides, without surprise, with literature observations [43]. Indeed, considering the low permeability of the GOES in the normal direction as well as the inter-laminar airgaps, the magnetic flux tends to rapidly change its direction to flow in the plane of the laminations. This same behavior has been also observed in the case of the 90° and 54.7° in-plane orientations of the GOES stack under test with respect to the RD of the base of the magnetizing circuit.

— Magnetic flux measurements with arrays of 12 planar coil prototypes

The prototypes made up of arrays of 12-planar coils arrays have been used to measure the magnetic flux distribution within the laminations of the stack at the same positions considered with the single planar coils (see Figure III.31) previously presented.

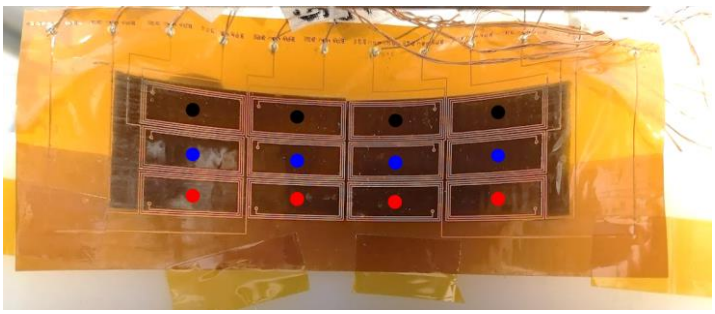

Figure III.33. Photography of a sensor prototype with an array of 12 planar coils, positioned in the airgap between the GOES stack and the base of the magnetizing circuit of the 90° demonstrator.

The results from the array of 12 planar coils, placed in the airgap between the GOES stack and the base of the magnetizing circuit are given in Figure III.34 for an imposed voltage of 70 V r.m.s. Each point of the figure represents one of the 12 planar coils of the array and the colors indicate the row position. Indeed, there are three rows of four coils each. The black points represent the upper row, the blue points represent the middle row and the red points represent the bottom row, exactly as the photography given in Figure III.33. Two in-plane orientations of the stack have been considered: 0° and 90°.

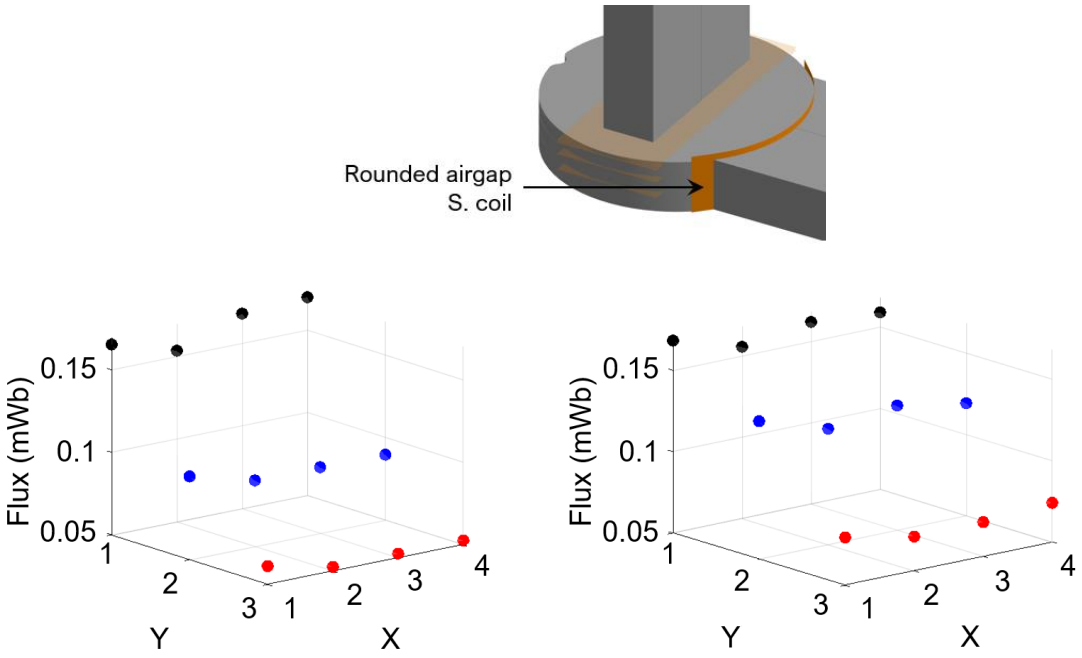


(a) in-plane orientation at 0° (b) in-plane orientation at 90°

Figure III.34. Flux measurements from the planar sensor prototype B made up of an array of 12 coils, positioned in the airgap between the GOES stack and the base of the magnetizing circuit of the 90° demonstrator under imposed voltage of 70 V r.m.s.

The peak value of the measured magnetic flux decreases from the first to the third row of coils. A much-reduced amount of flux reaches the third row of coils. This ties in with the observations made in the previous section about the decrease in flux from the stack top surface to the lower laminations.

To compare the two considered in-plane orientations, the measured fluxes when the RD of the GOES stack is aligned with that of the magnetizing circuit base (0° in-plane orientation) are a little bit higher than when it is oriented at 90° to the RD of the magnetizing circuit base.

Concerning the fluxes measured by the coil arrays positioned between the laminations of the GOES stack of interest (coil 1 position), they are presented in Figure III.35 for two in-plane orientations of the stack and under imposed voltage of 70 V r.m.s. We can say that, for each in-plane orientation, the results are quite similar from one row of coils to another.

In the following, considering that the sum of the magnetic fluxes measured by the 12 coils of the array is equivalent to the magnetic flux acquired by the single coil prototypes, only the measurements from the single coils are presented.

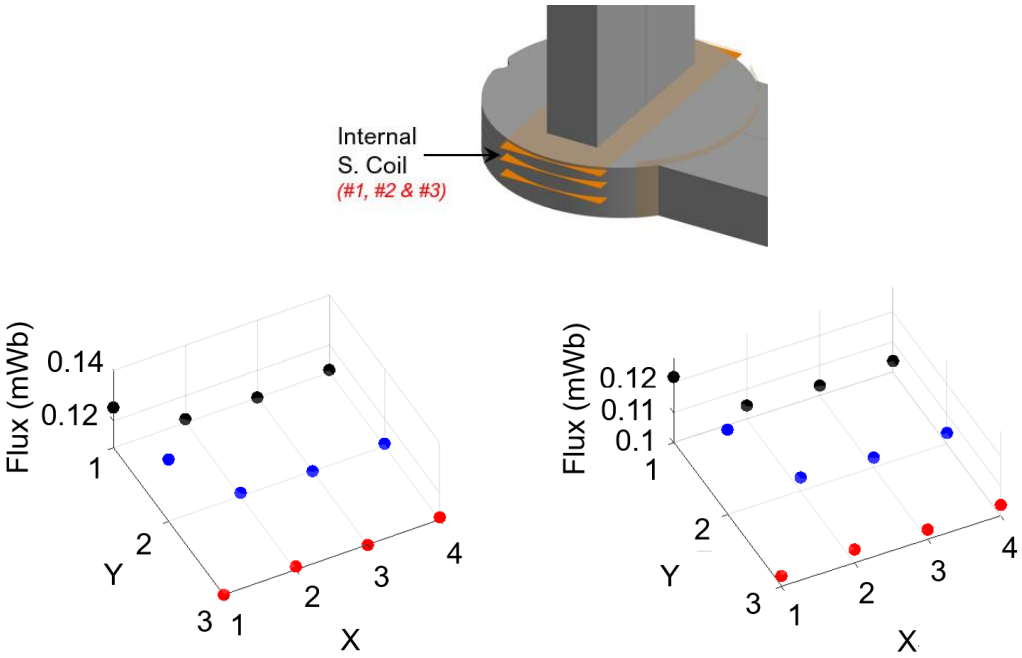


(a) in-plane orientation at 0° (b) in-plane orientation at 90°

Figure III.35. Flux measurements from the planar sensor prototype 1 made up of an array of 12 coils, under imposed voltage of 70 V r.m.s.

— The effect of the anisotropy of the GOES lamination stack

Let us recall that one of the main objectives of the experimental phase is to investigate the effect of anisotropy of the GOES lamination stack under test on the flux distribution in it and within the demonstrator. This section focuses on this purpose and compares the peak values of the magnetic flux measured by all the planar coils for different in-plane orientations of the GOES stack the RD with respect to the RD of the magnetizing circuit base while considering two imposed voltage levels: 10 and 70 V r.m.s.

The results of the measurements are given in Figure III.36 and Figure III.37

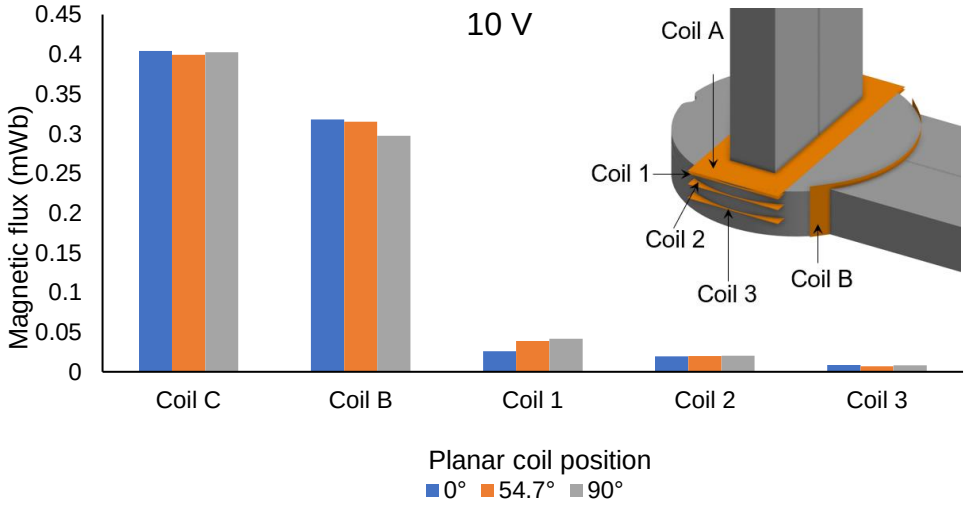


Figure III.36. Flux distribution under imposed voltage of 10 V r.m.s (90° configuration of the demonstrator).

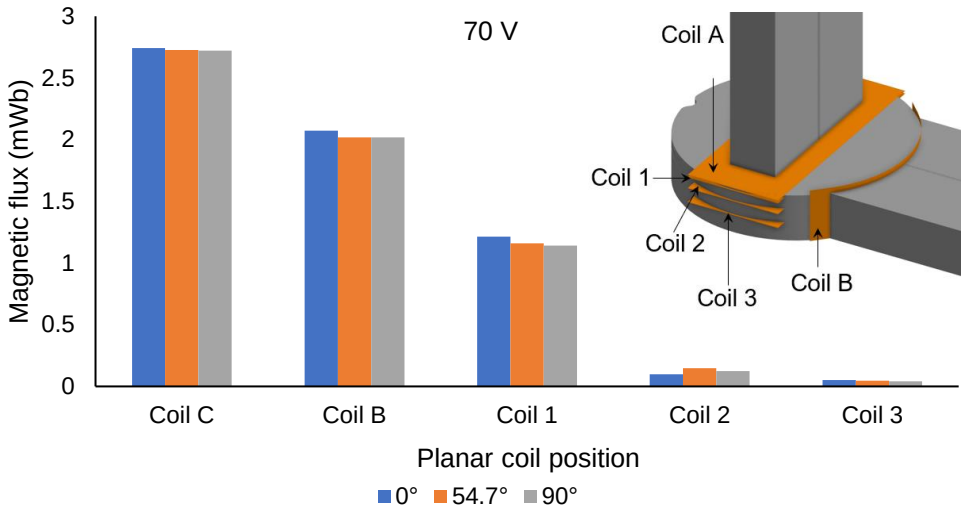


Figure III.37. Flux distribution under imposed voltage of 70 V r.m.s (90° configuration of the demonstrator).

Under both imposed voltages: 10 and 70 V r.m.s, the flux measured by the coils C and B are always higher when the RD of the GOES is aligned with that of the magnetizing circuit (0° in-plane orientation). This is in accordance with the theoretical behavior given the higher permeability in the RD of the GOES stack and consequently the total reluctance of the demonstrator which is lower in comparison with the other in-plane orientations.

Concerning the coils 1, 2 and 3 inserted inside the GOES stack (between the laminations) the behaviors are more complex.

For both imposed voltage levels, only a small amount of the total magnetic flux reaches the internal laminations of the stack. The higher in-plane permeability of the stack (whatever its orientation) in comparison with the permeability in its normal direction ($\mu_r$ = ~34) combined with the eddy currents on the stack surface favorize the magnetic flux to rapidly change the direction to flow in the plane of the first laminations.

At the low voltage level (10 V r.m.s), the magnetic flux measured by coil 1 is less important when the RD of the GOES stack is oriented at 0° to the RD of the magnetizing circuit base, that when the RD of the stack is oriented at 90° or 54.7°. This is due to the fact that for the 0° in-plane orientation, the incident flux mostly takes the RD of the stack surface which means that the coil 1 positioned four laminations further down detects only a small amount of flux. In contrast, for both 90° and 54.7° in-plane orientations, the measured amount of flux is a little bit higher because the incident flux further penetrates into the stack laminations.

Notice that this behavior remains the same until around 60-70 V where saturation phenomena become more pronounced.

For a higher voltage level (70 V r.m.s), the magnetic flux measured by coil 1 is more important when the RD of the GOES stack is oriented at 0° to the RD of the magnetizing circuit base, than when the RD of the stack is oriented at 90° or 54.7°. This behavior is contrary to that observed for low voltage levels. In fact, the incident flux, due to the saturation effects, tends to penetrate further down into the laminations. This results in a higher magnetic flux measured by coil 1 for the 0° in-plane orientation in comparison with the other in-plane orientations mirroring the flux behavior observed thanks to coils B and coil C.

On the other hand, the coil 2 measures a higher magnetic flux for the 90° and 54° in-plane orientations than for the 0° in-plane orientation of the stack. This is due to the position of coil 2 which still far from the saturated zone, thus, we observe an equivalent behavior to that of coil 1 at low imposed voltage.

Finally, the coil 3 shows very similar flux values for the three considered in-plane orientations of the stack. The difference observed are very low (only about 46 µWb).

At last, in order to corroborate all the observations made above and the significant differences between the measured flux values from an in-plane orientation to another, an analysis of the results with regard to the repeatability study in section 3.2 presented in the following.

— Analysis of the results with regard to the repeatability study

Table III.2 and Table III.3 compares the measured relative differences [calculated by equation *(II.13)]* with the repeatability errors obtained for each planar coil and presented in section 3.2 for two voltage levels: 10 and 70 V.

Table III.2. Repeatability errors vs measured relative differences at 10 V

| *Planar coil* | *Voltage level* | *Repeatability error* | *Relative difference between the 0° and 90° in-plane orientations* | *Relative differences between the 0° and 54.7° in-plane orientations* |
|---|---|---|---|---|
| Coil C | 10 V | 0.53 % | 1.61% | 0.54% |
| Coil A and B | | 1.28% | 9.3% | 3.72% |
| Coil 1 | | 4.1% | 56.3% | 60.6% |
| Coil 2 | | 4.1% | 16.28% | 12.86% |
| Coil 3 | | 5.25%. | 1.47% | 6.0% |

Table III.3. Repeatability errors vs measured relative differences at 70 V

| *Planar coil* | *Voltage level* | *Repeatability error* | *Relative difference between the 0° and 90° in-plane orientations* | *Relative differences between the the 0° and 54.7° in-plane orientations* |
|---|---|---|---|---|
| Coil C | 70 V | 0.53 % | 0.60% | 0.75% |
| Coil A and B | | 1.28% | 4.03%, | 2.73% |
| Coil 1 | | 4.1% | 6.1% | 4.6% |
| Coil 2 | | 4.1% | 20% | 50% |
| Coil 3 | | 5.25%. | 17.93% | 8.5% |

In general, even though the relative differences (related to the flux measurements) from an in-plane orientation to another are relatively low, they surpass the repeatability errors. Thus, the differences observed could be attributed to the anisotropic properties of the GOES stack under test. Nevertheless, the observed variations remain unsignificant in comparison with the predominant electromagnetic phenomena in the demonstrator namely eddy currents and saturation.

— Distortion of measured voltage waveforms

A distortion of the voltage waveforms measured across the terminals of the planar coils inserted between the laminations of the GOES stack under test (coils 1, 2 and 3) has been observed in certain measurements particularly for applied voltage levels between 30 V and 70 V r.m.s. This distortion concerns especially the coil 1 and it was more pronounced for the 54.7° and 90° in-plane orientations of the stack. Its repercussion on the flux waveforms is obvious as the latter are obtained from the time integration of the voltage waveforms. The evolution of the distortion of the voltage waveforms measured by coil 1 as well as the calculated flux waveforms as function of the applied r.m.s voltage is presented in Figure III.38 for the 0° in-plane orientation.

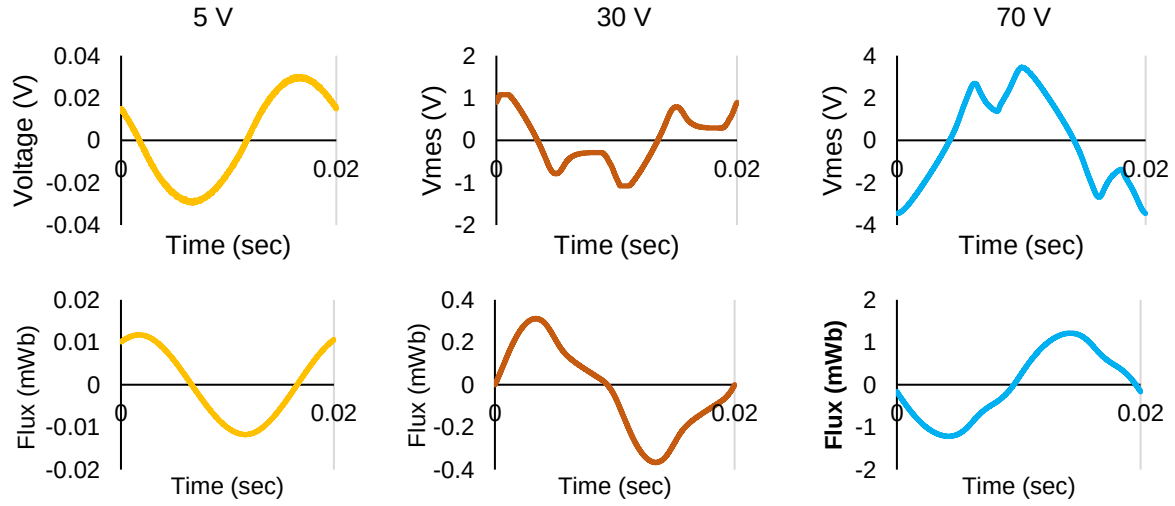


Figure III.38. Evolution of the distortion of the voltage waveforms measured by coil 1 and the calculated flux waveforms as a function of the imposed r.m.s. voltage (0° in-plane orientation).

These distortions can be attributed to the combined effects of saturation and strong eddy currents, within the first laminations of the stack under test. This matches with the results of Figure III.34 showing the measured magnetic fluxes by a sensor prototype including an array of 12 coils. The fluxes measured by the first row of coils correspond to high flux density values close to saturation (between 1.5 and 1.7 T).

### 3.5.2. Iron loss measurements

As mentioned before, the other important aspect behind the development of this experimental demonstrator is the study of the total iron losses under different excitation conditions indented to be representative of the working conditions of turbogenerators and the associated end-region losses.

Figure III.39 offers a comparison of the total active power absorbed by the demonstrator (total losses) measured as function of the imposed voltage for three in-plane orientations of the GOES stack.

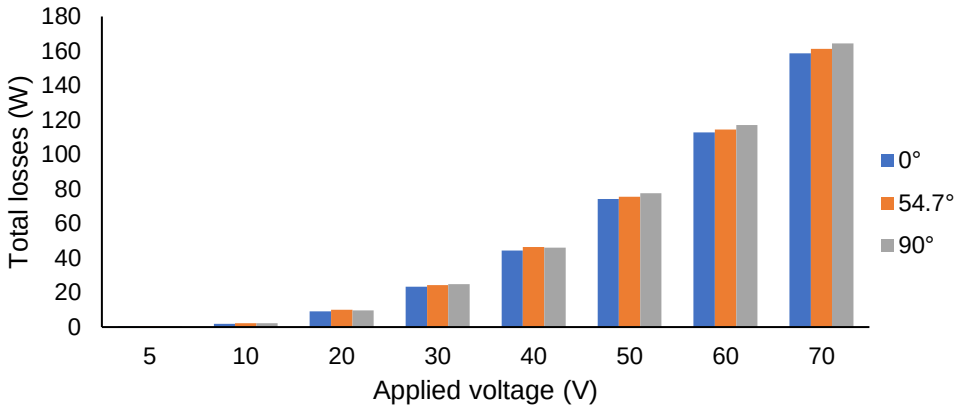


Figure III.39. Total active power absorbed by the demonstrator (total losses) as function of the imposed voltage for three in-plane orientations of the GOES stack.

One can note that the total active power absorbed by the demonstrator is always lower for the 0° in-plane orientation of the GOES stack than for the 54.7° and 90° in-plane orientations. This coincides with the expected theorical behavior of GOES of which the RD exhibits lower losses. For an imposed voltage of 70 V r.m.s, the total active power is equal to 160 watts for the 0° in plane orientation of the stack.

By following the power balance procedure introduced in section 3.4, the iron losses related to the GOES stack under test have been determined by subtracting the copper losses of the excitation coil and the magnetizing circuit iron losses from the total active power absorbed by the demonstrator under the investigated measuring conditions. The obtained results are presented in Figure III.40 as function of the imposed voltage for three in-plane orientations of the GOES stack.

The contribution of the stack losses is compared in Figure III.41 with the copper losses of the excitation coil and the magnetizing circuit losses.

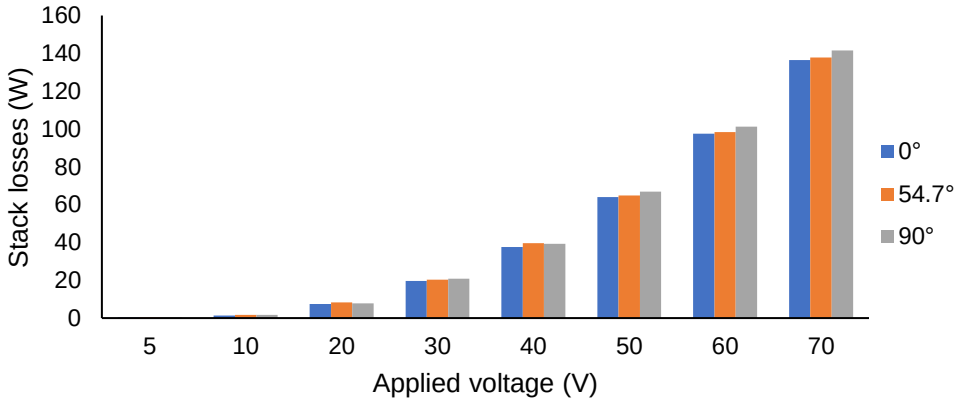


Figure III.40. Stack losses as function of the imposed voltage for three in-plane orientations of the GOES stack.

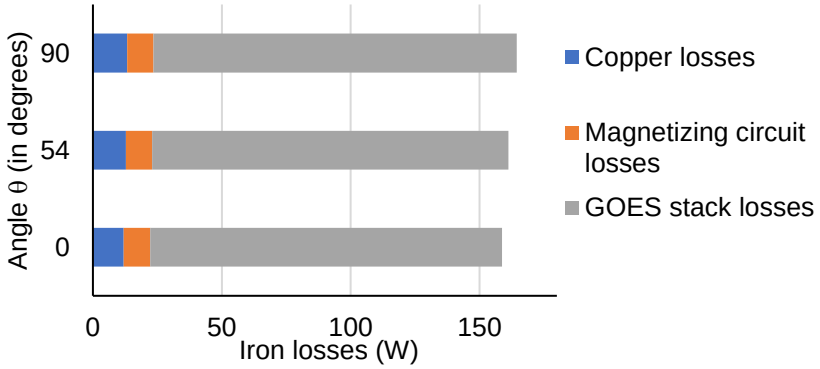


Figure III.41. Comparison of the stack losses with the copper losses and the magnetizing circuit losses for an imposed voltage of 70 V r.m.s and for three in-plane orientations of the GOES stack.

The Epstein frame measurements made on the investigated GOES in Chapter II have shown that its 50 Hz iron losses do not exceed a few W/kg in the worst case (close to saturation). This represents a fraction of only a few watts of the total losses of the stack. Therefore, it is clear that the stack losses are mainly due to the eddy currents generated by the incident flux penetrating into the laminations of the stack.

In view of these results, the impact of the anisotropy of the GOES lamination stack on the losses is much less significant in comparison with the eddy current losses.

Finally, the relative differences from one in-plane orientation to another have been calculated for the iron losses at an imposed voltage of 70 V r.ms, while using the 0° in-plane orientation as the reference. A relative difference of 3.6% has been obtained between the 0° and 90° in-plane orientations, and of 1.6% between the measurements of the 0° and 90° in-plane orientations.

These differences are not very high, but are significant considering the maximum repeatability error of 1.51%. Thus, the effect of the anisotropy has been constated.

Overall, it plays a role since it modify the flux distribution and the iron loss values, but the effects remain unsignificant compared to the effects of the eddy current losses.

— About penetration of flux into the GOES stack in a direction at intermediate angle to the plane of the laminations (120° configuration)

The measurements made on the 120° configuration of the demonstrator are, for the most part, very similar to the 90° configuration. They present the same tendencies in terms of the flux penetration as well as in terms of the associated losses with regard to the in-plane orientation of the RD of the GOES stack with respect to the RD of the magnetizing circuit base.

Therefore, considering that all the observations made on the 90° configuration apply to the 120° configuration and for more convenience, the results the 120° configuration results are not treated in this chapter, they are given in the Appendix C.

## 4. Synthesis

In this chapter an experimental prototype has been developed to investigate the magnetic behaviour of a GOES lamination stack under 3D magnetic flux path. The objective is to reproduce as far as possible the excitation conditions of turbogenerators. Both flux penetration and the associated losses have been experimentally quantified.

The results obtained will serve as a support for the numerical modeling of the demonstrator in Chapter IV.

# Chapter IV. 3D Numerical Modelling Applied to the Demonstrator

---

*In the previous chapters, anisotropic behavior law and iron loss models of GOES have been implemented in the FEM software code_Carmel and validated for academic applications. Also, an experimental demonstrator has been designed and devolved to measure the magnetic flux and iron loss distribution within a GOES lamination stack submitted to 3D magnetic flux attacks.*

*In this chapter, the numerical modeling of the experimental demonstrator is developed within code_Carmel. The 90° configuration of the demonstrator has been simulated under different excitation conditions as in the experiments in order to study and compare the global behavior of the demonstrator (especially the behavior of the GOES stack of interest) against the experimental behaviors.*

---

# Table of content

# 1. Considerations for the FEM Simulation

A series of FEM simulations has been performed to study the electromagnetic behavior of GOES under the influence of non-conventional flux attacks using the software code_Carmel. These simulations have two main objectives:

- Replicate the behavior of the experimental demonstrator within the FEM environment by the use of the integrated anisotropic behavior law and iron loss models developed in Chapter II.
- Provide a better understanding of the phenomena in terms of flux penetration into the GOES lamination stack and its distribution as well as the associated iron losses as function of the in-plane anisotropy of the stack.

However, the non-linear scheme of code_Carmel does not allow to solve the strongly anisotropic non-linear case. In this work, in order to analyze the phenomena of interest as realistically as possible, the simulations have been performed under two hypotheses:

- *Anisotropic linear case,* to observe the effect of the in-plane orientation of the GOES lamination stack (set by the angle α, as defined in Chapter III) within the demonstrator at low flux density levels.
- *Isotropic non-linear case,* to consider the saturation of the material for two specific in-plane orientations of the GOES lamination stack (α = 0° and α = 90°).

In both cases, the simulations have been performed using magnetostatic and magnetodynamic formulations. All the details taken into account for the simulations and their configurations are briefly presented in this section.

## 1.1. 3D geometry & meshing

For the 3D numerical simulation, we have considered the 90° configuration of the demonstrator. For the GOES lamination stack, the first seven laminations have been modeled individually and have been separated from each other by insulation layers of 0.05 mm thickness. This modelling aligns with the knowledge from previous works in the literature [19] [43] and the experimental measurements presented in section 3.5 of chapter III, that have shown that the most of the magnetic flux is concentrated within the first laminations of the GOES stack.

The rest of the stack has been represented by solid volumes equivalent in size to the sets of 14, 22 and 25 laminations used experimentally. Besides, additional airgaps of 0.135 mm have been considered in-between the laminations where the flexible planar coils have been positioned for executing the experimental measurements. The details of the geometry and the positioning of the insulating layers are given in Figure IV.1.

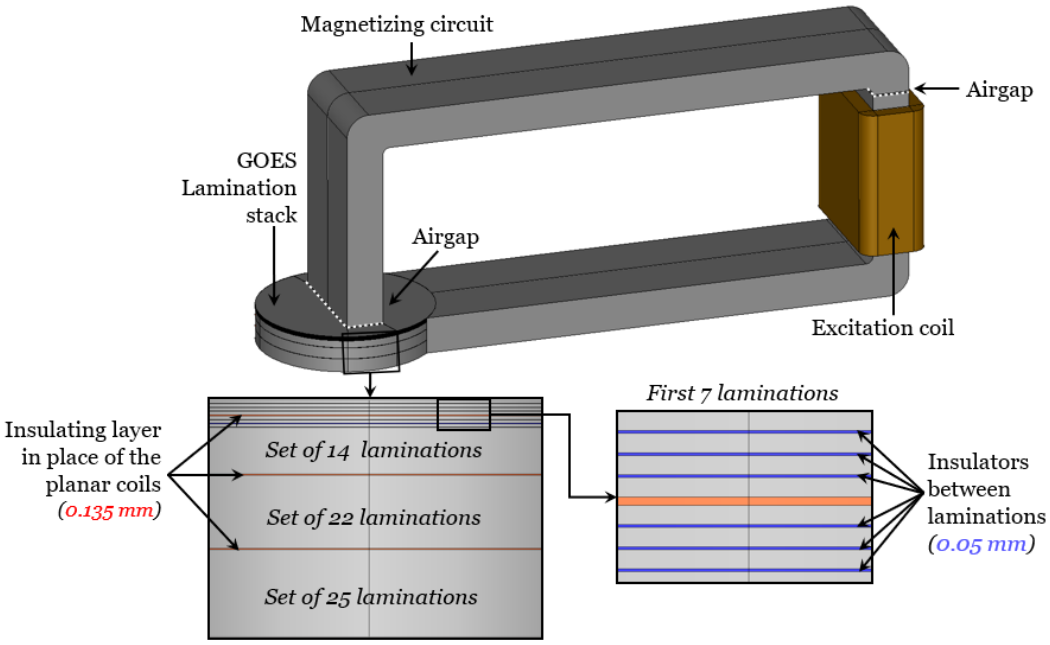


Figure IV.1. 3D Geometry of the 90° demonstrator and the different air-gaps considered in the modeling (0.135 mm airgaps in orange, 0.05 mm insulation layers in blue).

Furthermore, two additional airgaps have been included in the demonstrator geometry. One located in-between the two halves of the magnetizing circuit (on top of the excitation coil) and another at the joint between the GOES lamination stack and the magnetizing circuit leg (see Figure IV.1). The equivalent size of these two airgaps has been adjusted to match the flux levels measured experimentally by Coil C in the magnetizing circuit.

Additionally, virtual search coils have been defined for computing the magnetic flux at the same locations as the planar experimental coils, closed contours have been added in the GOES stack of which the edges coincide with the size and position of the planar coils used in measurements (see Figure IV.2).

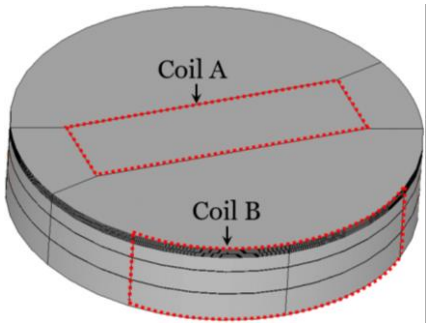


Figure IV.2. Closed surfaces for computing the magnetic flux.

— Modeling of the magnetizing coil (the excitation source)

The excitation coil has been modeled by an assembly of eight different volumes, positioned around the magnetizing circuit. This coil has an internal section of 0.01 $m^2$. The

simulations have been made by applying the same number of Amp turns as the experimental measurements.

— Meshing

Once the 3D geometry of the demonstrator has been modeled, a 3D domain meshing has been generated. This has been achieved by using the SMESH module within SALOME platform [120]. A combination of tetrahedrons, prisms and quadrangles has been adopted with 527,000 elements in total. A reasonable refinement of the meshing with respect to the thickness of the stack laminations has been achieved for applying the magnetodynamic formulation. Two layers of finite elements have been considered in each of the first seven laminations of the stack. The details of the mesh with a zoom on the GOES stack are presented in Figure IV.3 and Figure IV.4.

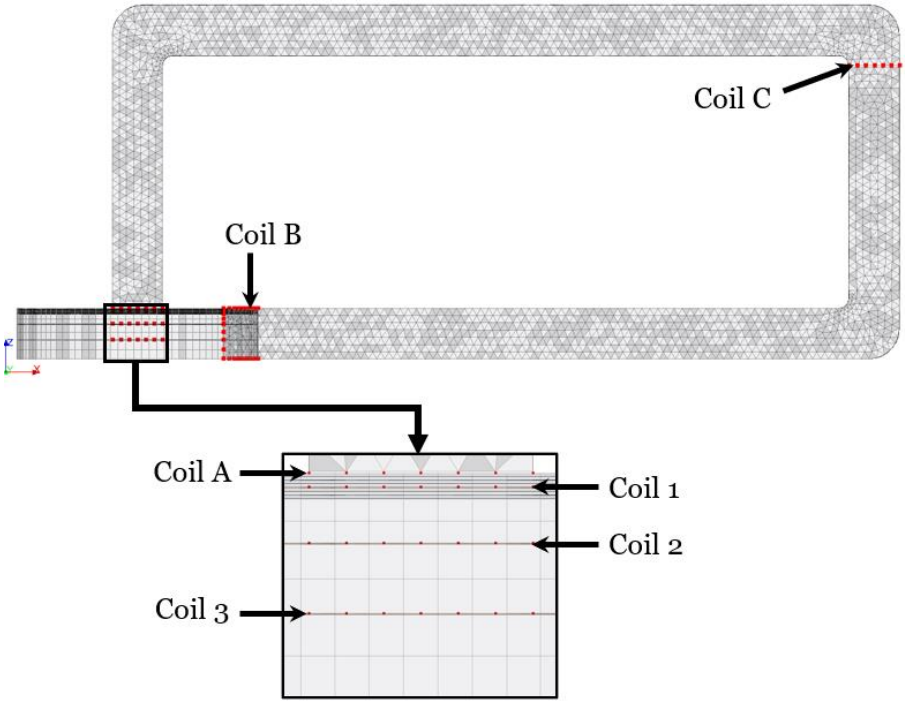


Figure IV.3. 3D mesh of the experimental demonstrator with detailed position of the coils.

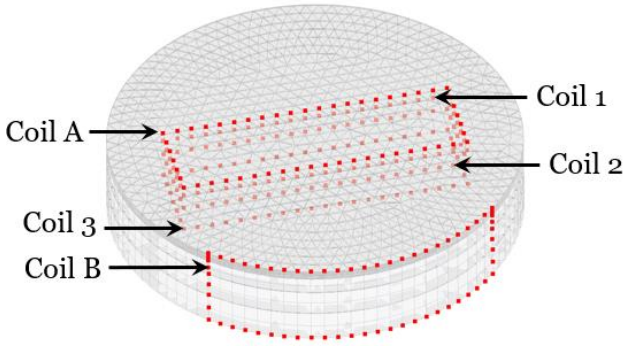


Figure IV.4. 3D View of the search coils within the GOES lamination stack.

### — Boundary conditions

An air-box including the geometry of the demonstrator has been considered. It satisfies the boundary condition ***B.n = 0*** on all its the faces. No other boundary condition has been required for the simulations, as insulating layers have been modeled between the first layers of the stack. This is sufficient to apply the magnetodynamic formulation in A-φ configuration.

## 1.2. General considerations for the numerical simulation

### — Resolution: linear and non-linear solvers

The simulations have been realized using the magnetostatic vector potential **A** formulation and the magnetodynamic **A**-φ formulation. Due to the non-symmetric nature of the full permeability tensor (modified Enokizono approach), the direct solver MUMPS [121] have been employed for the linear resolution of the problem.

Adequate magnetic behavior laws have been used for the different magnetic materials of the demonstrator as summarized in Table IV.1.

Table IV.1. Behavior laws of the magnetic materials

| Domain | Linear case | Non-linear case |
|---|---|---|
| Magnetizing circuit | Isotropic permeability tensor (from experimental data) | Isotropic Marrocco law |
| GOES lamination stack | Anisotropic permeability tensor (Enokizono/Diagonal) | Isotropic Marrocco law |

In the linear case, permeability tensors (either diagonal for the magnetizing circuit or full for the GOES stack of interest) have been considered. These tensors have been estimated from the experimental measurements according to the maximum excitation currents and the corresponding magnetic flux density levels. For the non-linear case, the behavior laws of both materials (magnetizing circuit and the GOES stack) have been taken into account by Marrocco equation given by *(IV.1)* [122], identified from the associated experimental data.

$$H = \frac{B}{\mu_0}\left[\frac{B^{2\alpha}}{B^{2\alpha}+\tau}(c-\varepsilon)+\varepsilon\right] \qquad (IV.2)$$

where α, τ, ε and c are the Marrocco coefficients. They have been identified by the least-square method.

The Newton-Raphson scheme implemented in code_Carmel has been used to solve the non-linear system.

— Electrical conductivity

In the magnetodynamic simulations, only the first seven laminations of the stack under test have been considered as conductive materials. This allows the consideration of eddy current developments within the GOES laminations. The electrical conductivity has been assumed as isotropic, it is equal to 2.17 MS/m.

— Other considerations

The FEM simulations have been performed under imposed current. In order to compare with the measurements, additional measurements have been realized on the demonstrator for the same current levels imposed in the simulations. These measurements have been performed for three main in-plane orientations of the GOES stack (0°, 54.7° and 90°). The experimental magnetic fluxes obtained from these additional characterizations follow the same tendencies observed in Chapter III. A more detailed comparison of these measurements is given in the Appendix D.

# 2. Linear case

The linear simulations must be performed with special care because of the magnetic flux directed at the plane surface of the GOES lamination stack. Indeed, in this configuration, the magnetic flux mostly circulates through the first laminations of the stack, reaching unrealistic flux density levels (as there is no saturation).

Hence, the simulations have been carried out for a current value 0.43 A, which is the r.m.s experimental current under an imposed voltage of 5 V r.m.s for an in-plane orientation of the stack of 0° (the lowest current experimentally applied).

Three in-plane orientations for the GOES lamination stack (α = 0°, 54.7° and 90°) have been simulated. The corresponding permeability tensors have been identified for a flux density level of 0.1 T. The simulations have been achieved at the industrial frequency of 50 Hz.

Results of the simulations have shown that the distribution of the magnetic flux density and magnetic field vectors have been affected by two main factors: the in-plane orientation of the RD of the GOES lamination stack and the presence of eddy currents that oppose the flux penetration on the stack surface. In the following, the results are analyzed on the basis on these two factors.

## 2.1. Effect of the anisotropy of the GOES lamination stack

### 2.1.1. Magnetostatic simulation

The magnetic flux density and magnetic field distribution maps, obtained from the magnetostatic simulation are presented in Figure IV.5 to Figure IV.6.

In this case, the GOES lamination stack exhibit different behaviors according to the considered in-plane orientation. These effects are particularly evident regarding the magnetic flux density distribution maps (see Figure IV.5). Indeed, whatever the stack in-plane orientation, the flux density vectors tend to follow the RD of the GOES laminations for which we obtain the highest flux density levels given the higher relative permeability along RD. On the other hand, the magnetic field vectors (see Figure IV.6) seem to normally penetrate into the GOES laminations, no matter the in-plane orientation of the stack. However, at the 90° and 54.7° in-plane orientations, the magnetic field extend around a larger area, following the RD of the GOES lamination stack near the borders of the magnetizing circuit leg.

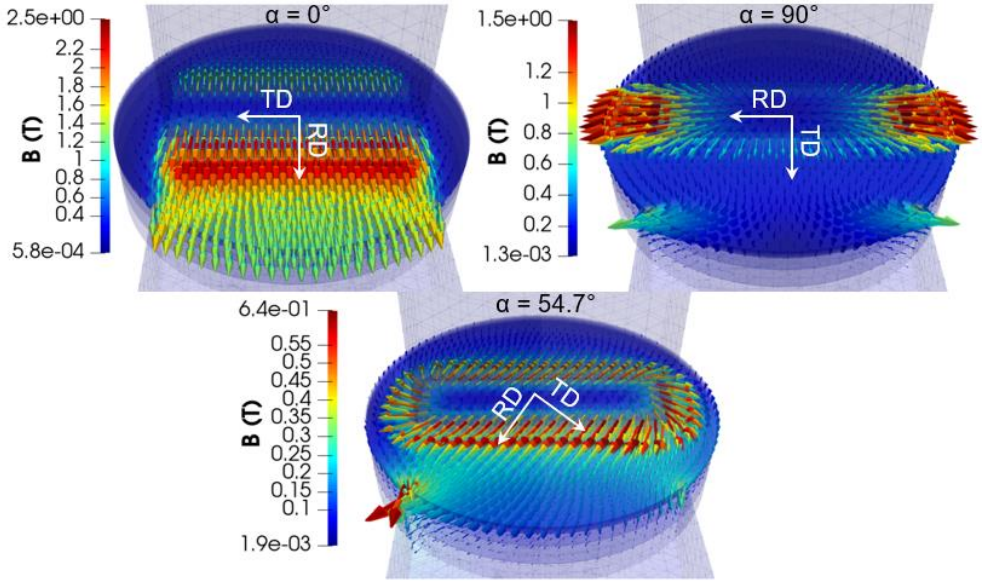


Figure IV.5. Flux density distribution maps from the magnetostatic linear simulations for the in-plane orientations of the RD of the GOES stack (α = 0°, 90° and 54.7°) for a magnetizing current of I = 0.43 A r.m.s.

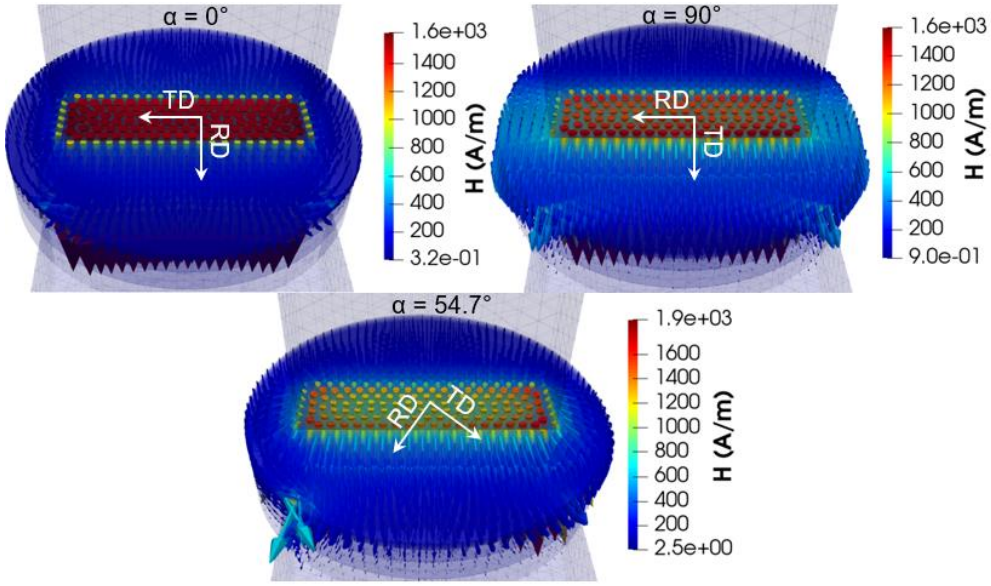


Figure IV.6. Magnetic field distribution maps from the magnetostatic linear simulation in the three in-plane orientations of the RD of the GOES stack (α = 0°, 90° and 54.7°) for a magnetizing current of I = 0.43 A r.m.s.

These differences in behavior can be reasonably attributed to the way the magnetic flux flows through the stack. Indeed, different mechanisms can be observed depending on the stack orientation.

For the in-plane orientation α = 0°, the incident magnetic flux tends to rapidly change its direction to flow in the plane of the laminations and then goes back to its path back through the magnetizing circuit base. This results in high flux densities (>2 T) and magnetic field levels of 1600 A/m.

In contrast, for the in-plane orientations 90° or 54.7°, the magnetic flux seems to follow a less direct path towards the magnetizing circuit base, and flows through a more significant number of laminations (along the stack height). In this case, the flux density and magnetic field levels are less important in the surface of the first lamination (than when for the 0° in-plane orientation), and distribute inside the GOES stack itself.

The distribution of the magnetic flux density and magnetic field vectors inside the GOES lamination stack, can be better appreciated in Figure IV.7 and Figure IV.8 respectively for 0° and 90° in-pane orientations of the RD of the stack (α = 0° and α = 90°). Through the figures, it is clear that inside the stack [see (b), (c) and (d) in Figure IV.7 and Figure IV.8], the values of both magnetic flux density and magnetic field are quite low, compared to the values observed within the top lamination [see (a) in Figure IV.7 and Figure IV.8]. This confirms the decrease in the flux measured made by the flexible planar coils 1, 2 and 3 inserted in between the laminations of the GOES stack (in chapter III section 3.5.1) as well as the given explanations to interpret the results of the flux measurements, mainly:

- The very low permeability of the GOES stack in the normal direction.
- The low magnetizing current value i.e., no saturation.

The flux density and magnetic field decrease as the distance of the laminations from the stack top surface (flux entry) increases.

On top of that, it can be observed that both the magnetic field and flux density levels inside the stack are more important when the GOES lamination stack is positioned towards α = 90° [see (b), (c) and (d) in Figure IV.8]. This behavior coincides with the observations made during the experimental magnetic flux measurements (in chapter III section 3.5.1) and with the expected theoretical behavior for a GOES lamination.

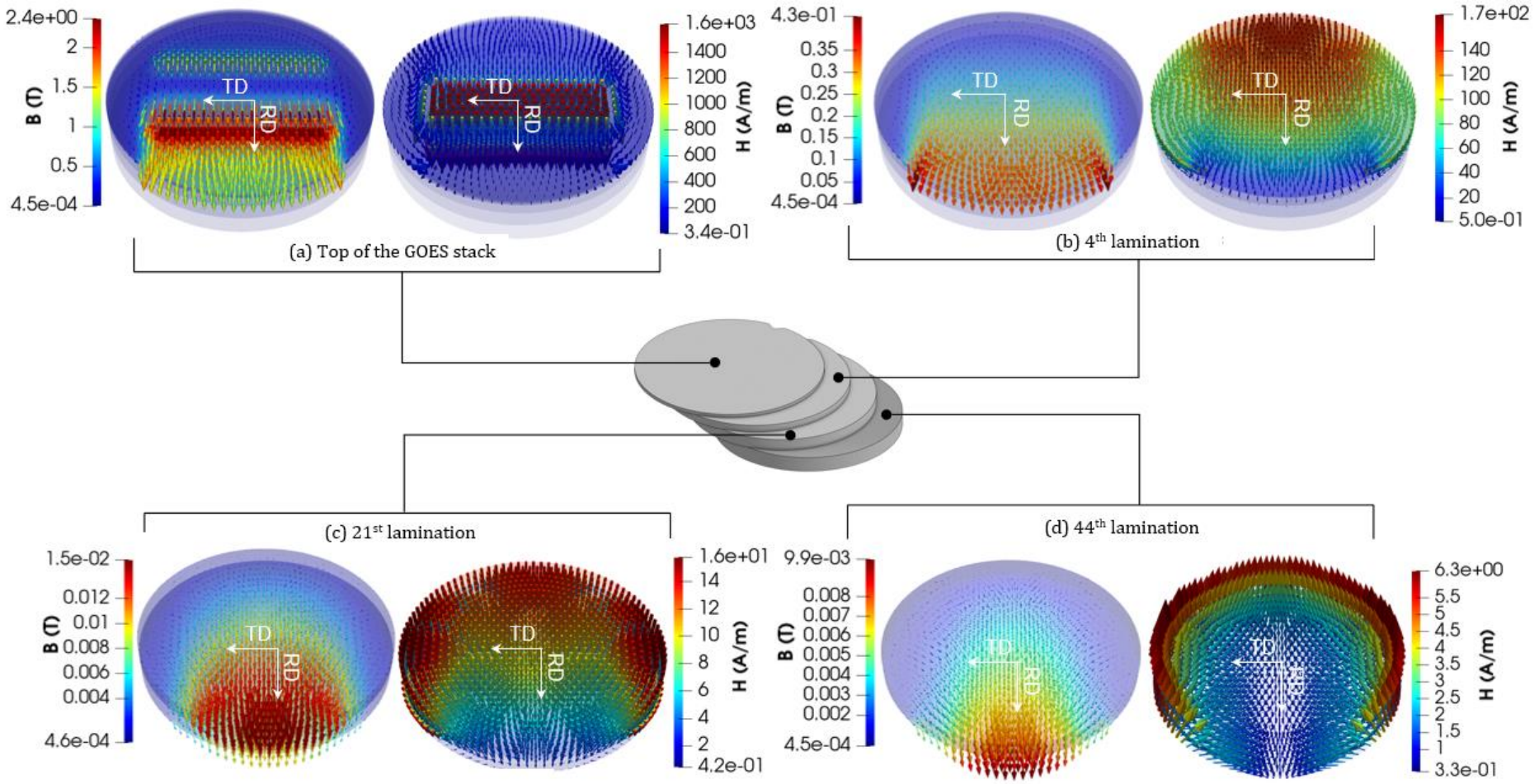


Figure IV.7. Magnetostatic simulation of the evolution of **H** (A/m) and **B** (T) field distributions within the GOES lamination stack for the 0° in-plane orientation and a magnetizing current of I = 0.43 A r.m.s.

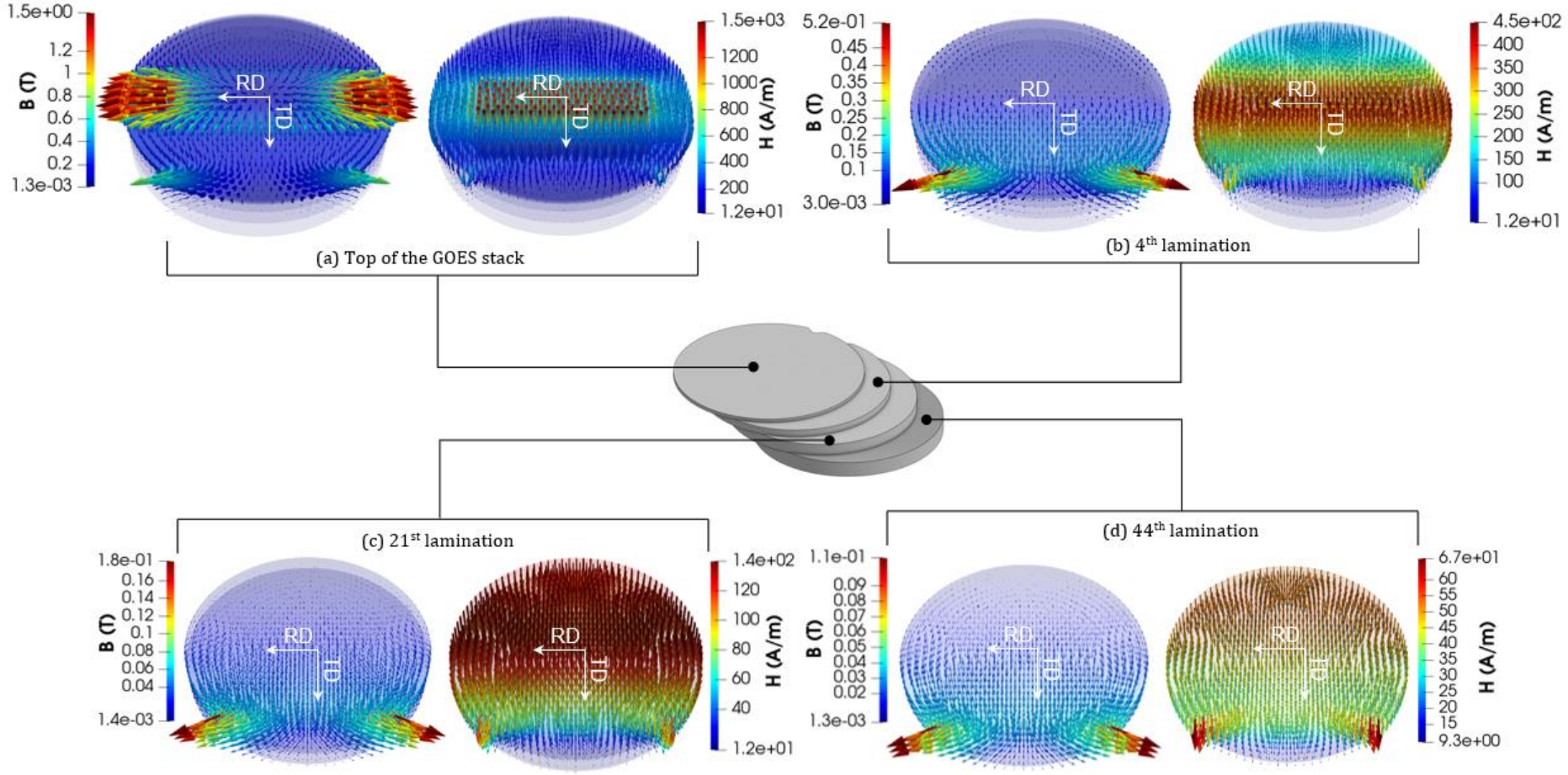


Figure IV.8. Magnetostatic simulation of the evolution of **H** (A/m) and **B** (T) field distributions within the GOES lamination stack for the 90° in-plane orientation and a magnetizing current of I = 0.43 A r.m.s.

### 2.1.2. Magnetodynamic simulation

Up until this point, only the magnetostatic field distribution maps have been presented. However, taking into account the effect of eddy currents is fundamental for the representation of the demonstrator, and this is only possible with the magnetodynamic simulations.

A similar effect of the anisotropy has been observed in the magnetodynamic simulations. The same behavior patterns have been observed in the GOES lamination stack according to the considered in-plane orientation (angle α). Nevertheless, in the magnetodynamic case, the magnetic flux density levels are higher than in the magnetostatic case at the surface of the stack (see Figure IV.9), while the magnetic field strengths are lower (see Figure IV.10).

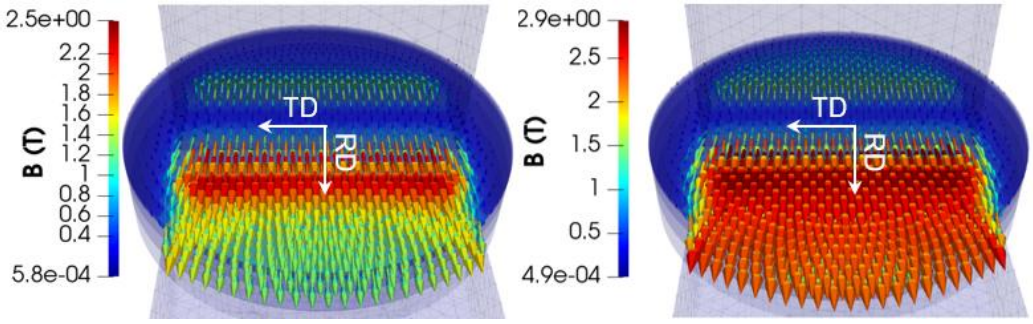


*(a) Magnetostatic* *(b) Magnetodynamic*

Figure IV.9. Flux density distribution maps from the magnetodynamic linear simulation for the 0° in-plane orientation and a magnetizing current of I = 0.43 A r.m.s.

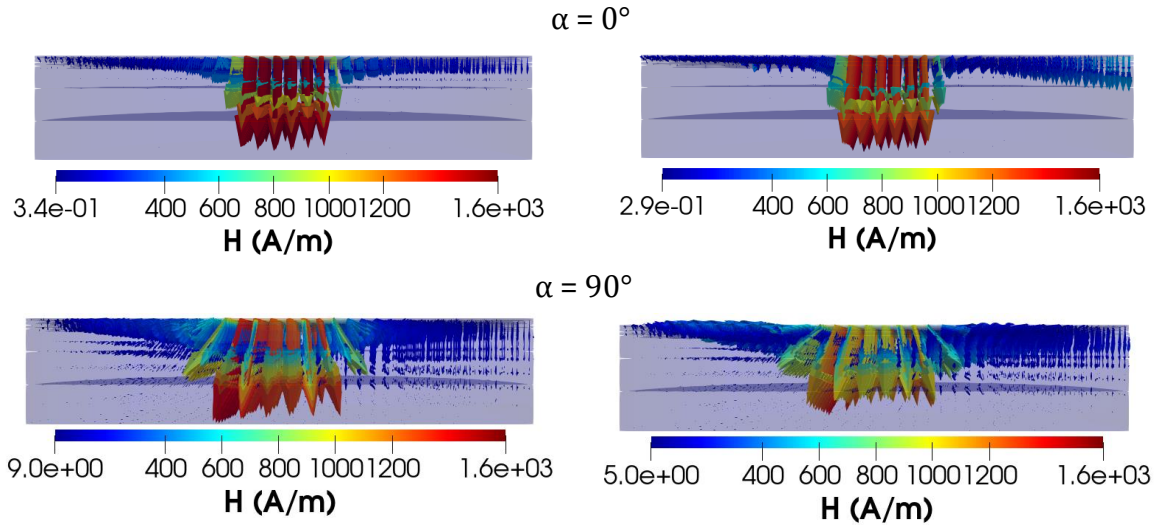


*(a) Magnetostatic* *(b) Magnetodynamic*

Figure IV.10. Cross-section view of the GOES stack: comparison of the magnetic field distribution maps from magnetostatic and magnetodynamic formulations for a magnetizing current of I = 0.43 A r.m.s.

Given the fact that both simulations have been made with the same mesh, the same excitation current and the same configuration of the airgap, the differences in the field distributions are due to the effect of eddy currents represented in the magnetodynamic case. In fact, the eddy currents induced by the flux entry into the stack surface oppose the flux penetration i.e., limit its depth and imped the flux to penetrate into the lower laminations of the stack. The flux is thus confined within a reduced section (due to the skin effect) increasing the magnetic flux density levels (stack surface severely saturated) and reducing the intensity of the magnetic field in the GOES lamination stack.

To better visualize these phenomena, the distributions of the classical eddy currents losses within the surface of the GOES stack are shown for 0° and 90° in-plane orientations in Figure IV.11.

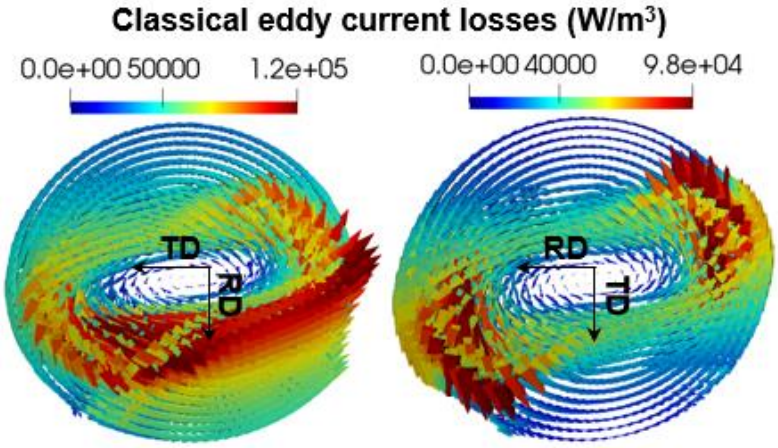


Figure IV.11. Distribution of the classical eddy current losses for 0° and 90° in-plane orientations and a magnetizing current of I = 0.43 A r.m.s.

It is clear that the anisotropy of the GOES laminations influence the distribution of eddy currents within the stack further increasing the skin effect and classical losses along RD. This effect also has repercussions in terms of the **H** (A/m) and **B** (T) field distributions within the inside the GOES stack as illustrated in Figure IV.12and Figure IV.13.

The figures show that the magnetic field vectors concentrate mostly around the edge area of the laminations (inside the stack) increasing the magnetic field levels due to the skin effect. This behavior is particularly evident for the 0° in-plane orientation of the stack [see (b), (c) and (d) in Figure IV.12].

Also, there is a clear difference in the field distribution maps between the 0° and 90° in-plane orientations. The magnetic field and flux density are higher inside the stack at the 90° in plane orientation [see (b), (c) and (d) in Figure IV.12 and Figure IV.13], matching the observations made during the magnetostatic simulations.

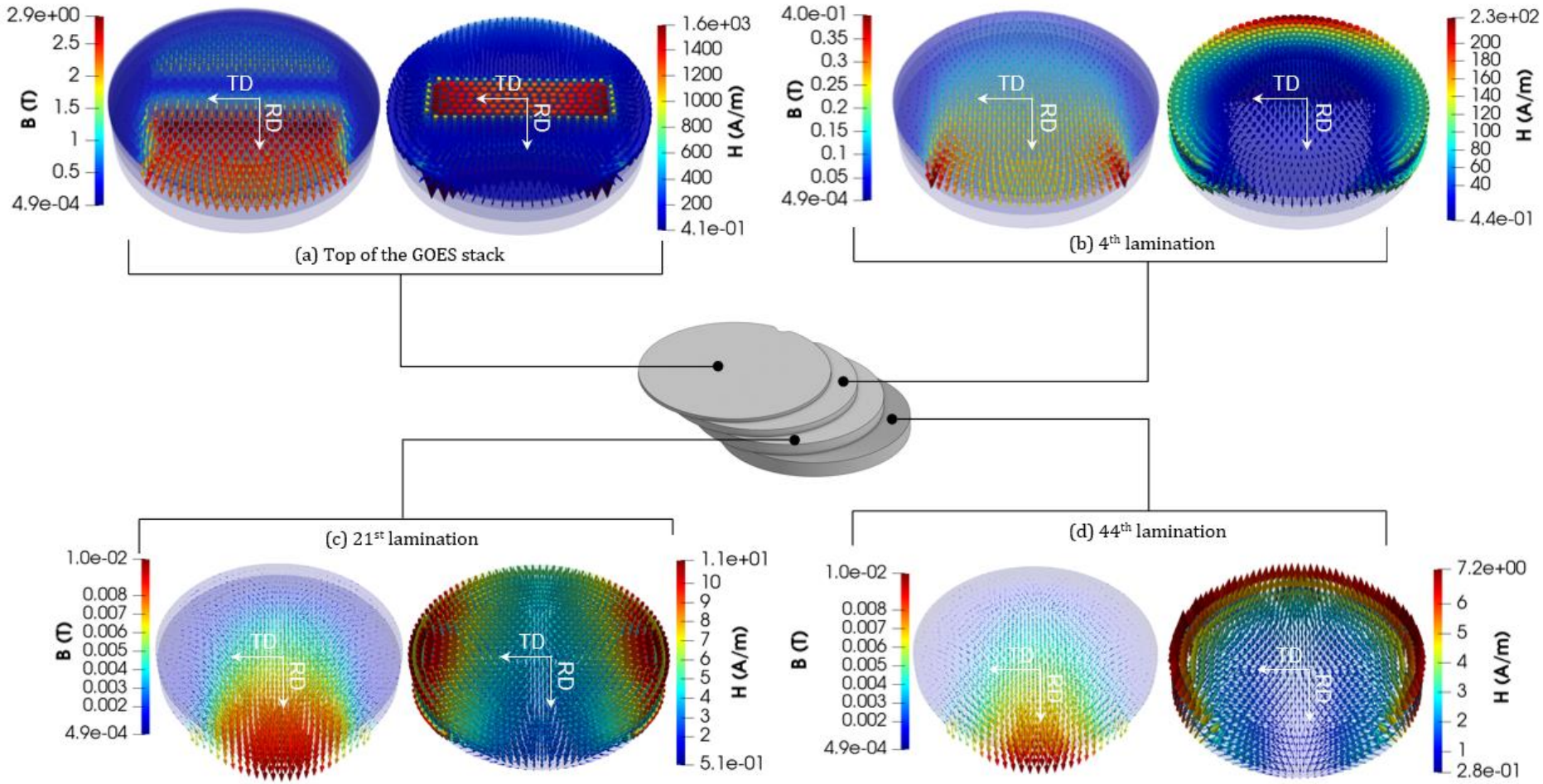


Figure IV.12. Magnetodynamic simulation of the evolution of the **H** (A/m) and **B** (T) field distributions within the GOES lamination stack for the 0° in-plane orientation and a magnetizing current of I = 0.43 A r.m.s.

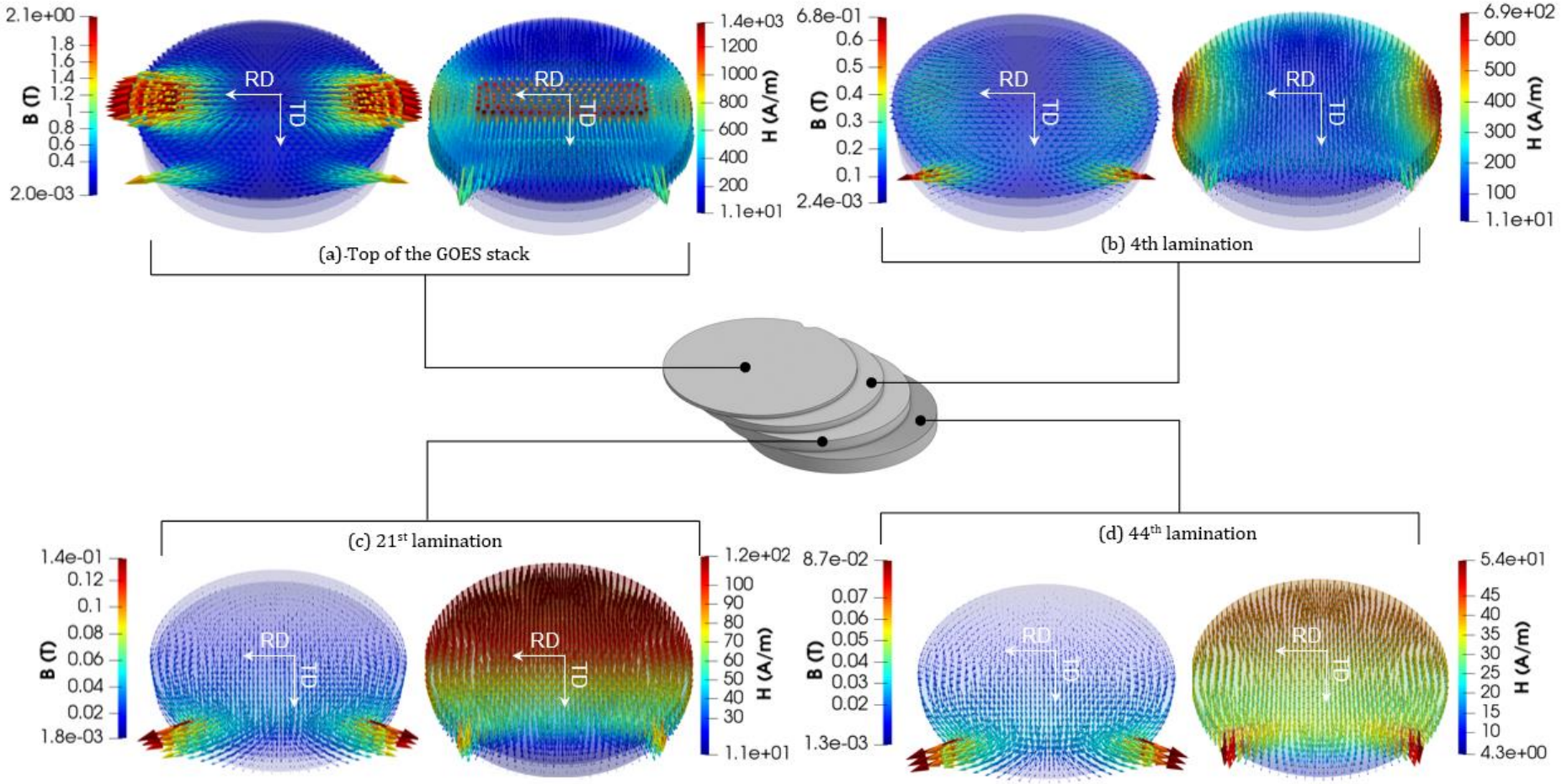


Figure IV.13. Magnetodynamic simulation of the evolution of the **H** (A/m) and **B** (T) field distributions within the GOES lamination for the 90° in-plane orientation and a magnetizing current of I = 0.43 A r.m.s.

### 2.1.3. Simulation vs measurements

The magnetic flux peak values obtained from the search coils in the FEM simulation environment have been compared with the corresponding measured magnetic flux values (see Chapter III). The evolution of the magnetic flux peak values inside the GOES lamination stack is represented in the following figures:

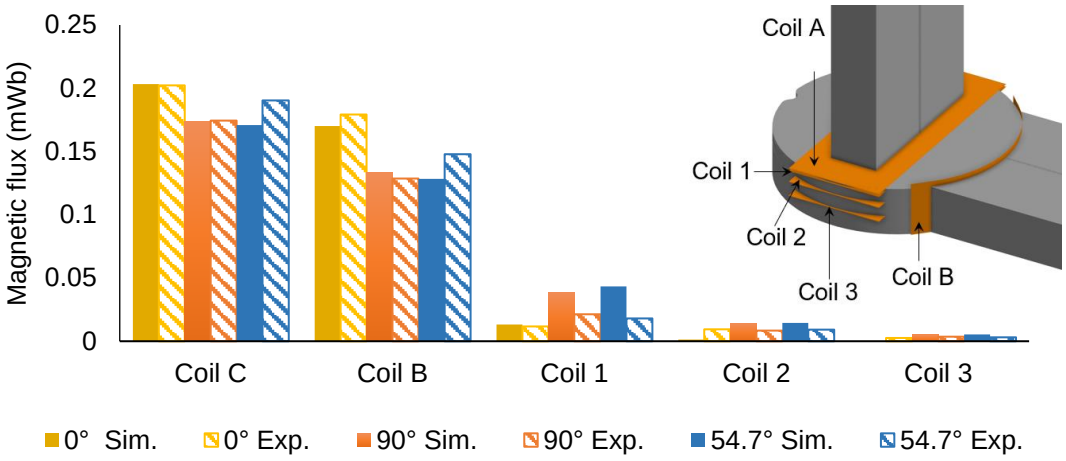


Figure IV.14. Comparison of the experimental and simulated (in magnetostatic) magnetic flux peak values for an excitation current I = 0.43 A r.m.s.

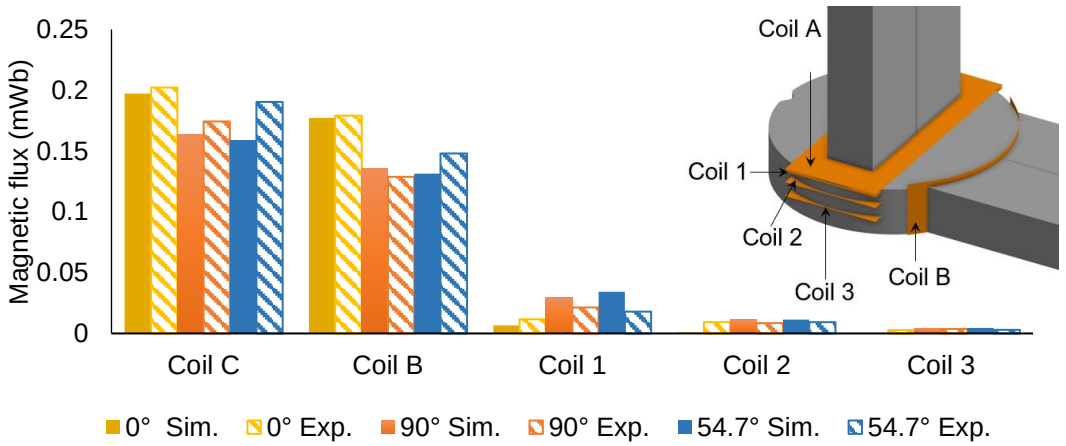


Figure IV.15. Comparison of the experimental and simulated (in magnetodynamic) magnetic flux peak values for an excitation current I = 0.43 A r.m.s.

On the whole, the simulated and measured magnetic fluxes seem to follow the same proportions. However, there are some discrepancies between the latter. Both magnetostatic and magnetodynamic simulations underestimate the flux outside the stack (measured by Coil C and Coil B) while inside the latter, they overestimate them (coil 1, 2 and 3). Nonetheless, considering the simulation hypotheses (linearity of the GOES, same permeability tensors), it can be concluded that the global behavior of the magnetic flux is similar to what was observed experimentally.

On the other hand, the differences between the magnetic flux values in magnetostatic and magnetodynamic formulations are also noticeable. As already discussed, the magnetic flux is lower in the magnetodynamic case due to the effects of eddy currents.

Furthermore, the magnetic flux measured outside the stack by the coil C has a similar magnitude as that of measured by coil B. Taking into account the strong decrease in magnetic flux values acquired by the coils inside the stack (Coils 1, 2 and 3), is possible to assume that most of the magnetic flux circulates through the first lamination of the stack as previously observed through the simulations above.

## 2.2. Iron loss computation

As detailed in section 5.2. of Chapter II, the iron losses have been calculated in post processing thanks to the anisotropic iron loss model implemented in the FEM environment. The losses for the considered operating point (I = 0.43 A r.ms., 5 V r.m.s) were too weak to be measured properly by the power analyzer of the power supply. So, the total active power absorbed has been estimated from the total apparent power $S_{tot}$ and the power factor $F_p$, Then, following the power balance procedure presented in section 3.4 of Chapter III, the iron losses associated to the GOES lamination stack are determined. The obtained losses are inferior to a watt (see Table IV.2).

Table IV.2. Stack iron losses measured for the considered operating point (I = 0.43 A r.ms., 5V r.m.s)

| **In-plane orientation of the stack (angle α)** | **Measured iron losses (W)** |
|---|---|
| 0° | 0.22 |
| 54.7° | 0.27 |
| 90° | 0.29 |

The choice of this low voltage level in the linear case FEM simulation is constrained by the unrealistic flux density values that could be obtained for higher voltage levels making inconceivable any comparison with measured losses.

These total losses contain the quasi-static, excess and eddy current losses within the GOES lamination stack. However, with such low loss value, a comparison of the estimated and computed iron loss values **is not relevant**. Therefore, this section focuses on general analysis of the losses, considering the results of the magnetodynamic simulation and taking into account the eddy current losses in the GOES stack.

— Application of the anisotropic iron loss model

The iron loss model implemented in code_Carmel has been applied to post-process the iron losses. For recall, this model allows to calculate the three iron loss components: the quasi-static losses the excess losses as well as the classical losses from the analytical equation only valid for excitations in the plane of the laminations.

The numerical model being able to provide the classical eddy current losses, at least within the first laminations that have been discretized and modeled with their electrical conductivity, the classical loss part from the anisotropic iron loss model has not been considered, it has been replaced by the FEM eddy current losses. Thus, to get the total iron losses in the GOES stack, the considered components are: the quasi-static and excess losses calculated by the anisotropic iron loss model from the in-plane magnetic flux density as well as the FEM classical eddy currents.

Considering that the applied magnetic field is along the mean geometric path length of the device, the value of the angle θ required for the iron loss model corresponds to the angular in-plane orientation of the GOES lamination stack i.e., $\alpha = \theta$.

The quasi-static and excess losses computed by the anisotropic iron loss model (in the plane of the laminations) for a magnetizing current of I = 0.43 A r.m.s (magnetodynamic linear simulation) can be observed in Figure IV.16 for the main in-plane orientations of the stack.

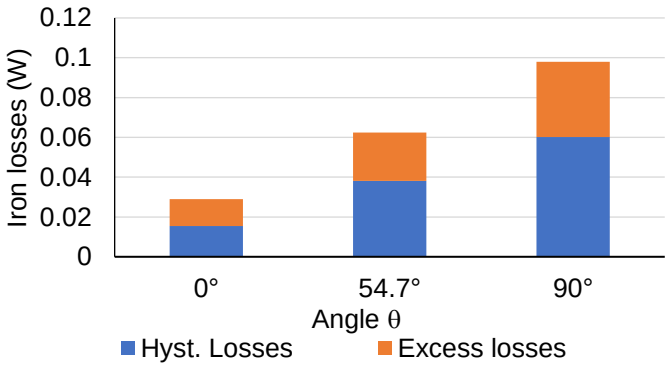


Figure IV.16. Hysteresis and excess losses calculated by the anisotropic iron loss model (in the plane of the laminations) for a magnetizing current I = 0.43 A r.m.s (magnetodynamic linear simulation).

The highest losses are obtained for the 90° in-plane orientation, which coincides with the expected behavior of the GOES at low induction levels (in the plane of the laminations) [61].

— FEM eddy current losses

Figure IV.17 shows the average eddy current losses computed for the conductive laminations of the GOES stack as function of the lamination position for 3 in-plane orientations.

The eddy current losses progressively decrease from the top surface of the GOES along the stack height.

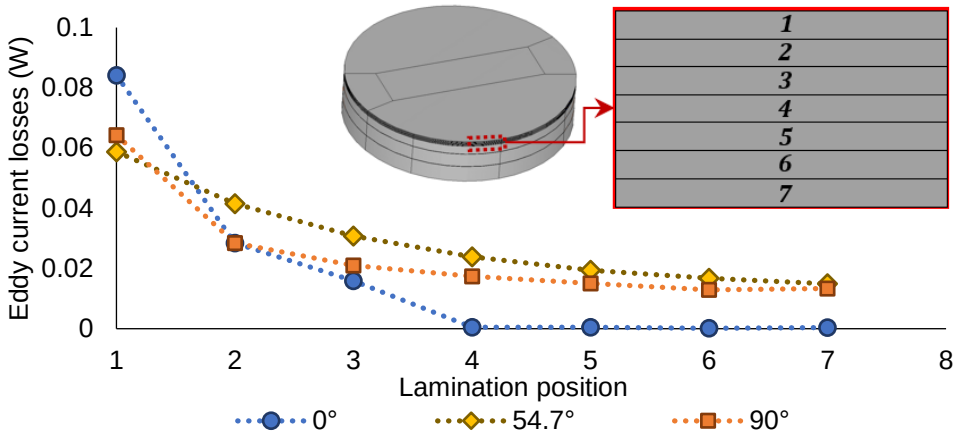


Figure IV.17. FEM eddy current losses for the first seven laminations as function of the position of the lamination in the stack for 3 in-plane orientations (α = 0°, 54.7° and 90°) and a magnetizing current of I = 0.43 A r.ms. (Magnetodynamic linear simulation).

Nevertheless, a significant difference can be observed between the three in-plane orientations of the stack. For the 0° in-plane orientation (α = 0°), the losses are mainly observed within the first three laminations of the stack, while for the other in-plane orientations (α = 0° and α = 90°), even seven laminations have been modeled independently, the modeling shall be refined to better represent the complete behavior.

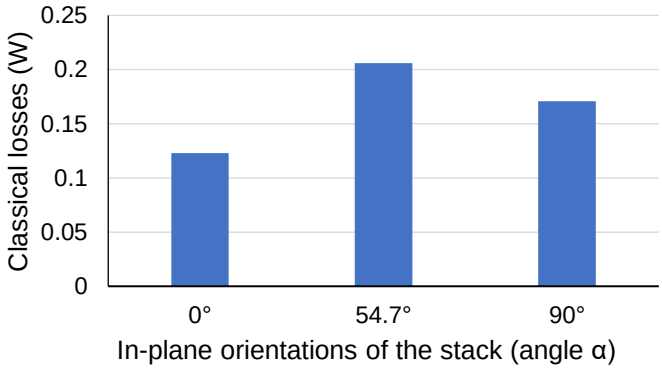


Figure IV.18. FEM classical eddy current losses of the stack for three in-plane orientations and a magnetizing current I = 0.43 A r.m.s (magnetodynamic linear simulation).

The stack total classical losses are presented in Figure IV.18 for three in-plane orientations of the stack to analyze the global tendency.

The most important eddy current losses are obtained the 54.7° in-plane orientation of the stack. The difference regarding the two other in-plane orientations of the stack can be attributed to the fact that for the 54.7° in-plane orientation, the magnetic flux penetrates further down into the stack height, increasing the magnetic flux density in a larger area and thus the classical losses.

— Computed losses vs measured losses

Lastly, even if the comparison is not relevant in view of the very low values resulting from the very low imposed current, the computed total iron losses (sum of the quasi-static, excess and FEM classical eddy current losses) are given in Figure IV.19 and compared with the experimental losses of the stack for a magnetizing current of 0.43 A r.m.s.

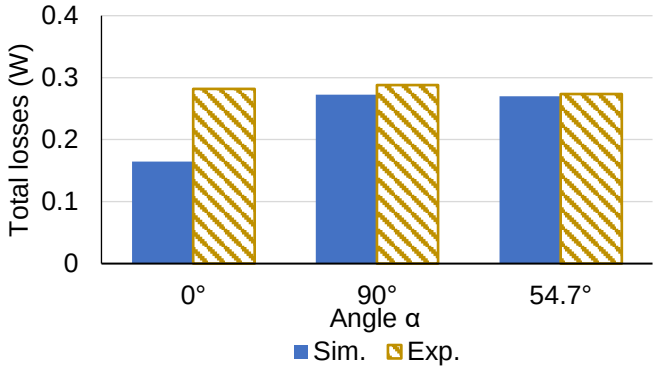


Figure IV.19. Computed total iron losses (linear anisotropic magnetodynamic simulation) vs experimental losses in the GOES lamination stack for a magnetizing current I = 0.43 A r.m.s.

Globally, the values of the computed iron losses follow the same proportions than the experimental ones (section 3.5.2 in Chapter III). The classical losses are the most important part of the total losses, and the total iron losses depend on the in-plane orientation (angle α) of the RD of the GE0S stack.

Again, given the low values of the losses obtained for the set low voltage, this comparison is not relevant. Non-linear simulations are achieved in the following section under a higher imposed current to evaluate the stack losses.

# 3. Non-linear case

Having analyzed the effect of anisotropy within the GOES lamination stack, non-linear simulations have been performed to observe the effect of the saturation. As mentioned previously, the non-linear scheme of code_Carmel does not allow to solve the strongly anisotropic non-linear case, these simulations therefore do not account for the anisotropy. However, in the specific case of the GOES lamination stack with the in-plane orientations α = 0° and α = 90°, the resulting magnetic field is globally along the applied magnetic field direction. Under this hypothesis, a scalar non-linear B-H law can be employed to have a qualitative estimation of the influence of the saturation. The simulations have been carried out using the non-linear Marrocco equation, at a current level of about I = 2.06 A r.m.s corresponding to a flux density of 0.6 T within the magnetizing circuit. For this study, both magnetostatic and magnetodynamic formulations have been used with two different behavior laws (RD and TD laws), based on the RD and TD experimental data. The simulations have been achieved at 50 Hz.

## 3.1. Eddy currents and saturation effect

The results from the non-linear simulations are illustrated in Figure IV.20, and Figure IV.21 for the 0° in-plane orientation of the stack. As the GOES is isotropic, the flux density and magnetic field vectors are uniformly distributed throughout the surface of the laminations.

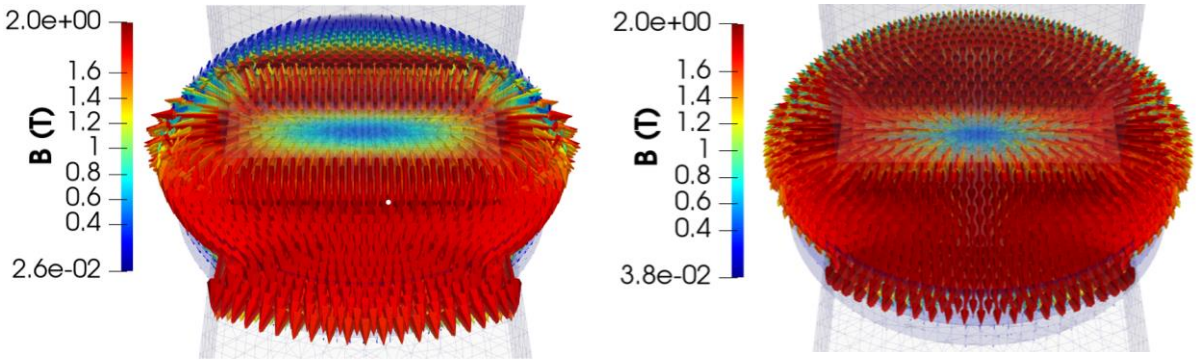


*(a) Magnetostatic* *(b) Magnetodynamic*

Figure IV.20. Flux density distribution maps from magnetostatic and magnetodynamic non-linear simulations for the 0° in-plane orientation and a magnetizing current I = 2.6 A r.m.s.

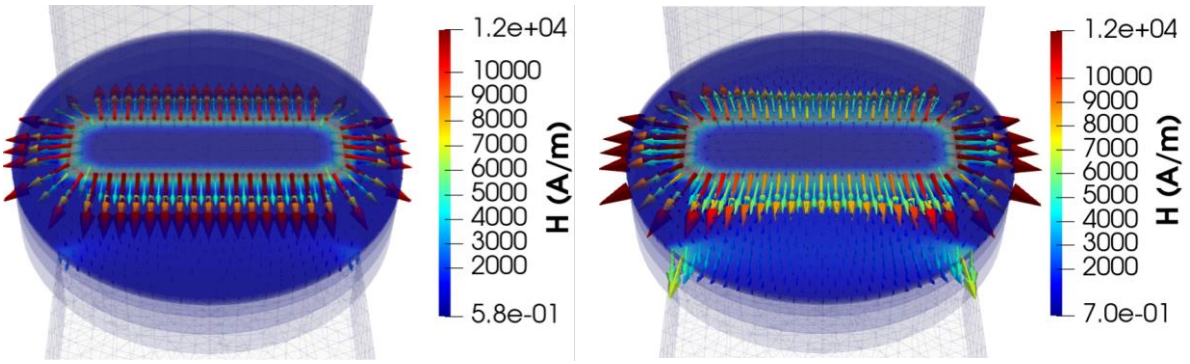


*(a) Magnetostatic* *(b) Magnetodynamic*

Figure IV.21. Magnetic field distribution maps from magnetostatic and magnetodynamic non-linear simulations for the 0° in-plane orientation and a magnetizing current I = 2.6 A r.m.s.

The top laminations of the stack are strongly saturated in both magnetostatic and magnetodynamic formulations. In the magnetodynamic case, the effect of eddy currents is visible. The skin effect leads to a higher magnetic flux density at the surface of the first lamination compared to the magnetostatic case.

The effect of eddy current is also observed on the magnetic field distribution maps. The magnetic field vectors escape from the center of the GOES lamination stack into the inner laminations along the regions near the edges of the magnetizing circuit leg, reaching important magnetic field levels in the magnetostatic case against lower levels in the magnetodynamic one (see Figure IV.21).

Lastly, the evolution of the **H** (A/m) and **B** (T) field distributions inside the GOES lamination stack are shown in Figure IV.22 and Figure IV.23. Both 0° and 90° field distribution maps from the magnetodynamic non-linear simulation are presented.

As in the previous simulations, the magnetic flux density is mostly concentrated within the first laminations of the stack. Nevertheless, this time, because of the higher imposed current and the non-linearity, the high saturation of the first laminations leads the magnetic flux to penetrate further within the GOES lamination stack and reach lower laminations than in the previous linear case. This results in high magnetic field and flux density values within the top laminations of the stack (see (a) and (b) in Figure IV.22 and Figure IV.23). On the other hand, in the laminations positioned lower (see (c) and (d)), the magnetic field and flux density values are much lower and homogeneous.

It can be notice that the flux density levels have changed according to the considered behavior law (along 0° or 90°), following the behavior from the previous simulations and matching the experimental observations in section 3.5 of Chapter III.

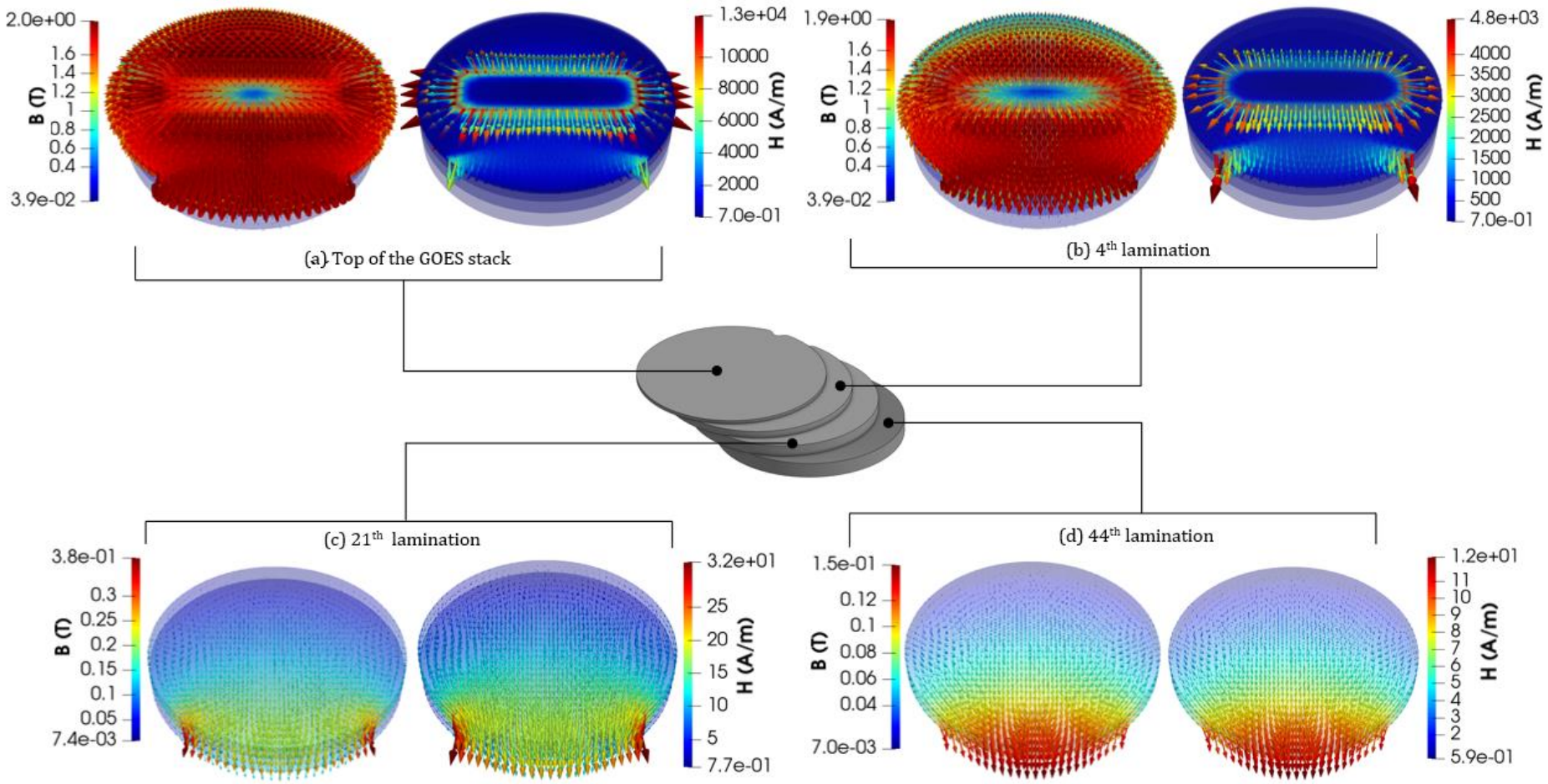


Figure IV.22. Magnetodynamic non-linear simulation of the **H** (A/m) and **B** (T) field distributions within the GOES lamination for the 0° in-plane orientation and a magnetizing current I = 2.6 A r.m.s.

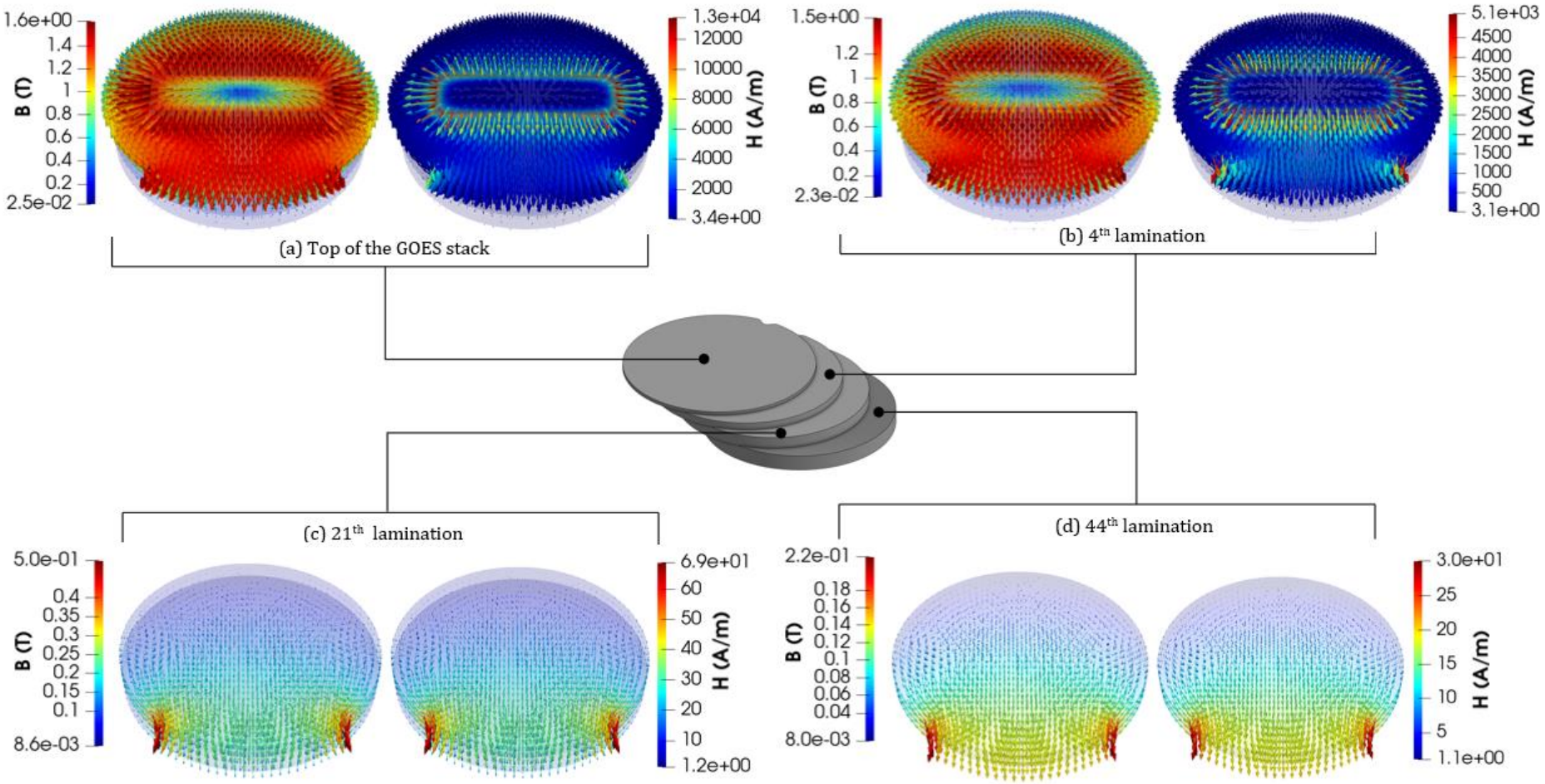


Figure IV.23. Magnetodynamic non-linear simulation of the of **H** (A/m) and **B** (T) field distributions within the GOES lamination stack oriented for the 90° in-plane orientation and a magnetizing current of I = 2.6 A r.m.s.

## — Simulation vs measurements

As for the linear case, the flux peak values obtained from the different FEM search coils have been compared with the corresponding measured flux values for a magnetizing current of 2.6 A r.m.s. The results are presented in Figure IV.24.

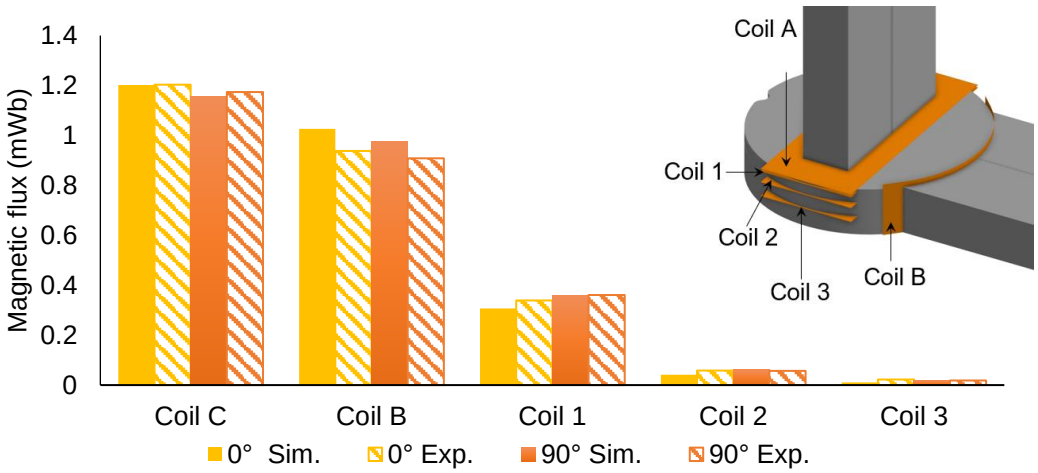


Figure IV.24. Comparison of the experimental and simulated (in magnetodynamic) fluxes peak values measured for an excitation current I = 2.6 A r.m.s.

Globally, the computed flux values from FEM are very close to the experimental ones. The trends observed in the previous simulations are maintained.

## — About the magnetic flux waveforms

Experimentally, a deformation of the magnetic flux waveforms measured by the planar coil 1 has been observed for high imposed voltages (see Chapter III, section 3.5). Very similar distortions of the flux waveform are observed in the non-linear magnetodynamic simulations. A comparison between the simulated and experimental flux waveforms is presented in Figure IV.25 for a magnetizing current of 2.6 A r.m.s (around 30 V r.ms) and for the 0° in-plane orientation. We can observe that the FEM simulation slightly overestimates the flux.

A similar distortion (but less pronounced) has been also observed in the non-linear magnetostatic simulation where the eddy current effect is not considered (see Figure IV.26). Considering that the distortions have been only observed for the non-linear simulations, the distortion observed in the non-linear magnetodynamic simulation (Figure IV.25) could be due to the combined effect of saturation of GOES laminations together with the development of strong eddy currents within the first laminations of the stack.

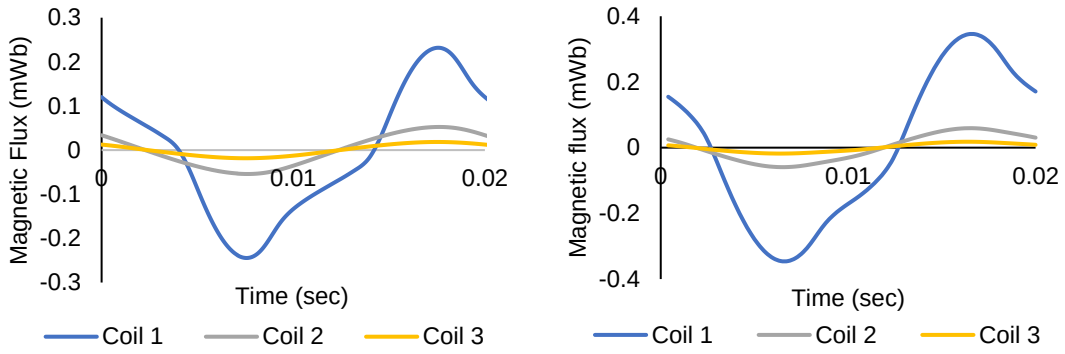


(a) Measurements (b) FEM simulation

Figure IV.25. Comparison between the experimental and simulated (in magnetodynamic) magnetic flux waveforms inside the GOES lamination stack for a magnetizing current I = 2.6 A r.m.s..

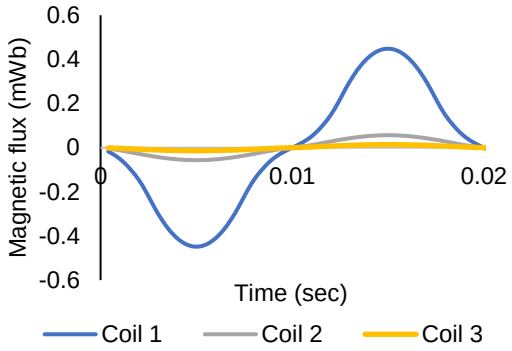


Figure IV.26. Magnetic flux waveforms observed inside the GOES lamination stack for a magnetizing current I = 2.6 A r.m.s (non-linear magnetostatic simulation).

## 3.2. Iron loss computation

### — Application of the anisotropic Iron loss model

As in the previous case, the anisotropic iron loss model implemented in code_Carmel has been applied in post-processing to calculate the hysteresis (quasi-static) and excess losses within the GOES lamination stack. The results are synthetized in Figure IV.27.

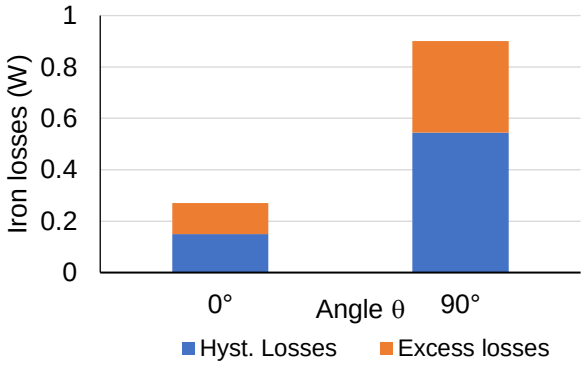

Figure IV.27. Hysteresis and excess loss parts calculated by the anisotropic iron loss model in the plane of the laminations for a magnetizing current I = 2.6 A r.m.s (magnetodynamic non-linear simulation).

Both loss contributions are very low, which is in accordance with the average flux inside the GOES stack and the mass of the latter in comparison with the specified iron losses of this GOES grade. On the other hand, and as expected, the iron losses are higher when the GOES stack is oriented with its TD along the main flux path.

— FEM eddy current losses

In Figure IV.28, the average classical eddy current losses for the first seven conductive laminations of the stack are presented as function of the lamination position for a magnetizing current of 2.6 A r.m.s. Let us recall that the first seven laminations have been individually modeled in FEM. The rest of the stack has been represented by solid volumes.

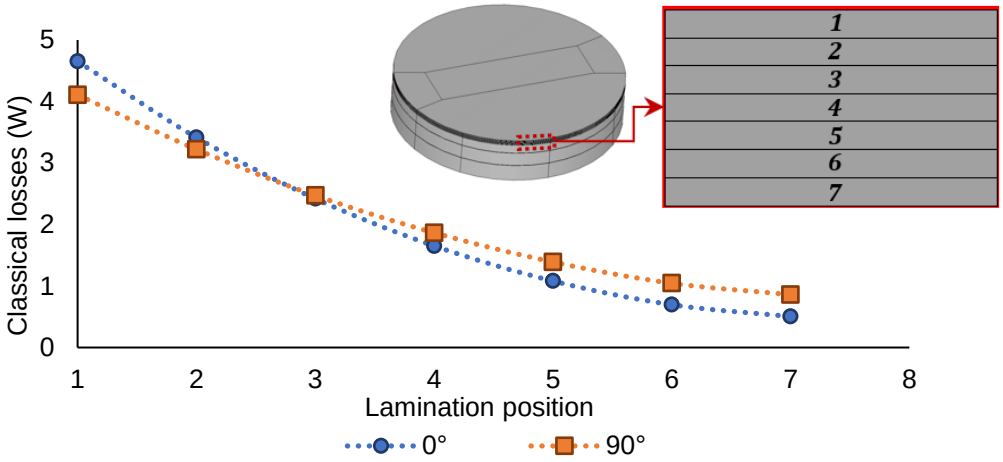


Figure IV.28. FEM classical eddy current losses for the first seven laminations as function of the lamination position in the stack for two in-plane orientations (0° and 90°) and a magnetizing current I = 2.6 A r.m.s (magnetodynamic non-linear simulation).

As expected, the classical eddy current losses are more important in the first laminations of the stack, as these laminations are directly submitted to the normal flux attack. The eddy current losses rapidly decrease for the lower laminations.

Figure IV.29 shows the total classical eddy current losses in the entire stack. They are a little bit lower for the 0° in-plane orientation of the GOES stack (RD behavior law in FEM) than for the 90° one (TD behavior law in FEM). This difference, however, is not significant (14.4 W in the RD against 14.9 W in the TD) but seems to indicate that a higher permeability results in lower eddy current losses.

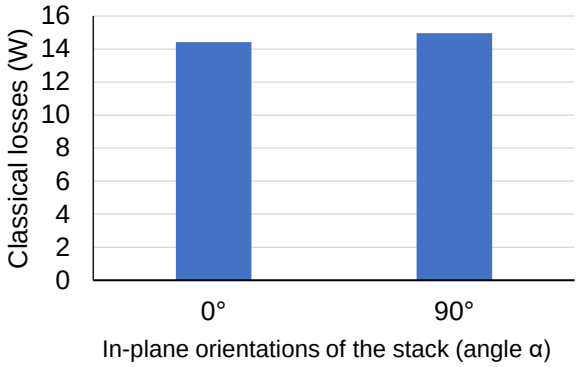


Figure IV.29. FEM classical eddy current losses of the stack for the in-plane orientations 0° and 90° and a magnetizing current I = 2.6 A r.m.s (magnetodynamic non-linear simulation).

— Total losses

At last, the computed total losses (sum of the hysteresis, excess and classical eddy current loss components) within the GOES lamination stack are given in Figure IV.30 and compared with the experimental losses.

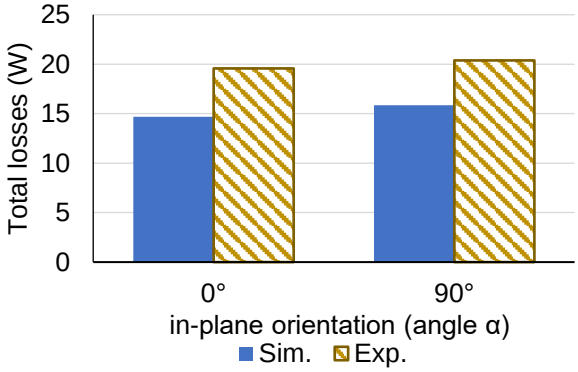


Figure IV.30. Computed total iron losses (non-linear isotropic magnetodynamic simulation) vs experimental losses in the GOES lamination stack for a magnetizing current I = 2.6 A r.m.s.

The result of the computed total losses is satisfactory regarding the experimental losses and the global tendencies remain quite similar. The discrepancies could be explained mainly by, on the one hand, the hypothesis related to the use of a scalar non-linear B-H curve and, on the other hand, by the consideration of the classical losses in only the first seven laminations; the contribution of the remaining 61 laminations of the stack having been estimated by applying the classical iron loss approach. However, their value is not very important, and in a way, their effect is neglected in the simulation. Finally, the main conclusion with such results is that the total losses associated to a flux penetrating into the plane surface of the GOES laminations are quasi totally due to classical eddy current losses. The second aspect is related to the way the magnetic flux penetrates in the stack before being totally in the lamination plane. In our specific case, only few laminations are involved in such process.

# 4. Synthesis

The numerical simulations of the demonstrator have been carried out in two steps. The first one is based on the hypothesis of a linear anisotropic behavior the GOES stack of interest. The obtained results in terms of magnetic flux distribution within the height of the stack and the associated iron losses are in good agreement with the experimental measurements. In the second step, non-linear behavior of the stack has been considered in order to analyze the effects of saturation. Even if the simulations were isotropic, the obtained results give consistent tendencies regarding the experiment. Finally, we have shown quantitively that the total losses are dominated by significant classical eddy current losses in the plane surface of the GOES lamination stack.

Finally, the main aspect to retain is that the orthogonal magnetic flux rapidly penetrates the lamination stack before being in the lamination plane. In our case we observed that less than 10 laminations were involved in this process. Although this behavior is more or less independent from the in-plane orientation, one can observe an expected tendency when comparing the 0° in-plane orientation (less losses) and 90° in-plane orientation (higher losses). All these observations made from the simulations have been observed experimentally.

# Conclusion

This PhD work dealt with the experimental and numerical study of the magnetic behavior of grain oriented electrical steels submitted to out of plane magnetic flux attacks. To that end, it was necessary to consider an accurate representation of the GOES material for the modelling of the end-region losses in high power turbo-generators.

To be able to represent the complex anisotropic behavior of the magnetic core at end-regions of turbo-generators, it was necessary to have reliable magnetic material models. Starting from the characterization, with the Epstein frame, of GOES laminations provided by EDF, their anisotropic magnetic properties were modelled and validated against measurements. First, the anisotropic behavior law, represented by a full permeability tensor, was modelled using an original approach combining the Enokizono *et al.* [68] and Fiorillo *et al.* [60] models. The proposed approach is well adapted when considering unidirectional magnetic characterizations, such as those provided by the Epstein frame. Second, the iron losses were determined, in post-processing of the FE analysis, by a performant model proposed by C. Appino *et al.* [61]. Both material models were implemented in the FE analysis and compared against measurements for academic examples: the Epstein frame that shows a quite homogeneous magnetic flux density distribution and a ring core exhibiting a strong inhomogeneous flux density. The Epstein frame results showed the improvement brought by the implemented models, especially regarding the proposed full permeability anisotropic tensor when compared to the conventional diagonal anisotropic tensor. At the opposite, the ring core example emphasized the limitations related to the ability of the numerical scheme implemented in code_Carmel to solve strongly non-linear and anisotropic problems.

The second aspect of the work was related to the design and fabrication of an experimental demonstrator able to represent complex magnetic flux trajectories within a stack of GOES laminations. Compared to the experimental devices found in the literature, the proposed demonstrator is able to account for both the angle of the magnetic flux attack with respect to the plane of the GOES stack and the orientation of the latter within the lamination plane. Two main configurations for the magnetic flux attack were considered: 90° and 120°. The measurements, made with search coils placed at different locations in the stack of interest, showed that the anisotropy influences both the distribution of the magnetic flux, i.e., the way the magnetic flux penetrates the stack, and the iron losses. Indeed, differences in flux and loss values could be observed between the configurations with the stack oriented at 0° and 90° with respect to the RD of the magnetizing circuit. However, the role of the in-plane anisotropy was not very significant when considering the strong eddy current losses that develop on the surface of the first

laminations. In addition, no major differences were found in the behavior of the GOES lamination stack as function of the magnetizing circuit leg inclination, at least for the considered angles (flux attack configurations 90° and 120°).

Finally, the last part of the work was dedicated to the 3D numerical modelling of the experimental demonstrator. The behavior law and iron loss models have been used to model the characteristics of the GOES lamination stack, including virtual search coils at the same locations as the experiment. Several simulations were carried out in magnetostatic and magnetodynamic formulations, using two main configurations: the linear anisotropic case and the non-linear isotropic case. These simulations were complementary to the experimental observations for the investigation of the GOES lamination stack. The global experimental tendencies were observed and more detailed analysis of the flux and losses distributions have been made. The main points are:

- Confirmation that the classical eddy current losses are the main component of the total losses within the GOES lamination stack.
- The orthogonal magnetic flux rapidly penetrates into the GOES lamination stack and is quasi-totally in the lamination plane after crossing the very first laminations of the GOES stack.
- The iron losses tend to increase slightly as function of the in-plane orientation: 0° in-plane orientation (less losses) and 90° in-plane orientation (higher losses).

Overall, the results from the numerical simulation are satisfactory in terms of tendencies when compared to the experimental measurements.

Finally, this work has contributed, to some extent, to the global end-regions loss problematic from the experimental and modelling point of view. It also constitutes a solid basis for future developments related to the FE modeling of devices involving grain-oriented materials with the software code_Carmel. Indeed, these electrical steels are present not only in turbo-generators but also in power transformers. These developments are intrinsically linked to the improvement of the non-linear scheme in code_Carmel in order to assure the numerical stability and convergence.

It would be interesting to carry out additional numerical simulations of the experimental demonstrator for different leg configurations (120° and 135°). Indeed, one expects the eddy current losses to decrease with an increasing angle. Different grain-oriented materials can also be studied in order to test the behavior of the models and to observe if the grade and thickness of the material influence the distribution of the magnetic flux and iron losses.

Once the non-linear anisotropic model is implemented in code_Carmel, the next natural step would be to perform a numerical simulation with the real geometry of the end-region

of a high-power turbo-generator and compare the computed losses with real measurements of a turbo-generator under different regimes of operation.

Finally, to further improve the numerical modelling of the end-region of high-power turbo-generators two additional numerical developments can be carried out.

The first one concerns the extension of the anisotropic behavior law and iron loss model treated in this thesis, to be used at higher induction levels. These models currently capable of representing the behavior of GOES up to around 1.2 T as the non-linear behavior of GOES changes at higher induction levels.

The second concern the development of a model for the homogenization of the stacked GOES laminations. Such a model would facilitate the modelling of electrical machines with multiple stacked GOES laminations possibly reducing the total number of elements and computation time.

# Appendix A

For recall the simplified electrical diagram for one phase of a synchronous machine with a non-salient pole rotor and a constant airgap is given by:

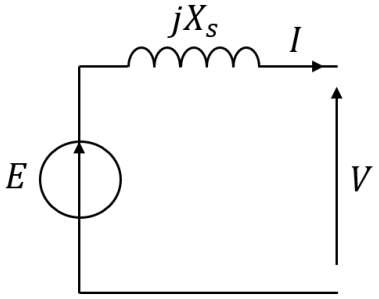


Figure A.1. Simplified diagram for one phase of a synchronous machine.

Where E is the excitation voltage, V is the voltage in the terminals of the generator, I is the armature current, $X_s$ is the synchronous reactance and the armature resistance is assumed to be negligible.

From this circuit we can derivate the expression $E = V + jX_sI$ and the corresponding phasor diagram in lagging operation (see Figure A.2).

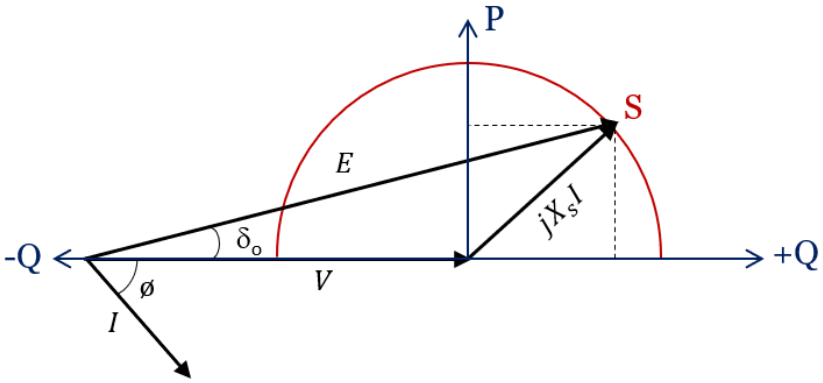


Figure A.2. One-phase diagram for a generator operation in lagging conditions.

Where $\delta_o$ Is the angle between the excitation and terminal voltage (E and V) and Ø Is the angle between the excitation voltage and the armature current (E and I) that serves to obtain the power factor (pf = cos Ø).

It is also possible to have the machine in leading operation, in which the current leads the voltage (see Figure A.3). In this case the machine will absorb reactive power from the grid and provide active power, and the equation will be $E = V - jX_sI$

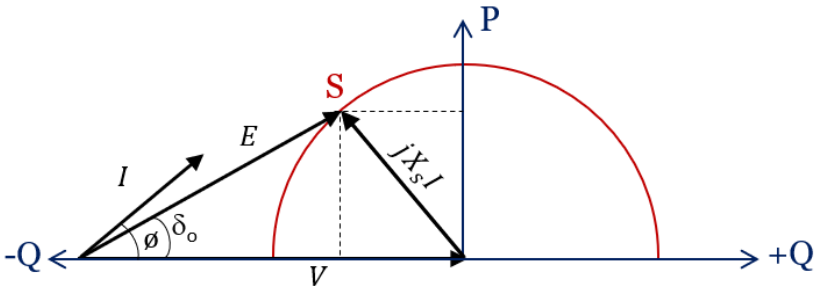


Figure A.3. One-phase diagram for a generator operation in leading conditions.

The operational limits of the synchronous machine provided in section 1.2.3 of chapter I are calculated taking into account the presented phasor diagrams, according to the nominal values of the machine, the insultation class and stability limits in the different regions.

# Appendix B

- Flux measurements in the 90° configuration

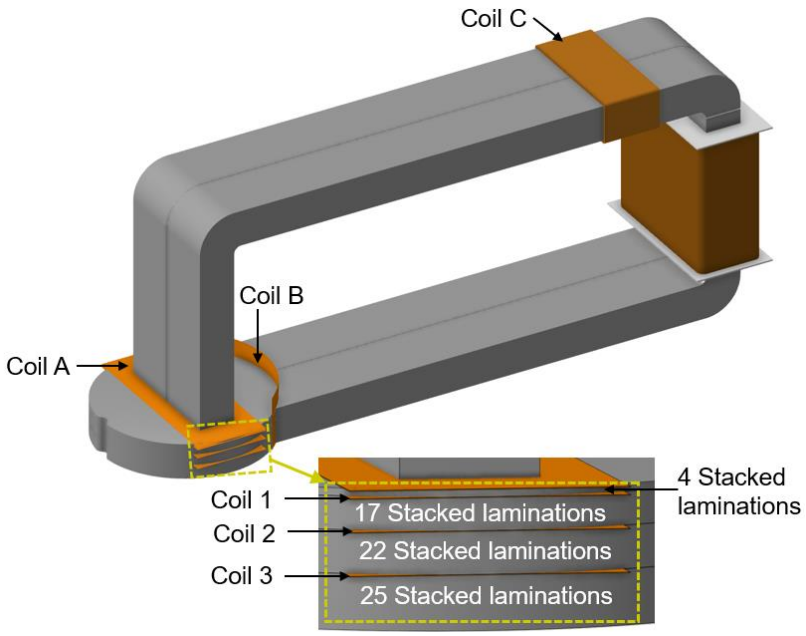


Figure B.1. Position of the coils in the 90° demonstrator

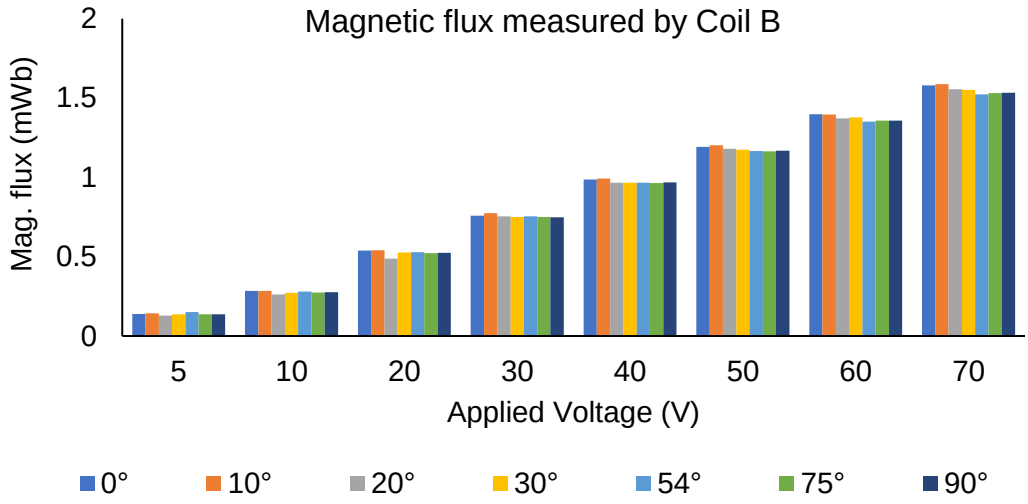


Figure B.2. Evolution of the magnetic flux measured by Coil B as function of the applied voltage and with different in-plane orientations of the stack in 90° configuration.

- Iron loss measurements in the 90° configuration

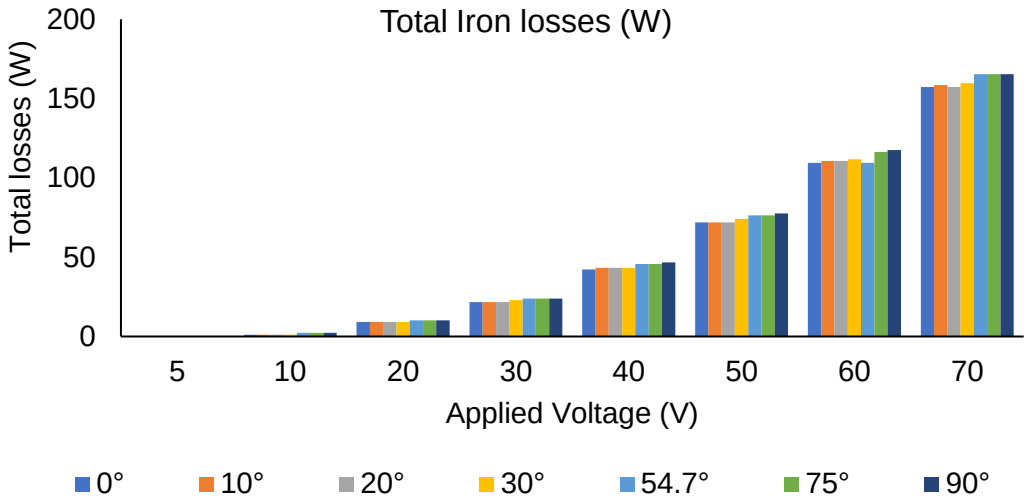


Figure B.3. Evolution of the Total active power absorbed by the demonstrator (total losses) measured as function of the applied voltage and with different in-plane orientations of the stack in 90° configuration.

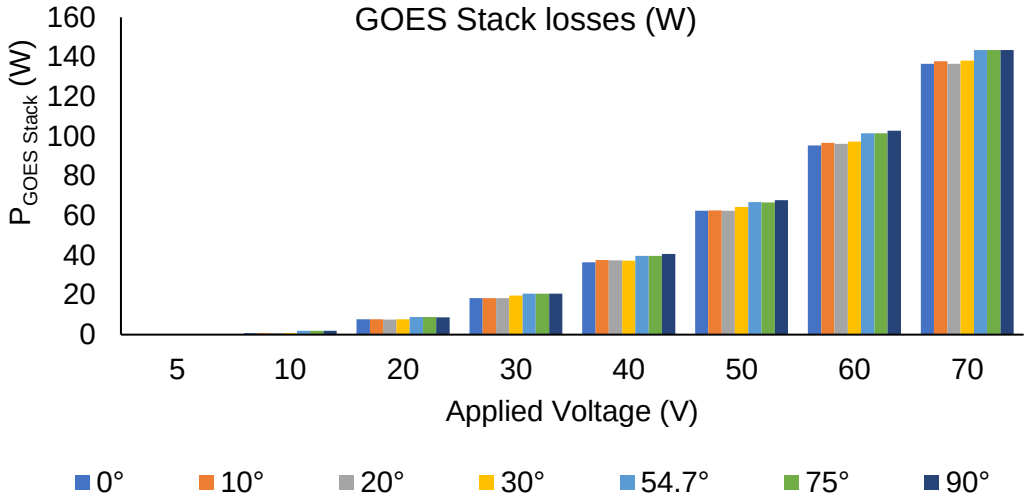


Figure B.4. Evolution of GOES stack losses measured as function of the applied voltage and with different in-plane orientations of the stack in 90° configuration.

# Appendix C

- Flux measurements in the 120° configuration

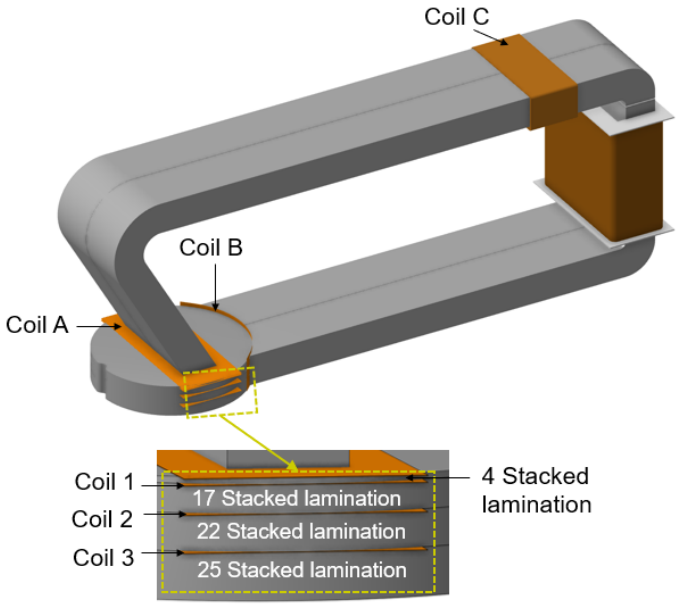


Figure C.1. Position of the coils in the 120° demonstrator.

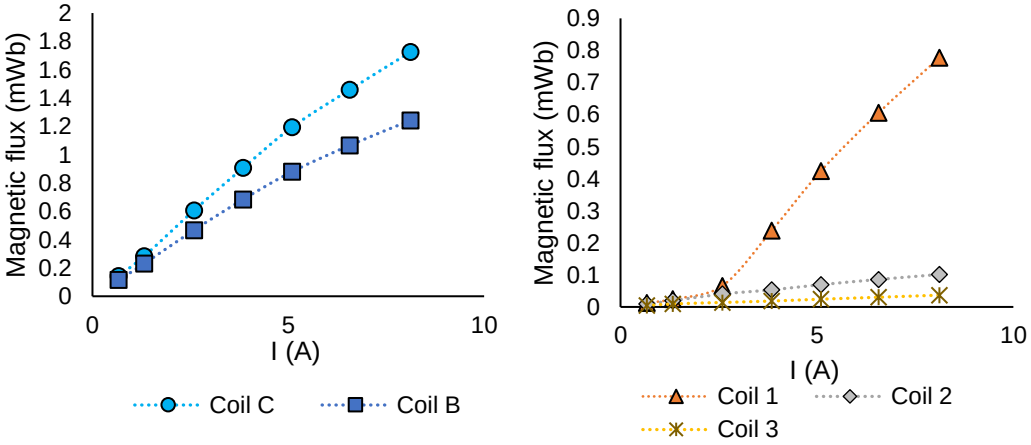


Figure C.2. Evolution of the magnetic flux as function of the position of the coils within the experimental demonstrator in 120° configuration.

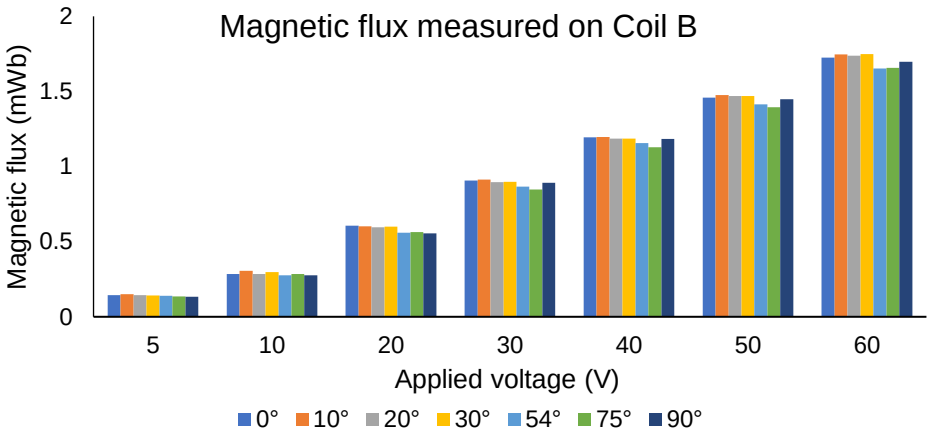


Figure C.3. Evolution of the magnetic flux measured by Coil B as function of the applied voltage and with different in-plane orientations of the stack in 120° configuration.

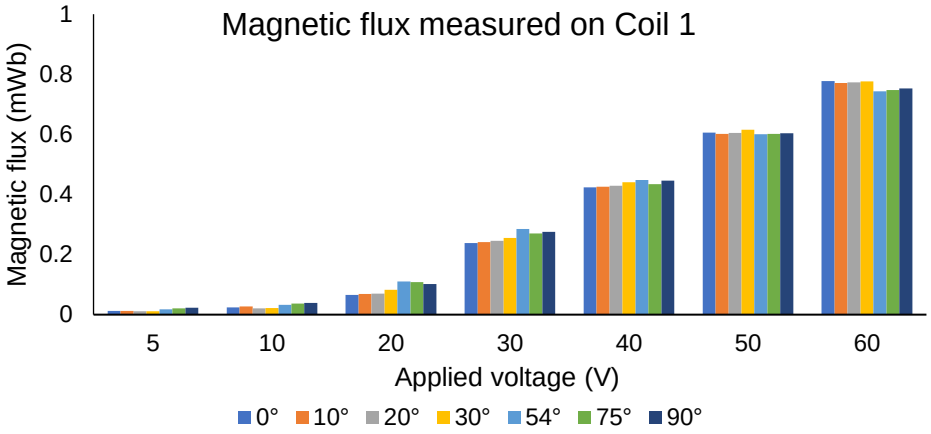


Figure C.4. Evolution of the magnetic flux measured by Coil 1 as function of the applied voltage and with different in-plane orientations of the stack in 120° configuration.

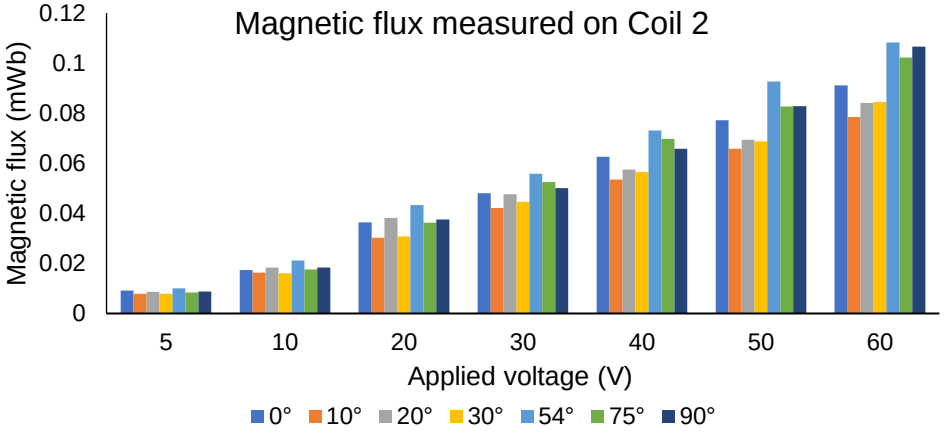


Figure C.5. Evolution of the magnetic flux measured by Coil 2 as function of the applied voltage and with different in-plane orientations of the stack in 120° configuration.

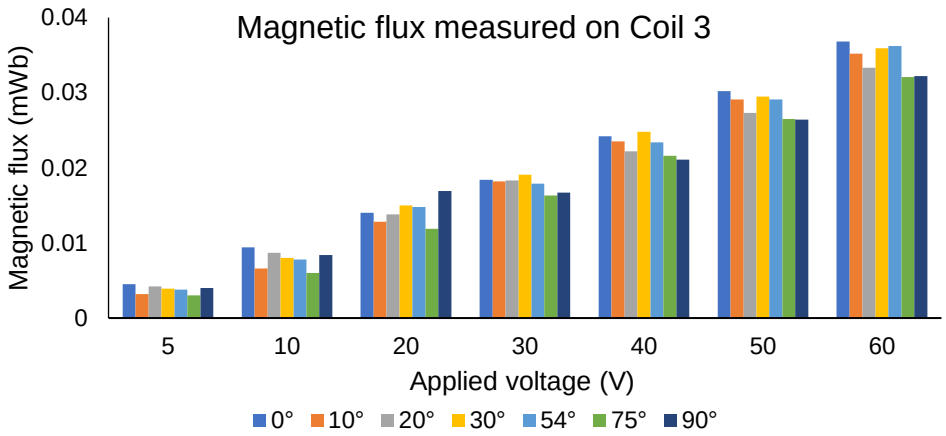


Figure C.6. Evolution of the magnetic flux measured by Coil 3 as function of the applied voltage and with different in-plane orientations of the stack in 120° configuration.

- Iron loss measurements in the 120° configuration

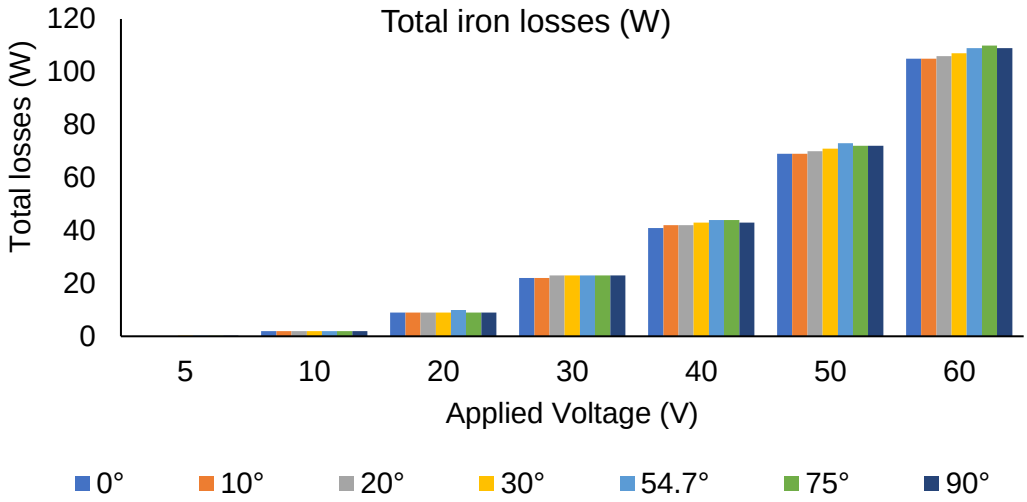


Figure C.7. Evolution of the Total active power absorbed by the demonstrator (total losses) measured as function of the applied voltage and with different in-plane orientations of the stack in 120° configuration.

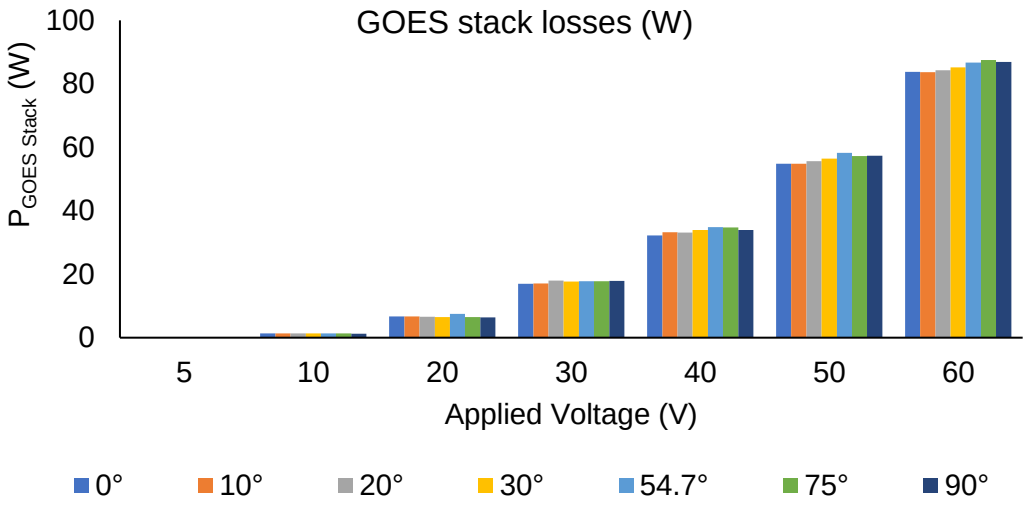


Figure C.8. Evolution of GOES stack losses measured as function of the applied voltage and with different in-plane orientations of the stack in 120° configuration.

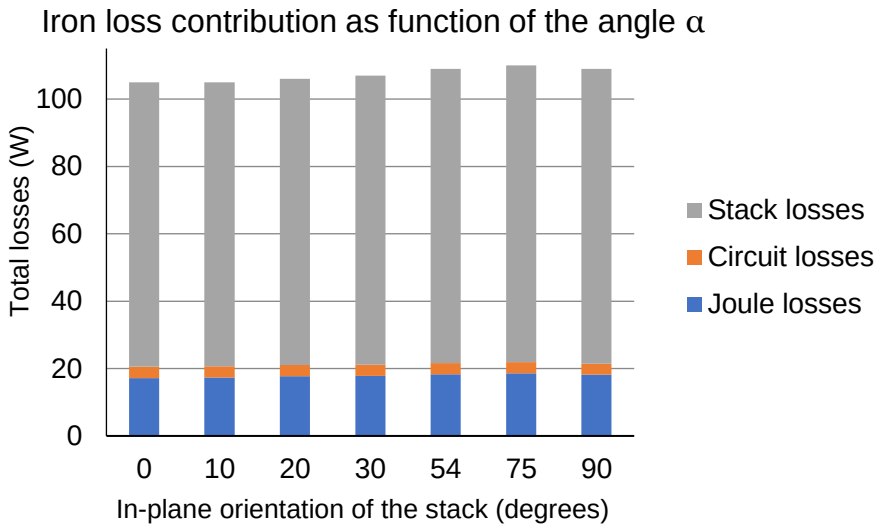


Figure C.9. Comparison of the stack losses with the copper losses and the magnetizing circuit losses for an imposed voltage of 60 V r.m.s and for seven in-plane orientations of the GOES stack in 120° configuration.

# Appendix D

- Comparison between flux measurements with imposed voltage and current in the 90° demonstrator

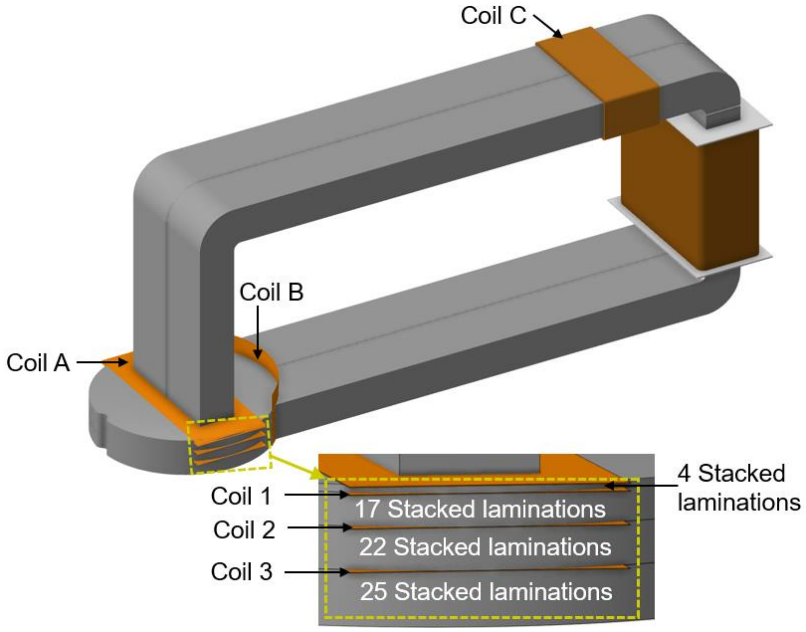


Figure D.1. Position of the coils in the 90° demonstrator.

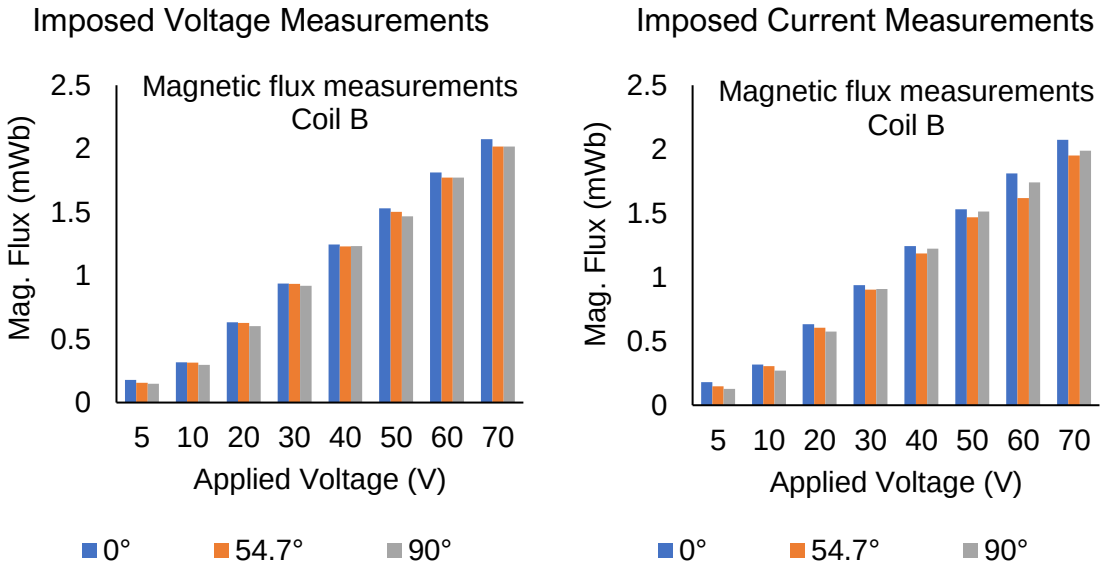


Figure D.2. Comparison of the magnetic flux measurements performed in Coil B of the 90° demonstrator, with imposed voltage and imposed current at three different in-plane orientations of the GOES stack (0°, 54.7° and 90°).

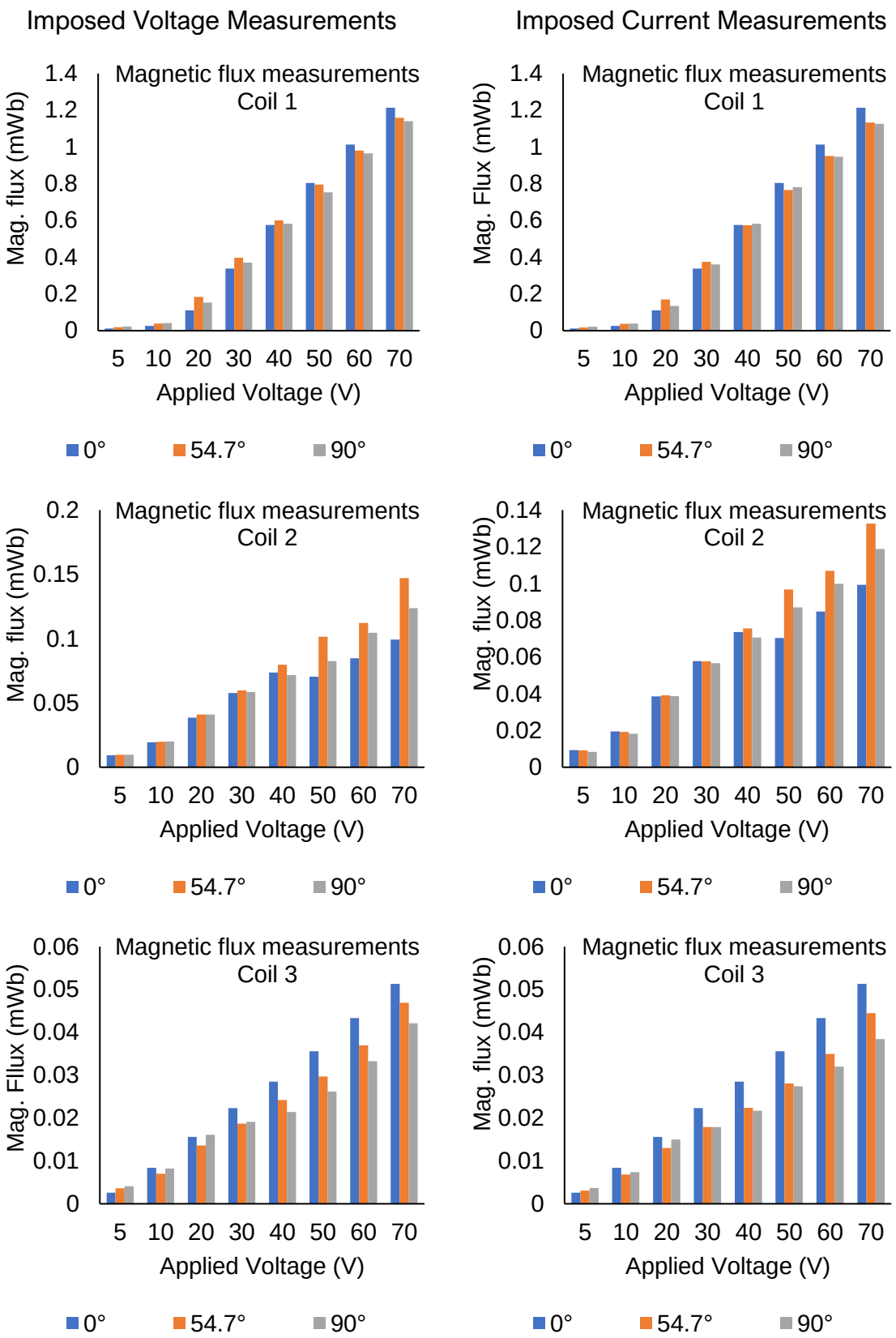


Figure D.3. Comparison of the magnetic flux measurements performed in Coils 1, 2 and 3 of the 90° demonstrator, with imposed voltage and imposed current at three different in-plane orientations of the GOES stack (0°, 54.7° and 90°).

# References

[1] "World nuclear association: Nuclear power in france," [Online]. Available: https://www.world-nuclear.org/information-library/country-profiles/countries-a-f/france.aspx. [Accessed 25 10 2021].

[2] General Electric, "Water-cooled generator (GEN-W)," 2021. [Online]. Available: https://www.ge.com/gas-power/products/generators/water-cooled. [Accessed 13 december 2021].

[3] G. Klempner and I. Kerzenbaum, Operation and Maintenance of Large Turbo-Generators, Institute of Electrical and Electrical Engineers, 2004.

[4] G. Vogt, "Etude des phénomènes électromagnétiques dans les zones frontales des grandes machines synchrones outils de test sur le 125 MW," 2013.

[5] F. Bernot, "Alternateurs synchrones de grande puissance (partie 3)," *Techniques de l'ingenieur,* 2003.

[6] X. Shi, "Contribution à la simulation du mouvement en 3D avec la méthode des éléments finis, appliquée à la modélisation des machines électriques," PhD thesis, Univ. Lille, 2005.

[7] L. James, "Large Turbine-Generators - The British Story, 15th Hunter Memorial Lecture," *Electron and Pwr.,* no. 19, pp. 304-306, 1973.

[8] A. Jack and B. Mecrow, "A Method to Calculate Turbogenerator End Region Fields and Losses and Validation using Measured Results," *IEEE Transactions on Energy Conversion,* Vols. EC-2, no. 1, pp. 100-107, 1987.

[9] G.-J. Tang, H.-C. Jiang, Y.-L. He and Q.-F. Meng, "Electromagnetic forces and mechanical responses of stator windings before and after rotor interturn short circuit in synchronous generators," *Mathematical Problems in Engineering,* vol. 2020, no. ID 5892312, p. 19, 2020.

[10] S. Pangonilo, "VER PANGONILO, PEE RPEQ," 9 January 2010. [Online]. Available: https://pangonilo.com/2010/01/insulation-class-and-temperature-rise.html. [Accessed 13 december 2021].

[11] O. Barré and B. Napame, "The insulation for machines having a high lifespan expectancy, desing, test and acceptace criteria issues," *Machines MDPI,* vol. 5, no. 7, p. 34, 2017.

[12] P. Richardson, "Stray losses in synchronous electrical machinery," *Journal of the Institution of Electrical Engineers - Part I: General,,* vol. 92, no. 59, pp. 437-438, nov. 1945.

[13] R. Winchester, "Stray Losses in the Armature End Iron of Large Turbine Generators," *Transactions of the American Institute of Electrical Engineers. Part III: Power Apparatus and Systems,* vol. 74, no. 3, pp. 381-391, 1955.

[14] R. L. Stoll and P. Hammond, "Calculation of the magnetic field of rotating machines. Part 5: Field in the end region of turbogenerators and the eddy-current loss in the end plates of stator cores," *Proceedings of the Institution of Electrical Engineers,* vol. 113, no. 11, november 1966.

[15] P. J. Lawrenson, "The magnetic field of the end-windings of turbo-generators," *Proceedings of the IEE - Part A: Power Engineering,* vol. 108, no. 42, p. 538549, 1961.

[16] J. A. Tegopoulos,, "Current Sheets Equivalent to End-Winding Currents of Turbine-Generator Stator and Rotor," *Transactions of the American Institute of Electrical Engineers. Part III: Power Apparatus and Systems,* vol. 81, no. 3, p. 695-700, april 1962.

[17] A. J. Tegopulos, "Determination of the Magnetic Field in the End Zone of Turbine Generators," *IEEE Transactions on Power Apparatus and Systems,* vol. 82, no. 67, pp. 562-572, 1963.

[18] Colot Y.; Coustere A.; Timotin, A.; Tugulea, A.; Barthelemy , J.; Roux J., "Etude théorique expérimentale des pertes par courants de Foucault crées dans les structures magnétiques feuilletées".

[19] C. J. Carpenter, "Theory of flux penetration into laminated iron and associated losses," *Proceedings of the Institution of Electrical Engineers,* vol. 124, no. 7, pp. 659-664, 1977.

[20] M. L. Barton, "Loss calculation in laminated steel utilizing anisotropic magnetic permeability," *IEEE Transactions on Power Apparatus and Systems,* Vols. PAS-99, no. 3, pp. 1280-1287, 1980.

[21] D. J. Scott, S. J. Salon and G. L. Kusik, "Electromagnetic forces on the armature end windings of large turbine generators I - steady state conditions," *IEEE Transaction on Power Apparatus and Systems,* Vols. PAS-100, no. 11, pp. 4597-4603, 1981.

[22] S. J. Salon, D. J. Scott and G. L. Kusic, "Electromagnetic Forces on the End Windings of large turbine generators II - Transient conditions," *IEEE Power Engineering Review,* Vols. PER-1, no. 11, pp. 38-39, 1981.

[23] G. K. M. Khan, "Calculation of Forces and Stresses on Generator End-Windings - Part I: Forces," *IEEE Transactions on Energy Conversion,* vol. 4, no. 4, pp. 661-670, 1989.

[24] D. Howe, B. Tech and P. Hammond, "Distribution of axial flux on the stator surfaces at the ends of turbogenerators," *Proc. IEE,* vol. 121, no. 9, pp. 980-990, 1974.

[25] D. Howe, B. Tech and P. Hammond, "Examination of the axial flux in stator cores with particular reference to turbogenerators," *Proc. IEE,* vol. 121, no. 2, pp. 1536-1542, 1974.

[26] K. Ito, T. Tokumasu, S. Nagano, M. Tari and S. Doi, "Simulation for Design Purposes of Magnetic Fields in Turbine-Driven Generator End Region," *IEEE Trans. on Power Apparatus and Syst.,* Vols. PAS-99, no. 4, pp. 1586-1596, 1980.

[27] B. Mecrow, A. Jack and C. Cross, "Electromagnetic desing of turbogenerator stator end regions," *IEEE Procedings,* vol. 136, no. 6, 1989.

[28] D. Jacobs, R. Minors, J. Steel, C. Myerscough and R. M.L.J., "Calculation of losses in the end region of turbogenerators," *Proceedings of the Institution of Electrical Engineers,* vol. 124, no. 4, pp. 356-362, 1977.

[29] V. Silva, Y. Marechal and A. Foggia, "Surface impedance method applied to the prediction of eddy currents in hydrogenerator stator end regions," *IEEE Transactions on Magnetics,* vol. 31, no. 5, pp. 2072-2075, 1995.

[30] V. Silva, G. Meurnier and A. Foggia, "A 3D finite-element computation of eddy currents and losses in the stator end laminations of large synchronous machines," *IEEE Transactions on Magnetics,* vol. 32, no. 3, pp. 1569-1572, 1996.

[31] S. Richard, "Etude electromagnetique des parties frontales des alternateurs en regimes permanent et transitoires," Grenoble, 1997.

[32] M. Fujita, T. Tokumasu, H. Yoda, H. I. K. Tsuda and S. Nagano, "Magnetic field analysis of stator core end region of large turbogenerators," *IEEE Transactions on Magnetics,,* vol. 36, no. 4, pp. 1850-1853, 2000.

[33] L. Jinxiang, S. Yutian and Y. Guijie, "Calculation and analysis of 3D magnetic field for end region of large turbogenerators," in *International Conference on Electrical Machines and Systems*, Nanjing, China, 2005.

[34] Y. Yao, H. Xia, G. Ni, X. Liang, S. Yang and P. Ni, "3-D eddy current analysis in the end region of a turbogenerator by using reduced magnetic vector potential," *IEEE Transactions on Magnetics,* vol. 42, no. 4, pp. 1323-1326, 2006.

[35] K. Yamazaki and e. al., "Eddy Current Analysis Considering Lamination for Stator Core Ends of Turbine Generators," *IEEE Trans. Magn.,* vol. 44, no. 6, pp. 1502-1505, 2008.

[36] R. Lin, A. Haavisto and A. Arkkio, "Analysis of Eddy-Current Loss in End Shield and Frame of a Large Induction Machine," *IEEE Transactions on Magnetics,* vol. 46, no. 3, pp. 942-948, 2010.

[37] H. M. Hamalainen, J. Pyrhonen, J. Nerg and J. Puranen, "3-D Finite Element Method Analysis of Additional Load Losses in the End Region of Permanent-Magnet Generators," *IEEE Trans. Magn.,* vol. 48, no. 8, pp. 2352-2357, 2012.

[38] F. Huo, W. Li, L. Wang, Y. Zhang, C. Guan and Y. Li, "Numerical Calculation and Analysis of Three-Dimensional Transient Electromagnetic Field in the End Region of Large Water–Hydrogen–Hydrogen Cooled Turbogenerator," *IEEE Trans. Ind. Electron.,* vol. 61, no. 1, pp. 188-195, 2014.

[39] J. Han, P. Zheng, Y. Sun, Y. Lv, D. Tao, B. Ge and W. Li, "Numerical analysis of end part temperature in the turbogenerator end region with magnetic shield structure under different operation conditions," *International Journal of Thermal Sciences,* vol. 132, pp. 267-274, 2018.

[40] Y. Liang, H. Yu and X. Bian, "Finite-Element Calculation of 3-D Transient Electromagnetic Field in End Region and Eddy-Current Loss Decrease in Stator End Clamping Plate of Large Hydrogenerator," *IEEE Trans. Ind. Electron.,* vol. 62, no. 12, pp. 7331-7338, 2015.

[41] K. Motoyoshi, H. Kometani, N. Sora and S. Maeda, "Large-Scale 3D Electromagnetic Field Analysis for Estimation of Stator End Region Loss in Turbine Generators," *IEEJ Journal of Industry Applications,* vol. 6, no. 6, pp. 340-345, 2017.

[42] L. Wang, W. Li, F. Huo, S. Zhang and C. Guan, "Influence of Underexcitation Operation on Electromagnetic Loss in the End Metal Parts and Stator Step Packets of a Turbogenerator," *IEEE Trans. Energy Convers.,* vol. 29, no. 3, pp. 748-757, 2014.

[43] W. Wang, A. Nysveen and N. Magnusson, "Eddy current loss in grain-oriented steel laminations due to normal leakage flux," *IEEE Transactions on Magnetics,* vol. 57, no. 6, 2021.

[44] P. Weiss, "La variation du ferromagnétisme avec la temperature," *Comptes rendus des Séances de l'Académie des Sciences,* vol. 143, pp. 1136-1139, 1906.

[45] P. Weiss, "L'hyposthèse du champ moléculaire et la propiété ferromagnétique," 1907.

[46] F. Bloch, "Zur theorie des Austauschproblems und der Temanenzerscheinung der Ferromagnetika," *Z. Physik,* Vols. 295-335, no. 74, 1932.

[47] T. Waeckerlé, "Matériaux magnétiques doux cristallins Magnétisme et métallurgie appliqués," *Techniques de l'ingénieur Matériaux magnétiques en électrotechnique,* vol. TIB259DUO, no. d2121, 2010.

[48] S. Zurek, "Two-dimensional magnetisation problems in electrical steels," 2005.

[49] H. Jordan, "Die ferromagnetischen Konstanten fur schwache Wechselfelder," *Elektr. Nach. Techn.,* vol. 1, p. 8, 1924.

[50] G. Bertotti, "General properties of power losses in soft ferromagnetic materials," *IEEE Transactions on Magnetics,* vol. 24, no. 1, pp. 621-630, January 1988.

[51] N. P. Goss, "New development in electrical strip steels characterized by fine grain structure approaching the properties of a single crystal," *Discussion - Electrical steel,* 1935.

[52] M. F. Littman, "Grain-oriented silicon steel sheets," *Journal of Magnetism and Magnetic Materials,* no. 26, pp. 1-10, 1982.

[53] N. Morito, M. Komatsubara and Y. Shimizu, "History and Recent Development of Grain Oriented Electrical Steel at Kawasaki Steel," 1998.

[54] S. Taguchi, T. Yamamoto and A. Sakakura, "New grain-oriented silicon steel with high permeability "Orientcore HI-B"," *IEEE Transactions on Magnetics,* Vols. MAG-10, no. 2, pp. 123-127, 1974.

[55] K. J. Overshott and G. E. Foot, "The effect of tensile stress on the power loss of 3% grain-oriented silicon-iron," *IEEE Transactions on magnetics,* Vols. MAG-18, no. 6, 1982.

[56] e. a. M. Mizokami, "Nippon steel's high performance grain oriented electrical steel improving properties of transformer core," *Trafotech, Session III,* vol. Paper 4, pp. 20-25, 2010.

[57] B. Fukuda, K. Sato, K. Sugiyama, A. Honda and Y. Ito, "Loss reduction in grain-oriented Si-steel sheets by new domain refining technique," in *ASM Conf. Hard and Soft Magnetic Materials Symp.*, Cincinati, 1987.

[58] P. Beckley, D. Snell and C. Lockhart, "Domain control by spark ablation," *Journal of Applied Physics,* vol. 57, no. 1, pp. 4212-4213, 1985.

[59] L. Néel, "Les lois de l'aimantation et de la subdivision en domaines élémetaires dans un monocristal de fer," *J. Phys. Rad.,* vol. 5, p. 241, 1944.

[60] F. Fiorillo, L. R. Dupré, C. Appino and A. M. Rietto, "Comprenhensive Model of Magnetization Curve, Hysteresis Loops and Losses in Any Direction in Grain-Oriented Fe-Si," *IEEE Transcantions on Magnetics,* vol. 38, no. 3, 2002.

[61] C. Appino, E. Ferrara, F. Fiorillo, C. Ragusa and O. de la Barrière, "Static and Dynamic Energy losses along different diretions in GO steel sheets," *Journal of Magnetism and magnetic materials,* vol. 500, no. 166281, 2019.

[62] H. J. Williams, "Direction of domain magnetization in powder patterns," *Physical Review,* vol. 71, pp. 646-647, 1947.

[63] IEC 60404-4, *Magnetic materials - Part 4: Methods of measurements of d.c. magnetic properties of soft materials,* 2008.

[64] IEC 60404-6, *Magnetic materials - Part 6: Methods of measurements of the magnetic properties of soft metallic and powder materials at frequencies in the range 20 Hz to 200 kHz by the use of ring specimens,* International Electrotechnical Commision, 2003.

[65] IEC 60404-3, *Magnetic materials - Part 3: Methods of measurements of the magnetic properties of electrical steel strip by means of a single sheet tester,* International Electrotechnical Commission, 2010.

[66] N. Nencib, "Conception et validation d'un dispositif de caractérisation magnétique sous excitation bidimensionelle. Comportement des tôles FeSi en "champ tournant"," 1994.

[67] N. Nencib, A. Kedous-Lebouc and B. Cornut, "2D Analysis of Rotational Loss Tester," *IEEE Transactions on magnetics,* vol. 31, no. 6, pp. 3388-3390, 1995.

[68] M. Enokizono and N. Soda, "Finite element analysis of a transformer model core with measured reluctivity tensor," *IEEE Transactions on magnetics,* vol. 33, no. 5, 1997.

[69] A. Kedous-Lebouc, O. Messal and A. Youmssi, "Joint punching and frequency effects on practical magnetic characteristcis of electrical steels for high-speed machines," *Journal of Magnetism and Magnetic Materials,* vol. 426, pp. 658-665, 2017.

[70] M. De Wulf, D. Makaveev, Y. Houbaert and J. Melkebeek, "Design and calibration aspects of small size single sheet testers," *Journal of Magnetism and Magnetic Materials,* Vols. 254-255, pp. 70-72, 2003.

[71] Z. Gmyrek, "Single sheet tester with variable dimmensions," *IEEE Trans. Instrum. Meas.,* vol. 65, no. 7, pp. 1661-1668, 2016.

[72] M. Nakaoka, A. Fukuma, H. Nakaya, D. Miyagi, M. Nakano and N. Takahashi, "Examination of temperature characteristics of magnetic properties using a single sheet tester," *IEEJ Trans. Fundal. Mater.,* vol. 125, no. 1, pp. 63-68, 2005.

[73] N. Takahashi, M. Morishita, D. Miyagi and M. Nakano, "Examination of magnetic properties of magnetic materials at high temperature using a ring speciment," *IEEE Transactions on magnetics,* vol. 46, no. 2, pp. 548-551, 2010.

[74] A. T. Bui, "Caractérisation et modélisation du comportement des matériaux magnétiques doux sous constraninte thermique," 2011.

[75] M. Jamil, "Caractérisation et investigation des effets de la température d'utilisation sur les propriétés électromagnétiques des aciers magnétiques doux," Lille, 2021.

[76] M. Bali and A. Muetze, "Modeling the effect of cutting on the magnetic properties of electrical steel sheets," *IEEE Transactions of Industrial Electronics,* vol. 64, no. 3, pp. 2547-2556, 2016.

[77] A. Schoppa, J. Schneider, C. D. Wuppermann and T. Bakon, "Influence of welding and sticking of laminations on the magnetic properties of non-oriented electrical

steels," *Journal of Magnetism and Magnetic Materials,* Vols. 254-255, pp. 367-368, 2003.

[78] E. Hug., F. Dumas, J. M. Dumas and M. Clavel, "Influence des déformations plastiques sur le comportement magnétique d'alliages fer-silicium," *Rev. Métallurgie,* vol. 91, no. 2, pp. 1857-1866, 1994.

[79] H. Helbling, A. Benabou, A. Van Gorp, M. El Youssef, A. Tounzi, W. Boughanmi and D. Laloy, "Effect on magnetic properties of inhomogeneous compressive stress in thickness direction of an electrical steel stack," *Journal of Magnetism and Magnetic Materials,* vol. 500, 2020.

[80] T. Pera, "Lois d'aimantation anisotropes et non lineaires: modelisation et validation experimentale," Grenoble, 1994.

[81] D. Jiles and D. Atherton, "Theory of ferromagnetic hysteresis," *Journal of Magnetism and Magnetic Materials,* vol. 61, no. 1, pp. 48-60, 1986.

[82] L. Rayleigh, "Notes on electricity and magnetism - iii. on the behavior of iron and steel under the operation of feeble magnetic forces," *The London, Edinburgh and Dublin Philosophical Magazine and Journal of Science,* vol. 23, no. 142, pp. 225-245, 1887.

[83] F. Z. Preisach, "Ober die magnetische Nachwirkung," *Zeitschrift für Physik,* vol. 94, pp. 277-302, 1935.

[84] D. C. Jiles, A. Ramesh and X. Fang, "Application of the anisotropic extension of the theory of hysteresis to the magnetization curves of crystalline and textured magnetic materials," *IEEE Transactions of magnetics,* vol. 33, no. 5, 1997.

[85] A. Baghel, B. Sai Ram, K. Chwastek, L. Daniel and S. Kulkarni, "Hysteresis modelling of GO lamination for arbitrary in-plane directions taking into account the dynamics of orthogonal domain walls," *Journal of Magnetism and Magnetic Materials,* no. 418, pp. 14-20, 2016.

[86] A. Di Napoli and R. Paggi, "A Model of Anisotropic Grain-Oriented Steel," *IEEE Transactions of Magnetics,* Vols. MAG-19, no. 4, 1983.

[87] O. Biro, A. Stefan, P. Kurt and C. Yu, "A modified elliptic model of anisotropy in nonlinear magnetic materials," *COMPEL,* vol. 29, no. 6, pp. 1482-1492, 2010.

[88] T. Waeckerle, L.-L. Rouve and C. Talowski, "Study of anisotropic B-H models for transformer cores," *IEEE Transactions on magnetics,* vol. 31, no. 6, 1995.

[89] F. Ossart, T. Pera and T. Waeckerle, "Field computataion in non-linearanisotropics sheets usin the coenergy Model," in *1993 Digests of International Magnetics Conference*, Stockhom, Sweden, 1993.

[90] H. Bunge, Texture Analysis Materials Science, Mathematical Models, Butterworth-Heinemann, 1982.

[91] C. M.J., "Anisotropy of steel sheets and consequence for Epstein test," in *Proceeding of XVIII IMEKO World Congress "Metrology for a Sustainable Development"*, Rio de Janeiro, Brazil, 2006.

[92] K. Chwastek, A. Baghel, M. de Campos, S. Kulkarni and J. Szczyglowski, "A Description for the Anisotropy of Magnetic Properties of Grain-Oriented Steels," *IEEE Transactions on Magnetics,* vol. 51, no. 12, 2015.

[93] F. Jiang, M. Rossi and G. Parent, "Anisotropy model for modern grain oriented electrical steel based on orientation distribution function," *AIP ADVANCES,* vol. 8, no. 056104, 2018.

[94] G. Tolentino, J. Leite, G. Parent and N. Batistela, "Implementation of the Magnetic Anisotropy in 2D Finite Element Method Using the Theory of Orientation Distribution Functions," in *IEEE 19th Biennial Conference on Electromagnetic Field Computation (CEFC)*, Pisa, Italy, 2020.

[95] F. Koji, A. Takayuki and T. Norio, "A proposal of Finite-Element Analysis Considering Two-Dimmensional Magnetic Properties," *IEEE Transactions of Magnetics,* vol. 38, no. 2, 2002.

[96] H. S. Yoon, H. E. Young, Y. Zhang, S. Pan-Seok and S. K. Chang, "Comparison of Magnetic Reluctivity Models for FEA Considering Two-Dimensional Magnetic Properties," *IEEE Transactions on Magnetics,* vol. 45, no. 3, 2009.

[97] C. Steinmetz, "On the law of hysteresis," *Proceedings of the IEEE,* vol. 72, no. 2, pp. 197-221, 1984.

[98] S. Zurek, B. Koprivica and K. Chwastek, "Extended T(x) hysteresis model with magnetic anisotropy," in *15th Selected Issues of Electrical Engineering and Electronics (WZEE)*, Zakopane, Poland, 2019.

[99] B. Daniels, T. Overboom and E. Lomonova, "Coupled statistical and dynamic loss prediction of high-permeability grain-oriented electrical steel," *The Europan Physical Journal Applied Physics,* vol. 90, no. 10901, 2020.

[100] A. Moses, "Effects of stacking methods on Epstein-square power loss measurements," *PROC. IEEE,* vol. 124, no. 4, pp. 413-416, 1977.

[101] E. Tremolet de Lacheisseire, Magnetism: Materials and Applications, Springer, 2005.

[102] F. Ossart, "Numerical simulation of Epstein frame used for anisotropy measurements," *Journal of Magnetism and Magnetic Materials,* vol. 160, pp. 71-72, 1996.

[103] T. Nakata, N. Takahashi, Y. Kawase and M. Nakano, "Influence of lamination orientation and stacking on magnetic characteristics of grain-oriented silicon steel laminations," *IEEE Transactions on magnetics,* Vols. MAG-20, no. 5, pp. 1774-1776, 1984.

[104] L. A. Millan Mirabal, O. Messal, A. Benabou, Y. Le Menach, L. Chevallier, J.-Y. Roger and J.-P. Ducreux, "Study of the effect of the demagnetizing field in Epstein strips of grain-oriented electrical steels through 3D finite element analysis," *COMPEL - The international journal for computation and mathematics in electric and electronic engineering,* 2021.

[105] N. Hihat, J.-P. Lecointe, N. Olivier, S. Duchesne, E. Napieralska and S. Wiak, "Normal permeability of grain non-oriented, grain oriented and amorphous electrical steel sheets," *International Journal of Applied Electromagnetics and Mechanics,* vol. 46, no. 349-354, 2014.

[106] *MATLAB (R2018b),* Natick, Massachusetts: The MathWorks Inc., 2018.

[107] "code_Carmel," [Online]. Available: http://code_carmel.univ-lille.fr/?q=fr/node/15. [Accessed 22 septembre 2021].

[108] E. Durant, Magnétostatique, Masson et Cie, 1958.

[109] G. Fournet, Electromagnétisme : à partir des équations locales, Paris : Masson, 1985.

[110] L. Kettunen, K. Forsman and A. Bossavit, "Gauging in whitney spaces," *IEEE Transactions on magnetics,* vol. 35, no. 3, pp. 1466-1469, 1999.

[111] E. Tonti, "Finite Formulation of Electromagnetic Fields," *ICS Newsletter,* vol. 8, no. 1, pp. 5-12, 2001.

[112] A. Bossavit, "Whitney forms: a class of finite element for three-dimensional computations in electromagnetism," *Physical Science Measurement and*

*Instrumentation, Management and Education - Reviews, IEE Procedings A,* vol. 135(8), no. 493-500, pp. 493-500, 1998.

[113] C. Johnson, "Numerical solution of partial differential equations by the finite element method," *Cambridge University Press,* 1987.

[114] N. Ida and J. Bastos, Electromagnetics and Calculation of Fields, Springer, 1997.

[115] S. A. Spornic, *Automatisation des bancs de caractérisation 2D des tôles magnétiques,* France: PhD thesis, INP Grenoble, 1998.

[116] S. A. Spornic, A. Kedous-Lehouc and B. Comut, "Waveform dependence of magnetic properties under rotating field," in *1&2DM International workshop*, Grenoble, France, Sep. 9-7, 1998.

[117] T. Booth and H. Pfutzner, "Characteristics of transformer core materials for flux normal to the sheet plane," *Journal of magnetism and magnetic materials,* vol. 133, no. 1-3, pp. 183-186, 1994.

[118] H. Pfutzner, C. Bengtsson, T. Booth, F. Loffler and K. Gramm, "Three-dimensional flux distributions in transformer cores as a function of package design," *IEEE Transactions of magnetics,* vol. 30, no. 5, pp. 2713-2727, 1994.

[119] O. Inc., "Onshape Product Development Platform," 2022. [Online]. Available: https://www.onshape.com/.

[120] EDF-CEA, "Salome Platform," 2021, 2022. [Online]. Available: https://www.salome-platform.org/.

[121] Mumps Technologies, "MUMPS: Multifrontal Massively Parallel sparse direct Solver," [Online]. Available: http://mumps.enseeiht.fr/. [Accessed 2021].

[122] A. Marrocco, "Analyse numérique des problèmes en électrotechniques," *Ann. Sc. Math,* vol. 1, pp. 271-296, 1977.